Single-Photon and Photon-Number-Resolving Detectors Based on Superconducting Nanowires

THÈSE N^{O} 4323 (2009)

PRÉSENTÉE LE 20 FÉVRIER 2009

À LA FACULTE SCIENCES DE BASE

LABORATOIRE D'OPTOÉLECTRONIQUE QUANTIQUE

PROGRAMME DOCTORAL EN PHOTONIQUE

ÉCOLE POLYTECHNIQUE FÉDÉRALE DE LAUSANNE

POUR L'OBTENTION DU GRADE DE DOCTEUR ÈS SCIENCES

PAR

Francesco MARSILI

acceptée sur proposition du jury:

Prof. O. Martin, président du jury
Prof. A. Fiore, directeur de thèse
Prof. B. Deveaud-Plédran, rapporteur
Prof. G. Goltsman, rapporteur
Dr J. Ph. Poizat, rapporteur

ÉCOLE POLYTECHNIQUE
FÉDÉRALE DE LAUSANNE

Suisse
2009

Estratto

Il rivelatore di fotone singolo a nanofilo superconduttore (SSPDs) [1] é caratterizzato da alta sensibilità nel vicino infrarosso (efficienza di rilevazione η fino al 30%, per un tasso di conteggio oscuro DK di pochi Hz), alta velocità (frequenza di ripetizione fino a ~1 GHz) ed alta risoluzione temporale (jitter di ~20 ps piena ampiezza a metà del massimo, FWHM). Questo rivelatore funziona a temperature vicino ai 4 K, cosicché può essere montato su un discendente criogenico o su un refrigeratore. Tali caratteristiche fanno dell'SSPD un rivelatore molto promettente per le applicazioni di conteggio di singoli fotoni alle lunghezze d'onda usate in telecomunicazioni. La struttura di base di un SSPD è un filo di NbN superconduttore stretto (larghezza w=50-120 nm) e sottile (spessore th~4-10 nm), ripiegato in una struttura a meandro. La tipica area attiva del rivelatore (cioè la taglia del pixel) è Ad=10 x 10 μm^2 con un fattore di riempimento (f) che varia dal 40% al 60%. I meandri sono integrati in una linea di trasmissione complanare di 50 Ω di impedenza.

L'efficienza di rivelazione dell'SSPD è attualmente limitata dal suo coefficiente di assorbimento (α). Infatti, illuminando il dispositivo anteriormente, α non può superare il 30%. Il nostro approccio per aumentare α consiste nell'integrazione dell'SSPDs con strutture ottiche avanzate come lo specchio distribuito di Bragg (DBR) e la guida d'onda ottica. Ciò implica il trasferimento dell'impegnativa tecnologia dell'SSPD (deposizione di film sottili di NbN di alta qualità e litografia elettronica ad alta risoluzione) dai substrati usuali, cioè zaffiro e MgO, che permettono la deposizione di film sottili di NbN di qualità eccellente, ad un substrato ottico come il GaAs, su cui DBRs e guide d'onda possono essere realizzati facilmente.

Il primo passo è stato dunque l'ottimizzazione di un processo per la deposizione di film di NbN di alta qualità e di pochi nanometri di spessore su GaAs e AlAs/GaAs DBRs. Per evitare l'evaporazione di As dai substrati di GaAs, la temperatura del substrato è stata limitata a 400°C durante le deposizioni. Dal momento che il GaAs e i DBRs hanno un parametro reticolare molto diverso da quello dell'NbN, i parametri di processo sono stati dapprima ottimizzati rispetto alle proprietà superconduttive dei film di NbN deposti su MgO, che permette la crescita di film di alta qualità anche a basse temperature. Ciò ha permesso di separare l'influenza della stechiometria da quella della microstruttura sulle proprietà superconduttive dei film. I parametri di deposizione ottimizzati sono stati quindi usati per crescere film di NbN su GaAs e DBRs, supponendo ragionevolmente che cambiare il substrato non producesse un cambiamento nella stechiometria del film, ma soltanto nella sua microstruttura (tale ipotesi è stata successivamente confermata). Film di NbN di spessore tra i 150 e i 3 nm sono stati quindi deposti su substrati di MgO e GaAs e su DBRs. La tecnica di deposizione impiegata è la polverizzazione DC controllata in corrente in presenza di un magnetrone (configurazione circolare, planare, bilanciata) di un bersaglio di Nb in un plasma di N_2+Ar. I film di NbN deposti su MgO hanno una temperatura critica T_C=10 K, una larghezza di transizione ΔT_C=0.8 K ed un rapporto di resistività residua RRR=R(20K)/R(300K)=0.8 per th=4 nm, che sono valori allo stato dell'arte, prova della qualità eccellente del nostro processo di deposizione a bassa temperatura. La qualità dei film deposti su GaAs e DBRs è più bassa di quella dei film deposti su MgO. Tuttavia, film di NbN spessi 5.5 nm cresciuti su GaAs hanno ancora T_C=10.7 K, ΔT_C=1.1 K e RRR=0.7, che sono proprietà simili a quelle di film spessi 4.5 nm cresciuti su MgO. Tali film di NbN cresciuti su GaAs sono quindi stati giudicati idonei per la fabbricazione di dispositivi. In letteratura non sono mai stati riportati film sottili di NbN di tale alta qualità cresciuti su GaAs e DBRs. La degradazione delle proprietà superconduttive dei film di NbN su GaAs e su DBRs è stata attribuita all'alta densità di difetti nella loro microstruttura, dovuta ad un maggiore disaccordo nel parametro reticolare tra NbN e GaAs, ed ad una più scadente qualità della superficie dei substrati. Risultati preliminari indicano che la

qualità di questi film può essere migliorata pulendo la superficie dei substrati di GaAs/DBR più efficacemente o aggiungendo uno film tampone di MgO.

Abbiamo fabbricato SSPDs su film ultrasottili di NbN (th=3-7 nm) deposti in condizioni ottimali su MgO e GaAs usando litografia elettronica e un attacco reattivo in plasma. I parametri geometrici dei nostri rivelatori sono: A_d=5x5 μm^2, w=60-200 nm, f=40%-60%. I dispositivi sono stati quindi caratterizzati elettricamente ed otticamente. Dalla misura delle curve IV di strutture di prova è stato possibile dedurre importanti parametri fisici usati come figure di merito per valutare le proprietà superconduttive dei nanofili, o per la progettazione e la simulazione dei dispositivi. La qualità dei dispositivi fabbricati su GaAs è più bassa di quella su MgO, probabilmente a causa della qualità inferiore dei film e di problemi relativi al passo di litografia elettronica. Abbiamo misurato η e DK in funzione della corrente di polarizzazione su SSPDs fabbricati su MgO e GaAs. La migliore prestazione è stata esibita da un dispositivo con w=100 nm, f=40%, th=4 nm, che ha mostrato η=20% ed una potenza equivalente di rumore NEP=10^{-16} W/$Hz^{1/2}$ (a λ=1.3 μm e T=4.2 K), che sono valori allo stato dell'arte. Non è stato possibile misurare alte efficienze su dispositivi fabbricati su GaAs, ma si noti che, attualmente, sono stati caratterizzati soltanto i dispositivi di prima generazione (cioè fabbricati su substrati di GaAs dalla superficie di qualità scadente). Migliori risultati sono auspicabili con dispositivi fabbricati su film di NbN cresciuti su substrati di GaAs puliti o con uno strato tampone di MgO. Anche se gli SSPDs fabbricati su MgO hanno mostrato alta efficienza, il rendimento del processo di fabbricazione deve essere migliorato. Le variazioni della corrente critica lungo il nanofilo sono responsabili della pesante variazione nei valori di efficienza di SSPDs nominalmente identici. Per capire l'origine fisica delle costrizioni (cioè regioni in cui la superconduttività é soppressa) del nanofilo abbiamo effettuato una caratterizzazione spaziale dell'efficienza di un lungo nanofilo, seguita da una scansione SEM (microscopio elettronico a scansione) ad alta risoluzione lungo la sua intera lunghezza. Sono stati trovati due tipi di anomalie: minimi o picchi localizzati di efficienza. I picchi corrispondono probabilmente alle costrizioni. L'osservazione SEM non ha portato alla localizzazione di alcuna costrizione geometrica nella larghezza del nanofilo alla posizione dei picchi, il che suggerisce che le costrizioni siano dovute a inomogeneità nella qualità o nello spessore del film. I minimi di efficienza sono stati invece correlati con errori litografici.

Infine, abbiamo dimostrato un nuovo rivelatore capace di contare il numero di fotoni, il rivelatore a nanofili paralleli (PND). Tale rivelatore é significativamente migliore dei dispositivi esistenti in termini di sensitività, velocità e rumore di moltiplicazione alle lunghezze d'onda usate in telecomunicazioni. In particolare, il PND è caratterizzato da una frequenza di ripetizione (80 MHz) tre ordini di grandezza maggiore di ogni altro rivelatore alle lunghezze d'onda delle telecomunicazioni e una sensitività (NEP~10^{-18} W/$Hz^{1/2}$) uno-due ordini di grandezza migliore, con l'eccezione dei sensori a transizione di soglia (TES, che però richiedono una temperatura di funzionamento molto più bassa). Abbiamo sviluppato un modello elettrico equivalente del dispositivo per studiare il suo funzionamento. Inoltre, abbiamo definito le figure di merito delle prestazioni del dispositivo in termini di efficienza, velocità e sensibilità e analizzato la loro dipendenza dai parametri di progetto. Abbiamo poi sviluppato un modello per la completa caratterizzazione del dispositivo ed un procedimento per ricostruire la statistica di numero di fotoni di una luce sconosciuta usando il PND. La ricostruzione ha successo soltanto per basse intensità luminose, molto probabilmente a causa della limitata capacità di conteggio e dell'imperfetta calibrazione del rivelatore.

Keywords: crittografia quantistica; nanostrutture; film superconduttori sottili; polverizzazione; rivelatore di singolo fotone; NEP; rumore di moltiplicazione; telecomunicazioni; NbN; MgO.

[1] G. N. Gol'tsman, O. Okunev, G. Chulkova, A. Lipatov, A. Semenov, K. Smirnov, B. Voronov, A. Dzardanov, C. Williams, and R. Sobolewski, Appl. Phys. Lett. **79**, 705 (2001).

Abstract

Nanowire superconducting single photon detectors (SSPDs) [1] are characterized by very high sensitivity in the near infrared (detection efficiency η up to 30%, for a dark count rate DK of few Hz), speed (up to ~1 GHz repetition rate) and time resolution (jitter of 20 ps full width at half maximum, FWHM). They can be operated at temperatures near 4 K, so they can be packaged in cryogenic dipsticks or cryogen-free refrigerators. This features make SSPDs the most promising detectors for telecom-wavelength single-photon counting applications. The basic structure of an SSPD is a narrow (w=50 to 120 nm), thin (th~4-10 nm) NbN superconducting nanowire folded in a meander pattern. The typical detector active area (i.e. the size of the pixel) is A_d=10 x 10 μm^2 (which allows an efficient coupling with the core of optical fibers at telecom wavelengths) with filling factor (f, the ratio of the area occupied by the superconducting meander to the device total area) ranging from 40% to 60%. The meanders are embedded in a 50 Ω coplanar transmission line.

At present, the SSPD detection efficiency is limited by its absorbance (α, the ratio of the number of photons absorbed in the nanowire to the number of incident photons on the device active area). Indeed, it has been shown that in the classic front-illumination configuration α cannot exceed 30%. Our approach to increase α consists in integrating SSPDs with advanced optical structures such as distributed Bragg reflectors (DBRs) and optical waveguides. This requires to transfer the challenging SSPD technology (i.e. the deposition of high-quality few-nm thick NbN films and the nano-patterning by electron beam lithography, EBL) from the usual comfortable substrates, i.e. sapphire and MgO, which are known to allow the deposition of few-nm thick NbN films of excellent quality, to an optical substrate like GaAs, on which DBRs and waveguides can be easily obtained.

Our first task was then to optimize a process for the deposition of high-quality few-nm thick NbN films on GaAs and AlAs/GaAs-based DBRs. Because of the requirement of compatibility with GaAs, the substrate temperature used for the depositions is 400°C, in order to prevent As evaporation. As GaAs and DBRs are highly mismatched substrates, the deposition parameters were first optimized with respect to the superconducting properties of NbN films on MgO substrates, which allow the growth of high crystal quality NbN films at low temperature. This made easier to separate the influence of stoichiometry from that of microstructure. The optimized deposition parameters were then used to grow NbN films on GaAs and DBRs, under the reasonable assumption (later checked and confirmed) that changing the substrate would not produce a change in film stoichiometry, but only in its microstructure. NbN films ranging from 150nm to 3nm in thickness were then deposited on epitaxial-quality single crystal MgO, GaAs and DBRs structures. The deposition technique is the current controlled DC magnetron sputtering (planar, circular, balanced configuration) of Nb in an Ar + N_2 plasma. NbN films deposited on MgO exhibit superconducting critical temperature T_C=10 K, superconducting transition width ΔT_C=0.8 K and residual resistivity ratio RRR=R(20K)/R(300K)=0.8 for th=4 nm, which are state of the art values, proof of the excellent quality of our low-temperature deposition process. The quality of films deposited on GaAs and on DBRs is lower than that of NbN deposited on MgO, as for any thickness they systematically exhibit higher ΔT_C and lower T_C and RRR. However, 5.5 nm-thick NbN films on GaAs still exhibit T_C= 10.7 K, ΔT_C=1.1 K and RRR=0.7, which compares with 4.5 nm thick films on MgO, making them suitable for device fabrication. To our knowledge, the growth of such high quality thin NbN films on GaAs and DBRs, has never been reported in literature. The degradation of the superconducting properties exhibited by NbN films on GaAs and DBRs was attributed to a highly defected microstructure, due both to a higher lattice misfit between NbN and GaAs and to a poorer quality of the substrate surface. Encouraging preliminary results show that the quality of these films can be improved either cleaning the GaAs/DBR substrate surface more effectively or adding an MgO buffer layer.

SSPDs were fabricated on thin NbN films (th=3-7 nm) deposited under optimal conditions on MgO and GaAs by EBL and reactive ion etching. The geometrical parameters of our detectors are: A_d=5x5 μm^2, w=60-200 nm, f=40%-60%. The devices were then characterized both electrically and optically. I-V curves of test structures were measured, from which it was possible to deduce important

physical parameters used as figures of merit to estimate the superconducting properties of the nanowires, or for the design and the simulation of the devices. The quality of the devices fabricated on GaAs is poorer than those on MgO, most likely due to the lower quality of NbN films deposited on GaAs and to issues related to the EBL nano-patterning step. Measurements of η and of DK as a function of the bias current were performed on SSPDs fabricated on MgO and GaAs. The best performance was exhibited by a w=100 nm, f=40%, th=4 nm meander, showing η=20% and noise equivalent power NEP=10^{-16} W/Hz$^{1/2}$ (at λ=1.3 μm and T=4.2 K), which are state of the art values. This result showed for the first time that high performance NbN SSPDs can be realized on a different substrate and from a deposition process at lower temperature than previously reported. High detection efficiencies could not be measured with SSPDs fabricated on GaAs, but it should be noted that at present only first-generation devices (fabricated on GaAs substrates of poor surface quality) have been tested. Better results are expected from devices fabricated on the improved NbN films grown on clean or MgO-buffered GaAs substrates. Although SSPDs on MgO have shown high detection efficiency, the fabrication yield of high performance detectors has to be improved. Variations of the critical current along a nanowire are responsible for the wide distribution in efficiency values of nominally identical SSPDs. In order to understand the physical origin of the nanowire constrictions (i.e. regions of suppressed superconductivity) we performed a spatially-resolved characterization of η of a long straight nanowire, followed by a high resolution SEM (scanning electron microscope) scan on its whole length. Two types of inhomogeneities were evidenced, corresponding to localized efficiency dips and peaks. The peaks likely correspond to constrictions. SEM observations did not evidence any width narrowing at the position of the efficiency peaks, which suggests that constrictions might be due to thickness or quality inhomogeneities of the film occurring during the film deposition or later in the process. On the other hand, the efficiency dips have been correlated with lithography problems discovered on SEM images.

Finally, a new photon number resolving detector, the Parallel Nanowire Detector (PND), has been demonstrated, which significantly outperforms existing approaches in terms of sensitivity, speed and multiplication noise in the telecommunication wavelength range. In particular, it provides a repetition rate (80 MHz) three orders of magnitude larger than any existing detector at telecom wavelength, and a sensitivity (NEP=4.2x10^{-18} W/Hz$^{1/2}$) one-two orders of magnitude better, with the exception of transition-edge sensors (which require a much lower operating temperature). An electrical equivalent model of the device was developed in order to study its operation. The modeling predicts a physical limit to the reset time of the PND, which is lower than initially estimated. Furthermore, the figures of merit of the device performance in terms of efficiency, speed and sensitivity were defined and their dependency on the design parameters analyzed. Additionally, we developed modeling tools to fully characterize the device and an algorithm to estimate the photon number statistics of an unknown light using the PND. The reconstruction proved to be successful only for low photon fluxes, most likely due to the limited counting capability and the poor calibration of the detector. The PND, with its high repetition rate and high sensitivity, is then suitable for measuring an unknown photon number probability distribution assuming accurate calibration and sufficient counting capability.

Keywords: quantum communications; quantum cryptography; low light level; photodetectors; ultrafast devices; jitter; dark counts; NEP; magnetron sputtering; subwavelength structures, nanostructures; hot spot; thin superconducting films; superconducting single photon detector; photon number resolving detector; multiplication noise; telecom wavelength; NbN; MgO.

[1] G. N. Gol'tsman, O. Okunev, G. Chulkova, A. Lipatov, A. Semenov, K. Smirnov, B. Voronov, A. Dzardanov, C. Williams, and R. Sobolewski, Appl. Phys. Lett. **79**, 705 (2001).

Single-photon and photon-number-resolving detectors based on superconducting nanowires

Dedicated to my parents.

Preface

Sed quia vera tamen ratio naturaque rerum
cogit, ades, paucis dum versibus expediamus
esse ea quae solido atque aeterno corpora constent,
semina quae rerum primordiaque esse docemus,
unde omnis rerum nunc constet summa creata. [1]

This report presents the results of four years of experimental activity carried out by the author. The contents are organized in six chapters, as described in the following.

Chapter I is an introduction to the field. First, the applications that would benefit of high performance single photon detectors at telecommunication wavelengths and the existing approaches to these detectors are reported. Then, the nanowire superconducting single photon detector (SSPD) is introduced, presenting its microscopic working principle, its performance in terms of sensitivity, time resolution and speed, and a review of its practical applications reported over the years. Finally, the applications and the existing approaches to photon number resolving detectors are reviewed.

Chapter II describes the experimental techniques used. The experimental methods used for the deposition of NbN thin films and MgO buffer layers are described, so details are given about the substrates and the deposition system used and about the deposition protocols developed. The techniques used for the characterization of the superconducting properties and the thickness of the thin films produced are then presented. Finally, the setups for the device electrical and optical characterization are detailed.

Chapter III reports the details of device fabrication. First an introduction to the field of thin superconducting film technology is given, discussing the effect of film structure on superconducting properties and the effect of deposition conditions on film structure. The characterization of NbN films deposited on MgO, GaAs and DBRs is then presented. Finally, details of the successive device fabrication steps are reported.

In chapter IV the results of the characterization of these devices are presented. The electrical characterization of SSPDs fabricated on MgO and GaAs and the optical characterization of high performance SSPDs on MgO are reported. The results of the homogeneity characterization of our nanowires are then discussed.

The subject of chapter V is a new photon number resolving detector, the parallel nanowire detector (PND), that we recently demonstrated. In this chapter we present the working principle of the device, the results of the optical characterization, an extensive analysis of the device operation and corresponding design guidelines and the first application of a PND to reconstruct an unknown incoming photon number statistics.

Finally, the conclusions are drawn and the future prospects discussed in chapter VI.

[1] Tito Lucrezio Caro, De rerum natura **I**, 498 (I Century B.C.).

Contents

I: Introduction

1. Introduction

This chapter is organized as follows. First, the applications that would benefit of high performance single photon detectors at telecommunication wavelengths and the existing approaches to these detectors are reported (section 2). Then, an introduction to the nanowire superconducting single photon detector (SSPD) is given, presenting its microscopic working principle (section 3.1), its performance in terms of sensitivity, time resolution and speed (section 3.2), and a review of its practical applications reported over the years (section 3.3). Finally, the applications and the existing approaches to photon number resolving detectors are reviewed (section 4).

2. Single Photon Detectors (SPDs) at telecommunication wavelength

2.1. Applications of SPDs

i. Quantum key distribution

Quantum key distribution (QKD) is a means of distributing secret cryptography keys between two separate parties by encoding information in the states of individual photons, which makes the communication ultimately secure by the laws of quantum mechanics [1]. Single-photon detectors are a key technology in this field.

Since the first QKD experiment (in 1992, see [2]), which used a 32-cm free-space transmission line, the key distribution distance has continued to increase. The length of a QKD link is ultimately limited by absorption in the transmission medium and by the performance of the single-photon detector in terms of speed, time jitter, dark counts and detection efficiency. Practical quantum communication systems must be compatible with the existing telecommunication silica-based optical fibers, which have minimum transmission loss at wavelengths around 1310 and 1550 nm [3]. The development of single-photon detectors (SPDs) at telecommunication wavelengths is thus critical to the implementation of quantum information technologies in the real world.

The ideal SPD for QKD would have high speed, low jitter, negligible dark counts, and high detection efficiency at telecom wavelengths. Indeed, in order to extend the length of the QKD link we need to tolerate more losses in the optical fiber. This is made possible by high detection efficiencies and low dark count rates. Also, the clock rate, and therefore the key exchange rate, depends on the jitter and on the recovery time of SPDs.

ii. Non-classical photon source characterization

Most of the early QKD experiments used the Bennett and Brassard 1984 (BB84) protocol [4] with an attenuated laser light as photon source. With this approach, secure keys could not be generated because of its vulnerability to a photon number splitting (PNS) attack [5].
A way to prevent a PNS attack is to use a deterministic single-photon source. Motivated by this reasoning, in recent years intensive research on single-photon sources was carried out worldwide [6]. Although progress has been made in the development of single-photon sources emitting at telecom wavelengths, their characterization in terms of emission lifetime (using a time-correlated single-photon counting technique [7]) and residual two-photon emission probability (using a Hambury Brown and Twiss, HBT, interferometer [8]) remains challenging, as it requires single-photon detectors.

More generally, quantum (particularly entangled) light states are very attractive for the optical implementation of quantum information and quantum cryptography. For their characterization, single photon detectors with low jitter, negligible dark counts, high detection efficiency and high speed are needed. For instance, very recently, 100-km entanglement distribution over optical fiber has been demonstrated by several groups [9, 10]. In these experiments, entanglement demonstration at longer distance was partly prevented (besides the low efficiency of the entangled-photon source) by the speed and dark count rate of the SPDs used, which substantially limited the achievable coincidence detection rates.

iii. Optical communications

Photon-counting detectors may be employed in long distance (e.g. deep space) optical communications links to reduce receiver complexity and improve receiver sensitivity [11]. However, to date these detection techniques have not been widely used, largely because available photon-counting detectors at typical telecommunication wavelengths suffer from poor detection efficiencies, low count rates, and high dark-count rates.

2.2. Approaches to SPDs

Silicon avalanche photodiodes (APDs) [12], with high detection efficiency (up to 76 % at 700 nm), low dark counts (~100 Hz) [13] and extremely low jitter (the temporal instrument response function, IRF, shows a 20 ps full width at half maximum, FWHM) [14] are the detectors of choice for visible-light photon counting, but they are insensitive to wavelengths beyond 1050 nm (Si bandgap).

For single-photon counting at telecom wavelengths, InGaAs APDs operated in Geiger mode [15] have been widely used. These detectors operate at 200K, they have detection efficiencies >20%, but their time jitter is in the 100 ps FWHM range and bias gating is essential to reduce the very high dark count rates (still >10 kHz in gated mode) [16, 17]. Moreover, count rates are limited to less than 5 MHz in order to avoid afterpulsing [18]. Recently, high-speed APD single photon detectors operating at telecom wavelength have been developed, using frequency up-conversion and a Si APD [19] and using sinusoidal gating of an InGaAs/InP APD [20]. However, the single-photon counting mechanism of APDs (ie. absorption, diffusion and avalanche) results in a non-gaussian IRF, which shows a long exponential tail [21]. This significantly affects the error probability caused by intersymbol interference in QKD systems. As a further complication, APDs are also characterized by parasitic afterglowing phenomena due to spontaneous photon emission during the avalanche process, which makes quantum communication systems more vulnerabile to eavesdropping [22].

Two new classes of superconducting devices with single photon counting capability at telecom wavelengths, the transition edge sensor (TES) and the nanowire superconducting single photon

detector (SSPD), have recently been demonstrated, which offer considerable advantages over conventional semiconductor detector technologies.
Transition edge sensors inside optical cavities [23] show extremely high (95%) detection efficiencies at telecom wavelengths and nearly zero dark counts (limited only by the background radiation), but they are affected by slow recovery times (several hundreds of nanoseconds in the best case) and by ~70 ns FWHM jitter. Furthermore, they operate at 100 mK and require a cryogenic SQUID readout, which complicates the experimental setup.

As described below, SSPDs [24], which we investigated in this report, have lower detection efficiency (up to 30% at λ=1.3 μm for a bare device [25] and to 57% at λ=1.5 μm for a device integrated in an optical cavity [26]) and finite dark counts (still in the range of few Hz [25], much lower than APDs), but they are potentially extremely fast (approaching telecommunication clock rates ~1 GHz [27]). Their IRF has a gaussian shape and shows 20 ps FWHM [28]. Furthermore, SSPDs can be operated at temperatures near 4 K, so they can be packaged in cryogenic dipsticks [29] or cryogen-free refrigerators [30]. This features make SSPDs the most promising detectors for telecom-wavelength single-photon counting applications.

3. The nanowire superconducting single photon detector (SSPD)

3.1. SSPD working principle

The basic structure of an SSPD is a narrow (width w=50 to 120 nm) thin (thickness th~4-10 nm) NbN superconducting nanowire folded in a meander pattern. The typical detector active area (i.e. the pixel size) is A_d=10 x 10 μm^2 (which allows an efficient coupling with the core of optical fibers at telecom wavelengths [3]) with filling factor (f, the ratio of the area occupied by the superconducting meander to the device total area) ranging from 40% to 60%. The meanders are embedded in a 50 Ω coplanar transmission line.

Since the working principle of SSPDs was first proposed with the Semenov, Gol'tsman, Korneev (SGK) hotspot model (2001) [31], significant advances have been made in the modeling of these detectors concerning the mechanism of photodetection [32, 33] and of dark count formation [34, 35], the jitter [36, 37], the speed limit [38] and the photo-induced normal domain size and healing time [39], which are in good agreement with experimental observations. However, at present, a comprehensive model of the physics of SSPDs is yet to be formulated. In the following, the essential lines of the Semenov, Gol'tsman, Korneev (SGK) hotspot model [31] are presented (section i). Although this model does not describe some important effects, its general principles are very intuitive, which makes it a good introduction to the field. The limits of SGK model are then analyzed, and the general aspects of its refinements are reported (see section ii).

i. The SGK hotspot model

The NbN nanowire, at a temperature well below the superconducting critical temperature T_C, is biased by a current I_B close to the superconducting critical current I_C. When a cooper pair [40] absorbs a photon of energy hν, a highly excited quasiparticle (electron) is created, whose energy is close to the incident photon energy. This high energy quasiparticle (QP) relaxes via electron-electron scattering, thus creating an avalanche of secondary QPs (Figure 3.1a). As the number of excited QPs in the avalanche increases, their average energy decreases. When the average energy reaches ~0.1 eV (approximately the Debye energy), the excited QPs relax by emitting phonons, which efficiently break

other Cooper pairs. As the average energy of the excited QPs decreases towards the superconducting energy gap Δ [40], their number increases (ideally up to ~hν/Δ) and if the rate of QP multiplication exceeds the rate of out-diffusion, their effective temperature T_e rises above T_C (Figure 3.1b).

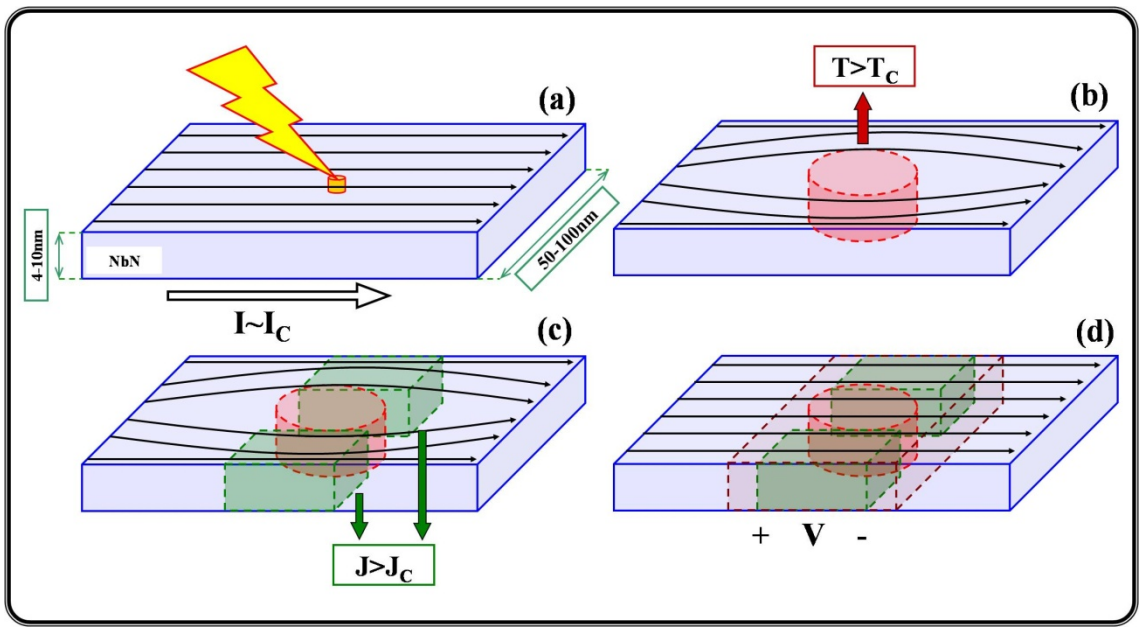

Figure 3.1. Schematics of the photo-generated hotspot (a,b) and of the current-assisted formation of a normal barrier (c,d) across an ultathin nanowire kept at temperature much lower than its T_C. The black arrows indicate the flow of the supercurrent biasing the nanowire.

The absorption of a single photon results then in the local suppression of superconductivity and the formation of a normal domain (or hot-spot), whose diameter d_{HS} is significantly smaller than the nanowire width w (see [41] for the analytical expression of d_{HS}). The appearance of a normal region in the current biased superconducting nanowire results in a redistribution of the supercurrent, which is expelled from the hotspot towards the still superconducting part of the nanowire cross section (Figure 3.1c). Therefore, the current density in the superconducting sidewalks increases and if the condition:

$$\frac{I_B}{I_C} > 1 - \frac{d_{HS}}{w} \qquad (1)$$

is satisfied, it exceeds the superconducting critical current density, which results in the formation of a resistive barrier in the entire cross-section of the nanowire (Figure 3.1d). With the proper read-out scheme ([24], chapter II) this local superconducting to normal transition can be detected. After ~30ps (the quasiparticle relaxation time τ_e [42]) from the absorption of the photon, the hotspot heals due to relaxation and outdiffusion of quasiparticles and finally collapses, so the superconductivity is restored, and the nanowire is ready to detect another photon.

ii. Limits and refinements of the SGK model

The limits of the SGK hotspot model and its refinements proposed over the years are presented in the following.

First, this model does not explain the increase of the single-photon detection efficiency η (defined as the ratio of the number of counts measured to the number of photons incident on the device active

area) with decreasing the operating temperature (observed in typical devices, [28]) and does not describe the origin of dark counts and of their exponential dependency on the bias current [28].
At present, a precise understanding of the temperature dependence of η is still lacking. On the other hand, theoretical arguments [32, 35] in good agreement with experimental evidence [34] explain the origin of dark counts and their exponential dependency on I_B/I_C as the thermal (current-assisted) unbinding of vortex-antivortex pairs (VAPs) [43] present in the nanowire.

Condition (1) implies a step-like threshold behavior in the dependency of η on the normalized bias current I_B/I_C for a given hot-spot size d_{HS}, which disagrees with experimental data. Indeed, increasing the bias current, the experimental η-I_B/I_C curves show a knee-like transition from an exponential increase at low values of I_B/I_C (i.e. below the threshold current I_B^t) to a roughly flat η at high bias (above threshold: $I_B>I_B^t$) [44]. Moreover, as d_{HS} depends on the energy of the absorbed photon, increasing with it [41], condition (1) predicts a step-like cut-off in the dependency of η on the photon wavelength λ at fixed bias current. Experiments show instead that, above the threshold wavelength ($\lambda>\lambda^t$), η decreases exponentially with increasing λ [32, 44]. The photodetection mechanism beyond cut-off was recently explained in terms of a photon-assisted VAP unbinding event, i.e. of a dark count triggered by the absorption of a low energy photon [33]. Experimental results are in very good agreement with this scenario [33, 45].

Using (1), it is possible to estimate the size of the hotspot at a given wavelength ($d_{HS}(\lambda^*)$) from the value of $I_B^t(\lambda^*)$ extracted from the experimental η-I_B/I_C curve [44], relative to the wavelength λ^*. The value of $d_{HS}(\lambda^*)$ can be cross-checked with that obtained from the analytical expression of d_{HS} [41] and from the value λ^t extracted from the experimental η-λ curve [32] measured at $I_B=I_B^t(\lambda^*)$ (so that $\lambda^*=\lambda^t$). The values of the hotspot size for infrared photons estimated in this way (using devices fabricated on "thicker" films, i.e. 5-10 nm [32, 44]) is comparable or less than the Ginsburg-Landau coherence length ξ [46] (~8nm), which makes the hotspot too small to produce the current redistribution predicted by the SGK model (as it would be tunneled by cooper pairs without energy dissipation). This discrepancy is eliminated by a refinement of the model [32], which attributes the formation of the normal domain across the nanowire to a photo-induced reduction in the concentration of superconducting electrons, which then cannot carry the bias current. In other words, this advanced model predicts that no normal spot is required for the resistive barrier to appear.

Moreover, according to [37], the current-assisted mechanism for the formation of a resistive region across the nanowire proposed by the SGK model should result in a delay between the appearance of the initial normal hotspot and the formation of the barrier due to current redistribution. This delay corresponds to the time (t_d) required by the superconducting energy gap in the still superconducting sidewalks to be reduced to zero by the overcritical current density [47]. This prediction was confirmed by experimental results [37] and a value of t_d~70 ps was measured (with a 10 nm thick, 130 nm wide SSPD at 810 nm photon wavelength). Considering both the mechanism of hotspot formation and of gap suppression, the SSPD photoresponse time was estimated to be more than twice the QP relaxation time τ_e~30 ps (i.e. ~75 ps [36]).

Even with this refinement, the SGK model overestimates the speed limit of SSPDs (which is identified with the 30 ps QP relaxation time), disregarding the influence of the nanowire kinetic inductance [38] and of the circuit in which the device is embedded [39] (see section 3.2.ii).

Finally, the picture presented above neglects the Joule self-heating of the resistive barrier produced by the bias current flowing through it. The modeling of the electrothermal response of the system right after the formation of the first normal region across the nanowire [39] predicts an enlargement of the resistive domain, which heals on larger time scales.

3.2. SSPD performance

i. Efficiency and dark counts

The efficiency of SSPDs can be quoted in several ways. Here the most used definitions will be presented and explained.

The most useful quantity from the point of view of applications is the system detection efficiency SDE, which describes the efficiency of a fiber-coupled detector. It is the ratio of the number of counts measured with the detector to the number of photons coupled to the fiber. SDE is the product of the coupling efficiency (χ) and the device single-photon detection efficiency (η): $SDE=\chi\cdot\eta$.

χ takes into account all the losses between the fiber input and the detector, and it is defined as the ratio of the number of photons that reach the device active area (A_d, i.e. the pixel size, typically 10x10 μm^2) to the number of photons coupled to the fiber. χ can be made very close to 100% through a careful design of the optical coupling system.

The device single-photon detection efficiency η is defined as the ratio of the number of counts measured to the number of photons incident on the device active area. η can be written as the product of the device absorbance α and the nanowire intrinsic single-photon detection efficiency (η^I), i.e. the probability that the absorption of a photon in the nanowire triggers the resistive state formation: $\alpha\cdot\eta^I$.

We rely on the simplified SGK hotspot model [31] to asses that η^I depends on the parameters of the superconducting material, on the nominal geometry of the nanowire (i.e. its thickness and width) and on its homogeneity [48].

The absorbance α only depends on the optical properties of the meander structure and of the incident field. An incident photon can remain unabsorbed if it is reflected or transmitted through the meander. The absorbance sets an important limitation to the SDE, as it has been shown that in the classic front-illumination configuration α cannot exceed 30% for the film thickness (~4 nm) which typically maximizes η^I [49]. Two approaches to increase α have already been demonstrated:

i. The use of back-illumination (i.e. through the substrate) which reduces the index mismatch with NbN. In this way α can be increased up to 45% [49].
ii. The integration of the SSPD with an optical cavity designed to concentrate the field in the NbN nanowires. This approach resulted in a η as high as 57% at λ=1.5 μm [26].

As both η^I and the dark count rate DK increase with the bias current (see section 3.1), the largest detection efficiency values correspond to rather high dark count rates. The optimal operation regime of the SSPD is thus a trade-off of maximum η and the highest acceptable DK.

The figure of merit for the sensitivity of the detector is expressed by the noise equivalent power (NEP), which can be defined for quantum detectors as [50] as $NEP=h\nu\sqrt{2DK}/\eta$.

The last generation of SSPDs reaches a detection efficiency of η=10 % at telecom wavelengths with dark count rate of $DK=10^{-4}$Hz, yielding a NEP in the range of 10^{-21} W/Hz$^{1/2}$ [25].

ii. Recovery time and jitter

In order to estimate the speed performance of the SSPDs, the microscopic mechanism for the formation and growth of the resistive barrier can be completely disregarded. As proposed in [38] it is sufficient to use the simple equivalent circuit illustrated in Figure 3.2a. A central feature of this model is the kinetic inductance of the wire L_{kin} [51], which can be much larger than its geometric (magnetic) inductance for thin films. The phto-induced formation of the normal hotspot is simulated by the switch opening (at t=0), so that the nanowire acquires a resistance R_{HS} for a time t_{HS}, which, neglecting the delay in the resistive state formation [37] and the Joule heating [39], can be considered of the order of

30 ps, as predicted by the SGK hotspot model. The resistance R_{out} accounts for the read-out circuit. In most cases, the read-out consists in a transmission line terminating with a matched RF preamplifier, so that R_{out}=50 Ω (see chapter II for further details). As long as the switch is open, the current flowing through the SSPD (I_{SSPD}) decays from its initial value I_B with a time constant $\tau_{fall}=L_{kin}/(R_{out}+R_{HS})$, towards a final value $I^{\infty}=I_B R_{out}/(R_{out}+R_{HS})$. This decay is interrupted when the switch closes (at $t=t_{HS}$). I_{SSPD} then recovers to its original value I_B with the time constant $\tau_{rise}=L_{kin}/R_{out}$ (Figure 3.2b).

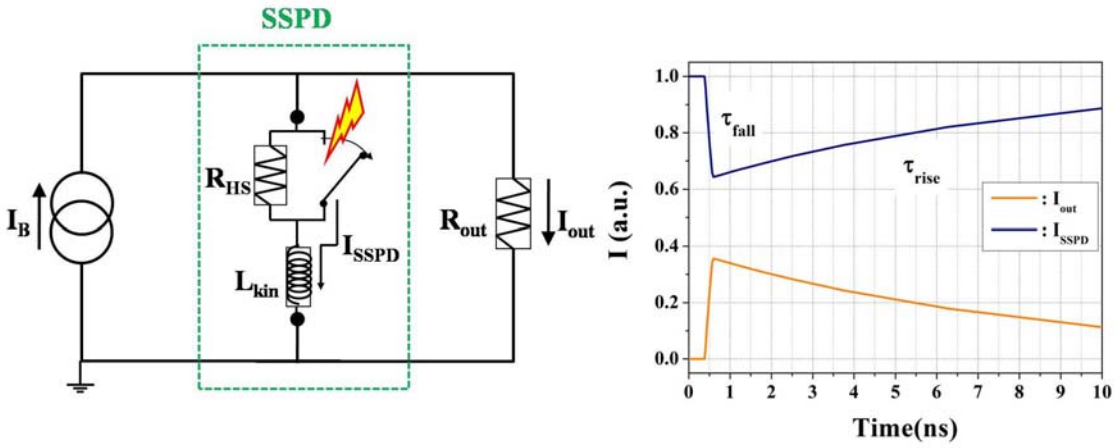

Figure 3.2. a. Equivalent electrical circuit of an SSPD. b. Inductance-limited recovery of a 10x10 μm^2 SSPD (i.e. of a 100 nm wide, 500 μm long NbN nanowire) simulated with the cricuit shown in Figure a.

As $R_{HS}>>R_{out}$=50 Ω, τ_{fall} is $<<\tau_{rise}$, which results in an asymmetric output electrical pulses (I_{out}, which is measured). The speed performance of the SSPD is then limited by τ_{rise}, i.e. by its kinetic inductance. This has important implications for high-speed applications of these devices, as explained in the following.

In order to quantify the speed of the device, we can take $f_0=(t_{reset})^{-1}$ as the maximum repetition frequency, where t_{reset} is the time that I_{SSPD} needs to recover to 95% of the bias current after a detection event (i.e. $t_{reset}\sim 3\tau_{rise}$). For a standard 10x10 μm^2 SSPD the typical value of its kinetic inductance is L_{kin}~400 nH [38], which results in a cut-off frequency below 100 MHz. However, the speed issue has been addressed with the introduction of more complex parallel structures (see [25, 27] and chapter V).

The time resolution of SSPD was characterized measuring their temporal instrument response function (IRF) in [52]. A 10x10 μm^2 SSPD was probed in single-photon detection regime with ~2 ps wide laser pulses (<70 fs optical jitter). The histogram of the photoresponse arrival time is close to a gaussian and does not have a long tail, as observed in conventional APDs. The histogram FWHM is 18 ps, which is one order of magnitude lower than the jitter values reported for InGaAs APDs. It is believed [36] that the jitter of SSPDs is due to the delayed superconducting energy gap suppression mechanism (see section 3.1.ii) during the formation of the normal barrier and that it is currently limited by "constrictions" (i.e. regions of suppressed superconductivity) in the nanowire. In support of this assessment is the decrease in the jitter observed improving the homogeneity of the nanowire width (from 35 ps [53] to 18 ps FWHM [52]).

3.3. Applications of SSPDs

The first full implementation of a fiber-based quantum key distribution (QKD) link at λ=1.550 μm using SSPDs mounted in a cryogen-free refrigerator was reported in 2006 [54]. An increase in the length of the secure link compared to that obtained with InGaAs APDs was shown, due to the lower dark count rate of SSPDs. The length of the secure link was only 42.5 km, due to the low clock rate of the system (3.3 MHz). However, due to the short recovery time and low jitter of SSPDs, it is possible to boost the system clock rate to the GHz range.
This is the approach used in [55], which reports the first QKD experiment to enable the creation of secure keys over 200 km of optical fiber (λ=1.55 μm), which at present is the longest terrestrial QKD over a fiber link. This striking result was achieved thanks to the use of a 10-GHz system clock frequency and SSPDs, with their low dark count rate and low, gaussian-shaped jitter.
This performances also allowed the demonstration of the first entanglement-based QKD experiment over a 100-km optical fiber [56].

The impressive improvement in the field of near infrared light sources characterization brought by the high time resolution and low dark counts of SSPDs was first demonstrated in [57], where quantum dot single photon emitters at λ=1.3 μm were fully characterized in terms of emission lifetime and residual two-photon emission probability with these detectors.
The low dark count rate of SSPDs also allowed the first characterization of fiber-generated entangled photon pairs (λ=1.55 μm) without any post-measurement corrections [58] (i.e. without the need of subtracting the contribution of the dark counts produced by the detectors).
Furthermore, due to the high temporal resolution of these detectors it has been possible to demonstrate for the first time [59] entanglement swapping with photon pairs [60] using completely autonomous continuous-wave photon sources which do not require any synchronization.

Finally, SSPDs were used in a photon-counting optical receiver (λ=1.55 μm) to demonstrate error-free optical communication at a data rate of 1.25 Gbit/s [61], which at present is the best performance reported for this kind of receivers.

4. Photon number resolving detectors (PNRDs)

4.1. Applications

In most single-photon detectors, a multi-photon detection event results in the same response as a single photon event, which implies that it is not possible to directly measure the number of photons in a light pulse if the pulse duration is smaller than the detector response time.
However, photon number resolving detectors (PNRDs) are required in the fields of quantum communication, quantum information processing and of quantum optics for two class of applications. In one case PNRDs are needed to reconstruct the incoming photon number statistics by ensemble measurements. This is the case of the characterization of nonclassical light sources such as single photon [62] or *n*-photon [63] sources or of the detection of PNS attacks in quantum cryptography [5]. In the second case PNRDs are needed to perform a single-shot measurement of the photon number. Applications of this kind are linear-optics quantum computing [64], quantum repeaters [65] and conditional-state preparation [66].
Moreover, a linear detector with single-photon sensitivity can also be used for measuring a temporal waveform at extremely low light levels, e.g. in long-distance optical communications, fluorescence spectroscopy, and optical time-domain reflectometry.

4.2. Approaches to PNRDs

Among the approaches proposed so far to PNR detection, detectors based on charge-integration or field-effect transistors [67-69] are affected by long integration times, leading to bandwidths <1 MHz. Transition edge sensors (TES [23, 70]) show extremely high (95%) detection efficiencies but they operate at 100 mK and show long response times (several hundreds of nanoseconds in the best case). Approaches based on photomultipliers (PMTs) [71] and avalanche diodes (APDs), such as the visible light photon counter (VLPC) [63, 72], 2D arrays of APDs [73, 74] and time-multiplexed detectors [75, 76] are not sensitive or are plagued by high dark count rate and long dead times in the telecommunication spectral windows. Arrays of SPDs additionally involve complex read-out schemes [74] or separate contacts, amplification and discrimination [77].

In this report (chapter V), an alternative approach is investigated, the Parallel Nanowire Detector (PND), which uses spatial multiplexing of superconducting nanowires on a subwavelength scale to provide a single electrical output proportional to the photon number. The device presented significantly outperforms existing PNR detectors in terms of simplicity, sensitivity, speed, and multiplication noise.

5. References

[1] N. Gisin, G. Ribordy, W. Tittel, and H. Zbinden, Rev. Mod. Phys. **74**, 145 (2002).
[2] C. H. Bennett, F. Bessette, G. Brassard, L. Salvail, and J. Smolin, J. Cryptol. **5**, 3 (1992).
[3] **www.corning.com;** SMF-28 optical fiber.
[4] C. H. Bennett, and G. Brassard, Proceedings of the International Conference on Computers, Systems & Signal Processing, Bangalore, India, 1984, Vol. 11, p. 176.
[5] G. Brassard, N. Lütkenhaus, T. Mor, and B. C. Sanders, Phys. Rev. Lett. **85**, 1330 (2000).
[6] A. J. Shields, Nature Photon. **1**, 215 (2007).
[7] W. Becker, in Advanced Time-Correlated Single Photon Counting Techniques, Springer Series in Chemical Physics Vol. 81, Springer, Berlin, 2005.
[8] R. H. Brown, and R. Q. Twiss, Nature **177**, 27 (1956).
[9] T. Honjo, H. Takesue, H. Kamada, Y. Nishida, O. Tadanaga, M. Asobe, and K. Inoue, Opt. Express **15**, 13957 (2007).
[10] H. Hübel, M. R. Vanner, T. Lederer, B. Blauensteiner, T. Lorünser, A. Poppe, and A. Zeilinger, Opt. Express **15**, 7853 (2007).
[11] J. Pierce, IEEE Trans. Commun. **26**, 1819 (1978).
[12] T. E. Ingerson, R. J. Kearney, and R. L. Coulter, Appl. Opt. **22**, 2013 (1983).
[13] P. G. Kwiat, A. M. Steinberg, R. Y. Chiao, P. H. Eberhard, and M. D. Petroff, Phys. Rev. A **48**, R867 (1993).
[14] S. Cova, A. Longoni, and A. Andreoni, Rev. Sci. Instr. **52**, 408 (1981).
[15] F. Zappa, A. Lacaita, S. Cova, and P. Webb, Opt. Lett. **19**, 846 (1994).
[16] G. G. Ribordy, N. Gisin, O. Guinnard, D. Stuck, M. Wegmuller, and H. Zbinden, J. Mod. Opt. **51**, 1381 (2004).
[17] Y. Kang, Y. H. Lo, M. Bitter, S. Kristjansson, Z. Pan, and A. Pauchard, Appl. Phys. Lett. **85**, 1668 (2004).
[18] A. Yoshizawa, R. Kaji, and H. Tsuchida, Appl. Phys. Lett. **84**, 3606 (2004).
[19] C. Langrock, E. Diamanti, R. V. Roussev, Y. Yamamoto, M. M. Fejer, and H. Takesue, Opt. Lett. **30**, 1725 (2005).
[20] N. Namekata, S. Sasamori, and S. Inoue, Opt. Express **14**, 10043 (2006).
[21] S. Cova, M. Ghioni, A. Lotito, I. Rech, and F. Zappa, J. Mod. Opt. **51**, 1267 (2004).
[22] C. Kurtsiefer, P. Zarda, S. Mayer, and H. Weinfurter, J. Mod. Opt. **48**, 2039 (2001).
[23] A. E. Lita, A. J. Miller, and S. W. Nam, Opt. Express **16**, 3032 (2008).
[24] G. N. Gol'tsman, O. Okunev, G. Chulkova, A. Lipatov, A. Semenov, K. Smirnov, B. Voronov, A. Dzardanov, C. Williams, and R. Sobolewski, Appl. Phys. Lett. **79**, 705 (2001).
[25] G. Gol'tsman *et al.*, IEEE Trans. Appl. Supercond. **17**, 246 (2007).
[26] K. M. Rosfjord, J. K. W. Yang, E. A. Dauler, A. J. Kerman, V. Anant, B. M. Voronov, G. N. Gol'tsman, and K. K. Berggren, Opt. Express **14**, 527 (2006).
[27] M. Tarkhov *et al.*, Appl. Phys. Lett. **92**, 241112 (2008).
[28] A. Korneev *et al.*, Appl. Phys. Lett. **84**, 5338 (2004).
[29] W. Słysz *et al.*, Appl. Phys. Lett. **88**, 261113 (2006).
[30] R. H. Hadfield, M. J. Stevens, S. S. Gruber, A. J. Miller, R. E. Schwall, R. P. Mirin, and S. W. Nam, Opt. Express **13**, 10846 (2005).
[31] A. D. Semenov, G. N. Gol'tsman, and A. A. Korneev, Physica C **351**, 349 (2001).
[32] A. Semenov, A. Engel, H. W. Hübers, K. Il'in, and M. Siegel, Eur. Phys. J. B **47**, 495 (2005).
[33] A. D. Semenov, P. Haas, H. W. Hübers, K. Ilin, M. Siegel, A. Kirste, T. Schurig, and A. Engel, Physica C **468**, 627 (2008).

[34] A. Engel, A. D. Semenov, H. W. Hübers, K. Il'in, and M. Siegel, Physica C **444**, 12 (2006).
[35] M. Bell, A. Sergeev, V. Mitin, J. Bird, A. Verevkin, and G. Gol'tsman, Phys. Rev. B **76**, 094521 (2007).
[36] A. Pearlman *et al.*, IEEE Trans. Appl. Supercond. **15**, 579 (2005).
[37] J. Zhang, W. Słysz, A. Pearlman, A. Verevkin, R. Sobolewski, O. Okunev, G. Chulkova, and G. N. Gol'tsman, Phys. Rev. B **67**, 1325081 (2003).
[38] A. J. Kerman, E. A. Dauler, W. E. Keicher, J. K. W. Yang, K. K. Berggren, G. Gol'tsman, and B. Voronov, Appl. Phys. Lett. **88**, 111116 (2006).
[39] J. K. W. Yang, A. J. Kerman, E. A. Dauler, V. Anant, K. M. Rosfjord, and K. K. Berggren, IEEE Trans. Appl. Supercond. **17**, 581 (2007).
[40] M. Tinkham, in Introduction to Superconductivity, McGraw Hill Inc., New York, 1996, Chap. 3.
[41] A. Semenov, A. Engel, K. Il'in, G. Gol'tsman, M. Siegel, and H. W. Hübers, Eur. Phys. J. AP **21**, 171 (2003).
[42] K. S. Il'in, M. Lindgren, M. Currie, A. D. Semenov, G. N. Gol'tsman, R. Sobolewski, S. I. Cherednichenko, and E. M. Gershenzon, Appl. Phys. Lett. **76**, 2752 (2000).
[43] J. E. Mooij, in Percolation, Localization, and Superconductivity, Plenum Press, New York, 1984, p. 325.
[44] A. Verevkin, J. Zhang, R. Sobolewski, A. Lipatov, O. Okunev, G. Chulkova, A. Korneev, K. Smimov, G. N. Gol'tsman, and A. Semenov, Appl. Phys. Lett. **80**, 4687 (2002).
[45] A. D. Semenov *et al.*, Supercond. Sci. Technol. **20**, 919 (2007).
[46] M. Tinkham, in Introduction to Superconductivity, McGraw Hill Inc., New York, 1996, Chap. 4.
[47] M. Tinkham, in Introduction to Superconductivity, McGraw Hill Inc., New York, 1996, Chap. 11.
[48] A. J. Kerman, E. A. Dauler, J. K. W. Yang, K. M. Rosfjord, V. Anant, K. K. Berggren, G. N. Gol'tsman, and B. M. Voronov, Appl. Phys. Lett. **90**, 101110 (2007).
[49] V. Anant, A. J. Kerman, E. A. Dauler, J. K. W. Yang, K. M. Rosfjord, and K. K. Berggren, Opt. Express **16**, 10750 (2008).
[50] A. J. Miller, S. W. Nam, J. M. Martinis, and A. V. Sergienko, Appl. Phys. Lett. **83**, 791 (2003).
[51] A. M. Kadin, in Introduction to superconducting circuits, Wiley, New York, 1999, Chap. 2.
[52] A. Verevkin *et al.*, J. Mod. Opt. **51**, 1447 (2004).
[53] J. Zhang, W. Slysz, A. Verevkin, O. Okunev, G. Chulkova, A. Korneev, A. Lipatov, G. N. Gol'tsman, and R. Sobolewski, IEEE Trans. Appl. Supercond. **13**, 180 (2003).
[54] R. H. Hadfield, J. L. Habif, J. Schlafer, R. E. Schwall, and S. W. Nam, Appl. Phys. Lett. **89**, 241129 (2006).
[55] H. Takesue, S. W. Nam, Q. Zhang, R. H. Hadfield, T. Honjo, K. Tamaki, and Y. Yamamoto, Nature Photon. **1**, 343 (2007).
[56] T. Honjo *et al.*, Opt. Express **16**, 19118 (2008).
[57] C. Zinoni, B. Alloing, L. H. Li, F. Marsili, A. Fiore, L. Lunghi, A. Gerardino, Y. B. Vakhtomin, K. V. Smirnov, and G. N. Gol'tsman, Appl. Phys. Lett. **91**, 031106 (2007).
[58] C. Liang, K. F. Lee, M. Medic, P. Kumar, R. H. Hadfield, and S. W. Nam, Opt. Express **15**, 1322 (2007).
[59] M. Halder, A. Beveratos, N. Gisin, V. Scarani, C. Simon, and H. Zbinden, Nature Phys. **3**, 692 (2007).
[60] B. Yurke, and D. Stoler, Phys. Rev. A **46**, 2229 (1992).

[61] E. A. Dauler *et al.*, in Advanced Photon Counting Techniques (SPIE, Boston, MA, USA, 2006), pp. 637212.
[62] Z. Yuan, B. E. Kardynal, R. M. Stevenson, A. J. Shields, C. J. Lobo, K. Cooper, N. S. Beattie, D. A. Ritchie, and M. Pepper, Science **295**, 102 (2002).
[63] E. Waks, E. Diamanti, B. C. Sanders, S. D. Bartlett, and Y. Yamamoto, Phys. Rev. Lett. **92**, 113602 (2004).
[64] E. Knill, R. Laflamme, and G. J. Milburn, Nature **409**, 46 (2001).
[65] N. Sangouard, C. Simon, J. Minar, H. Zbinden, H. de Riedmatten, and N. Gisin, Phys. Rev. A **76**, 050301 (2007).
[66] C. Sliwa, and K. Banaszek, Phys. Rev. A **67**, 030101 (2003).
[67] M. Fujiwara, and M. Sasaki, Appl. Opt. **46**, 3069 (2007).
[68] E. J. Gansen, M. A. Rowe, M. B. Greene, D. Rosenberg, T. E. Harvey, M. Y. Su, R. H. Hadfield, S. W. Nam, and R. P. Mirin, Nature Photon. **1**, 585 (2007).
[69] B. E. Kardynal, S. S. Hees, A. J. Shields, C. Nicoll, I. Farrer, and D. A. Ritchie, Appl. Phys. Lett. **90**, 181114 (2007).
[70] D. Rosenberg, A. E. Lita, A. J. Miller, and S. W. Nam, Phys. Rev. A **71**, 1 (2005).
[71] G. Zambra, M. Bondani, A. S. Spinelli, F. Paleari, and A. Andreoni, Rev. Sci. Instr. **75**, 2762 (2004).
[72] E. Waks, K. Inoue, W. D. Oliver, E. Diamanti, and Y. Yamamoto, IEEE J. Sel. Top. Quantum Electron. **9**, 1502 (2003).
[73] K. Yamamoto, K. Yamamura, K. Sato, T. Ota, H. Suzuki, and S. Ohsuka, IEEE Nuclear Science Symposium Conference Record, 2006 **2**, 1094 (2006).
[74] L. A. Jiang, E. A. Dauler, and J. T. Chang, Phys. Rev. A **75**, 62325 (2007).
[75] D. Achilles, C. Silberhorn, C. Śliwa, K. Banaszek, and I. A. Walmsley, Opt. Lett. **28**, 2387 (2003).
[76] M. J. Fitch, B. C. Jacobs, T. B. Pittman, and J. D. Franson, Phys. Rev. A **68**, 043814 (2003).
[77] E. A. Dauler, B. S. Robinson, A. J. Kerman, J. K. W. Yang, K. M. Rosfjord, V. Anant, B. Voronov, G. Gol'tsman, and K. K. Berggren, IEEE Trans. Appl. Supercond. **17**, 279 (2007).

II: Methods

1. Introduction

This chapter is organized as follows. The experimental methods used for NbN thin films depositions are described in section 2, where we present the details of the substrates (2.1) and of the DC magnetron sputtering system (2.2) used and all the deposition protocols developed (2.3). The thin film characterization is presented in section 3, where the measurement techniques for the film superconducting properties (3.1) and thickness (3.2) are described. Section 4 reports the experimental methods used for the deposition (4.1 and 4.2) and characterization (4.3) of MgO buffer layers. Finally, the setups for the device electrical and optical characterization are detailed in section 5.

2. DC reactive magnetron sputtering deposition of NbN films

2.1. Substrates used for NbN deposition

The substrates used for the deposition of NbN are MgO, GaAs, Distributed Bragg Reflector (DBR) structures fabricated on GaAs or GaAs with an MgO buffer layer on top (see section 4).

MgO substrates are square (10x10x0.25 mm^3 from *MTI corporation*, or 20x20x0.25 mm^3 from *MaTecK GmbH*), one side epi-polished and <100> oriented. Several MgO substrates from different suppliers have been compared to select the one which promotes the growth of superconducting NbN of the best quality (see chapter III).

DBR structures were fabricated on GaAs substrates by Molecular Beam Epitaxy (MBE) at EPFL by Dr. L. H. Li (design by Dr. D. Bitauld). The structure, presented in Figure 2.1, is a periodic superposition of GaAs/AlAs layers.

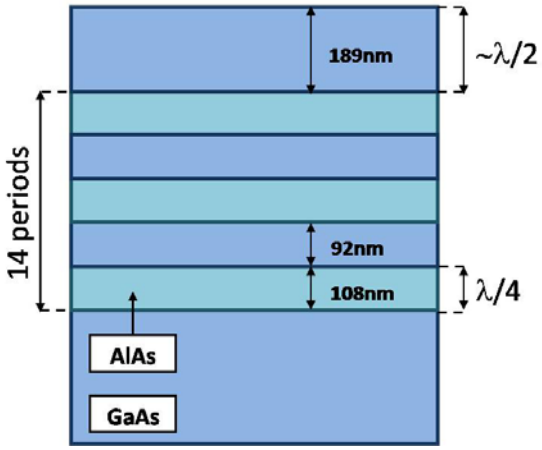

Figure 2.1. Cross-sectional view of the GaAs/AlAs DBR structure.

GaAs and DBR substrates are cleaved (usually into 10x10 mm^2 squares) from a 2" diameter, 0.35 mm thick wafer (*Wafer Technology Ltd.*), one side epi-polished, undoped and <100> oriented.

2.2. Description of the DC magnetron sputtering system

The schematics of the DC magnetron sputtering system is shown in Figure 2.2.

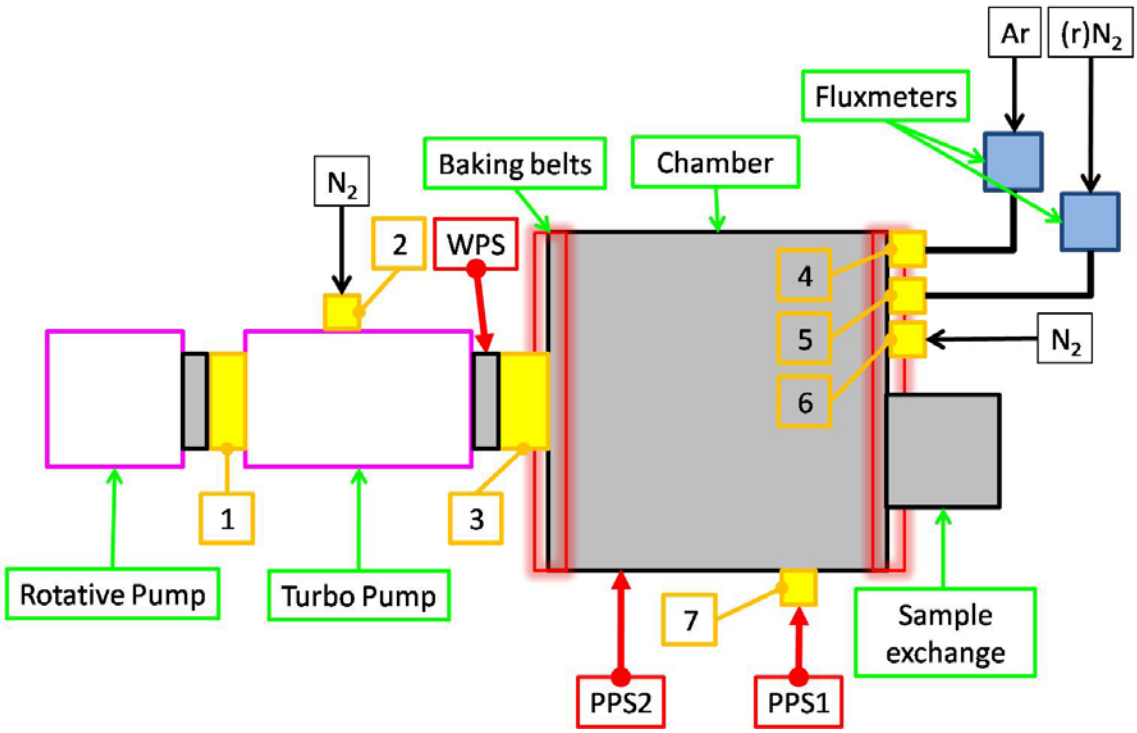

Figure 2.2. Schematics of the DC magnetron sputtering system.

Pumping group:

The pumping group consists in a rotative (primary) pump connected to the back of a turbomolecular (secondary) pump.

Valves:

The chamber is connected through five valves (3 to 7) to the pumping group (3), the process pressure sensor 1 (PPS1, 7), the venting N_2 line (6), the Ar (4) and reactive (r) N_2 (5) lines. Another two valves connect the turbomolecular pump to the rotative pump (1) and to the venting N_2 line (2). The aperture of valves (2) to (7) is controlled by the user on the valve control panel (VCP) in rack 1 (Figure 2.3). Valve (1) is controlled directly by the pump control (PC) in rack 1. All the valves except (3) are two state valves and can be commuted from the open to the closed state. Valve (3) can be set in three states: open, closed, and partially open. The aperture of valve (3) in the partially open state can be set by the user (from 0-closed to 10-open). For our process the aperture of valve (3) in the partially open state was 4. Valve (3) is switched to the partially open state before the plasma gasses are injected into the chamber, in order to prevent the pressure in the turbomolecular pump to rise above 10^{-3} mbar, which could cause damage.

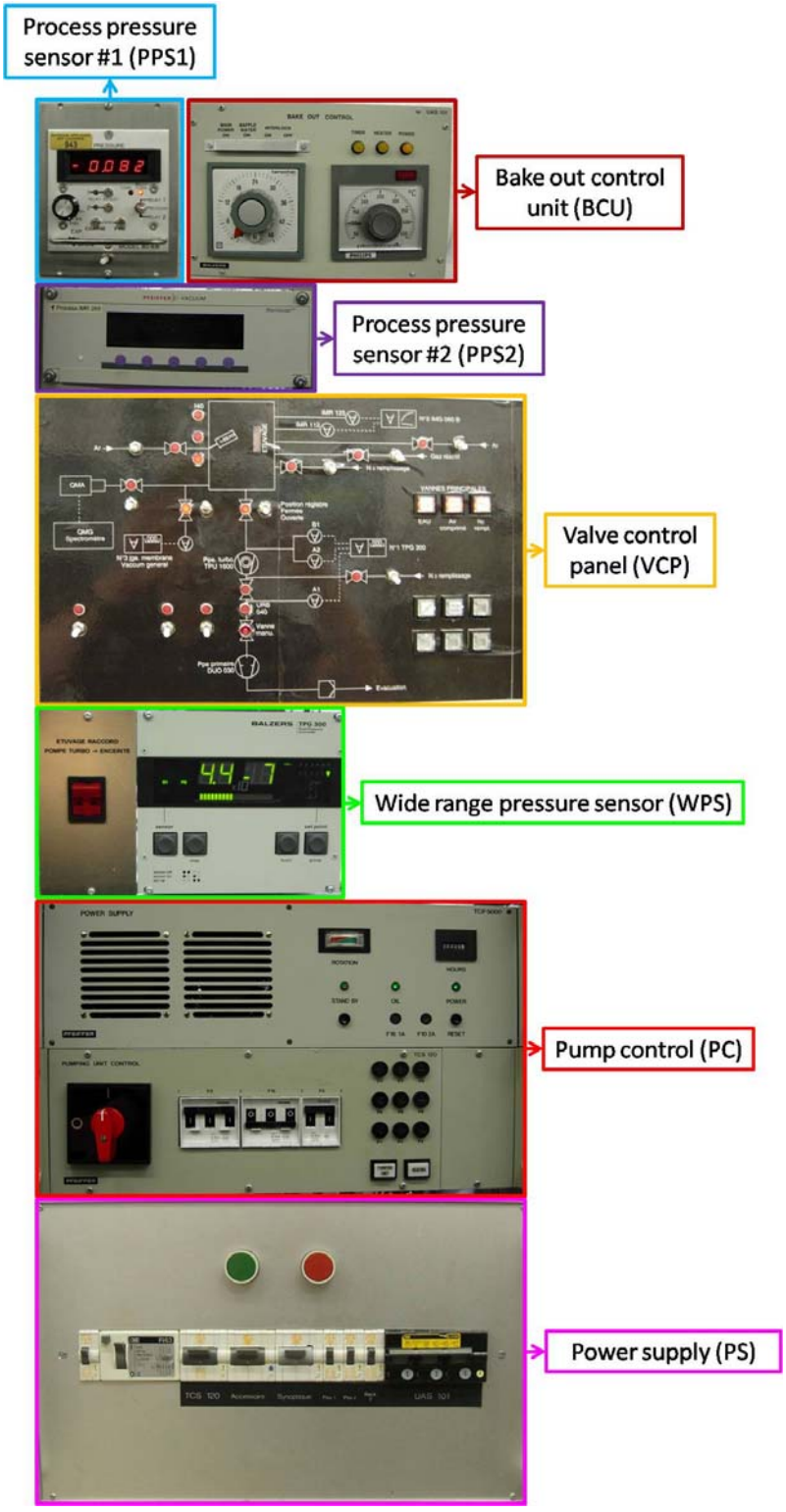

Figure 2.3. Rack 1.

Pressure sensors:

The pressure in the machine is measured by several sensors, connected at different points and whose output is read on three displays in rack 1 (Figure 2.3): the process pressure sensor 1 (PPS1), the process pressure sensor 2 (PPS2), the wide range pressure sensor (WPS).

PPS1: this unit reads the output of a capacitive pressure sensor connected to the chamber through valve (7). In this way the sensor can be excluded from the chamber ambient during the venting step, preserving the sensor from sudden pressure increases, which may cause damage to the membrane. PPS1 is used to determine the composition of the gas mixture (see section 2.3) used for the sputtering and to monitor the pressure in the chamber during the sputtering process. The reading is in mTorr. The reading has a drift with time so the read out circuit can be trimmed to set the reading back to zero. This sensor has four digit resolution and three possible ranges 1, 0.1, 0.01 mTorr. For our process only the 0.01 mTorr range is used.
PPS2: this unit reads the output of a cold cathode pressure sensor connected to the chamber. The reading is in mbar. PPS2 can also be used to monitor the pressure in the chamber during the sputtering process. This sensor has three digit resolution and the possible range is 10^{-6}-10^{-3} mbar.
WPS: this unit reads the outputs of a cold cathode and a Pirani pressure sensors connected between valve (3) and the turbomolecular pump. WPS is used to monitor the base pressure in the chamber in the pumping step and to decide when the sputtering process can be started (see section 2.3). The reading is in mbar. The range of the Pirani sensor is 1000-10^{-3} mbar. The range of the cold cathode sensor is 10^{-3}-10^{-8} mbar.

Fluxmeters:

Ar (99.9997% purity) and (r)N_2 (99.999%purity) fluxes are controlled by two fluxmeters. The fluxes are set on the fluxmeter control unit on rack 2 (see Figure 2.4). The fluxmeter control displays the value of the flux in % of 50 sccm (so if the reading of the display is for instance 20.0, the flux is 0.2x50 sccm=10 sccm).

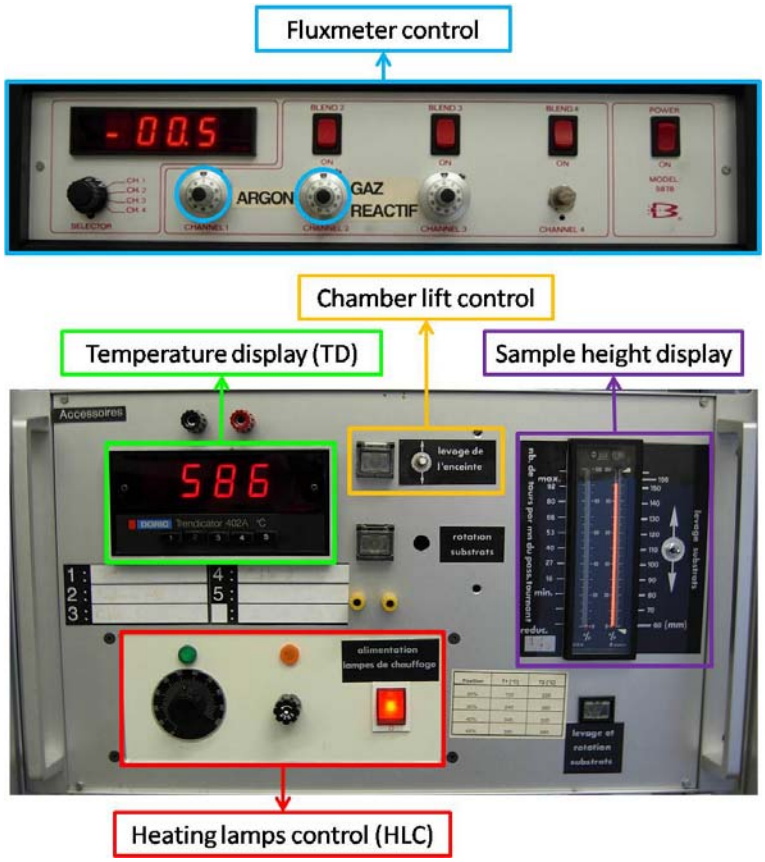

Figure 2.4. Rack 2.

Chamber:

A schematic view of the chamber is shown in Figure 2.5.

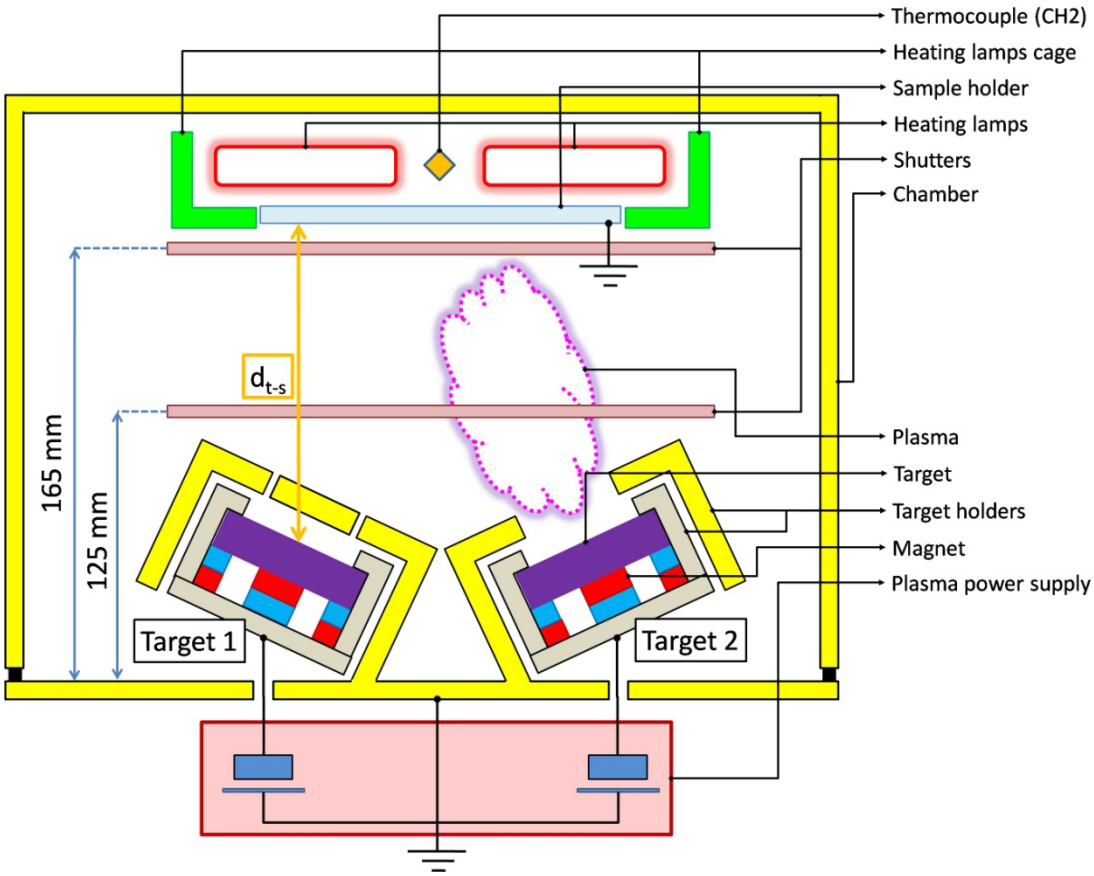

Figure 2.5. The chamber.

The chamber is equipped with two target holders, but only one (Target 2) is used for our process. The target holder consist of two pieces, an inner housing (in grey), on which the magnet and the target are mounted, and an outer shield (in yellow). The housing is connected to the negative voltage supplied by the plasma power supply unit. The shield is connected to the ground. The Nb target used are circular, 2" diameter, 99.95% purity (Kurt J. Lesker company).

The plasma power supply unit supplies the voltage to sustain the plasma. It can work in current, voltage, or power-controlled modes. For our process the current controlled mode is used. The maximum current that the unit can supply is 1A.

The chamber is equipped with two shutters, one close to the target and one close to the sample holder. The shutters are connected and they can only be moved together.

The samples are heated by two lamps, housed in a cage to prevent any deposition of material on them. The intensity of the emitted light can be set on the heating lamps control in rack 2 (Figure 2.4). MgO and GaAs are transparent in the wavelength rage where the lamps emit most of the light power, so the substrates cannot be heated by direct illumination. The substrates are instead mounted on thin a Mb holder which is heated by the lamps through irradiation and heats the substrates by conduction. The choice of Mb as a material for the sample holder is due to the combination of its high thermal conductivity (138 $W \cdot m^{-1} \cdot K^{-1}$ at 300 K), its high oxidation-resistance in air and ease of machining. To

improve thermal contact between the substrates and the holder, they are glued with liquid In (see section 2.3). Two sample holders were fabricated: a *thick* and a *thin* sample holder (see Figure 2.6).

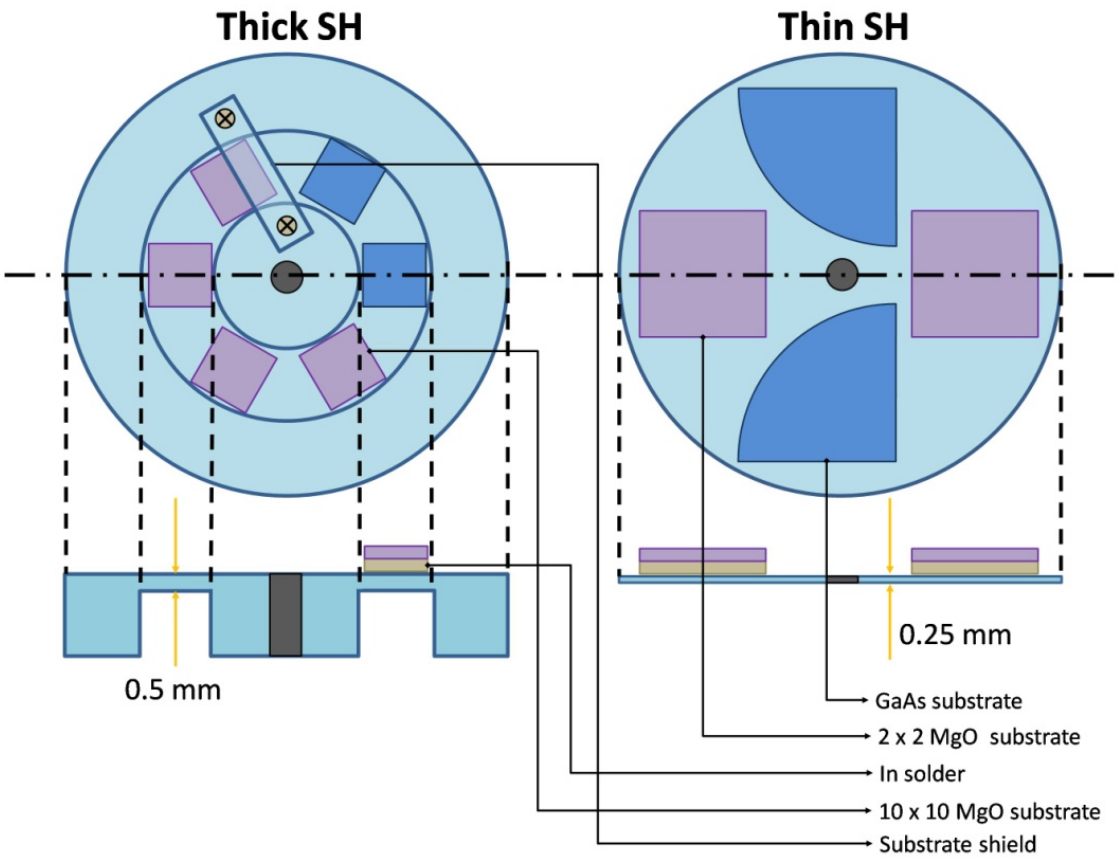

Figure 2.6. Sample holders.

The thick sample holder has an annular groove 10 mm wide where it is 0.5 mm thick. In this area up to six 10x10 mm^2 substrates can be mounted. The thin sample holder is a 0.25 mm thick disk, which can house larger substrates, such as 20x20 mm^2 MgO substrates or quarters of a GaAs wafer. When illuminated, the temperature on the surface of the thin sample holder is higher than on the thick one (see below), so the In solder gets too fluid to hold the small substrates. The thin sample holder has the advantage to allow an higher substrate temperature (for the effects of substrate temperature on the quality of NbN films, see chapter III), but it can only be used with large substrates. The thick sample holder can house only smaller substrates (10x10 mm^2 maximum) and it allows the mounting of up to three metallic shields (in stainless steel), which can be fixed by two screws as shown in Figure 2.6. The shield prevents the deposition on part of the substrate, which allows measuring the thickness of films thicker than 20nm using a profilometer (see section 3.2).

The distance between the target and the substrate holder ($d_{t\text{-}s}$) can be changed turning an external knob connected on a varistor. The resistance of the varistor gives then a measure of $d_{t\text{-}s}$, whose value can be read on a display in rack 2 (Figure 2.4).

The temperature of the substrates is monitored with a thermocouple placed in the middle of the two heating lamps, whose signal can be read on a display (TD, channel 2) in rack 2 (Figure 2.4). The maximum temperature reached is ~600°C. Another thermocouple is available (TD, channel 1) inside the chamber, which was used to measure the temperature drop from in between the heating lamps to the surface of the sample holder. When the temperature between the heating lamps was 600°C, the

temperature drop on the surface of the thick and thin sample holder was ~190°C and ~50°C, respectively.

2.3. Protocol for deposition: mounting of MgO/GaAs/DBR substrates → unmounting of NbN+MgO/GaAs/DBR samples

Venting the chamber:

1. Turn off the pumps.
2. Close valve (7).
3. Start baking the chamber at 50°C.
4. Turn off the water cooling of the targets.
5. Wait for the turbomolecular pump to slow down.
6. Let the venting N_2 in the chamber opening valves (2) and (6). Wait for the pressure to rise (~80 mbar on the WPS).
7. Take the sample exchange stage out of the chamber and unmount the sample holder. Insert the sample exchange stage back into the chamber. Unmount the samples from the sample holder (see the Unmounting samples section).
8. Open the chamber and remove the exfoliated material with the vacuum cleaner. If necessary, clean the mobile parts (see the Cleaning the mobile parts section).
9. Adjust the two shutters independently to shield the target and the sample holder.
10. Close the chamber.
11. Leave the venting N_2 flux and the baking on until a new vacuum cycle is started.

Unmounting samples:

This operation is performed on substrates (MgO, GaAs, DBRs) on which thin (3-100 nm) NbN films have been deposited. As the unmounting involves heating the substrates in air, the temperature of the hotplate and the duration of the procedure are critical (for the effect of heating, see chapter III). This operation should be completed in no more than 10 min.

1. *For thick films (more than 20 nm thick) only*: unmount the shadowing mask.
2. Put the sample holder on the hot plate set at a temperature of 245°C and let it thermalize for 2 min.
3. Unmount each sample and assign it a progressive number one sample after the other (to unmount 6 samples this step takes ~5 min).
4. Clear all the In from the SH using the tweezers and the N_2 gun.

Cleaning the mobile parts:

The mobile parts are (see Figure 2.5): the two shutters, the target holder (two pieces), the cage of the heating lamps (two pieces). It is on these parts that most of the sputtered material is deposited, so with time it can wrinkle and peel in sheets. As these sheets are conducting, they may fall on the target and create a short with the target holder and so ground the target. If this happens during a deposition, the plasma is quenched and a new vacuum cycle must be started.

1. Remove the wrinkling sheets from the mobile parts scratching with an iron brush.
2. Clean the mobile parts with isopropyl alcohol in an ultrasonic bath.
3. Dry the mobile parts with the N_2 gun.

Preparing samples:

This procedure is performed only on GaAs and DBR substrate to cleave the 2" wafer into 10x10 mm^2 squares.

1. Cleave the sample with a diamond-tip scriber. As GaAs is face centered cubic (fcc) and the substrates are <100> oriented, they can be easily cleaved into squares along the {011} or the {0-11} planes.
2. Due to the cleaving, the surface of the substrates is covered with GaAs dust, which showed to significantly degrade the quality of NbN films (see chapter III). The substrates must then be cleaned in an ultrasonic bath: 5 min in trichloroethylene, 5 min in isopropyl alcohol.

Mounting samples:

This operation is performed on bare substrates (MgO, GaAs, DBRs), so the temperature of the hotplate is not critical.

1. Put the sample holder on the hot plate set at a temperature of 315°C and let it thermalize for 1 min.
2. Put some In on the circular ring grooved in the thick sample holder and wait it to melt, then spread it uniformly in the area where the sample is to be mounted.
3. Put the substrate on the liquid In spot and rotate it to ensure a good coverage of the In on the back surface. After sticking the substrate, clear all the liquid In from around it using tweezers and the N_2 gun. Important: be extremely careful not to stick any In drops on the substrate during the sticking/clearing operation. In case of contamination, discard the substrate.
5. Take the sample holder off the hot plate, put it on its support and wait for it to cool down. *For thick films (more than 20 nm thick) only*: mount the shadowing mask.
4. Mount the sample holder on the sample exchange stage and insert it into the chamber.

Starting a vacuum cycle:

The protocol is different whether the deposition is performed on MgO or on GaAs/DBRs/MgO+GaAs. The difference lays in how long the substrates are kept at 400°C, which can be days for MgO but can't be longer than 6 hr for GaAs. This is due to the fact that heating GaAs in vacuum even at 400°C causes As evaporation, resulting in a deviation of the DBR reflectivity spectrum from the designed one (see cap III).

1. Stop the venting N_2 flow to the pumps and to the chamber closing valves (2) and (6). Turn off the baking.
2. Start the pumping group.
3. When the pressure on the WPS is ~$1x10^{-2}$ mbar, start baking the chamber at 100°C, open the valve to the PPS1, start the cooling of the targets.

For chamber/target conditioning:

4. Start the heating lamps.
5. Wait at least 6 hr pumping. The base pressure to be attained is at least ~$5x10^{-7}$ mbar on the WPS.

For depositions on MgO substrates:

4. Start the heating lamps.
5. Wait at least 12 hr pumping. The baking must be stopped at least 4 hr before the deposition. The base pressure to be attained for the deposition is ~$1x10^{-7}$ mbar on the WPS.

For depositions on GaAs/DBR substrates:

4. Wait at least 12 hr pumping. The baking must be stopped at least 4 hr before the next step. The base pressure to be attained is ~$1x10^{-7}$ mbar on the WPS.
5. Start the heating lamps. The pressure in the chamber rises. Wait for the base pressure to decrease below ~$3x10^{-7}$ mbar on the WPS (normally in 3-4 hr).

6. Start the deposition (see the Deposition section).

Conditioning the chamber:

This operation is performed before starting a deposition cycle, in case another material had been sputtered in the chamber.

1. Mount an old grooved target on the target holder T2.
2. Mount the sample holder on the sample exchange stage (performing a sputtering step without the sample holder results in a deposition on the heating lamps, which is to be avoided).
3. Start the vacuum (see the Starting a vacuum cycle section).
4. Open the Ar and (r)N_2 lines to the chamber opening valves (4) and (5), respectively. The base pressure might increase because of some residual gas in the lines. Wait for the pressure to decrease again down to ~$5x10^{-7}$ mbar on the WPS (~5 min).
5. Change the aperture of valve (3) between the chamber and the pump from fully open to partially open. The value of pressure read on the WPS decreases, because the sensors are connected to the ambient after the valve on the side of the turbomolecular pump (see Figure 2.2).
6. Trim the PPS1 and set its reading to zero.
7. Set the Ar flux (f_{Ar}) to obtain a value of the Ar pressure on the PPS1 of P_{Ar}=1.675 mTorr. Set the N_2 flux (f_{N2}) to obtain a value of the total pressure on the PPS1 of P_{tot}=2.5 mTorr.
8. Turn the plasma on in current-controlled mode with cathode current I_c=250mA. Record the initial cathode voltage $V_c^{(i)}$.
9. Keep the plasma on for 1 hr. Keep the shutters on.
10. Record the final cathode voltage $V_c^{(f)}$. Turn the plasma off.
11. Turn the heating lamps off.
12. Wait the temperature on the TD (channel2) to decrease below 40°C.
13. Open the chamber (see the Opening the chamber section).

Conditioning the target:

This operation is performed on fresh Nb targets.

In planar circular magnetron configurations plasma electrons are forced away from the center and the edges of the target where the magnetic field converges toward the magnets [1] and they are compressed in at an intermediate radius, where the plasma and the ion bombardment of the target are most intense. This results in an annular trenched erosion pattern of the target [2] (Figure 2.7).

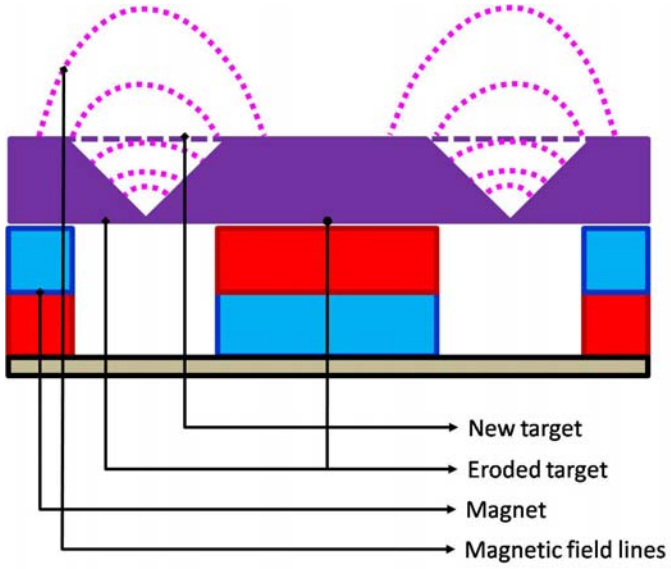

Figure 2.7. Cross-sectional view of the target (eroded in solid purple and fresh in dashed purple), of the magnets and of the magnetic field lines.

Operating voltages are lower for eroded targets due to the significant increase in the effective area. When using a fresh target, the voltage required to sustain the optimized plasma used to sputter the optimum superconducting films is too high for the plasma power supply.
For this reason fresh targets need to be conditioned, i.e. eroded to the point the optimized plasma can be sustained.

1. Mount an new target on the target holder T2.
2. Mount the sample holder on the sample exchange stage (performing a sputtering step without the sample holder results in a deposition on the heating lamps, which is to be avoided).
3. Start the vacuum (see the Starting a vacuum cycle section).
4. Open valves (4) and (5). The base pressure might increase because of some residual gas in the lines. Wait for the pressure to decrease again down to ~$5x10^{-7}$ mbar on the WPS (~5 min).
5. Change the aperture of valve (3) fully open to partially open.
6. Trim the PPS1 and set its reading to zero.
7. Set the Ar flux to 40 on the fluxmeter control unit (0.4x50 sccm=20 sccm). Wait 5 min for the Ar pressure reading on the PPS1 (P_{Ar}) to be stable at P_{Ar}~3.800 mTorr.
8. Turn the plasma on in current-controlled mode with I_c=250 mA. Record the cathode voltage $V_c^{(i)}$ (it should be ~500 V).
9. Keep the plasma on for 3 hr. Keep the plasma shuttered.
10. Record the cathode voltage$V_c^{(f)}$. Its value should be significantly lower $V_c^{(i)}$ (~390 V) because of the target erosion. Turn the plasma off.
11. Turn off the heating lamps.
12. Wait the temperature on the TD (channel 2) to decrease below 40°C.
13. Open the chamber (see the Opening the chamber section).

Deposition:

1. Start the vacuum (see the Starting a vacuum cycle section).

2. Open the valves (4) and (5). The base pressure might increase because of some residual gas in the lines. Wait for the pressure to decrease again down to ~$5x10^{-7}$ mbar on the WPS (~5 min).
3. Change the aperture of valve (3) fully open to partially open.
4. Trim the PPS1 and set its reading to zero.
5. Set the Ar flux (f_{Ar}) to obtain the desired Ar pressure on the PPS1 (P_{Ar}).
6. Wait 15 min for P_{Ar} to be stable.
7. P_{Ar} may have drifted, in this case set f_{Ar} again to obtain the desired P_{Ar}.
8. Wait 15 min for P_{Ar} to be stable.
9. P_{Ar} may have drifted, in this case set f_{Ar} again to obtain the desired P_{Ar}. Note down this last value of f_{Ar}.
10. Set the (r)N_2 flux (f_{N2}) to obtain the desired total pressure on the PPS1 (P_{tot}).
11. Wait 10 min for P_{tot} to be stable.
12. P_{tot} may have drifted, in this case set f_{N2} again to obtain the desired P_{tot}.
13. Wait 10 min for P_{tot} to be stable.
14. P_{tot} may have drifted, in this case set f_{N2} again to obtain the desired P_{tot}. Note down this last value of f_{N2}.
15. Turn the plasma on in current-controlled mode with I_c=250mA. Important: the optimized values of P_{tot} and P_{N2}/P_{tot}, which allow the deposition of high quality superconducting films, are such that the plasma will not start because its impedance is too high.
    To start the plasma:
    i. Set the f_{Ar} to 30 on the fluxmeter control unit and start the plasma (which will start).
    ii. Wait ~1 min. In this phase fresh Nb is exposed on the target.
    iii. Slowly decrease the Ar flux down to the value noted at step 9.
16. *For thick films (above 20 nm):* wait for the cathode voltage V_c to be stable. V_c is considered stable if it varies of no more than +/- 1 V in 10 min.
    For thin films (below 20 nm): wait 10 min.
17. Note down the steady value of V_c Note down the presputtering time. Note down the temperature reading on the TD, channel2 (it should be ~600°C).
18. Open the shutters and start the chronometer.
    For thick films (above 20 nm): note down V_c and P_{tot} every 2 min.
    For thin films (below 20 nm): note down V_c and P_{tot}.
    Wait for the deposition time (T_d) to expire. T_d is given by the nominal thickness (th_n) that the film to be grown is expected to have, divided by the nominal deposition rate ($r_d^{(n)}$, see the Calculating the nominal deposition rate section).
19. Turn the plasma off.
20. Wait 1 min, then note down P_{tot}.
21. Set f_{N2} to zero. Wait 1 min, then note down P_{Ar}.
22. Set f_{Ar} to zero. Wait 1 min, then note down the reading of the PPS1. The drift of the zero during the deposition should be within +/- 0.010 mTorr.
23. Turn the heating lamps off.
24. Close valves (4) and (5). Switch valve (3) to open position.
25. Wait the temperature on the TD (channel2) to decrease below 40°C (~6 hr).
26. Open the chamber (see the Opening the chamber section).

Calculating rate:

In case the deposition is the first after the target conditioning step, T_d is given by the ratio of the nominal thickness th_n to the measured deposition rate (i.e. measured thickness / deposition time) of the

first deposition performed after the conditioning of the previous target. Otherwise, T_d is given by the ratio of the nominal thickness th_n to the measured deposition rate of the previous deposition.
The deposition rates for the optimized deposition parameters are in the range of few Å/s.

3. Thin film characterization

3.1. Electrical characterization

The superconducting properties of different samples are estimated and compared using four parameters: the superconducting critical temperature (T_C), the superconducting transition width (ΔT_C), the residual resistivity ratio (RRR) and the superconducting critical current density (J_C). In the following sections, the experimental procedures used to measure these parameters are presented.

i. T_C, ΔT_C, RRR measurements on films

The superconducting critical temperature (T_C), the superconducting transition width (ΔT_C), and the residual resistivity ratio (RRR) of films are extrapolated from the measurement of their resistance as a function of temperature (R vs T). The setup used for these measurements shown in Figure 3.1.

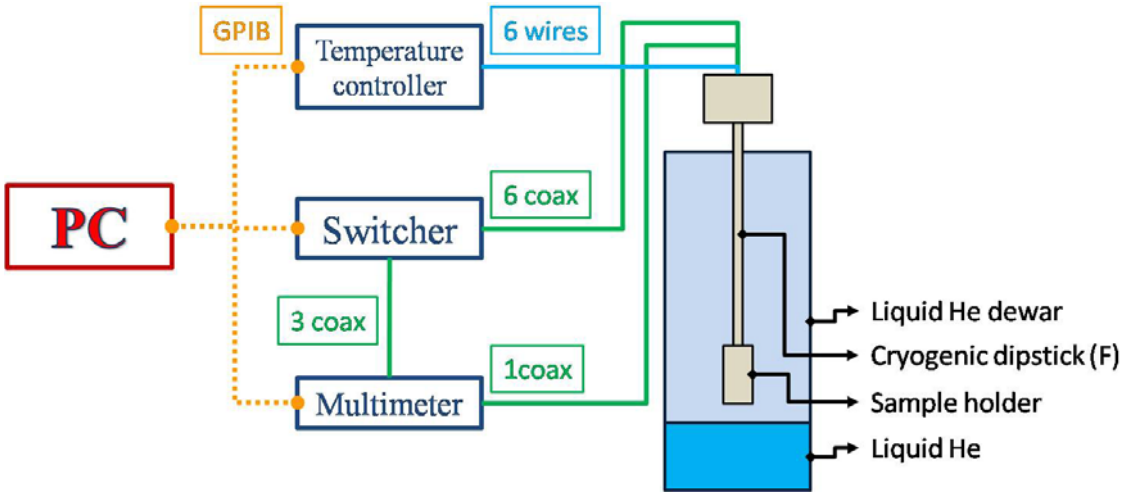

Figure 3.1. Block diagram of the set-up for R vs T measurements. The temperature controller is a Conductus LTC10 or a Lake Shore 325 , the switcher is a HP 3488A, the multimeter is an HP 3458A.

The sample holder

Samples are mounted on a cryogenic dipstick (F-dipstick) and inserted in a liquid He dewar. The sample holder of the F-dipstick is sketched in Figure 3.2. The temperature of the samples is measured with a Si diode temperature sensor (in green) housed in the body of the sample holder underneath the samples, whose signal is sent to the temperature controller (Conductus, LTC10 or Lake Shore, 325). Temperature is measured using four wires: two wires to supply the bias current (10 μA) and two to measure the voltage. The sample holder is held above the liquid He level in the cold He vapors, so the temperature of the samples can be varied changing the power dissipated in a strip line thin film resistor (in light red) in thermal contact with the sample holder. The control of temperature is performed by the temperature controller which uses a Proportional-Integral-Derivative (PID) feedback technique to control the current flowing through the resistor (2 wires). The body of the sample holder is in copper (in light orange), allowing a good thermal coupling between the strip line resistor, the temperature

sensor and the sample, which are centered one respect to the other and stacked one above the other, being separated by just 0.5 mm of copper. The cable feed-trough are sealed using cryogenic varnish (Lake Shore, VGE-7031) and a sealing cap can be screwed on top of the sample holder. Samples are then sealed and not directly in contact with liquid He or its gases and they can exchange heat only by conduction, mostly through copper, which makes the reading of the temperature sensor a reliable estimate of the actual temperature of the samples.

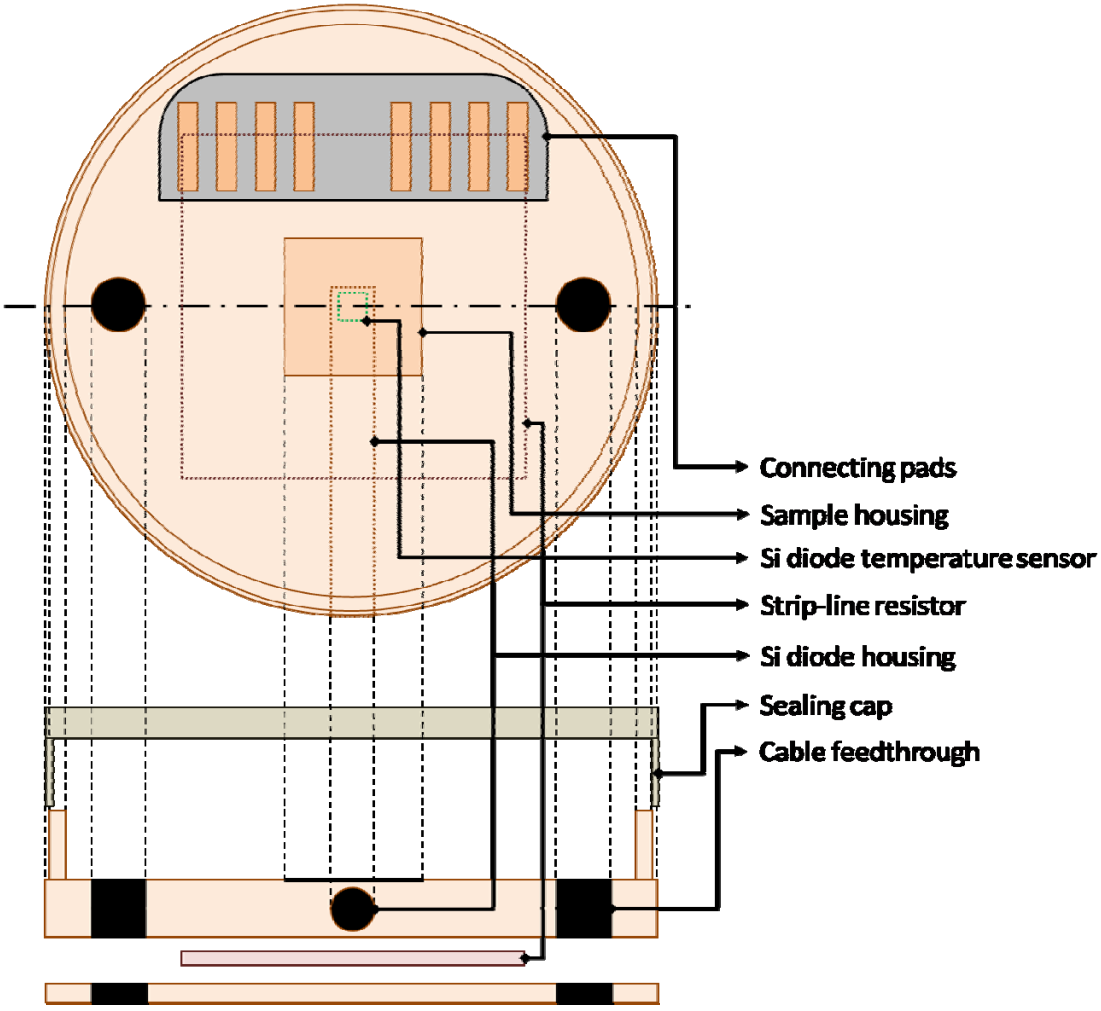

Figure 3.2. Sample Holder of the F-dipstick.

Sample preparation

After unmounting samples from the sputtering machine (see section 2.3), the steps to follow to prepare them for R vs T measurements are the following:

1. Cleave the sample with a diamond-tip scriber. As the substrates (MgO, GaAs) are both face centered cubic (fcc) and <100> oriented, they can be easily cleaved along the {011} or the {0-11} planes (Figure 3.3(a)). A 1 mm wide stripe must first be cleaved and discarded (Figure 3.3(b)) as the quality of the film might be lower on the border of the sample. Then a 3 mm wide stripe is cleaved (Figure 3.3(c)), which is used for T_C/I_C measurements. The remaining part is used for thickness measurements (see section 3.2).

2. Crush In balls at the four edges of the sample (Figure 3.3(d)), in order to make them stick on the NbN film. These In contacts allow a cold soldering to the wires of the sample holder.
3. Glue the sample to the sample housing graved in the sample holder (Figure 3.3(e)) using cryogenic varnish (Lake Shore, VGE-7031).
4. Stick the Cu wires of the sample holder to the In contacts fabricated at step 2 and crush another In ball on each contact (Figure 3.3(f)).

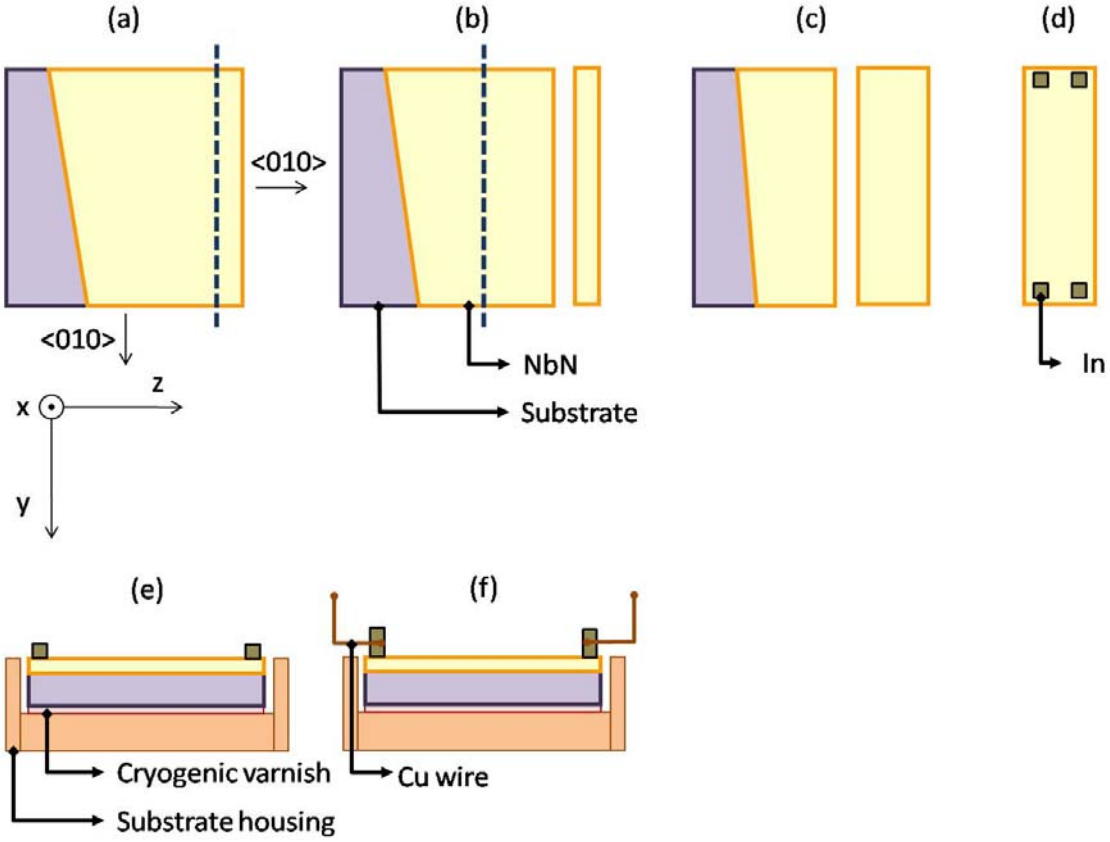

Figure 3.3. Sample preparation flow for R vs T measurements.

Electrical path

The electrical path of the set-up is sketched in Figure 3.4. Up to two samples can be tested in the same temperature sweep cycle. Each sample is soldered to four Cu wires using In solder. The Cu wires are soldered with Sn to the Cu pad of the sample holder. Phosphor-bronze (Cu-Sn-P alloy) wires (Lake Shore, QL-32) are Sn-soldered to the same pads and make the connection to cryogenic coaxial cables (Lake Shore, Type C: solid copper center conductor, aluminized shield). Having a high thermal resistance, the phosphor bronze wires are used to reduce the heat flow from room temperature to the samples through the cables. The cryogenic coaxial cables are then Sn-soldered to room temperature BNC coaxial connectors. The two samples are connected to a switcher (HP 3488A), which closes the connection between either of them and a multimeter (HP 3458A). The multimeter performs a resistance measurement in the four-wire configuration (with a bias current of 50 μA).

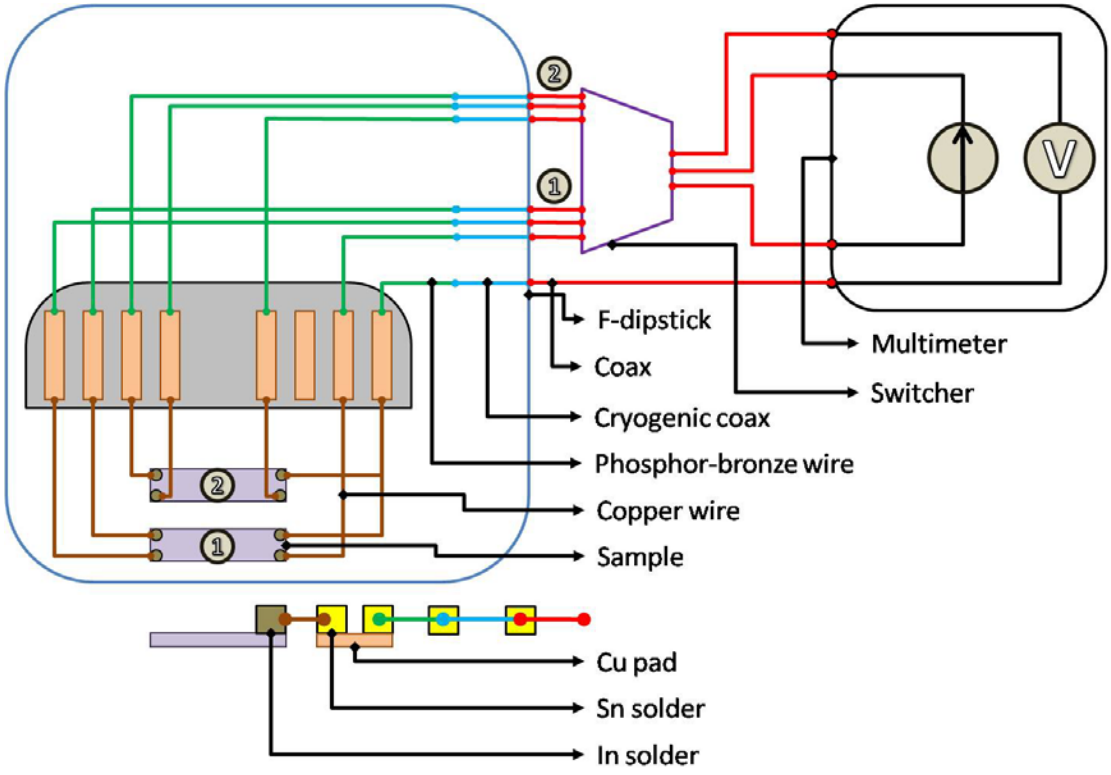

Figure 3.4. Sketch of the electrical path for R vs T measurements.

R vs T measurement

The R vs T measurements are performed automatically through a LabVIEW program which drives the temperature controller, the switcher and the multimeter by GPIB. The program allows setting the initial and final values and the step of the temperature sweep, the accuracy of temperature control, the number of times resistance is measured for each temperature. The program flow at the n^{th} step is as follows:

i. On the temperature controller, set the target temperature to the value $T^{(n)}$.
ii. Loop for checking when the difference between the actual temperature and $T^{(n)}$ is within the desired tolerance.
iii. Once the actual temperature is $\sim T^{(n)}$, make the switcher close the connection between the multimeter and sample 1 and measure the resistance. Then make the switcher open the connection to sample 1 and close the one to sample 2, and measure the resistance. Perform this step until the desired number of resistance readings is acquired.
iv. Generate the next target temperature value: $T^{(n+1)} = T^{(n)} + \Delta T$, where ΔT is the step of the sweep.

T_C, ΔT_C and RRR calculation

The typical resistance versus temperature curve R(T) measured with the procedure described above is shown in Figure 3.5.

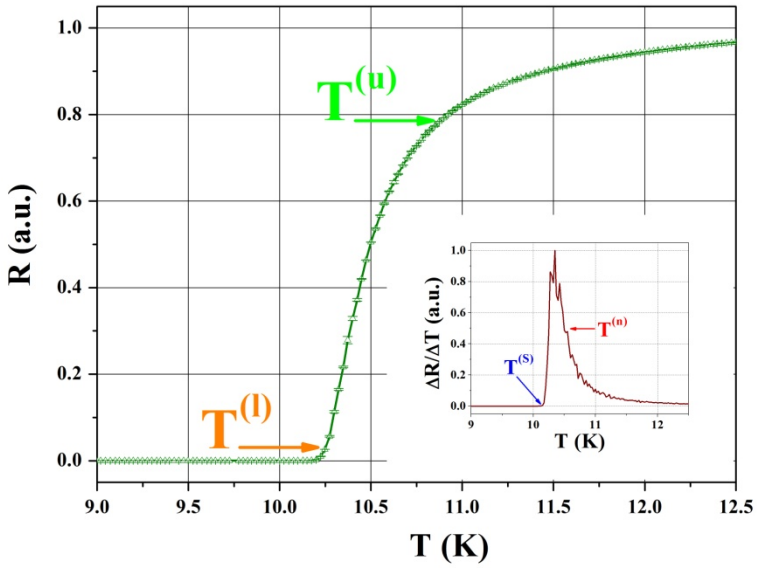

Figure 3.5. Example of an R vs T curve. Inset: incremental ratio ΔR/ΔT as a function of T. The temperatures $T^{(s)}$, $T^{(n)}$ $T^{(l)}$ and $T^{(u)}$ are highlighted.

The values of T_C and ΔT_C are calculated as follows:

1. Calculate the incremental ratio ΔR/ΔT for each temperature (see the inset of Figure 3.5):

$$\left.\frac{\Delta R}{\Delta T}\right|_{T^{(i)}} = \frac{R\left(T^{(i+1)}\right) - R\left(T^{(i)}\right)}{T^{(i+1)} - T^{(i)}}$$

   and normalize the curve with its maximum value.

2. Take the temperature $T^{(n)}$ after the maximum of the incremental ratio for which $\Delta R / \Delta T\big|_{T^{(n)}} = 0.5$.
3. Take the highest temperature $T^{(s)}$ before the maximum for which ΔR/ΔT=0.
4. Calculate the average normal resistance value $\overline{R}$ averaging the values of the resistance of the film from $T^{(n)}$ to $T^{(s)}$+2 K.
5. Define the lower $T^{(l)}$ and upper $T^{(u)}$ bounds of the transition as follows:

$$\begin{cases} R\left(T^{(l)}\right) = 0.1\overline{R} \\ R\left(T^{(u)}\right) = 0.9\overline{R} \end{cases}$$

6. Calculate T_C and ΔT_C with:

$$\begin{cases} T_C = \dfrac{T^{(u)} + T^{(l)}}{2} \\ \Delta T_C = T^{(u)} - T^{(l)} \end{cases}$$

The reason for this method to calculate T_C and ΔT_C resides in the fact that the onset and the shape of the superconducting to normal transitions of the samples measured varied significantly, depending on their thickness and on the deposition conditions (see chapter III). With our method we take into account both the onset (in the upper bound for the calculation of $\overline{R}$:$T^{(s)}$+2 K) and the shape (in the lower bound $T^{(n)}$) of the transition in the calculation of its lower $T^{(l)}$ and upper $T^{(u)}$ bounds. For a comparison, simply taking $\overline{R}$ equal to the value of resistance at T=20 K as often reported in literature, would lead to an overestimation of T_C, as even above the transition the resistance of the film keeps increasing with temperature (as shown in Figure 3.5). Finally, this method may be non-standard, but placing $T^{(u)}$ on the knee of the transition (Figure 3.5) it underestimates T_C anyway.

The Residual Resistivity Ratio (RRR) is calculated as the ratio between the resistance of the film at room temperature and at 20 K: RRR=R(300K)/R(20K).

ii. J_C measurements on films

After the measurement of resistance as a function of temperature, the dependence of the superconducting current density as a function of temperature (J_C vs T) can be measured. The setup used for these measurements is shown in Figure 3.6.

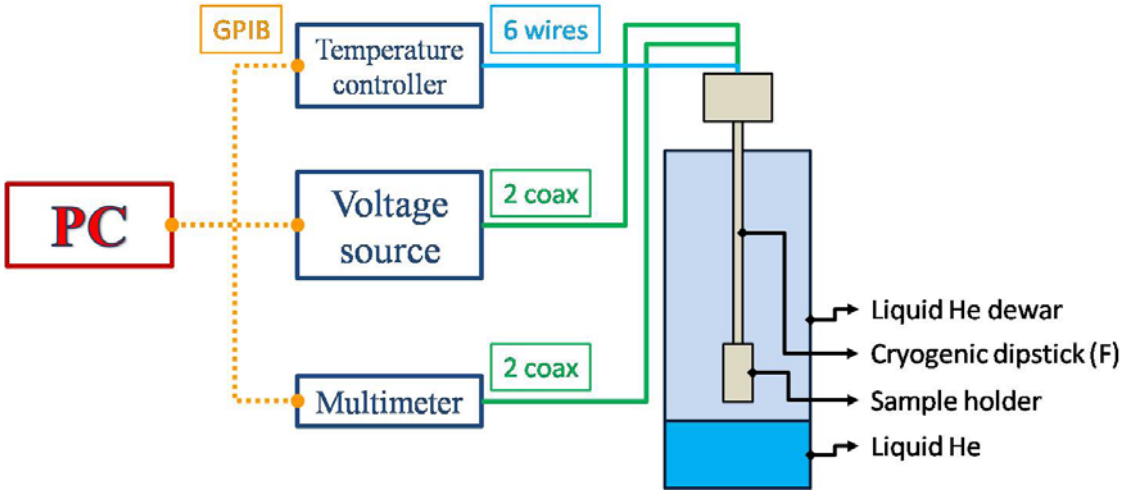

Figure 3.6. Block diagram of the set-up for for J_C vs T measurements. The temperature controller is a Conductus LTC10 or a Lake Shore 325 , the the voltage source is an HP 4155A, the multimeter is an HP 3458A.

Samples are mounted on the F-dipstick and inserted in a liquid He dewar as for the R vs T measurements.

Sample preparation

The same sample used for R vs T measurements is used for J_C vs T measurements. As the critical current of a 3 mm wide sample would be too high (several Amperes) for the voltage source used (HP 4155), a constriction must be fabricated in the superconducting film. A 50 µm wide bridge is then

defined with a diamond tip scriber (see Figure 3.7). The sample is mounted on the F-dipstick as described in section 3.1.i.

Electrical path

The electrical path of the set-up is sketched in Figure 3.7. As these measurements were not routinely performed, the set up was conceived to test only one sample in the same temperature sweep cycle, but it could be easily upgraded to allow the testing of up to two samples with the introduction of a switcher.

The sample is biased through the series of the voltage source (V_B) and a bias resistor (R_B=50 Ω) and the voltage across it (V_S) is measured by a multimeter (HP 3458A).

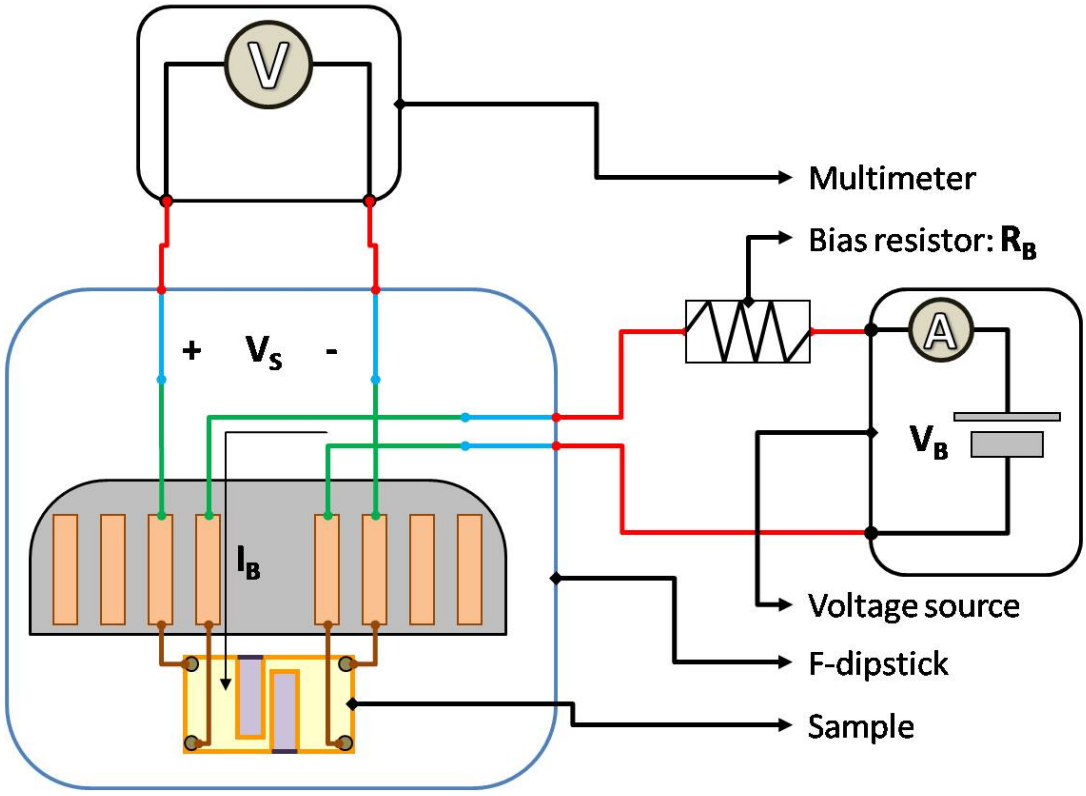

Figure 3.7. Sketch of the electrical path for J_C vs T measurements.

J_C vs T measurement

The measurement of J_C vs T is performed automatically through a LabVIEW program which drives the temperature controller, the voltage source and the multimeter by GPIB. The program allows setting the initial and final values and the step of the temperature sweep, the accuracy of temperature control, the step of the voltage sweep performed for each temperature, the number of times the voltage across the device is measured for each step of the voltage sweep. The program flow at the n^{th} step is as follows:

i. On the temperature controller, set the target temperature to the value $T^{(n)}$.
ii. Loop for checking when the difference between the actual temperature and $T^{(n)}$ is within the desired tolerance.

iii. Once the actual temperature is ~$T^{(n)}$, start to increase the bias voltage from zero with the voltage step set. For each bias voltage value, measure the voltage V_S across the sample and the current I_B through it. As long as the sample is superconducting, the current is $I_B=V_B/R_B$. When the critical current is exceeded, the sample switches to the hotspot resistive state (see chapter IV), so the current drops to the value $I_B=V_B/(R_B+R_n)$, where R_n is the resistance of the normal part of the film. At the point of the sweep right after the curve I_B vs V_S shows a maximum, the sweep is stopped and the maximum value of I_B is taken as the critical current value of the sample at temperature $T^{(n)}$: $I_C(T^{(n)})$.

iv. Calculate the critical current density value of the film at temperature $T^{(n)}$ as follows: $I_C(T^{(n)})= I_C(T^{(n)})=I_C(T^{(n)})/(w\cdot th)$, where w and th are the width of the bridge and the thickness of the film, respectively.

v. Generate the next target temperature value: $T^{(n+1)}= T^{(n)}+\Delta T$, where ΔT is the step of the sweep.

3.2. Thickness measurements:

As during the sputtering process there is no real time control of the deposited thickness, which is controlled only through the deposition time T_d, an accurate estimation of the growth rate is crucial (see section 2.3). That requires a reliable way to measure the thickness of the sputtered films. Depending on the range of thicknesses to be measured, two methods are adopted: profilometry or Atomic Force Microscopy (AFM).

i. Profilometry

For films of thickness th>20 nm, a metallic shadowing mask is mounted on the sample (see Figure 2.6) before the deposition. The mask prevents the deposition on part of the substrate (see Figure 3.3), so the thickness can be measured using a profilometer. The scans are performed from the MgO part towards the NbN part. The reference for leveling the raw scan data is taken on the NbN part. The minimum thickness that can be measured in a reliable way with the profilometer used is ~20 nm.

ii. AFM

For films thinner than 20 nm, the thickness is measured with an AFM. This requires creating a pattern where the film is etched away, in order to have a reference in the AFM scan. The procedure is the following:

1. Clean the sample in acetone and isopropyl alcohol (Figure 3.8 (a)).
2. Spin a negative photoresist (AZ 5214 E) on the sample (Figure 3.8 (b)). The spinning is performed at 5000 rpm, for 30 s with 3 s acceleration time. After the spinning, the photoresist is left to dry for 1 min at room temperature, followed by 5 min at 90°C. The thickness of the photoresist is ~1.4 μm.
3. Expose the photoresist with uv light (2 s) trough a mask which defines a set of parallel stripes 10μm wide. Develop the photoresist: 3 min in the developer (MF 319), followed by 1 min in water to stop the development (Figure 3.8 (c)).
4. Etch the NbN film through the photoresist mask in a CF_3 (50sccm) + O_2 (5sccm) plasma. The base pressure in the chamber is $2.5x10^{-5}$ Torr, the total pressure when the gases are introduced is 55 mTorr and the RF power is 150 W. The etch rate for NbN was measured to be ~140 Å/min, for GaAs it is ~40 Å/min and for MgO it is not relevant (Figure 3.8 (d)). As this etching process is not selective for GaAs, the procedure presented here cannot be used measure NbN thickness on GaAs.

5. Strip the photoresist in a stripping solution (QZ 3298) for 5 min, followed by 1 min in water (Figure 3.8 (e)).
6. Perform an AFM scan 20 x 20 μm^2 across one of the stripes (512lines/512samples, tip velocity 25 µm/s).
7. On the acquired scan, take ten cross-sections and measure the height of the step on both sides of the stripe. The average of these twenty values is taken as the thickness of the film.

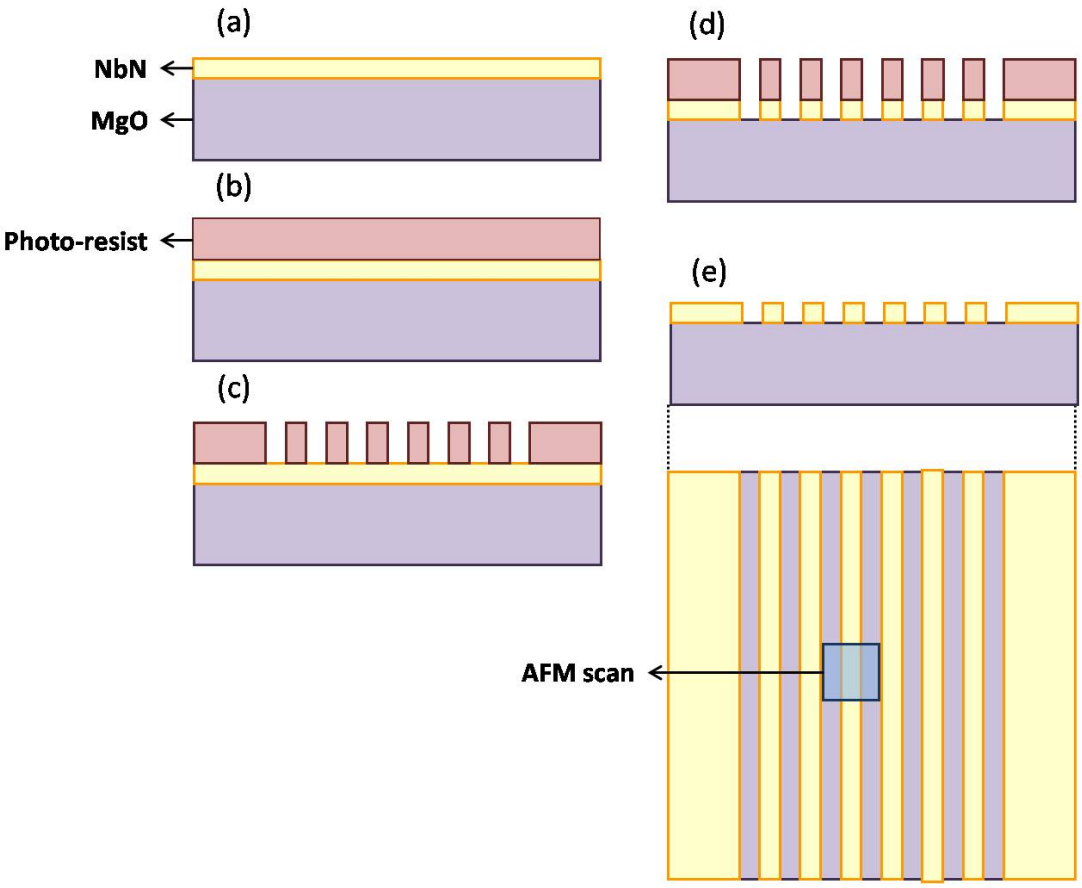

Figure 3.8. Sample preparation flow for the AFM measurement of film thickness.

As the NbN etch performed at step 4 is more selective for MgO than GaAs, thickness measurements are performed only on NbN+MgO samples. The thickness of thin NbN films on GaAs substrates or DBRs is estimated measuring the thickness of the NbN film deposited on an MgO substrate in the same deposition run.

4. RF magnetron sputtering deposition of MgO buffer layers

The preliminary tests for the deposition of MgO buffer layers on GaAs substrates were performed mostly by the student A. Surrente, in collaboration with the author. This experimental activity is presented in detail in [3]. Therefore, only the main points of the experimental methods will be reported in the following.

The deposition of MgO buffer layers (see chapter III) on GaAs substrates was carried out by power-controlled RF magnetron sputtering (in planar, circular configuration) of an MgO target in an Ar plasma. The sputtering system is analogous to the one sketched in Figure 2.5 (except for the fact that the DC voltage source is replaced by an RF one).

4.1. Substrate holder and sample mounting

The substrate holder allows to mount only samples of fixed size, i.e. square (10x10 mm^2) or rectangular (15x10 mm^2). In order to obtain samples of the desired dimension, the 2" GaAs wafer was cleaved as described in section 2.3. It is important to note that the GaAs substrates used in this set of preliminary experiments were not cleaned in an ultrasonic bath, but just with a compressed nitrogen flow.

Once the samples are mounted in their housings, they are mechanically clamped through a metal mask fixed on to the substrate holder by two screws. The mask also shields part of the substrate from deposition, which allows measuring the thickness of the layer grown using the profilometer method described in section 3.2. Finally, the substrate-holder is mounted in the deposition chamber, which was left in air (no load-lock system is available) and the vacuum cycle is started.

4.2. Deposition

A stoichiometric MgO target (2" diameter, 99.95% purity) was used, placed at 115 mm from the substrate. According to the results reported in [4], the crystalline quality of MgO films does not significantly change whether the deposition is carried out in a plasma of pure Ar or of Ar + O_2. Therefore, in order to reduce the number of parameters to control, we chose to perform the depositions in an atmosphere of pure Ar (99.9997% purity).

The background pressure was in the low 10^{-6} mbar range, and the pressure during sputtering was between $1{,}16 \cdot 10^{-2}$ and $1{,}30 \cdot 10^{-2}$ mbar, with a constant Ar flux of 14 sccm. In order to maximize film uniformity, the substrates were rotated at a speed of 40rpm. Substrates were not intentionally heated.

Once the plasma was started, before opening the shutter and starting the deposition, a pre-sputtering step (3 to 20 min duration) was carried out to clean the target.

Because of the small size the target it is possible to reach very high surface power densities, which cause the target surface to heat up. As MgO is dielectric, large temperature gradients can build up through the target thickness. Therefore, the stress induced by the different thermal expansion of different sections of the target may cause the target to crack [5]. For this reason, the RF power (P_{RF}) was limited to 60 and 80 W.

4.3. Thickness measurements

For each power level, thick (~200 nm) and thin (10-20 nm) MgO buffer layers were deposited. The thickness of both the thick and thin samples was measured by the profilometer method (section 3.2). As the thin layers are at the limit of the resolution of the profilometer, the measure of their thickness must be considered just as an indication of the order of magnitude.

The deposition rates, estimated from the thick samples, are 222 Å/h at P_{RF}=60 W and 295 Å/h at P_{RF}=80 W.

5. Electro-optical characterization of devices

Electrical and electro-optical measurements of devices were performed in a different dipstick setup (D-dipstick), which allows coupling of light to the device.

5.1. Electrical characterization set up

The setup used to measure current-voltage (I-V) curves of the devices with the cryogenic dipstick (D-dipstick) is shown in Figure 5.1.

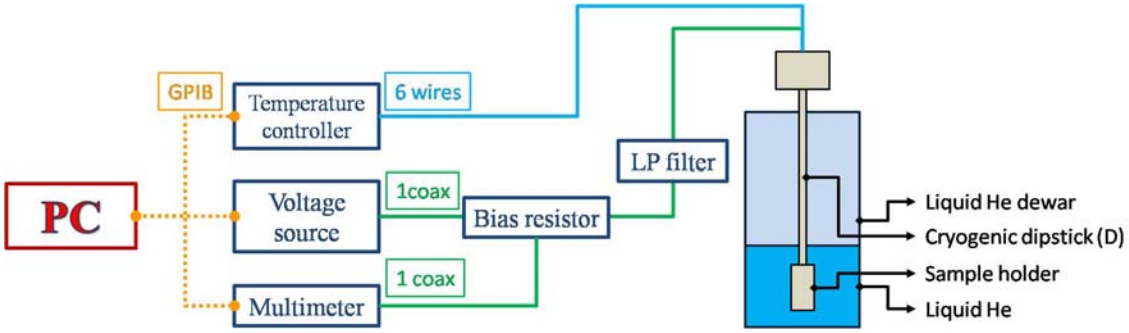

Figure 5.1. Block diagram of the set-up for I-V measurements using the D-dipstick. The temperature controller is a Lake Shore 325 , the voltage source is a Yokogawa 7651, the multimeter is an HP 3458A.

Sample holder

Samples are mounted on a cryogenic dipstick (D-dipstick) and inserted in a liquid He dewar. The basic structure of the head of the D-dipstick is the same as the F-dipstick (see section 3.1.i), with just few modifications reported in the following.

The body of the sample holder (Figure 5.2) can be removed from the head of the D-dipstick, which has the same structure as the one shown in Figure 3.2. This allows us to connect the devices to the pads through wire-bonding (see below).

In order to minimize the heat transfer to the devices through the cables, beryllium oxide heat sink chips (LakeShore) were thermally anchored to the sample holder through cryogenic varnish and used as pads. A total of ten pads is available on the sample holder, allowing to test many devices in the same cryogenic cycle.

The whole head of the D-dipstick is made of gold-plated OFHC (Oxygen-Free High Conductivity) copper (in light yellow), allowing a good thermal coupling between the strip line resistor, the temperature sensor and the sample. For I-V measurements the dipstick head is normally dipped in the liquid He with a pierced cap, in order to ensure a good thermalization of the whole system (i.e. sample, cables and sample holder) at 4.2 K, but it can also be sealed and held above the liquid He level in the cold He vapors when the temperature of the samples needs to be swept.

A single-mode optical fiber (FC/PC, 1260 – 1625 nm operating wavelength) is fed to the dipstick head, where it can be coupled to a short focal length lens to illuminate the devices for their optical characterization (see section 5.2).

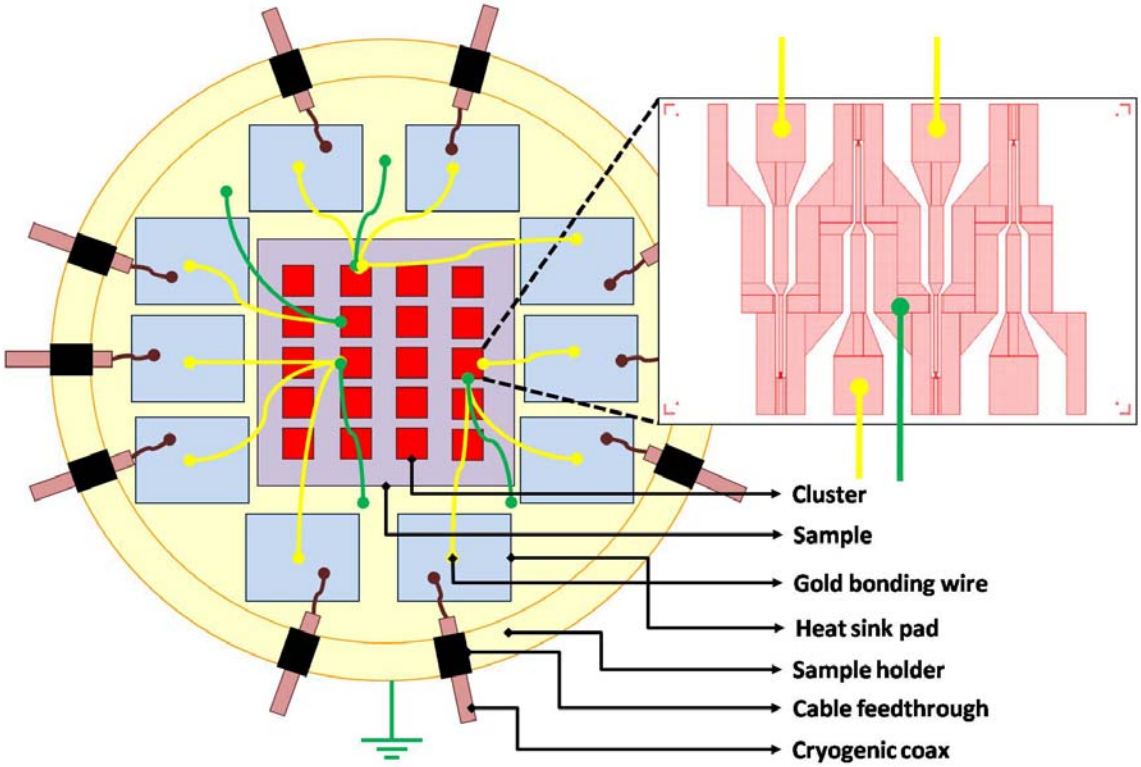

Figure 5.2. Sample Holder of the D-dipstick and electical path.

Sample Mounting

The steps to follow to mount the devices on the sample holder for characterization are the following:

1. Unmount the sample holder from the D-dipstick head.
2. Glue the sample to the 1x1 cm^2 sample housing graved in the sample holder (Figure 5.2) using silver paint.
3. Bond with a gold wire (yellow wire in Figure 5.2) the central conductor of the strip-line transmission line connected to the devices (inset of Figure 5.2, see chapter III for details on the fabrication) to the pads. As both the device pads and the sample holder pads are in gold, the bonding work easily.
4. Bond with a gold wire (green wire in Figure 5.2) the ground of each 4-device cluster (inset of Figure 5.2) to the sample holder, which is at the ground of the measurement setup. The gold plating of the sample holder allows an easy bonding.
5. Mount the sample holder on the D-dipstick head.
6. Pass the cryogenic miniature coaxial cables (red in Figure 5.2) through the feedtroughs of the sample holder (in black) and solder their core to the pads using In (as described in section 3.1.i).

Electrical path

Up to ten devices can be tested in the same cryogenic cycle. Each device is wire bonded with a gold wire to a beryllium oxide heat sink pad. On the same pad, the core of a cryogenic semi-rigid coaxial cable (LakeShore, type C, ~3 GHz bandwidth) is In soldered. The core conductor of the coax

is in solid copper, the shield is in aluminum. In order to minimize the heat flow through the cables from room temperature to the devices, the semi-rigid copper coaxial cables are then Sn soldered to rigid cryogenic coax cables (LakeShore, type SR), whose core and shield are in carbon steel and stainless steel, respectively. These cables are then Sn-soldered to room temperature SMA coaxial connectors.

I-V curves measurement

The equivalent electrical circuit for I-V curve measurements is shown in Figure 5.3.
As the number of electrical cables in the D-dipstick is limited to ten, in order to maximize the number of devices tested in a single cryogenic cycle a two-wire measurement configuration is used. The bias current (I_B) is supplied by a low noise voltage source V_B (Yokogawa 7651) connected to a precision (1%) bias resistor (R_B) and to a passive inductive low pass filter which reduces the electrical noise and protects the device from current spikes. The value of I_B is determined measuring the voltage drop across R_B by a multimeter (HP 3458A). The Voltage across the device (V_{SSPD}) is determined as: $V_{SSPD}=V_B-R_BI_B$. Therefore, the value of V_{SSPD} includes the voltage drop across the stray resistance of the cables, which causes the superconducting branch of the I-V curve to have nonzero slope.

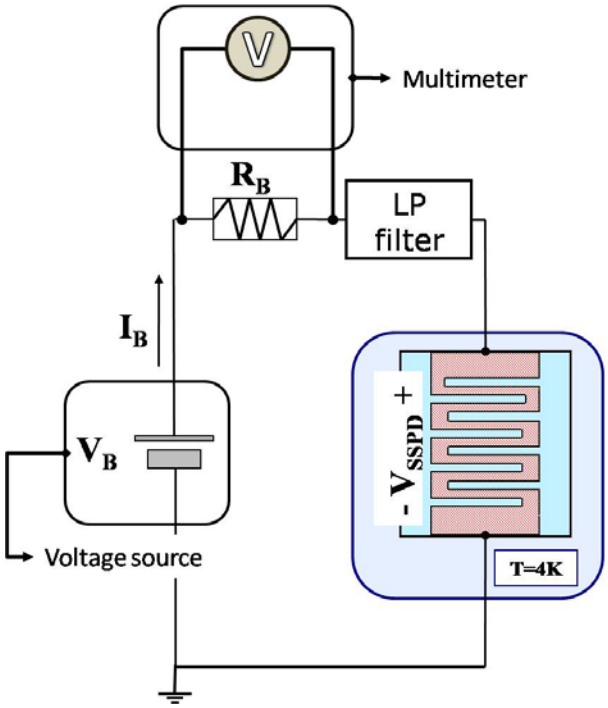

Figure 5.3. Equivalent electrical circuit of the setup for I-V measurements.

5.2. Optical characterization set up

The setup for the optical characterization of the devices with the cryogenic dipstick (D-dipstick) is shown in Figure 5.4.

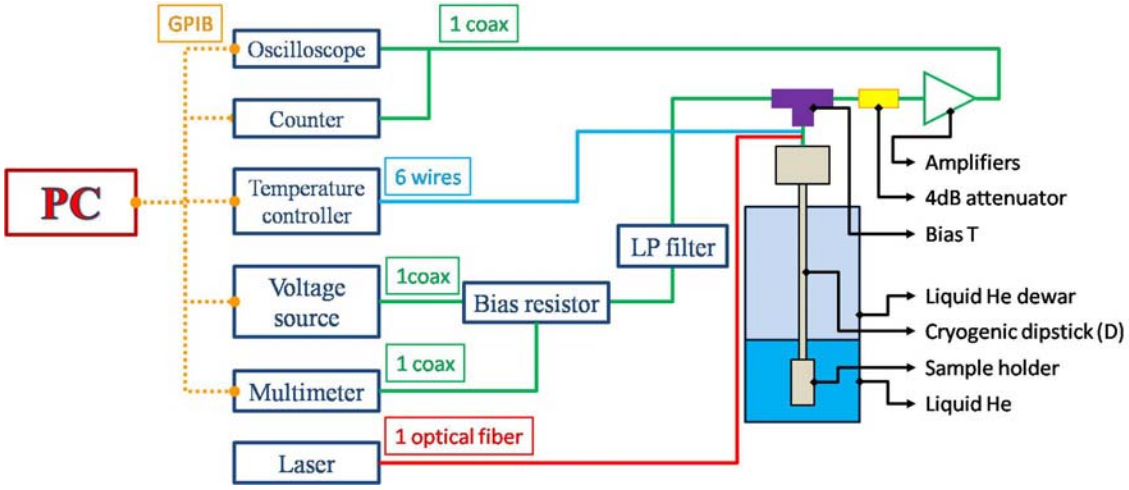

Figure 5.4. Block diagram of the set-up for optical characterization using the D-dipstick. The temperature controller is a Lake Shore 325 , the voltage source is a Yokogawa 7651, the multimeter is an HP 3458A, the counter is a Stanford research systems SR 400, the oscilloscope is a Tektronix TDS 5104 (1 GHz bandwidth) or an Agilent Infiniium DCA-J 86100 C (40 GHz bandwidth).

Sample holder

Samples are mounted (as described in section 5.1) on the D-dipstick sample holder described in section 5.1 (Figure 5.2) and inserted in a liquid He dewar.

The photons are fed to the devices through a single-mode optical fiber (FC/PC, 1260 – 1625 nm operating wavelength) fed to the dipstick head and coupled with a 3mm focal length aspheric lens placed 7 cm from the plane of the chip in order to insure uniform illumination of the devices. The maximum variation of the light intensity on the 1x1 cm^2 sample surface relative to its value on the lens optical axis is 25% and by an extensive calibration of the intensity distribution on the sample plane it has been possible to estimate the number of incident photons per device area with an error of 5%. The attenuation of the whole system is ~10^{-7}.

The devices were optically probed using a fiber-pigtailed, gain-switched laser diode at 1.3 μm wavelength (100ps-long pulses, 26 MHz maximum repetition rate) or a mode-locked Ti:sapphire laser at 700 nm wavelength (40ps-long pulses after propagation in the optical fiber, 80 MHz repetition rate). The maximum number of incident photons per optical pulse was ~ 0.5 for the 1.3 μm laser, and ~ 100 for the 700 nm laser.

Optical characterization

The equivalent electrical circuit for electro-optical measurements is shown in Figure 5.5.

The bias current I_B is supplied to devices through the DC port of a 10MHz-4GHz bandwidth bias-T connected to the voltage bias circuit already described (section 5.1), avoiding the latching effects associated with the current bias.

As shown in Figure 5.4, the AC port of the bias-T is connected through a BNC coaxial cable to a 4 dB attenuator connected to the series of two, room-temperature, low-noise amplifiers (Mini-Circuits ZX60-3018G+, 18 bB gain, 20 MHz-3 GHz bandwidth). The amplifiers are battery powered. The attenuator reduces the electrical noise on the device due to reflections at the amplifier input. Without

the insulation provided by this attenuator the critical currents of our devices were suppressed by up to 10%.
The amplified signal is then fed to a 1 GHz-bandwidth single shot oscilloscope (Tektronix TDS 5104), to a 40 GHz-bandwidth sampling oscilloscope (Agilent Infiniium DCA-J 86100 C) or to a 300 MHz counter (Stanford Research Systems SR 400) for time resolved measurements and statistical analysis.
As the cryogenic and room temperature coaxial cables and the input impedance of the amplifiers are all 50 Ω-matched, they can be replaced in the equivalent electrical circuit by an lumped 50 Ω resistor (R_{out}) connected in parallel to the device (Figure 5.5).

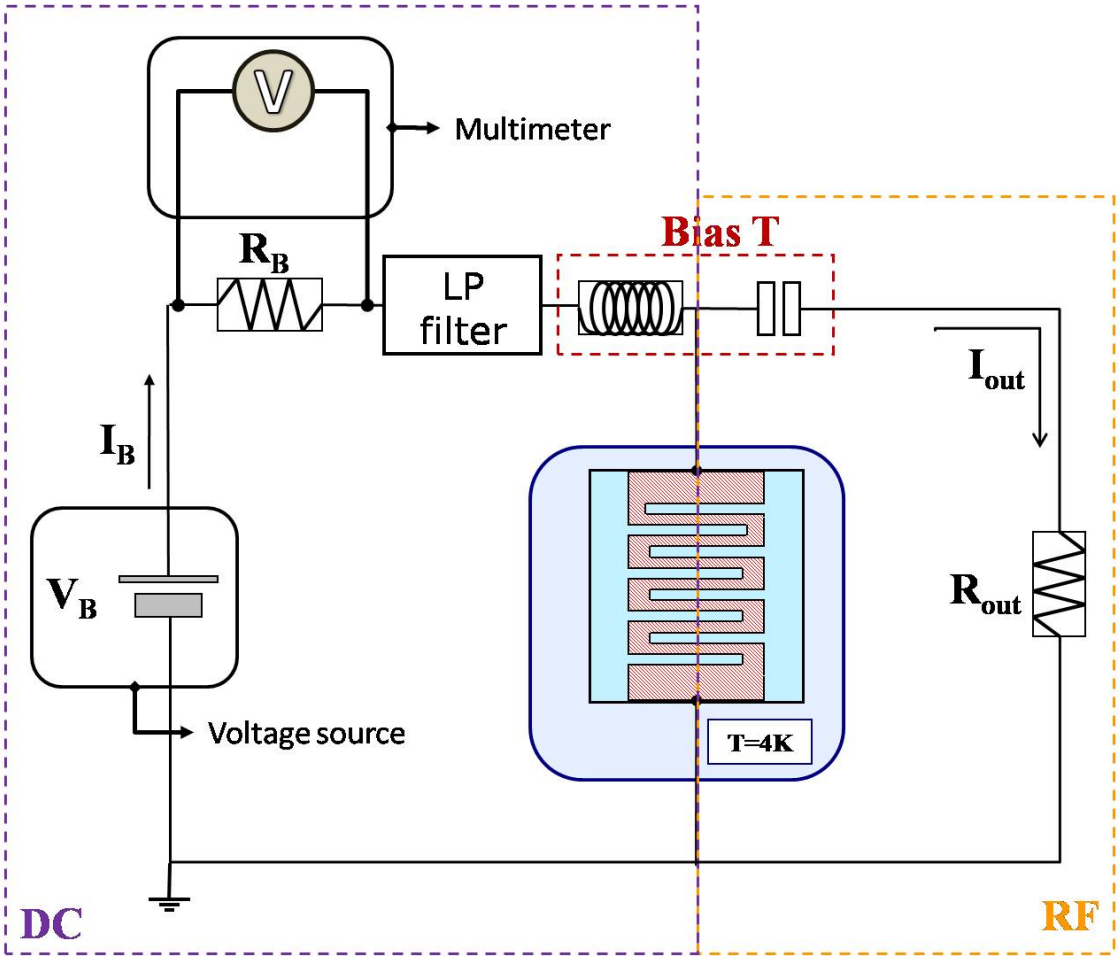

Figure 5.5. Equivalent electrical circuit of the setup for optical characterization.

5.3. Cryogenic probe station

The cryogenic probe-station (Janis) used for the electrical and optical characterization of the devices is shown in Figure 5.6. This setup was build and used by dr. D. Bitauld, and it will be briefly described here for completeness.

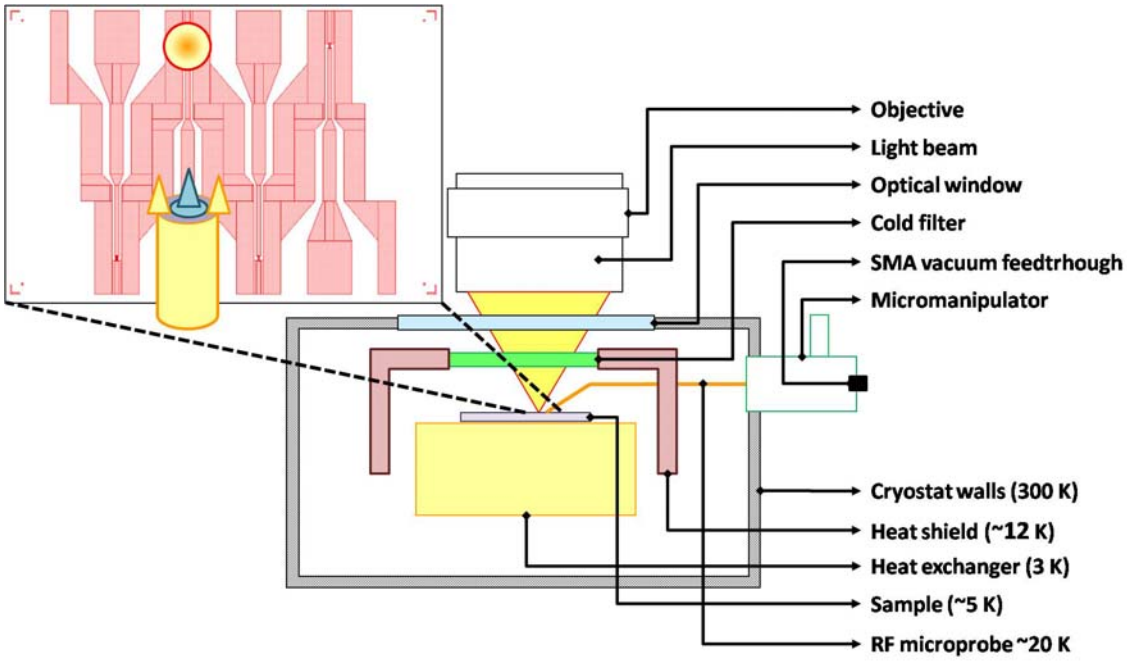

Figure 5.6 Schematics of the cryogenic probe station setup.

The heat exchanger stage is cooled down to a temperature as low as 3 K. The sample is attached using silver paint to a gold-plated copper sample mount. In order to block the black body radiation at 300 K from the walls of the probe station a heat shield (T~ 12-13 K) is mounted around the sample. The stray light and the 300 K black body radiation that would couple to the sample through the optical window is heavily reduced by a cold filter whose optical bandwidth (700-1500 nm) is centered around the wavelength of interest for most of the measurements, i.e. λ=1.3 µm.

Electrical contact with the devices is established using a 40-GHz RF microprobe connected to a coaxial cable and mounted on a micromanipulator arm. In this way, any device on the sample can be individually contacted in the same cryogenic cycle. The microprobe is cooled at ~20-25 K using copper braids connected to the 10 K stage of the probe station. Because of the heat flow from the microprobe to the sample, the temperature of the devices is about T~5 K.

The room-temperature bias and readout circuitry (analogous to the one presented in sections 5.1 and 5.2) is connected to the cold RF probe through coaxial cable and a SMA vacuum feedthrough.

The light is fed to the sample through a single-mode optical fiber coupled with a long working distance objective, allowing the illumination of a single device.

The 1300 nm wavelength light is collimated from the output of a single mode fiber and focused into a small spot by a microscope objective. Two different objectives were used with numerical aperture (NA) of 0.3 or 0.4. The objective and the whole optical setup are mounted on an XYZ translation stage so that it is possible to move the spot on the surface of the sample. The beam spot size was measured by scanning it perpendicularly to a 250 µm-long, 100 nm-wide nanowire (see chapter IV) and monitoring the profile of the photo-counts. This resulted in a peak with a width of 5.6 µm (FWHM) for the NA= 0.3 objective and 2.2 µm (FWHM) for the NA= 0.4 one.

6. References

[1] D. L. Smith, New York: McGraw-Hill, Inc., Chapter 9 (1995).
[2] M. Gurvitch, J. Vac. Sci. Technol. A **2**, 1550 (1984).
[3] A. Surrente, Projet de semestre d'hiver (2006).
[4] P. Vuoristo, T. Mantyla, P. Kettunen, and R. Lappalainen, Vacuum **42**, 1001 (1991).
[5] F. Wang, S. Müller, and R. Wördenweber, Thin Solid Films **232**, 232 (1993).

III: Fabrication

1. Introduction

As already pointed out in chapter I, the device absorbance (α, the ratio of the number of photons absorbed in the SSPD nanowire to the number of incident photons on the device active area A_d) sets an important limitation to the system detection efficiency (SDE) of SSPDs. Indeed, it has been shown that in the classic front-illumination configuration α cannot exceed 30% [1].

Two approaches to increase α have already been demonstrated:

i. The use of back-illumination (i.e. through the substrate) which reduces the index mismatch with NbN. In this way α can be increased up to 45% [1]
ii. The integration of the SSPD with an optical cavity designed to concentrate the field in the NbN nanowires [2].

The first solution is unpractical, making the alignment of the device with an optical fiber challenging. The cavity-integrated SSPDs reported so far need back-illumination (which yields the same problems as the first solution) and the mirror of the cavity is in gold [2], which limits the maximum α achievable.

Our approach is to integrate SSPDs with advanced optical structures such as distributed Bragg reflectors (DBRs) and optical waveguides. This requires to transfer the challenging SSPD technology (i.e. the deposition of high-quality few-nm thick NbN films and the nano-patterning by electron beam lithography) from the usual comfortable substrates, i.e. sapphire and MgO, which are known to allow the deposition of few-nm thick NbN films of excellent quality [3-7], to an optical substrate like GaAs, on which DBRs and waveguides can be easily obtained. Our first task was then to grow few-nm thick NbN films on GaAs and AlAs/GaAs-based DBRs (see chapter II and section 4.3.iii for the details of the structure) with state of the art superconducting properties, which, to our knowledge, has never been reported in literature. This requires in particular the use of a lower deposition temperature (~400°C, as compared to ~800°C, typically used for the deposition on sapphire) in order to prevent As evaporation [8]. As a first step, we optimized the process on MgO substrates, which are known to allow the growth of high crystal quality NbN films at low temperature [3, 4] (having the same crystal structure and a lattice misfit of just 5.5% with respect to the NbN superconducting crystal phase).

Deposition conditions influence the superconducting properties indirectly through film structure: crystal structure, lattice parameter, grain size, island structure. The following sections are meant to give insight on the effect of film structure on superconducting properties (section 2) and on the effect of deposition conditions on film structure (section 3).
The characterization of the NbN films deposited on MgO, GaAs and DBRs is presented in section 4. Details of the successive fabrication steps, performed at the Photonics and Nanotechnology Institute (IFN, Rome) are reported in section 5.

2. Structure of superconducting NbN thin films

This section presents the structural properties which strongly influence superconductivity of NbN thin films: crystal structure, lattice parameter and microstructure.

2.1. Which crystal structure, which lattice parameter?

The Nb-N phase diagram is very complex and difficult to establish experimentally. NbN_x exists in a variety of crystal structures depending on its stoichiometry (Figure 2.1, [9]). NbN_x superconducting properties strongly depend on its crystal structure and only the face centered cubic (fcc) NaCl structure (δ-NbN) shows a high T_C (see [10] for a review).

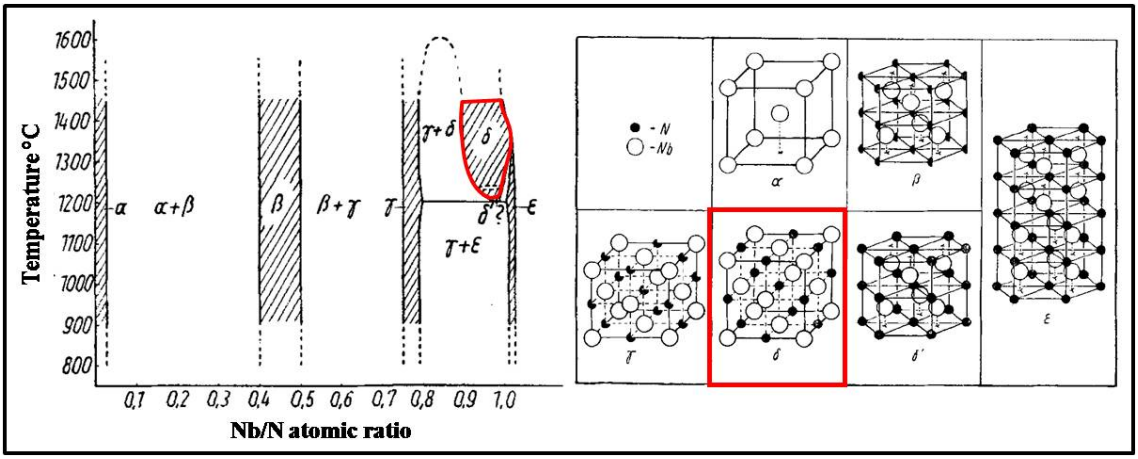

Figure 2.1. Phase diagram of the Nb-N system [9].

In bulk samples, δ-NbN_x has been reported over a significant stoichiometry range: $0.85 \le x \le 1.06$. Over this composition range the lattice parameter a_0 varies systematically from 4.37 Å to 4.39 Å (Figure 2.2). Density studies show that in nitrogen-poor compounds, the nitrogen sublattice is defective, while in nitrogen-rich compounds, the metal sublattice is defective [11].

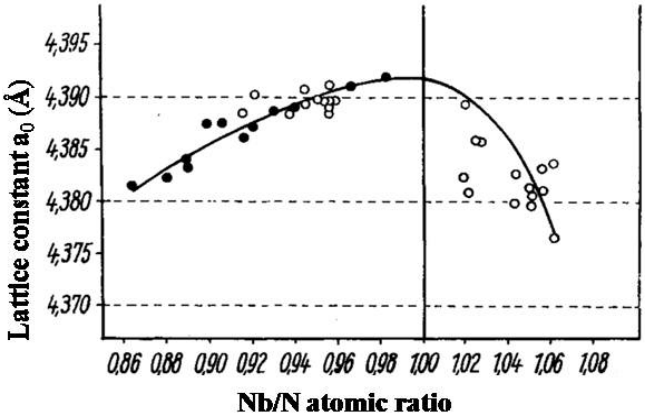

Figure 2.2. Variation of the lattice constant a_0 of the δ-NbN_x with stoichiometry [11].

Experimental studies on thin film samples have been performed [4, 12] showing a strong correlation between T_C of the δ-NbN and its lattice parameter a_0 (Figure 2.3). Several investigations [4, 13, 14] report independently that the maximum of T_C occurs for a_0=4.46 Å.

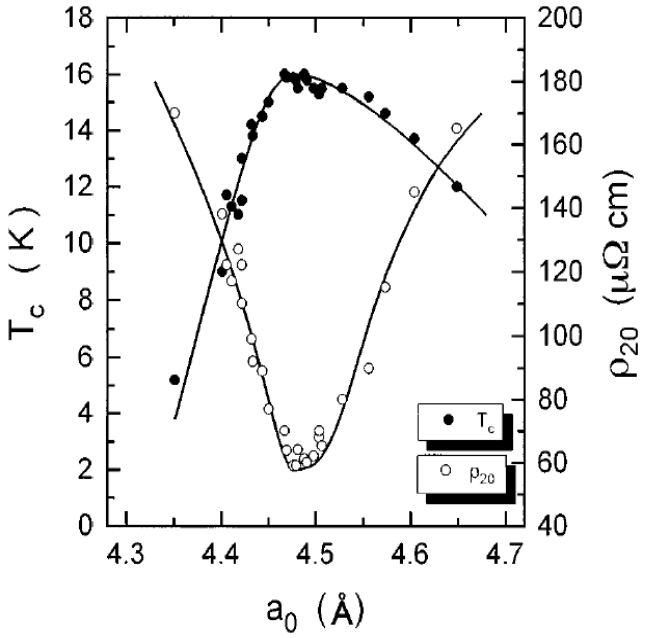

Figure 2.3. Variation of the superconductiong critical temperature (T_C) and of the resistivity at T=20K (ρ_{20}) with the lattic eonstant a_0 of the δ-NbN [4].

In conclusion, the stoichiometry in the film determines both the crystal phase, and the lattice parameters of the crystal phase. As the superconducting properties of NbN films depend on the crystal phase and the lattice parameter, they are in the end strongly affected by the Nb/N ratio in the film.

2.2. Influence of microstructure

For NbN films of several hundred nm thickness the superconducting critical temperature is insensitive to disorder. Indeed, T_C achieved in polycrystalline films [12, 13, 15-20] is just as high as those achieved in single-crystal NbN films [4, 21, 22]. Anyway, monocrystalline films show much lower normal-state resistivity ρ, much shorter magnetic penetration depth λ [4, 22] and longer superconducting coherence length ξ [22], which are attractive properties. Indeed, a shorter λ results in a lower kinetic inductance [23].

Microstructure is a far more critical factor for few-nm thick films, which are the subject of this study. Indeed, in superconducting two-dimensional (2D) disordered films (either homogeneously disordered [24] or granular [25]), the localization of charge carriers by Coulomb interaction and the corresponding enhancement of quantum fluctuations of the phase of the superconductor order parameter induces the superconductor-insulator transition (SIT) [26], which results in a decrease of T_C as crystal quality degrades with decreasing thickness [3-5, 15, 24].

Therefore, in order to prevent the SIT to occur in few-nm thick NbN films, a high crystal quality is necessary, i.e. the films must be monocrystalline or polycrystalline with large grain size and good electrical coupling between the grains [27]. High quality few-nm thick NbN films have been reported by several groups [3-6, 15, 28], with both monocrystalline [3, 6, 28] and polycrystalline [15, 28] microstructures. A recent study [28] reports a comparison between polycrystalline and single-crystal NbN films of the same thickness, showing an improvement of superconducting properties in the latter.

3. NbN thin film technology

3.1. Some notions of thin film deposition

The Thornton zone model [29] predicts film microstructure from primary deposition variables such as substrate temperature and working gas pressure (Figure 3.1). It was initially derived from observations on metal films deposited by magnetron sputtering [30], but it has proven to be universal [31], as it associates structural forms with the fundamental physical processes of deposition. Even though this model is not meant to be used in a detailed quantitative way, it provides general guidelines in interpreting experimental data and in establishing starting points in the development of deposition processes. This section in not meant to be a complete introduction on the subject, but rather a review to few key-concepts, which are used in the next sections. Ref. [31, 32] provide a more complete treatment of thin film deposition.

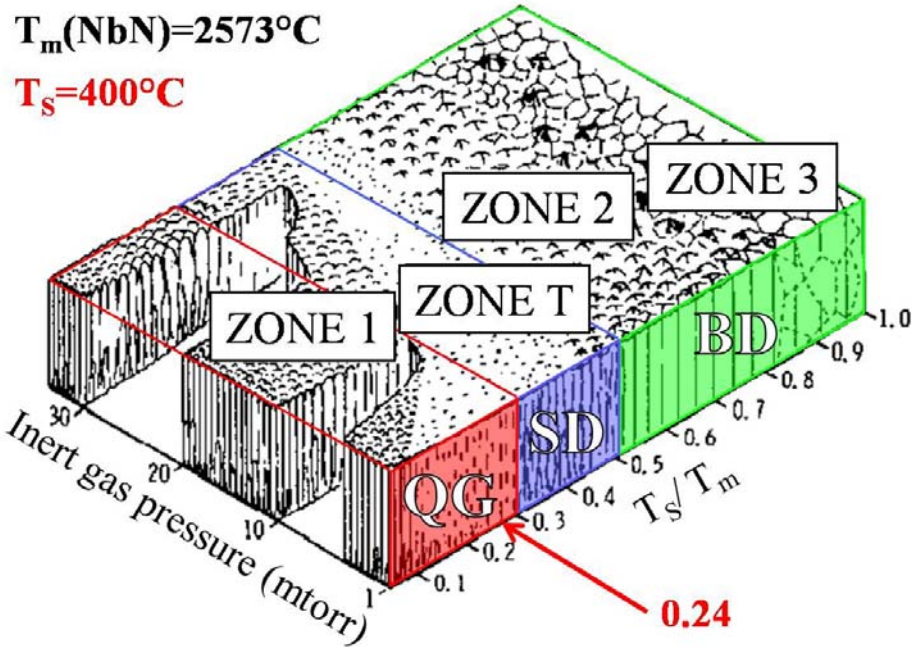

Figure 3.1. Schematic representation of the dependence of film microstructure on the substrate reduced temperature (T_S/T_m) and inert gas pressure [29].

Deposition can be pictured as occurring in three steps. First the arriving atoms and molecules transfer their kinetic energy to the lattice and become loosely bonded adsorbed atoms (transport step). Then they diffuse over the surface until they either are desorbed or become incorporated in the film (surface diffusion step). Finally, diffusion occurs within the bulk of the film and with the substrate (bulk diffusion step).

Thermal motion of atoms on the surface and in the bulk of the growing film strongly depends on the ratio between substrate temperature T_S and the binding energy of atoms in the solid. As the melting point T_m of a solid depends largely on the binding energy of its atoms, thermal motion of atoms scales with the ratio of T_S to T_m (in K), known as the reduced temperature. Thus each of the three basic processes (transport, surface diffusion, bulk diffusion) can be expected to dominate film growth over different ranges of T_S/T_m, resulting in different film structures. Such is the basis of the structure zone model [29].

For low reduced temperatures ($T_S/T_m<0.3$), thermal motion of the adsorbed material in negligible, so surface diffusion does not have time to occur before the deposition of the next atomic layer. In this regime, known as quenched growth regime, it is the transport process that dominates film growth, so that atoms become immobilized where they land (ballistic deposition). Films resulting from quenched growth processes may exhibit two kinds of microstructure:

- Zone 1 structure (Z1), consisting of columns typically tens of nm in diameter separated by voids a few nm across. The columns have poor crystallinity or are amorphous.
- Zone T structure (ZT), which consists of defected columns similar to those of Z1 but the voids are absent.

The Z1 voided columnar structure is a consequence of atomic self-shadowing, a purely geometric interaction between the roughness of the growing surface and the directions of the incident sputtered atoms which makes that high points on the growing surface receive more coating flux than valleys. When atoms are incident on the surface over a range of angles, self-shadowing increases. This is the case when the direction of the particles emanating from the source is randomized by collisions with the background gas during their trip to the substrate. So increasing the operating pressure from the molecular towards the fluid flow regime spreads the range of incident angles towards the completely random distribution and increases self-shadowing. Deposition pressure is then an important determinant of film structure in the quenched growth regime. Self-shadowing is also influenced by the initial substrate surface roughness and the apparatus configuration. Surface diffusion and self-shadowing are two competing processes, the first smoothing out film roughness, the latter increasing it, so increasing T_S/T_m can counteract self-shadowing.

ZT is promoted by energetic particle bombardment, which is associated with energy-enhanced processes. The nature of these bombarding particles closely depends on the deposition process [32], but the common effect is the promotion of a more dense microstructure through energy and momentum transfer to the atoms of the growing film (see [33] for a two-dimensional molecular dynamics simulation). Another common feature is that the energy flux carried to the substrate by particle bombardment depends strongly on the working gas pressure because the scattering with the gas dissipates the kinetic energy of the particles.

In conclusion, in the quenched growth regime the Z1 and ZT are competing structures, resulting from the balance of energetic particle bombardment which favors a dense microstructure, and self-shadowing which tends to produce an open structure. This balance is mainly controlled by the working gas pressure, so decreasing the deposition pressure at constant T_S/T_m promotes the transition from Z1 to ZT, as the incident particles neither become scattered into more oblique trajectories nor dissipate their kinetic energy in gas collisions.

For intermediate reduced temperatures ($0.3<T_S/T_m<0.5$), film growth is dominated by ad-atom surface diffusion. Films resulting from this growth regime exhibit this microstructure:

- Zone 2 structure (Z2), consisting of columns having tight grain boundaries between them. Crystalline columns are less defected than in *Z1* and *ZT*.

For high reduced temperatures ($T_S/T_m>0.5$), bulk diffusion dominates, so that the film loses all memory of the earlier steps of its growth. Films resulting from this growth regime exhibit this microstructure:

- Zone 3 structure (Z3), consisting of isotropic equiaxed grains.

3.2. NbN thin film optimization strategy

Choosing the deposition technique defines the deposition parameter space in which the optimization is to be performed. First the motivation of our choice of the deposition technique is exposed (section i), then our optimization strategy in the deposition parameter space is presented and motivated with the influence of deposition parameters on film structure (section ii).

i. Motivation of the optimization strategy

Which deposition technique?

As the superconducting properties of NbN strongly depend on its stoichiometry, since the first investigations in the early 70's T_C of thin films was optimized controlling the Nb/N ratio in a way that depends on the deposition technique adopted. With very few exceptions (see for instance the chemical vapour deposition, CVD, technique in [21]), NbN thin films have been produced by reactive sputtering of a Nb target in a plasma containing N_2 and Ar [3-5, 12, 13, 15-20, 22, 34, 35]. In this technique, NbN can be synthesized at a given partial pressure of the reactive gas (N_2) in the inert gas (Ar), and the stoichiometry of the film can be varied from the original metal to the most nitridized state in a number of different ways (see below). The main advantage of sputtering over CVD is that the sputtered atoms leaves the target with a high energy (of the order of the binding energy ~5 eV), which, as seen in section 3.1, is a critical parameter for the microstructure of the film.

High quality thin films (few hundreds of nm thick) were obtained in the early studies using both RF[1] [17] and DC[2] [12] reactive sputtering. High substrate temperatures (T_S>600°C) were necessary to promote the growth of those superconducting films, as the pressure in the chamber was of the order of tens of mtorr. At those pressures there is a considerable gas scattering of sputtered particles as they cross the plasma, with consequent loss of their initial high kinetic energy (thermalization) and randomization of their incident angles at the substrate, which promotes the undesirable porous Z1 microstructure (see section 3.1). The lower limit of operating pressure in sputtering is imposed by the need for the electrons ejected from the cathode to undergo ionizing collisions with the gas to sustain the plasma before they reach the anode and are removed.

Deposition at lower plasma pressure (few mtorr) and substrate temperature is possible using a magnetron (see [36] for a detailed discussion on the physics of magnetron sputtering). Since the 80's NbN films have been fabricated mainly by RF [4, 22, 34] and DC [3, 5, 13, 15, 16, 18-20, 34, 37] magnetron sputtering techniques in planar, circular configuration.

[1] i.e. applying a radio frequency (>1MHz) oscillating voltage across the electrodes between which the plasma is sustained.
[2] i.e. applying a DC voltage across the electrodes between which the plasma is sustained.

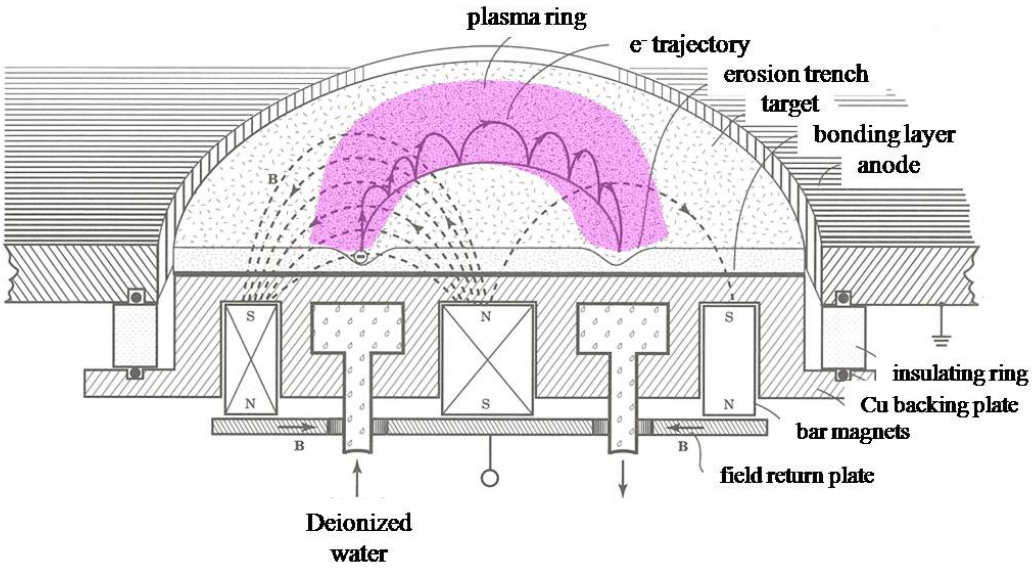

Figure 3.2. Cross sectional view of the planar, circular magnetron structure and behaviour. The electron orbit radius is shown much larger than the actual size for clarity. [36]

In magnetron sputtering, the minimum pressure to sustain the plasma is much lower because a crosswise magnetic field (see Figure 3.2) over the cathode traps electrons in closed orbits in that location, greatly increasing their path length before they finally escape to the anode by scattering. The sputtered particles retain then most of their kinetic energy, which reflects in high quality film structure even at low substrate temperature.

Moreover, localization of the plasma over the target by the magnetic field results in a much lower plasma density over the substrate than in the case of simple sputtering, so plasma ion bombardment on the substrate is heavily reduced. Ion bombardment can be also reintroduced and its strength controlled using unbalanced magnets [35, 38]. With magnetron sputtering then, ion bombardment is a controllable deposition parameter which can be used to modify film microstructure.

In conclusion, for the reason presented above, the deposition technique used in this study is the DC reactive magnetron sputtering in planar, circular, balanced configuration. The DC sputtering technique was chosen in order to avoid ion bombardment on the substrate that takes place in RF sputtering at every sign change in the potential between the electrodes.

Current or voltage control?

DC reactive magnetron sputtering of Nb in $Ar+N_2$ mixture has been performed in current (cathode current, I_c) control [3, 5, 16, 18-20, 34, 37] or voltage (cathode voltage, V_c) control [13, 15] modes. The motivation for our choice of the I_c-controlled mode is exposed in the following.

In reactive magnetron sputtering of a metal target like Nb, three possible sites for reaction with nitrogen are possible [39]: (a) at the target surface, (b) at the substrate, (c) during transfer from target to substrate. The last would require multiple collisions between Nb and N atoms, so it can be neglected in the magnetron sputtering case where the pressure is of the order of few mtorr and the mean free path of Nb of few cm [40]. Reactions (a) and (b) must then occur to obtain NbN. So the Nb/N ratio in the films depends in the end on the balance between the sputtering and nitridization rates of the target. To be able to change the stoichiometry of the films in a reproducible way it is then important to have control on the sputtering/nitridization balance.

While reactive sputtering is taking place in V_c-control mode, the current-voltage curve of the plasma exhibits an hysteresis loop (Figure 3.3). Following ref. [5], we explain this phenomenon in the following way. For low V_c, the nitridization rate r_n exceeds the NbN sputtering rate $r_{s,NbN}$ and the target is fully coated by NbN (poisoned state). Increasing V_c until it reaches a critical value for which $r_{s,NbN}>r_n$, part of the Nb on the target is exposed and sputtered. The Nb exposed on the target and deposited on the substrate getters the nitrogen in the chamber, so P_{N2} decreases. An avalanche process then starts, as the decrease of P_{N2} causes a further reduction in r_n. The result is that the target becomes completely uncoated, which reflects in a positive current jump on the current-voltage curve, as the secondary electron emission coefficient of Nb is higher than that of NbN. If V_c is then reduced below a critical value such that $r_n>r_{s,NbN}$, another avalanche process starts, which results in the nitridization of the target. As it is clear from Figure 3.3, for the same cathode voltage two stable states exist, corresponding to the poisoned/uncoated states of the target surface. In the first state films are deposited with excessive nitrogen, in the second with excessive Nb. The intermediate states of the target are unstable, but these states are the most interesting since they allow the deposition of films with the stoichiometry needed.

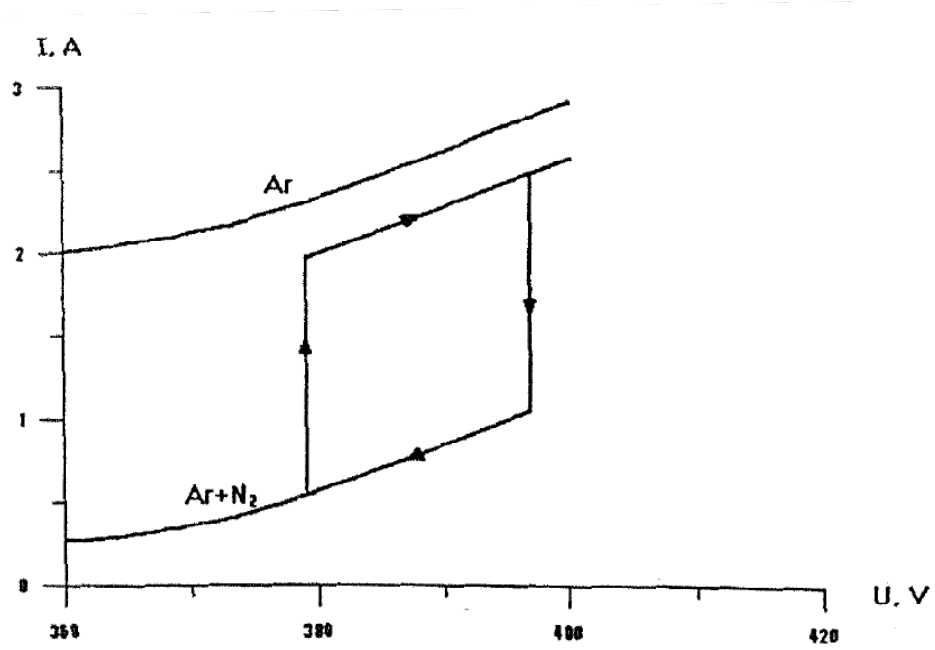

Figure 3.3. Current-voltage curve of a plasma of pure Ar and of the mixture Ar+N_2 in V_c-control mode [5].

In I_c-control mode no hysteresis effect takes place as the deviations from the equilibrium state are self-compensated. Indeed, if $r_{s,NbN}$ increases, more Nb is exposed on the target and sputtered. V_c is decreased due to the increased emission of secondary electrons from the target and $r_{s,NbN}$ returns to its initial value. On the other hand, if $r_{s,NbN}$ decreases, the NbN coated area on the target grows, V_c rises and so does $r_{s,NbN}$. So in this mode of operation there is a one-to-one correspondence between I_c, P_{N2} and the nitridization state of the target (Figure 3.4), i.e. with the stoichiometry of the deposited NbN films, which makes it possible to fabricate films with good reproducibility.

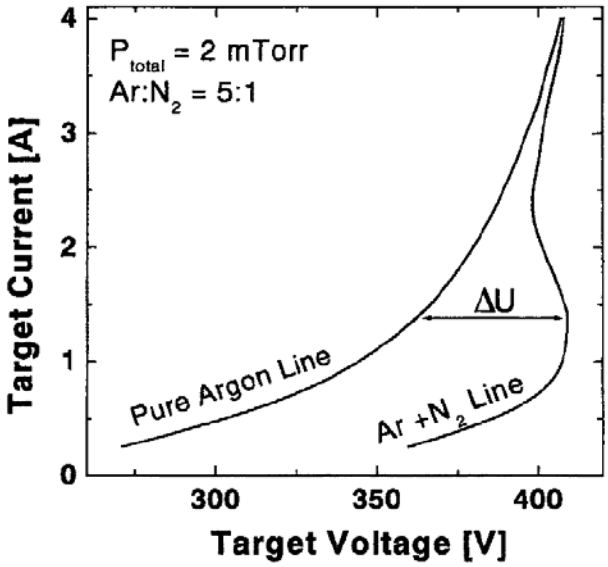

Figure 3.4. When the I_c is small, r_n is higher than $r_{s,NbN}$, so that the target surface is poisoned. If I_c is increased, $r_{s,NbN}$ exceeds r_n and the nitridized portion of the target surface decreases. The secondary electron emission coefficient of Nb is higher than the one of NbN so, as the Nb is exposed on the target, the cathode voltage must increase to maintain the discharge current constant [34], resulting in a negative resistance region in the current–voltage characteristics [3].

How to control stoichiometry?

In DC reactive magnetron sputtering in current-control mode, the sputtering/nitridization balance has been modified and monitored in several ways:

i. Changing the nitrogen concentration in the gas mixture $x_{N2}=P_{N2}/P_{tot}$, keeping P_{tot} and I_c constant [19, 20, 37].
ii. Changing the cathode current I_c (i.e. ΔU, see Figure 3.4) keeping P_{N2} and P_{tot} constant [3, 5].
iii. Changing nitrogen injection at fixed P_{Ar} and controlling its consumption, keeping I_c constant [18].
iv. Changing nitrogen injection at fixed P_{Ar} and monitoring the optical emission spectrum of the plasma, keeping I_c constant [34].

All the approaches have proven to be equally effective in optimizing the superconducting properties of NbN film. Technique (i) has been adopted in this study as the sputtering apparatus used did not allow performing an optimization using techniques (ii) and (iv), and because technique (i) is far more widely used and documented than (iii).

With approach (i), for given values of P_{tot} and I_c, it is possible to find the optimum value of x_{N2} which allows obtaining the sputtering/nitridization balance that results in the highest T_C. Still, it has to be considered that I_c, P_{tot}, target erosion and target predeposition conditioning also affect the sputtering/nitridization rates (see below), which results in a shift of the optimum value of x_{N2}. As I_c only affects the deposition and sputtering rates, it was fixed to a value that allowed controlling the thickness of few nm films (I_c=250 mA which results in r_d of few Å/s).

ii. Deposition parameters

Substrate temperature: T_S

As pointed in section 3.1, T_S determines the film growth regime, so it is one of the primary deposition parameters affecting the microstructure and then T_C [12, 15, 17].

Thin (3–10 nm) NbN films with relatively high superconducting critical temperature ($9K < T_C < 14K$) have been deposited by magnetron sputtering by several groups on R-plane sapphire [5, 6], Si and 3C-SiC buffered Si [28] at a substrate temperatures above 600°C. The melting point of NbN is T_m=2573°C [41], so the deposition in these studies is realized in the surface diffusion (SD) regime ($T_S/T_m > 0.3$, see Figure 3.1 in section 3.1).

Because of the requirement of compatibility with GaAs optical structures and of the limit in the maximum temperature achievable in our sputtering system , the substrate temperature used in this study is T_s=400°C in order to prevent As evaporation [8], so film deposition is realized in the quenched growth (QG) regime: T_s/T_m=0.24.

High quality few-nm thick NbN films can be produced also in the QG regime using reactive magnetron sputtering and suitable substrates or buffer materials [3, 4], but film optimization is more complicated with respect to the SD regime as film microstructure depends exclusively on the balance of energetic particle bombardment and self-shadowing, and then it can be influenced by a variety of deposition parameters such as plasma pressure, substrate surface roughness and apparatus configuration (see below). The film optimization is then more challenging but in principle possible.

Some groups also report a change in nitrogen concentration in the NbN film with a change in T_S which was inferred from the change in lattice parameter [12], or a shift in the maximum of the T_C-x_{N2} curve (at fixed Ptot) towards higher value of x_{N2} [16, 42]. The need for increased x_{N2} at higher substrate temperatures is presumably due to a decrease in the N_2 sticking coefficient as temperature increases.

On which substrate?

The substrate used for film deposition is a primary factor affecting microstructure and then T_C. High T_C NbN film of several hundred nm thickness have been deposited on several different substrates, such as sapphire [13, 16, 18], fused quartz [12, 16, 20] glass [12, 16, 18, 20], MgO [4, 12, 22], Si with its native oxide [13, 15, 20, 34]. As microstructure is a far more critical factor for few-nm thick films (see sec. 2.2), up to now high quality NbN film few nm thick have been grown only on A-, M-, R-sapphire [5-7] and <100> Si buffered with 3C-SiC [28] in the SD regime, or <100> MgO [3, 4] in the QG regime. Indeed, these substrates have a small crystalline lattice mismatch with δ-NbN and allow epitaxial growth of very thin NbN films.

As it is possible to grow high crystal quality NbN films at low temperature on MgO substrates [3, 4] (having the same crystal structure and a lattice misfit of just 5.5% with respect to the NbN δ phase), in this study the deposition parameters were first optimized as a function of the superconducting properties of NbN films on MgO substrates, which made easier to separate the influence of stoichiometry from the one of microstructure. The optimized deposition parameters were then used to grow NbN films on GaAs and DBRs, which are highly mismatched substrates, under the reasonable assumption (which was later checked and confirmed, see sec. 4.3.i) that changing the substrate would not produce a change in film stoichiometry, but only in its microstructure.

Plasma pressure: P_{tot}

As already pointed out, in the QG regime film microstructure is determined exclusively by the distribution of the angle of incidence of the sputtering yield and by the energetic particle bombardment.

In balanced magnetron systems charged particles are confined by the magnetic field in the vicinity of the cathode, so only few electrons and ions reach the substrate and the energy is delivered on the growing film from the gas phase mostly through condensation of sputtered atoms and

bombardment by fast neutrals. The latter are Ar^+ ions accelerated to the cathode at energies close to the discharge voltage that are neutralized upon impact with the cathode surface and reflected from it. Being neutral they can escape and reach the substrate with energy equal to their reflected value minus that lost in collisions with the working gas. Fast neutral bombardment during growth imitates the arrival of higher kinetic energy sputtered atoms, suppressing the formation of the voided Z1 structure [31, 33]. Fast neutrals make the structure dependent on the details of apparatus configuration such as the target mass relative to that of the working gas or the cathode shape [31].

Thus both the energy flux towards the substrate and the angular distribution of the sputtered atoms depend on gas scattering, whose amount is mostly determined by the plasma pressure P_{tot}. In the QG regime, P_{tot} is then the primary deposition parameter affecting microstructure and then T_C.

Furthermore, P_{tot} influences the sputtering/nitridization balance on the target, affecting the film stoichiometry. As a consequence, the optimum value of x_{N2}, resulting in the maximum value of T_C, changes with P_{tot} [4, 13, 19, 20, 34, 37] (see e.g. Figure 3.5).

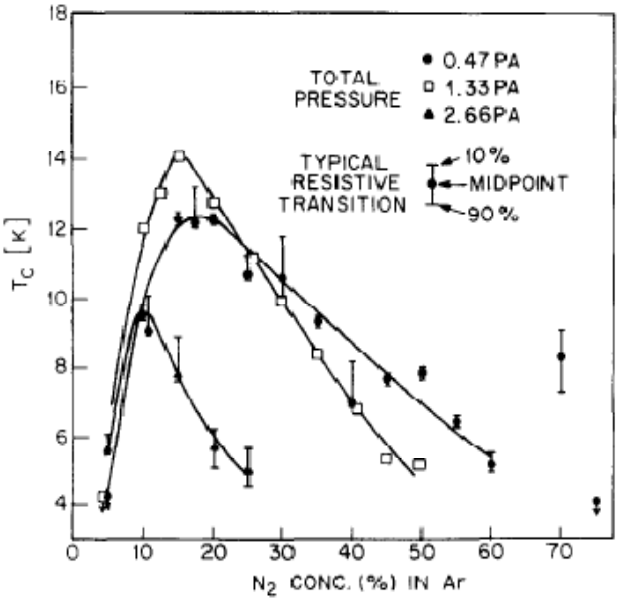

Figure 3.5. Superconducting critical temperature (T_C) of NbN films (thickness ~200-400nm) as a function of the mole concentration of N_2 in Ar for several total pressures. The vertical bars indicate the width of the normal to superconducting transition (10%-90%). [13]

The effect of P_{tot} on film microstructure is reflected on the fact that the height of the maxima of the T_C-x_{N2} curves for different P_{tot} depends on P_{tot}. Indeed, the plot of the maximum T_C as a function of P_{tot} shows a maximum [35, 43].

Stress measurements and transmission electron microscopy (TEM) observations [35, 37, 43] confirmed that the decrease of the optimum value of T_C for high P_{tot} is due to the transition from the ZT to the Z1 zone (due to the increased gas scattering). Increasing P_{tot} within the Z1 structural zone results in a decrease of T_C, as the vacancy concentration in the film increases. Reducing the total sputtering pressure within the ZT zone, film bombardment by fast neutrals becomes strong enough to damage the growing film, resulting in a decrease of T_C.

So the limits of P_{tot} range are determined by film degradation caused by destructive bombardment of the growing film by the fast neutrals at low pressures and high thermalization conditions at high pressures.

In this study, T_C was first optimized as a function of x_{N2} for P_{tot}=3.4 mtorr, then P_{tot} was further decreased down to 2.5 mtorr, the minimum pressure to sustain the plasma in the sputtering system used. Passing from 3.4 to 2.5 mtorr, no change in the optimum value of x_{N2} was observed (see section 4.i).

Target erosion

In planar, circular magnetron configurations, due to the magnetic mirror effect [36], plasma electrons are forced away from the center and the edges of the target where the magnetic field converges toward the poles of the magnets. Electrons are compressed in at an intermediate radius, where the plasma and the ion bombardment of the target are most intense. This radial confinement of the plasma results in an annular trenched erosion pattern of the target [44].

According to the few systematic studies on this subject [35, 45], target erosion affects both the stoichiometry and the microstructure of reactively sputtered NbN films.

Indeed, as sputtered particles have an initial velocity perpendicular to the cathode surface, in the case of a grooved target they will undergo more collisions and then be less energetic when reaching the substrate. From this perspective target erosion affects film microstructure in the same way as an increase of P_{tot} [35].

Furthermore, the significant increase in the effective area of the cathode results in a decrease in operating voltages and in the effective power density, and hence in a reduction in the sputtering rate [45]. If the sputtering rate decreases, then there will be a larger nitridized portion of the target. The overall effect is a change in the stoichiometry of the films equivalent to an increase of x_{N2} for the same P_{tot}: for this reason the maximum of the curve T_C-x_{N2} (at fixed P_{tot}) for an eroded target is translated towards lower values of x_{N2} [35].

It has been shown [35] that a way to make the film properties independent of the target erosion state is to use an unbalanced sputtering source.

In this study, NbN films with the best superconducting properties were deposited using fresh ungrooved targets, which resulted in cathode voltages of the order of V_c~650 V.

Predeposition conditioning

When controlling the film stoichiometry by x_{N2} at P_{tot} and I_c constant, it must be considered that in current-controlled DC reactive magnetron sputtering, the nitridization state of the target also depends on the initial state (poisoned/uncoated) of the target itself [18, 20].

Indeed, at intermediate x_{N2} (which result in the stoichiometries of interest), for the same value of N_2 flow (f_{N2}) the target can be more or less nitridized depending on whether the N_2 flow was increased from zero (uncoated target initial state) or decreased from a higher value (poisoned target initial state). The secondary electron emission coefficient of NbN is lower than the one of Nb so, as the target is covered with NbN, the cathode voltage must increase to maintain the discharge current constant [34]. This results in an hysteresis in the plot of cathode voltage vs f_{N2} at constant Ar partial pressure [20] (Figure 3.6).

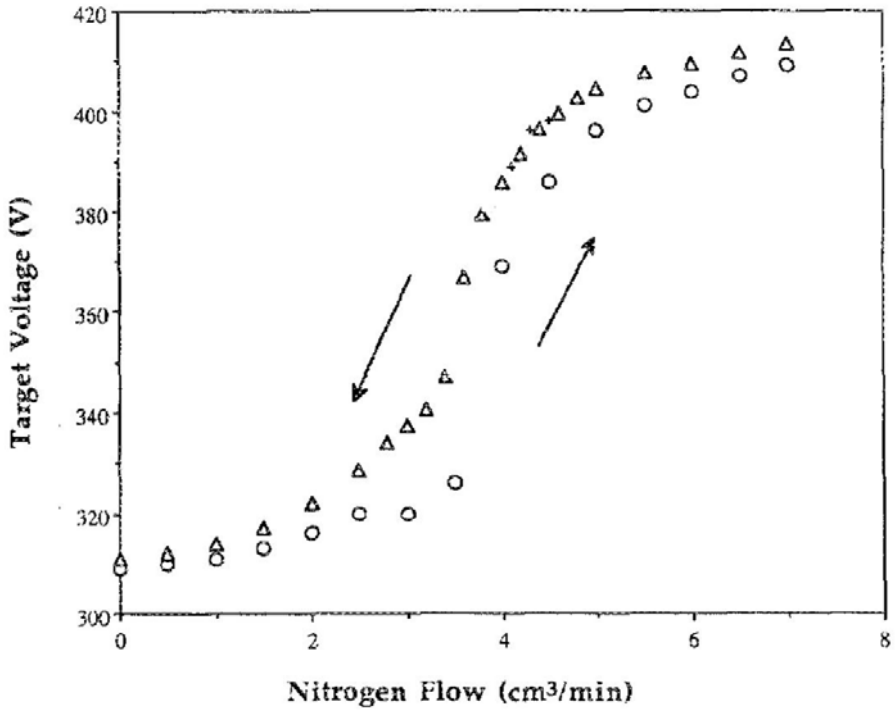

Figure 3.6. Cathode voltage hysteresis with nitrogen flow, at constant current and argon partial pressure. [20]

To have control on the stoichiometry of the films, depositions must be performed always on the same branch of the hysteresis curve, so the target must be conditioned, i.e. sputtered in pure Ar [18], or in an N_2 rich mixture [13, 20] in order to completely uncoat or poison it, respectively.
There is no evidence suggesting that a conditioning strategy results in better films, it is just important to ensure that the films are always deposited on the proper branch of the hysteresis curve. In this study, the target was was sputtered in pure Ar to expose fresh Nb before setting the desired f_{N2} and start the deposition (see chapter II).

Substrate bias: V_S

As explained above, in a balanced magnetron system charged particles are localized over of the cathode by the magnetic field, which results in a much lower plasma density over the substrate and a weaker ion bombardment on the growing film respect to ordinary sputtering. Anyway, the amount of energy delivered to the film through ion bombardment can be controlled changing the bias state of the substrate.
If V_S=0 V, the voltage drop between the plasma and the substrate equals the minimum anode sheath voltage drop [36] and the contribution of ion bombardment is negligible. If the substrate is left floating, electrons that escape the magnetic trap charge the substrate negatively, so it develops a self potential which is negative respect to ground, which increases the energy of bombarding Ar^+ ions [35]. Finally, the energy of ion bombardment can be further increased with a negative bias.
In this study, the substrate holder is connected to ground (see chapter II).

Target-substrate distance: d_{t-s}

Changing the distance between target and substrate affects films microstructure as it changes the number of collisions a particle experiences moving from one to the other and hence the thermalization condition of the sputtering yield and of fast neutrals [46].

In this study, the distance between target and substrate was kept at the maximum allowed by the sputtering system (85mm) to maximize film uniformity.

In conclusion, increasing T_S by intentional heating, changing thermalization conditions of the sputtering yield by lowering P_{tot} or by reducing d_{t-s}, increasing ion bombardment by applying a substrate bias, all result in an increase of T_C as all control surface diffusion and then the intergrain voids (for the Z1 structure) and defect concentration (for the ZT structure) in the same way.

Figure 3.7 shows a block diagram summarizing the relations presented in section 3.2 between deposition parameters, physics of the deposition and the film structure.

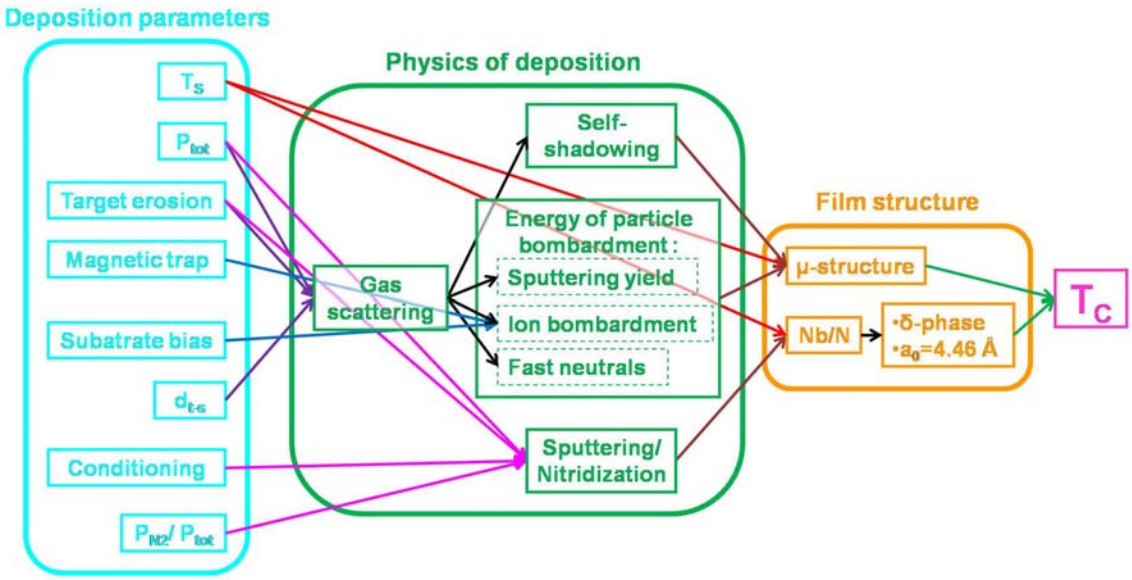

Figure 3.7. Block diagram summarizing section 3.2.

3.3. Microstructure characterization

Depending on film thickness, several methods have been reported to characterize film structure in terms of crystal phase, lattice constant, orientation of the film crystal respect to the substrate(epitaxial relation), microstructure (grain size and island structure for polycrystalline films, crystal defects for single-crystal films).

For NbN film of several hundred nm thickness the most widely used techniques are x-ray diffraction (XRD) [4, 13, 15, 18, 20], reflection high-energy electron diffraction (RHEED) [22] and cross-sectional transmission electron microscopy (TEM) in image and electron diffraction modes [4, 13].

In most of the studies on few nm thick films, structural characterization is performed by cross-sectional high resolution TEM (HRTEM) [3, 6, 28], as XRD cannot be used for sensitivity reasons [7].

Furthermore, an indirect but reliable estimation of the crystal quality of both hundreds of nm thick [4, 6, 13, 16, 19, 22] and few-nm thick [6, 15] films is given by the variation of resistance with temperature, which is characterized by the residual resistivity ratio, i.e. the ratio of the resistivity of the film at 300K to that at 20K: RRR= ρ(300 K)/ρ(20 K). Indeed, a thermally activated conduction process (RRR<1) implies a granular microstructure, i.e. a network of crystal grains surrounded by

non-conducting boundaries [47] such as voids, insulating material or absorbed nitrogen. On the other hand, metallic resistance-temperature characteristics with residual resistivity ratios RRR exceeding one strongly suggest high quality crystalline properties.

4. Experimental results

As exposed and motivated in section 3, NbN films ranging from 150nm to 3nm in thickness were deposited on epitaxial-quality single crystal MgO <100>, GaAs <100> un-doped (with and without an MgO buffer layer) and Distributed Bragg Reflector (DBR) structures fabricated on GaAs (see also chapter II). The deposition technique is the current controlled DC magnetron sputtering (planar, circular, balanced configuration) of Nb in an Ar + N_2 plasma. The deposition parameters are listed in Table 4-1.

Base pressure	$\sim 10^{-7}$ mbar
Cathode current (I_c)	250 mA
Substrate temperature (T_S)	400°C
Total Pressure (P_{tot})	3.4, 2.5 mtorr
Cathode voltage (V_c)	420 ÷ 650 V
Conditioning	uncoated
Substrate bias (V_S)	grounded
Target-substrate distance (d_{t-s})	85 mm

Table 4-1. Deposition parameters.

4.1. Characterization of the plasma

Following [20], the complete hysteresis curve of cathode voltage (V_c) with nitrogen flow f_{N2} at fixed Ar partial pressure (P_{Ar}=1.675 mtorr) was determined (Figure 4.1). To expose fresh Nb on the target it was sputtered for 60' in Ar only (P_{tot}=P_{Ar}=4 mtorr), then, with the plasma still on, P_{Ar} was set to the desired value for the experiment. The plasma was left to stabilize. The plasma was considered stable if V_c did not vary more than +/-2 V in 3'. N_2 was then added to the discharge in 0.5 sccm increments (purple branch of the hysteresis curve). The system was allowed reaching equilibrium for 3' before cathode voltage was recorded. After the target had become totally nitridized (operating above the hysteresis portion of the curve), the downward portion of the hysteresis curve was determined by decreasing the N_2 flow in 0.5 sccm steps (green branch).
The optimum operating point chosen for the deposition of high quality NbN films lays on the lower branch, as shown.

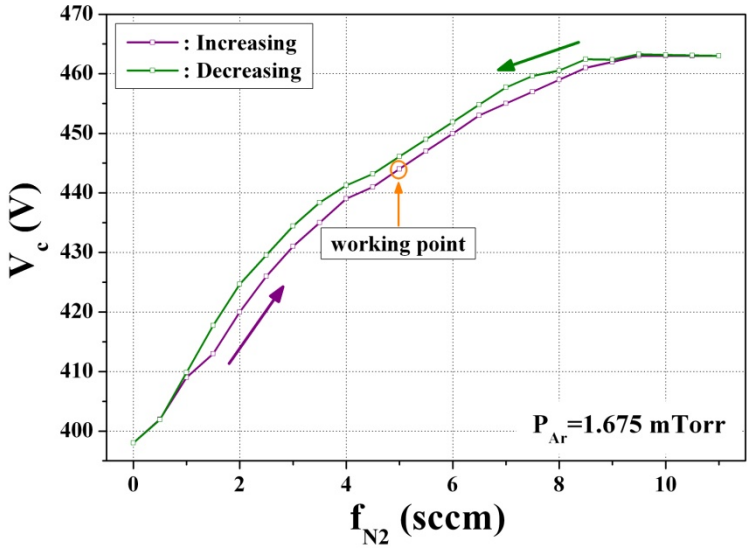

Figure 4.1. Cathode voltage V_c as a function of N_2 flux f_{N2} at constant Ar partial pressure P_{Ar}=1.675 mtorr and cathode current I_c=250 mA.

4.2. NbN on MgO substrates

Deposition parameters were optimized for the growth of NbN on MgO substrates. The optimized growth conditions were used to deposit NbN also on GaAs and DBRs, assuming they would not change for different substrates.

i. Deposition parameters optimization

Nitrogen concentration x_{N2}

Following [19, 20, 37], the superconducting properties of NbN thin films (*th*=90 to 120 nm) deposited on MgO were optimized studying the effects of a variation of the nitrogen partial pressure (P_{N2}) on the critical temperature T_C, on the superconducting transition width ΔT_C and on the critical current density J_C at constant total pressure P_{tot}=3.4 mtorr. x_{N2} was varied within the limits determined by the requirement to produce the NbN δ phase [48]. The target used for this set of depositions was deeply grooved, with V_c ranging from 412 V to 471 V.

T_C and J_C show a maximum as a function of nitrogen partial pressure for the same N_2 concentration $x_{N2}=P_{N2}/P_{tot}$=33% (Figure 4.2). The superconducting critical parameters of the optimum film are T_C=14.3 K, ΔT_C=0.3 K, J_C(4.2 K)=2 MA/cm^2.

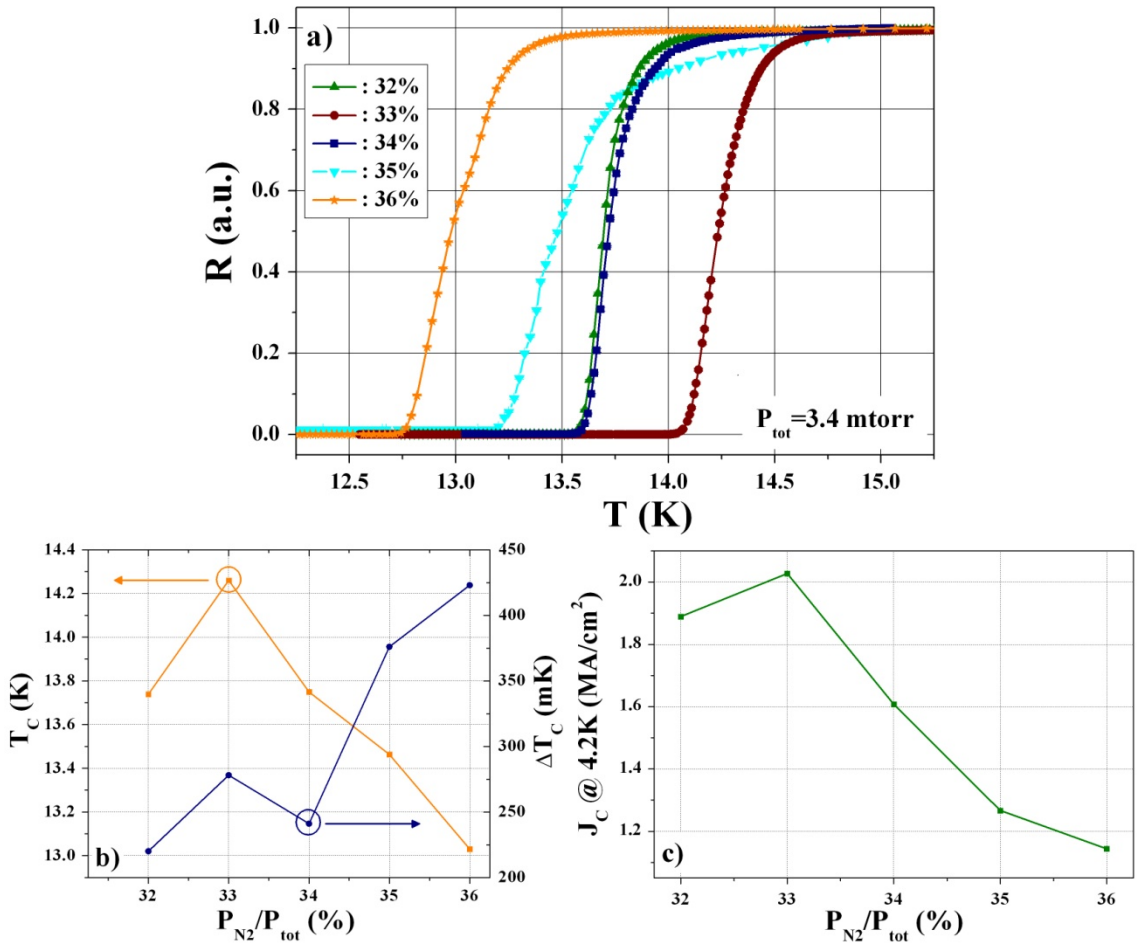

Figure 4.2. a. Resistance vs temperature dependence of NbN films (90 to 120 nm thick) deposited on MgO at five different nitrogen concentrations ($x_{N2}=P_{N2}/P_{tot}$=31 to 36%). b. Values of T_C and ΔT_C extracted from figure. a (see chapter II) as a function of x_{N2}. c. Superconducting critical current density at 4.2 K as a function of x_{N2} for the same samples. The samples were deposited at I_c=250 mA, T_S=400°C, P_{tot}=3.4 mtorr, V_c=412 to 471 V (grooved target), V_S=0 V, d_{t-s}=85 mm.

Total pressure P_{tot}

The critical temperature of the optimum film is ~2 K lower than the state of the art value for NbN films of the same thickness (see e.g. [4]), which was attributed to the microstructure of the films. In order to improve the superconducting properties of the films P_{tot} was then further decreased down to 2.5 mtorr, the minimum pressure to sustain the plasma in the sputtering system used. As P_{tot} affects the sputtering/nitridization balance on the target, it was necessary to check for a shift of the maximum of the T_C-x_{N2}. NbN thin films (*th*=120 to 150 nm) were deposited on MgO varying x_{N2} from 31% to 35%. The target used for this set of depositions was again deeply grooved, the cathode voltage was V_c~430 V.

As shown in Figure 4.3, passing from 3.4 to 2.5 mtorr, no change in the optimum value of x_{N2} was observed, but no improvement in the T_C was observed either. Therefore, P_{tot} proved not to be the critical parameter affecting the quality of NbN films.

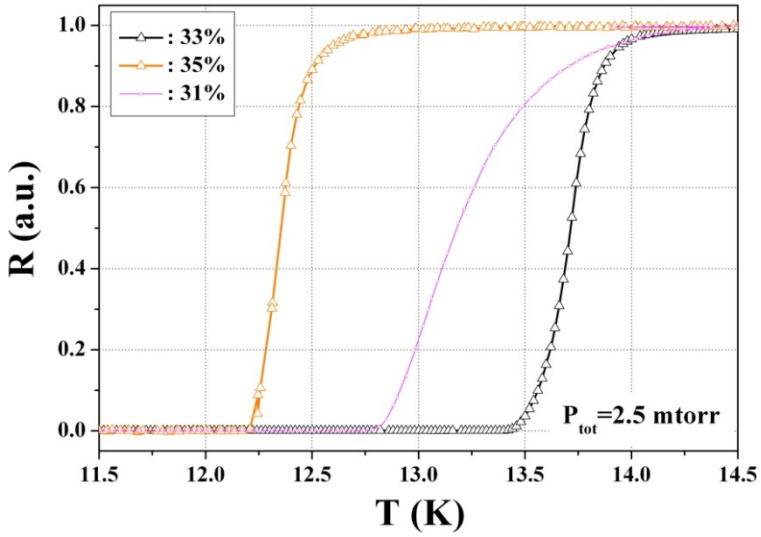

Figure 4.3. Resistance vs temperature dependence of NbN films (120 to 150 nm thick) deposited on MgO at three different nitrogen concentrations ($x_{N2}=P_{N2}/P_{tot}$=31, 33, 36%). The films were deposited at I_c=250 mA, T_S=400°C, P_{tot}=2.5 mtorr, V_c~430 V (grooved target), V_S=0 V, d_{t-s}=85 mm.

Target erosion

The critical factor significantly influencing the superconducting properties of NbN films is target erosion. As mentioned above, target erosion can be quantified by the decrease in the cathode voltage V_c with the sputtering time when all the other deposition parameters are kept constant (see Figure 4.4). In about three hours of sputtering, V_c drops from ~660 V for a fresh target to ~540 V for a grooved one.

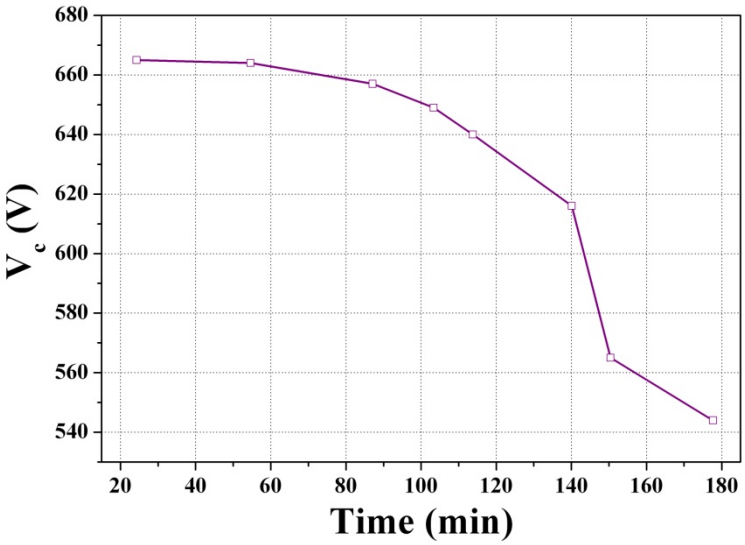

Figure 4.4 Decrease of the cathode voltage V_c with the sputtering time due to the Nb target erosion.

The degradation of the superconducting quality of NbN films with the decrease of V_c (i.e. with target erosion) is shown in Figure 4.5. A decrease of ~130 V in V_c results in a drop of ~4 K of T_C and in a factor seven increase of ΔT_C in NbN films of thickness th=100 ÷ 150 nm, deposited at the same x_{N2} and P_{tot}, due to the evolution of the film microstructure towards the Z1 highly defected, voided structure (see section 3.2.ii).

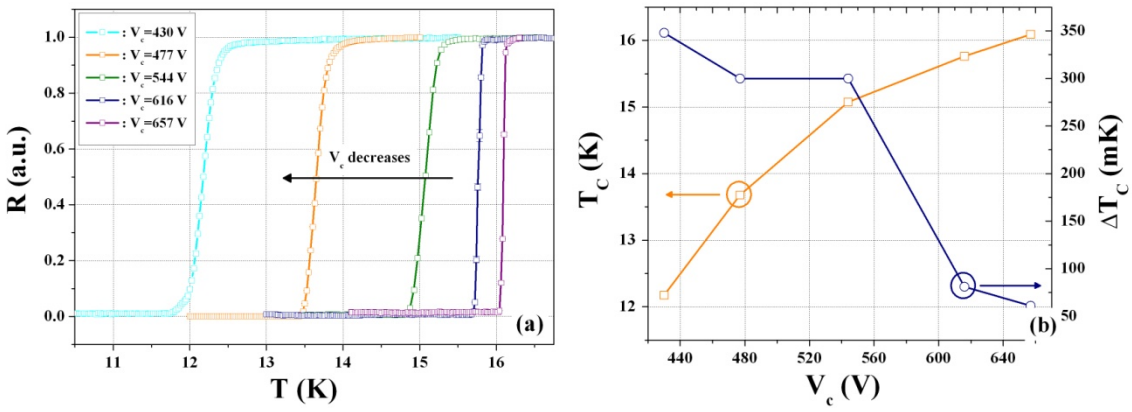

Figure 4.5. (a) Resistance as a function of temperature for NbN films of thickness th=100 ÷ 150 nm deposited under the same conditions of x_{N2}=33% and P_{tot}=2.5 mtorr, but using targets in different states of erosion (V_c decreases as the erosion increases). (b) Decrease of T_C and increase of ΔT_C with target erosion.

Using a fresh, ungrooved Nb target and the optimum values of x_{N2} and P_{tot} it was possible to grow NbN films with state of the art superconducting properties. An 150 nm thick film showed T_C=16.1K with a ΔT_C=60 mK and a residual resistivity ratio RRR=1.1, indicating that no intergrain voids were present [47]. Considered the high superconducting quality achieved with the samples deposited with fresh targets, it was assumed that the change in the target erosion state did not result in a substantial shift in the optimum value of x_{N2}. A further optimization of T_C as a function of x_{N2} for an ungrooved target was then considered unnecessary and the optimum value of x_{N2}=33%, found with a grooved target, was kept unchanged.

ii. Decreasing film thickness

As well documented in literature [3-5, 15, 24], decreasing film thickness leads to a degradation of their superconducting and electrical properties (see section 2.2). To investigate this dependence, NbN films ranging from 150 to 3 nm in thickness were deposited on MgO substrates under the same deposition conditions.

Decreasing thickness from 10 to 3 nm results in a sharp drop in the superconducting critical temperature and in an increase in the transition width (Figure 4.6a). Furthermore, the conduction process changes from metallic for 100 nm thick films to thermally activated for few nm films (Figure 4.6b) due to a much stronger grain boundary contribution as the grain size decreases.

The thinnest films (th=3 nm) still exhibit T_C=8.6 K, ΔT_C=0.9 K and RRR=0.6, which are state of the art values, proof of the excellent quality of our low-temperature deposition process.

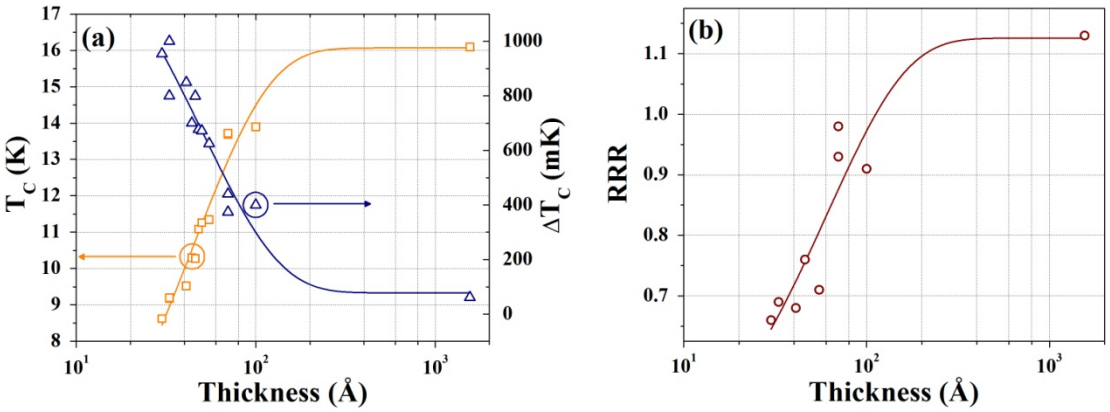

Figure 4.6. Decrease of T_C and increase of ΔT_C (a) and of the RRR (b) as NbN film thickness decreases. The thickness was measured with a stylus profilometer for thick (th>20 nm) films and by AFM for thin (th<20 nm) films (see chapter II). The films were deposited at I_c=250 mA, T_S=400°C, P_{tot}=2.5 mtorr, x_{N2}=33%, V_c~650 V (fresh target), V_S=0 V, d_{t-s}=85 mm.

iii. Choice of the best MgO substrate

As discussed above, the superconducting properties of NbN films depend on their microstructure (sec. 2.2), which, in the QG regime, is affected by the self-shadowing effect (sec. 3.1). Thus, the crystal finishing of the substrate on which NbN films are deposited is a critical issue. For this reason, a comparison was made on the superconducting properties of NbN thin films deposited on nominally identical MgO substrates from different suppliers.

The MgO substrates used were square (10 x 10 x 0.25 mm^3), one side epi-polished and <100> oriented, from MarketTech International, MaTecK GmbH and MTI Corporation. NbN films (100 nm thick) were deposited simultaneously on the three substrates. The highest T_C (see Figure 4.7) was exhibited by the NbN film grown on the MgO substrate from MTI Corporation, which was then chosen as supplier.

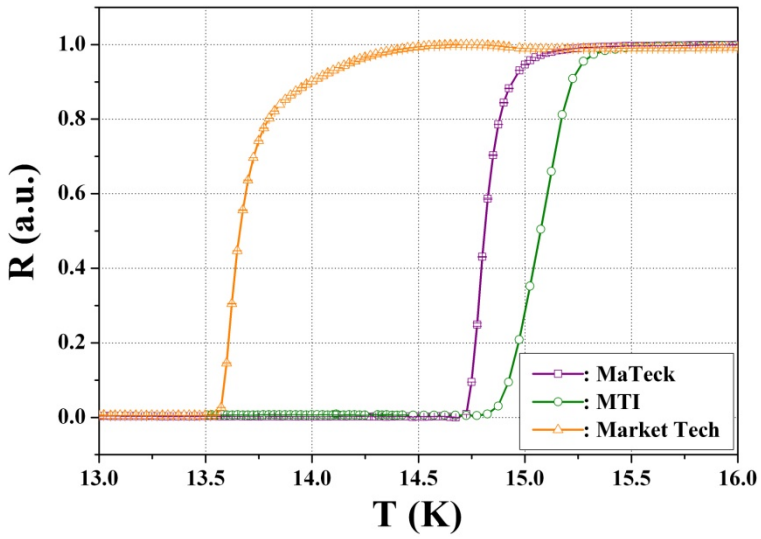

Figure 4.7. Resistance as a function of temperature for 100 nm thick NbN films deposited simultaneusly on nominally identical MgO substrates from different suppliers. The films were deposited at I_c=250 mA, T_S=400°C, P_{tot}=2.5 mtorr, x_{N2}=33%, V_c~600 V (fresh target), V_S=0 V, d_{t-s}=85 mm.

iv. Deposition on larger MgO substrates

At present, our fabrication process of SSPDs has still a very low yield. In order to obtain more good devices per fabrication run we tried to increase the surface of the wafers.

For this reason, a comparison was made between the superconducting properties of NbN thin films deposited simultaneously on one of the 10 x 10 x 0.25 mm^3 MgO substrates routinely used (MTI Corporation) and on a 20 x 20 x 0.25 mm^3 substrate (MaTecK GmbH). As shown in Figure 4.8, the quality of the NbN films grown on the two substrate is comparable.

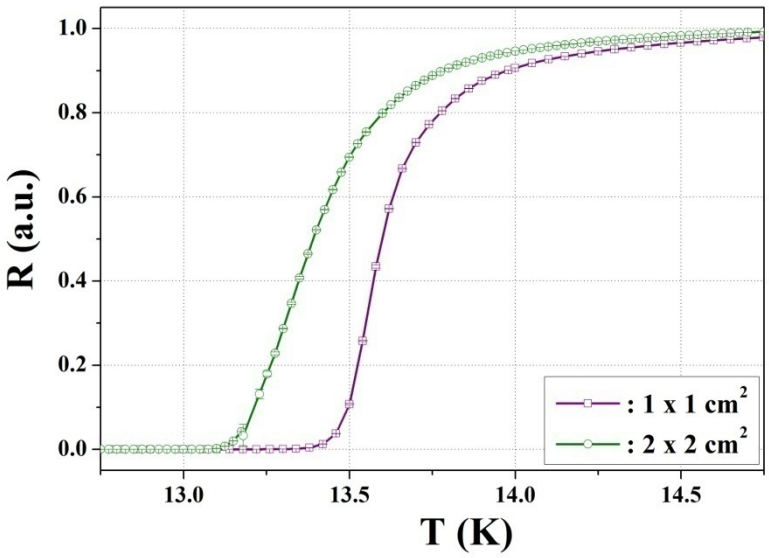

Figure 4.8. Resistance as a function of temperature for 7 nm thick NbN films deposited simultaneusly on a 10 x 10 x 0.25 mm^3 (violet) and on a 20 x 20 x 0.25 mm^3 (green) MgO substrate. The films were deposited at I_c=250 mA, T_S=400°C, P_{tot}=2.5 mtorr, x_{N2}=33%, V_c~650 V (fresh target), V_S=0 V, d_{t-s}=85 mm.

v.Baking test

After deposition, few-nm thick NbN films need to withstand repeated thermal cycling during the device fabrication process (see sec. 5 and chapter II). The effect of baking on the films was then investigated.

Two 4.5 nm-thick NbN films were cleaved in 2 parts, of which one was used to test how baking time and temperature affect the superconducting properties of NbN. The samples were glued with liquid In on the sample holders used for depositions (the thick or the thin sample holder, see chapter II) and then baked on the hotplate for different times and at different temperatures.

The first sample was glued on thin sample holder (to achieve a better thermal coupling between the hotplate and the film) and it was baked at a temperature of 345°C (the maximum achievable with the hotplate) for 4 min. The result of this worst-case test is a strong decrease in T_C of ~1 K (see Figure 4.9a), proof that baking is indeed a critical step.

The other sample was glued on the thick sample holder and it was baked at a temperature of 245°C (the minimum required to melt the In on the thick sample holder) for 7 min (which is the time needed to unload the thick sample holder with 6 samples on it, see chapter II). As shown in Figure 4.9b, no degradation of superconductivity is observable, which means that the sample un-mounting step after deposition (see chapter II) does not affect the quality of the films.

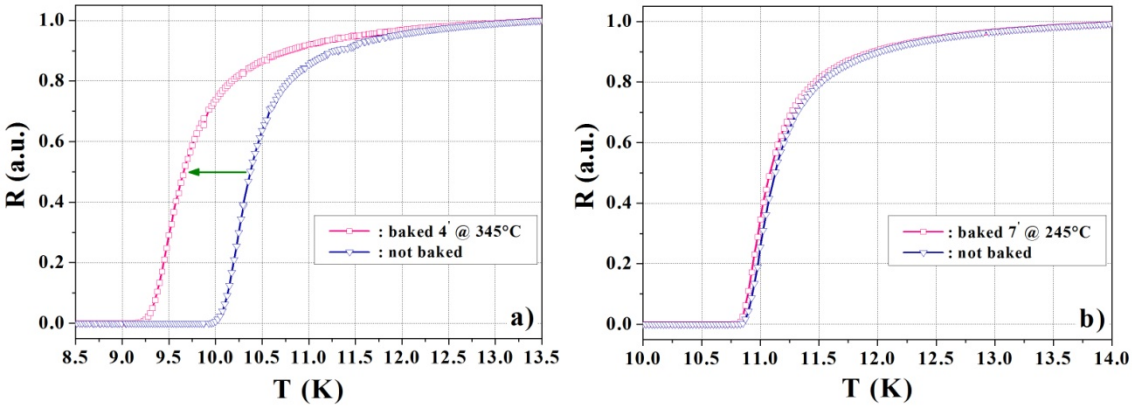

Figure 4.9. a. Resistance as a function of temperature for a 4.5 nm-thick NbN film baked at a temperature of 345°C for 4 min (pink) and not baked (blue). b. Resistance as a function of temperature for a 4.5 nm-thick NbN film baked at a temperature of 245°C for 7 min (pink) and not baked (blue). The films were deposited at I_c=250 mA, T_S=400°C, P_{tot}=2.5 mtorr, x_{N2}=33%, V_c=675 V (fresh target), V_S=0 V, d_{t-s}=85 mm.

4.3. NbN on GaAs and DBRs

i. Deposition parameters optimization

In order to check that the optimum value of x_{N2} found for NbN on MgO did not shift changing the substrate, a set of NbN films (*th*=120 to 150 nm) were deposited on GaAs varying x_{N2} from 31% to 35% at constant total pressure P_{tot}=2.5 mtorr. The target used for this set of depositions was deeply grooved, the cathode voltage was V_c~430 V.

As shown in Figure 4.10, no change in the optimum value of x_{N2} was observed with respect to MgO substrates. The superconducting critical parameters of the optimum film are worse than for NbN films of the same thickness deposited on MgO under the same conditions (see Figure 4.3), which was attributed to a lower quality film microstructure (see below).

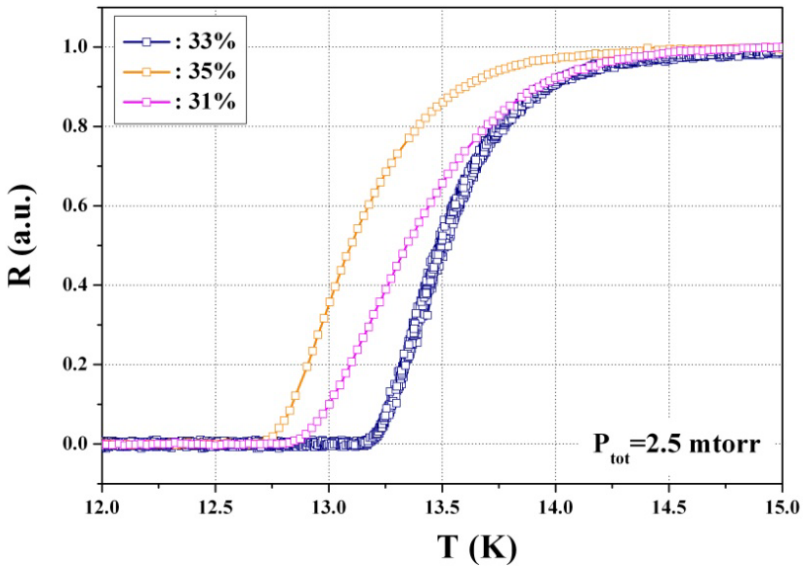

Figure 4.10 Resistance vs temperature dependence of NbN films (120 to 150 nm thick) deposited on GaAs at three different nitrogen concentrations (x_{N2}=P_{N2}/P_{tot}=31, 33, 35%). The films were deposited at I_c=250 mA, T_S=400°C, P_{tot}=2.5 mtorr, V_c~430 V (grooved target), V_S=0 V, d_{t-s}=85 mm.

ii. Decreasing film thickness

The superconducting and electrical properties of NbN films deposited on GaAs and DBRs were investigated as a function of thickness. NbN films ranging from 140 to 3 nm in thickness were then deposited on MgO GaAs and DBRs (see chapter II and section 4.3.iii) under the same deposition conditions.

No change in film properties was observed whether films were deposited on GaAs substrates or on DBRs. The quality of these films is lower than for NbN deposited on MgO, as for any thickness they systematically exhibit lower T_C (Figure 4.11b), wider superconducting transition (Figure 4.11c) and lower RRR (Figure 4.11d).

As T_C of NbN films deposited on GaAs and DBRs was maximized as a function of x_{N2} to obtain the optimum stoichiometry, the degradation of the superconducting properties exhibited by these films was attributed to a highly defected microstructure, due to the higher lattice misfit between NbN and GaAs and to a poorer quality of the substrate surface (see sec. 4.4).

NbN films on GaAs 5.5 nm thick still exhibit T_C= 10.7 K, ΔT_C=1.1 K and RRR=0.7, which compares with 4.5 nm thick films on MgO, making them suitable for device fabrication (see chap. IV).

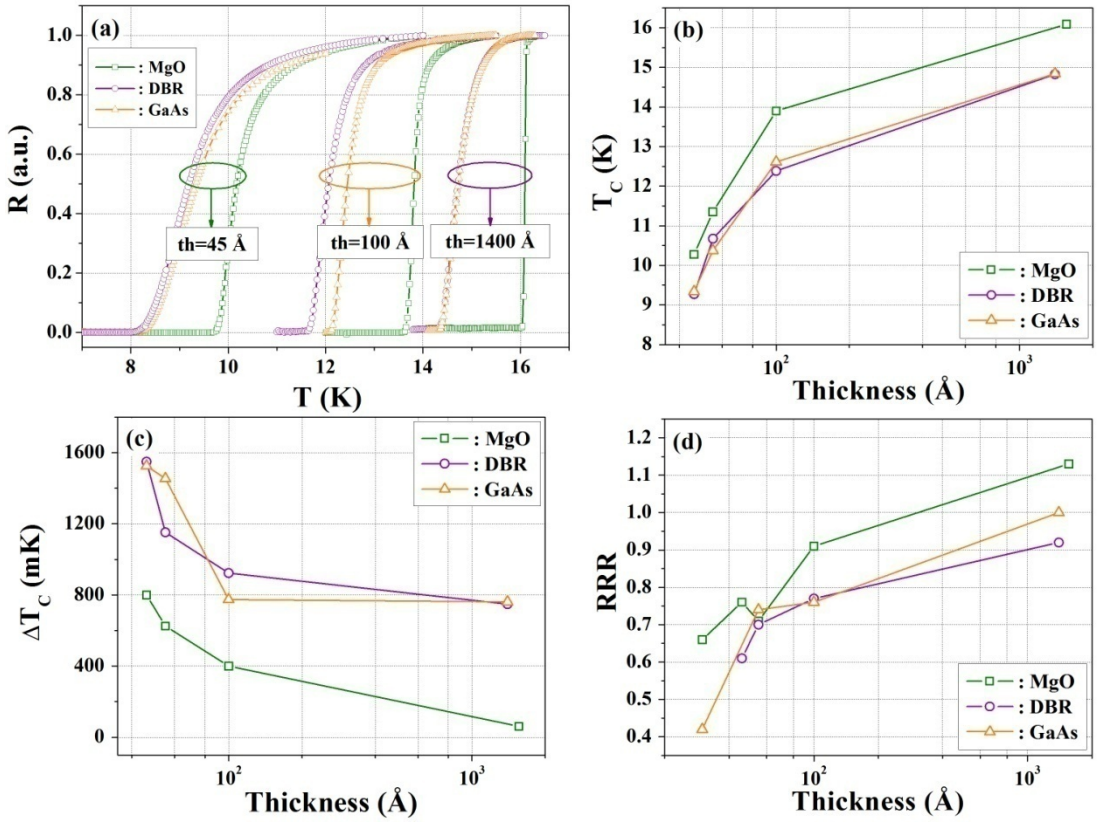

Figure 4.11 (a) Resistance as a function of temperature for NbN films of thickness th=45 ÷ 1400 Å deposited in the same sputtering run on MgO (green squares) dusty (see section 4.4.ii) GaAs (orange triangles) and DBRs (violet circles). (b-d) Decrease of T_C (b) and of the RRR (d) and increase of ΔT_C (c) as NbN film thickness decreases. The thickness was measured with a stylus profilometer for thick (th>20 nm) films and by AFM for thin (th<20 nm) films (see chapter II). The films were deposited at I_c=250 mA, T_S=400°C, P_{tot}=2.5 mtorr, x_{N2}=33%, V_c=645-665 V (fresh target), V_S=0 V, d_{t-s}=85 mm.

iii. Absorbance of NbN on DBRs

Description of the structure

The DBR structure on which the NbN film was deposited was optimized to enhance the absorption in the SSPD for light at λ=1.3 μm. The design was performed modeling the absorption of photons by SSPDs as a TE plane wave interacting with an infinite NbN grating (Figure 4.12). The structure was simulated by Dr. D. Bitauld with a simple one dimensional (1D) transfer matrix model and grown by molecular beam epitaxy (MBE) by Dr. L. H. Li.

The dielectric constants of the different materials were deduced either from measurements [49] or the literature. The parameters are: ε_{NbN}=-13+37i, ε_{GaAs}=3.414, ε_{AlAs}=2.909. The NbN oxide layer was not taken into account.

In our 1D model, the NbN grating was modeled as a continuous layer of the same thickness and effective dielectric constant $\varepsilon_{eff}=f\cdot\varepsilon_{NbN}+(1-f)$ (with f the filling factor of the grating), i.e. the weighted mean of NbN and air.

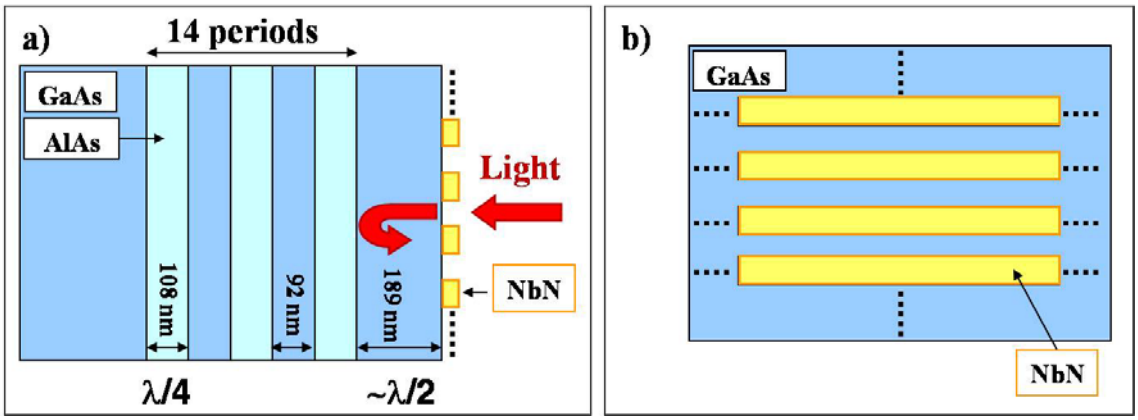

Figure 4.12. Cross-sectional (a) and top (b) views of the structure used for simulations.

The result of this simplified analysis is that an absorbance of α=72% for a grating of 100 nm-wide 5 nm-thick NbN nanowires with 40% filling factor.

Reflectometry results

In order to test the designed DBR structure, measurements of the reflectivity (R) as a function of wavelength were performed on a DBR on which a 7 nm-thick NbN layer (T_C=10.7 K) was deposited (Figure 4.13, green plot).

The reflectivity dip, corresponding to maximum absorption is blue-shifted of about 100nm respect to the designed 1300 nm value (Figure 4.13, in green). This results from a decrease in thickness of the final λ/2 GaAs layer ($T_{\lambda/2}$) in the DBR during the NbN deposition step (during the baking at 400°C before the sputtering of NbN, see chap. II), due to As evaporation (see also section 4.4.i).

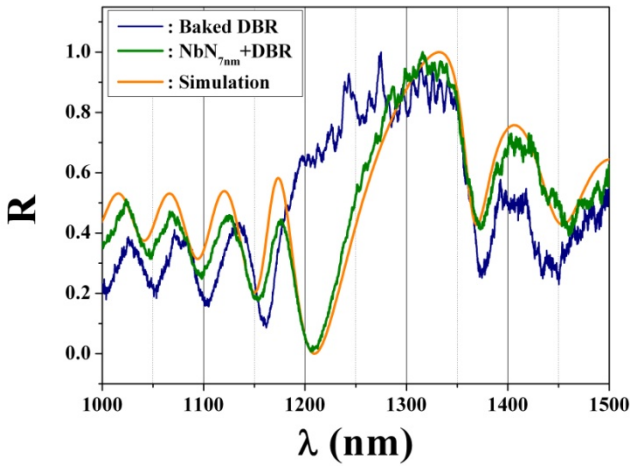

Figure 4.13. Reflectivity (R) as a function of wavelength (λ) for a NbN_{7nm} + DBR structure (experimental and simulation data in green and orange, respectively) and for a bare DBR structure after baking at 400°C in vacuum for 4 days (in blue).

Indeed, measurements of the reflectivity as a function of wavelength were performed on a bare DBR structure before and after baking at 400°C in vacuum for 4 days. The comparison between simulations and experiments (Figure 4.14, orange and blue curves, respectively) shows that, due to As evaporation, the thickness of the final λ/2 GaAs layer of the DBR decreased from $T_{\lambda/2}$=189 nm before baking (Figure 4.14a), which is the designed value (see Figure 4.12), to $T_{\lambda/2}$=165 after baking (Figure 4.14b).

For the NbN_{7nm}+DBR structure, comparing simulation and experiment (Figure 4.13, orange and green plots, respectively), we can infer that for the structure measured $T_{\lambda/2}$=160 nm. The R of a baked bare DBR structure for which $T_{\lambda/2}$=165 nm is also shown (Figure 4.13, in blue).

The absorbance of the NbN_{7nm} + DBR structure, derived from simulations, is α=90% at λ=1200 nm.

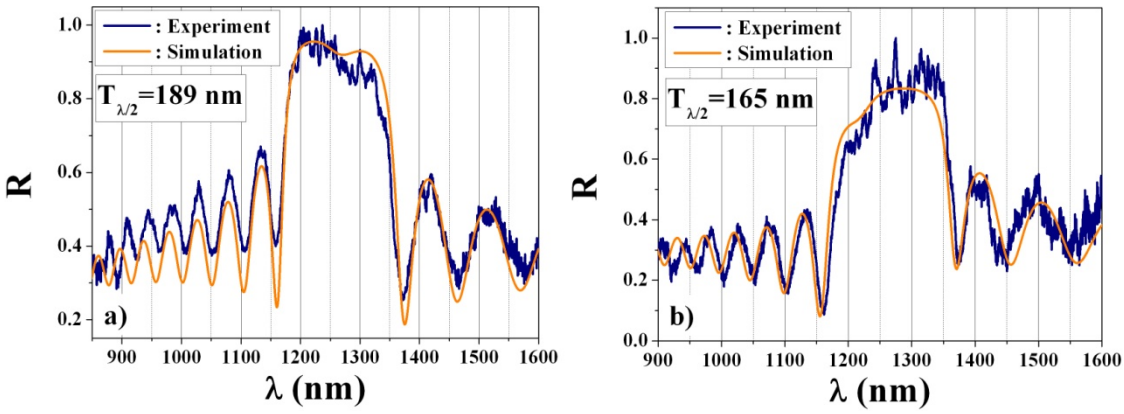

Figure 4.14. Reflectivity (R) as a function of wavelength (λ) for a DBR structure before (a) and after (b) baking it at 400°C in vacuum for 4 days. Experimetal data are plotted in blue, simulation results are in orange.

4.4. Approaches to improve T_C on GaAs and DBRs

As the degradation of the superconducting and electrical properties exhibited by NbN films deposited on GaAs and DBRs is most likely due to a defected microstructure, the goal was to identify the sources of these defects and to reduce them.

i. The baking problem: As evaporation

The first possible source of defects identified was the evaporation of As from the GaAs substrate or the final λ/2 layer when baking the chamber in vacuum at 400°C (before the sputtering of NbN, see chap. II), which could degrade the quality of the substrate surface. Indeed, As evaporation was believed to cause surface defects such as Ga droplets, but they were not observed with optical microscopy. Furthermore, the effect of a reduction of baking time on the superconducting properties of NbN thin films was studied, but no significant improvement was observed for a reduction from ~24 hours to ~4 hours. Arsenic evaporation results anyway in a blue-shift in the absorption peak of the NbN+DBR structure (see sec. 4.3.iii), which was then the reason to keep the baking time short when depositing NbN on DBRs.

ii. Substrate cleaning

The effect of cleaning the substrate surface was also investigated. Due to the cleaving of GaAs or of DBR 2" wafers in smaller pieces (see chap. II), the surface of the substrates used for NbN deposition is covered with GaAs macroscopic dust, which cannot be removed simply with a compressed nitrogen flow.

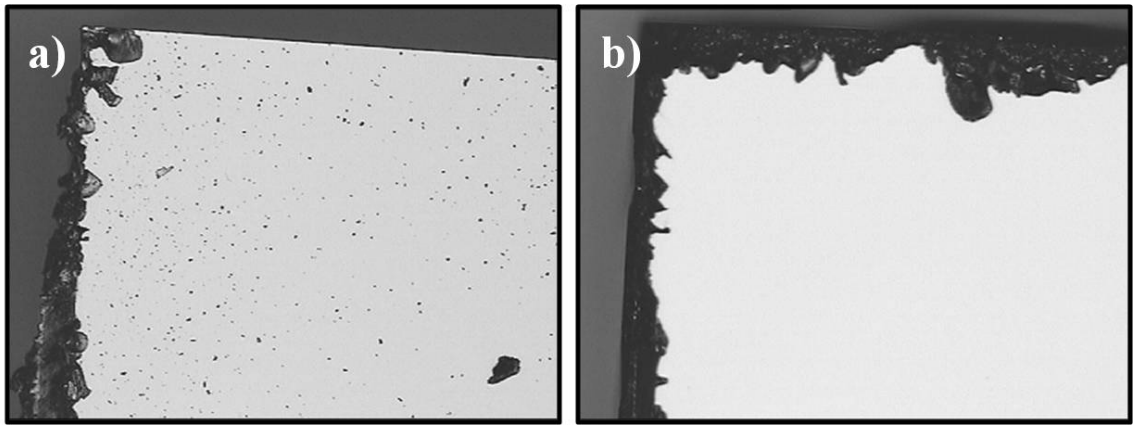

Figure 4.15. Optical microscope pictures (taken at the same magnification) of the surface of a dusty (a) and a clean (b) GaAs substrate.

This dust was not routinely removed, so NbN was deposited on a *dusty* surface (Figure 4.15a). In order to clarify whether this dust degraded NbN superconducting quality, NbN thin films were deposited in the same sputtering run on an MgO substrate, on a *dusty* GaAs substrate, and on a *clean* GaAs substrate. The *clean* sample was prepared washing the GaAs substrate in an ultrasonic bath, first in trichloroethylene, then in isopropanol (Figure 4.15b).
Preliminary results (Figure 4.16) show a significant improvement of the superconducting properties of the NbN film deposited on the *clean* GaAs substrate, as compared to the *dusty* substrate.

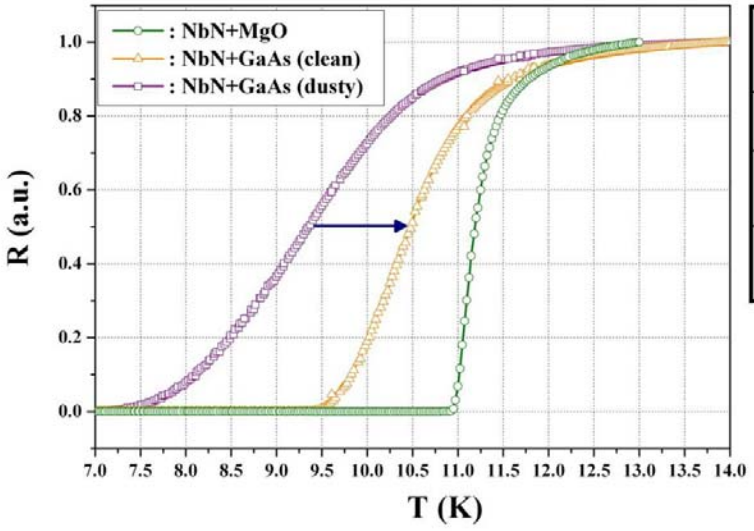

Sample	T_c (K)	ΔTc (mK)
MgO	11.25	500
GaAs (clean)	10.50	1400
GaAs (dusty)	9.30	2460

Figure 4.16. Resistance vs temperature dependence of NbN films deposited in the same sputtering run on: an MgO substrate (green circles), on a clean GaAs substrate (orange triangles) and on a dusty GaAs substrate (violet squares). The films were deposited at I_c=250 mA, T_S=400°C, P_{tot}=2.5 mtorr, x_{N2}=33%, V_c=660 V (fresh target), V_S=0 V, d_{t-s}=85 mm.

iii. Preliminary results with the MgO buffer layer

As the lattice mismatch of the superconducting δ-phase of NbN with GaAs is far larger than with MgO, the crystal quality of the NbN films grown on GaAs substrates is worse in terms of grain size, strain, crystal defects, which degrades its superconducting properties. We started to develop a process to deposit MgO buffer layers on GaAs substrates aiming for an enhancement of the microstructure of the NbN films grown on these structures.

MgO buffer layers ranging from 290 to 10 nm in thickness were deposited on GaAs <100> un-doped substrates by power controlled RF magnetron sputtering (planar, circular, balanced configuration) of stoichiometric MgO in an Ar plasma. The MgO depositions were carried out by A. Surrente in another sputtering system than the one described in chapter II, used to grow NbN (see [50] for further details).

For a first set of experiments, two values of the RF power (P_{RF}) were chosen (P_{RF}=60W and P_{RF}=80W), and thick (200-300 nm) and thin (10-20 nm) MgO buffer layers were deposited for each power level. Two thick-buffered (th_{MgO}=260 nm, deposited at P_{RF}=60 W and th_{MgO}=285 nm, deposited at P_{RF}=80 W) and two thin-buffered (th_{MgO}=10 nm, deposited at P_{RF}=60 W and th_{MgO}=20 nm, deposited at P_{RF}=80 W) samples were then chosen for the NbN deposition. A 7 nm-thick NbN film was then deposited in the same sputtering run on the selected MgO-buffered GaAs substrates, on a GaAs substrate, and on an MgO substrate.

The resistance as a function of temperature close to the critical temperature was measured for the six NbN films. Remarkably, NbN films deposited on the thick-buffered samples remain normal down to 4.5 K. A possible explanation is that the thick MgO buffer layers are more stressed than the thin ones, which affects the crystal quality of the NbN film and then its superconducting properties. This assessment is supported by the tendency to crack showed by thick buffer layers (see Figure 4.17).

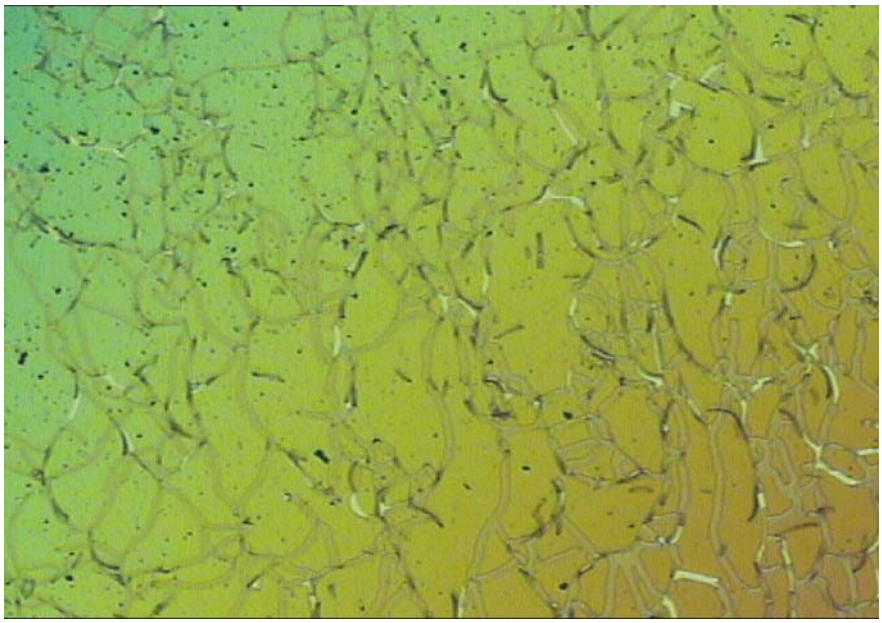

Figure 4.17. Optical microscope picture of the surface of a 265 nm-thick MgO buffer layer, deposited at P_{RF}=80 W.

A significant improvement (~50%) in terms of ΔT_C was instead found in the NbN films deposited on thin buffer layers, as compared to the film deposited on the bare GaAs substrate (Figure 4.18). We are presently further optimising deposition conditions for thin MgO buffer layers to achieve at the same time high T_C and low ΔT_C.

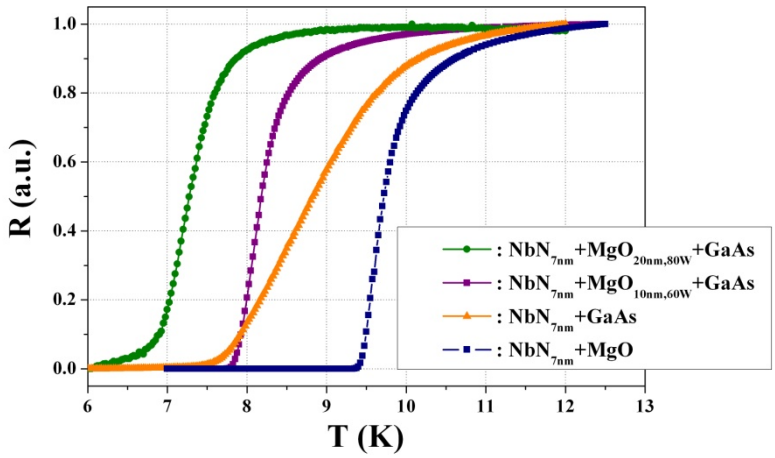

Figure 4.18. Resistance vs temperature dependence of 7 nm-thick NbN films deposited in the same sputtering run on an MgO substrate (blue squares), on a GaAs substrate (orange tringles), and on GaAs buffered with 20 nm-thick (green circles) and 10 nm-thick (purple stars) MgO buffer layers deposited at P_{rf}=80W and P_{rf}=60W, respectively. The thickness of the MgO buffer layer was measured with the profilometer method (see chapter II). The films were deposited at I_c=250 mA, T_S=400°C, P_{tot}=2.5 mtorr, x_{N2}=33%, V_c=650 V (fresh target), V_S=0 V, d_{t-s}=85 mm.

5. Device fabrication and design

The nanofabrication (performed at the Photonics and Nanotechnology Institute (IFN), Rome by A. Gaggero, Dr. F. Mattioli and Dr. R. Leoni) of SSPD and parallel nanowire detectors (PNDs) is described in section 5.1 and 5.2 respectively. Finally, in section 5.3 the characterization of our fabrication process is presented.

5.1. Fabrication process of standard SSPDs

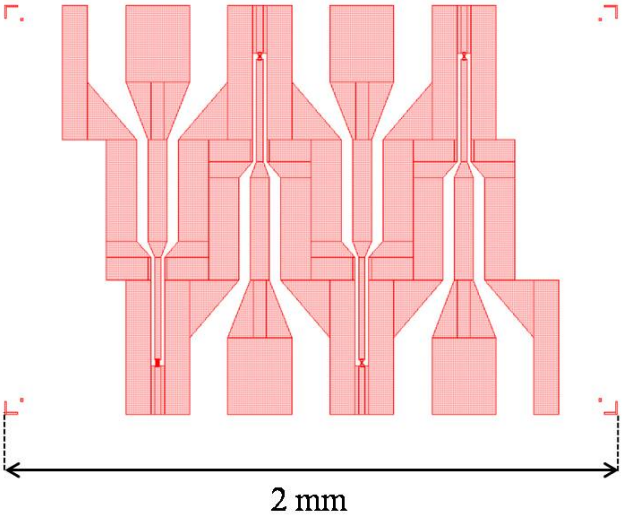

Figure 5.1. 4-device cluster and alignment markers (at the four corners of the mask). The width of the central conductor and of the gaps has been designed to obtain a 50Ω-matched strip line transmission line.

SSPDs were fabricated on few-nm thick NbN films deposited under optimal conditions on MgO and GaAs by two nanolithography steps, which were carried out by using an electron beam lithography (EBL) system equipped with a field emission gun (acceleration voltage 100 kV, 20 nm resolution). The design of the meander pattern was performed by the author using a layout design software (LASI, [51]).

In the first step e-beam lithography is used to define pads (patterned as a 50 Ω coplanar transmission line) and alignment markers on a 450nm-thick polymethyl methacrylate (PMMA, a positive tone electronic resist) layer. The sample is then coated with a Ti-Au film (60 nm Au on 10nm Ti) deposited by e-gun evaporation, which is selectively removed by lift-off from un-patterned areas. Devices are arranged in clusters of 4, sharing the same ground (see Figure 5.1). On each 10 x 10 mm^2 sample, a 4 x 5 matrix of clusters can be integrated for a total of 80 devices per sample.

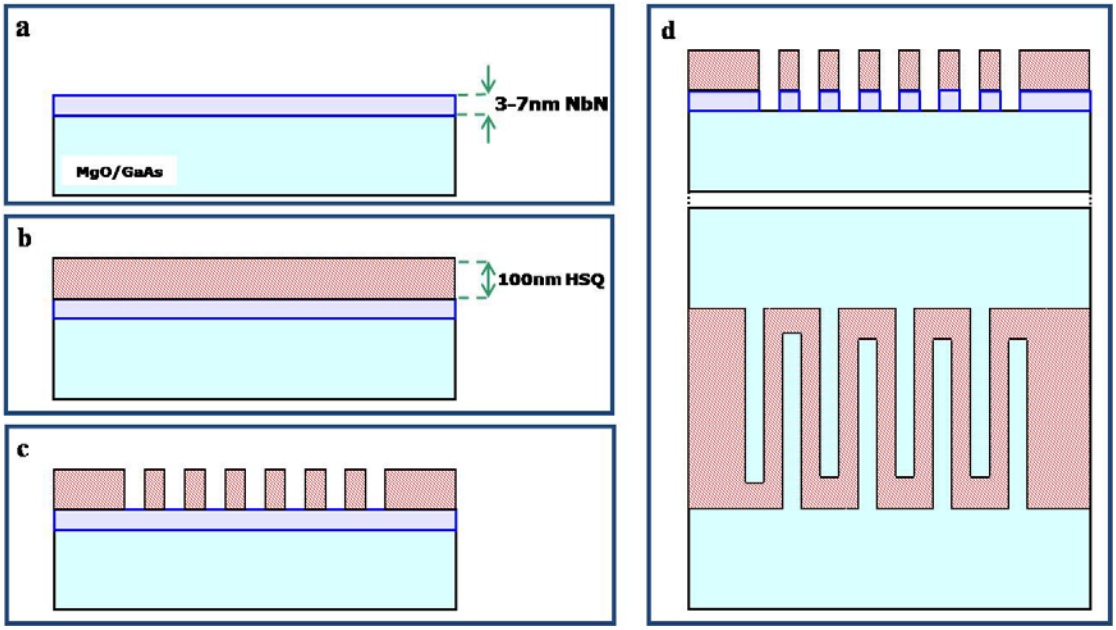

Figure 5.2. Simplified process flow diagram for the fabrication of SSPDs. Deposition of few-nm thick NbN films on MgO and GaAs by DC reactive magnetron sputtering (a), spin of 160nm thick HSQ layer (b), patterning of the meander in the HSQ by EBL (c), reactive ion etching of the exposed NbN (d).

In the second step (see Figure 5.2)., the meander pattern is defined by EBL in 160nm thick hydrogen silsesquioxane (HSQ FOX-14, a negative tone electronic resist) layer (Figure 5.2b, c). The alignment between the different layers is performed using the markers deposited in the first lithography step (alignment error of the order of 100 nm). All the unwanted material, i.e. the material not covered by the HSQ mask and the Ti/Au film, is then removed by using a fluorine based (CHF_3+SF_6+Ar) reactive ion etching (Figure 5.2d). The detector active area is A_d=5x5 μm^2. The nanowires are 60nm to 200nm wide and folded in a meander pattern with fill factors (f) ranging from 40% to 60% (Figure 5.3).

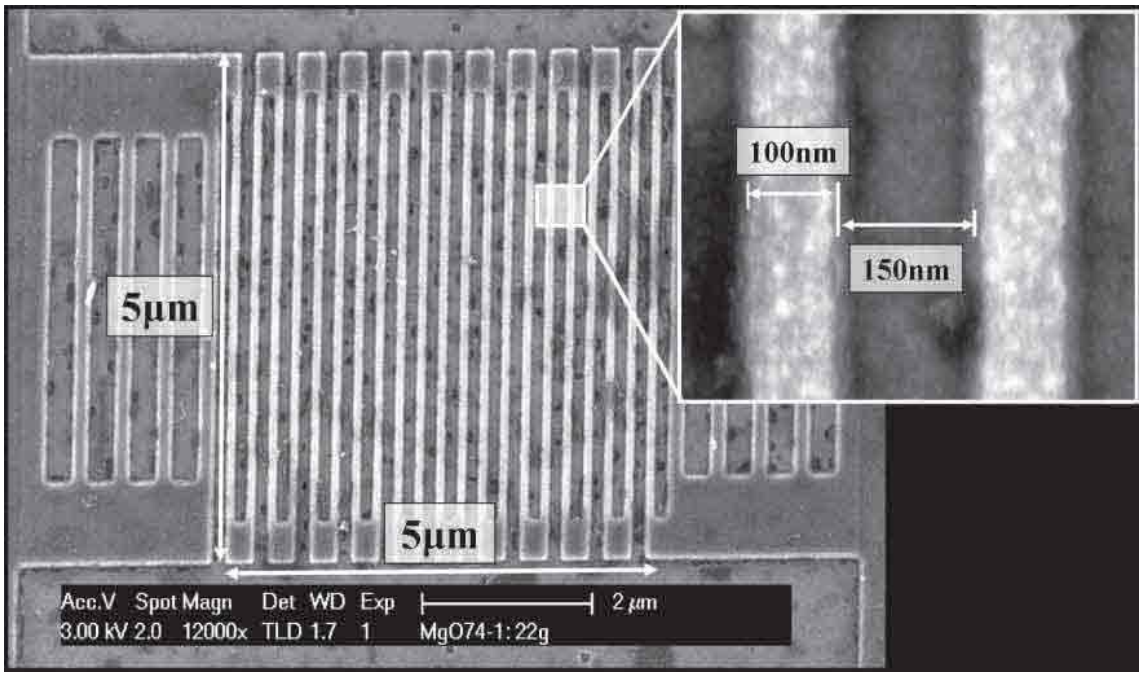

Figure 5.3. Scanning electron microscope (SEM) image of a standard SSPD. The nanowire width is w=100 nm, the fill factor is f=40%. The inset shows an ultra-high resolution image of two stripes. The mean width variation was estimated to be Δw~10 nm.

5.2. Fabrication and design of Parallel nanowire detectors

Different designs have been proposed for the parallel nanowire detectors (PNDs, see chapter V) which resulted in the structures shown in Figure 5.4. From the simple parallel connection of N meanders (see Figure 5.4a for a PND with N=14 parallel sections: 14-PND), we proceeded to the integration of a resistor in series to each nanowire (PND-R, Figure 5.4b-d). The first PND-R structure (see Figure 5.4b for a 8-PND-R) had the drawback of a contacting scheme which significantly limited the packing of the nanowires, and then the absorbance α of the device. That design was upgraded with the closely packed structure of Figure 5.4c (6-PND-R). Finally, a circular structure was designed for the efficient coupling with the core of a telecom-wavelength optical fiber (see Figure 5.4d for a 6-PND-R). The size of detector active area (A_d) ranges from 5x5 μm^2 to 10x10 μm^2 with the number of parallel branches varying from 4 to 14. The nanowires are 100 nm wide and the filling factor (f) of the meander is 40%. The length of each nanowire ranges from 25 to 100 µm.

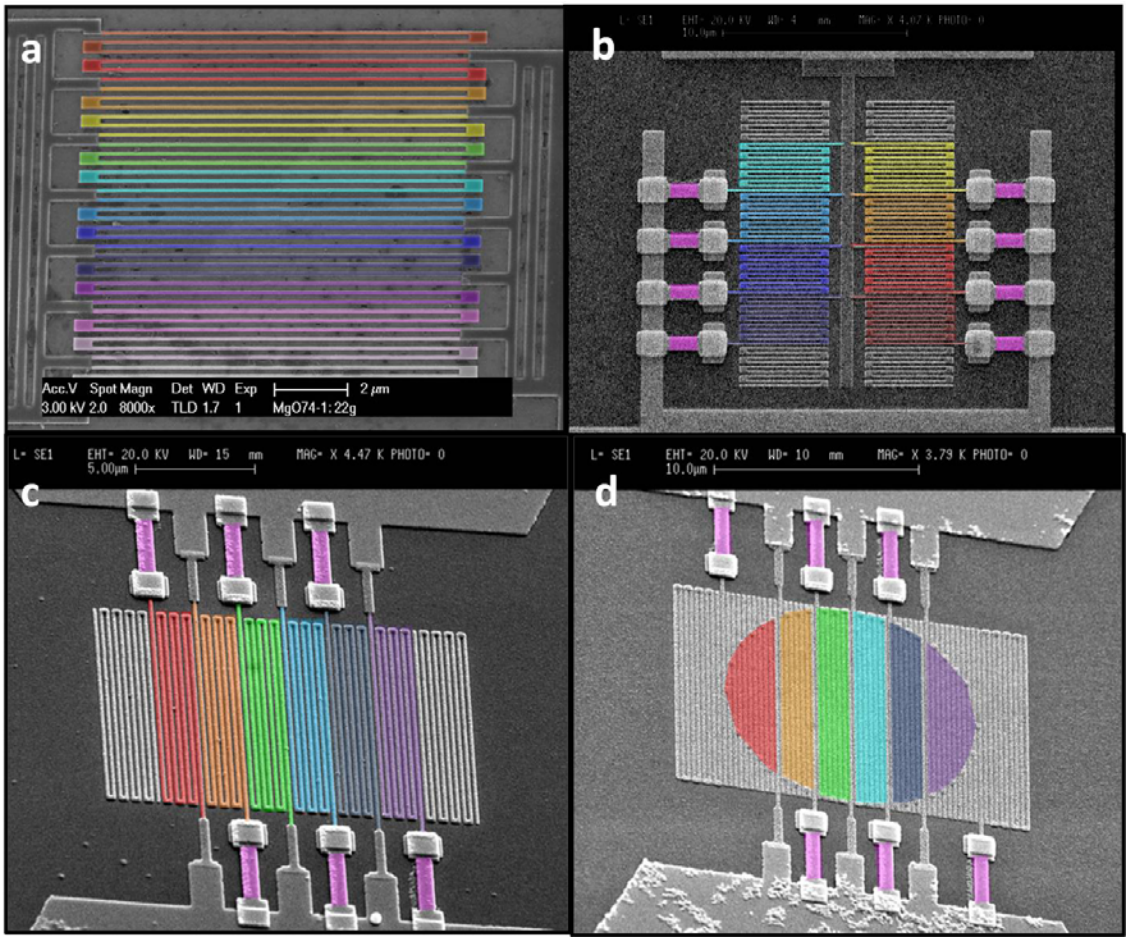

Figure 5.4. Scanning electron microscope (SEM) images of different designs of PNDs: (a) PND with N=14 (14-PND), (b) PND with N=8, series resistors (8-PND-R) and central conductor, (c) packed PND with N=6 and series resistors (6-PND-R), (d) circular PND with N=6 and series resistors (6-PND-R). The devices were fabricated on a 4nm thick NbN film on MgO. The nanowire width is w=100 nm, the meander fill factor is f=40%. The square devices have an active area of A_d=10x10 µm^2. The circular PND has a diameter of 10 µm. The active nanowires are in color. The series bias resistors of the PND-Rs are in pink. The floating meanders at the two edges of the PND-R pixel are included to correct for the proximity effect.

PNDs and PND-Rs were fabricated on 3-4 nm thick NbN films grown on MgO. The fabrication process of PNDs is the same as for SSPDs (see section 5.1). To fabricate PND-Rs, a third nanolithography step is necessary. The bias resistors (85nm AuPd alloy, 50%-each in weight) aligned with the two previous layers are fabricated by lift off via a PMMA stencil mask.

5.3. Fabrication process characterization

i. High-resolution SEM

The uniformity in width of the nanowires was verified by extensive scanning electron microscopy (SEM). To prevent charging effects, the devices were coated by a 10nm thick layer of OsO_4. This conductive coating, whose grain size is less than 1nm, allowed ultra-high resolution SEM imaging on the meanders. Figure 5.3 shows an SEM image of a w=100 nm, f=40% meander. Note that the contact pads on the two sides of the meander were also patterned with a low fill factor to reduce proximity effects during the EBL writing step. It was then possible to estimate the mean variation in the width of

the nanowire as Δw~10 nm, which agrees with the results of electrical characterization on test structures (see chapter IV).

ii. Device superconducting properties check

In order to check whether the fabrication process for SSPDs (described in section 5.1) affects the superconducting properties of the NbN film, the critical temperature T_C of a patterned meander (w=100 nm, f=40%) was compared to the T_C measured on a bare film deposited in the same run as the film used for the processing.

As shown in Figure 5.5, only a slight degradation of the superconducting properties (i.e. a broadening of the normal to superconducting transition) can be observed. Therefore, the standard fabrication process does not substantially affect the quality of the films.

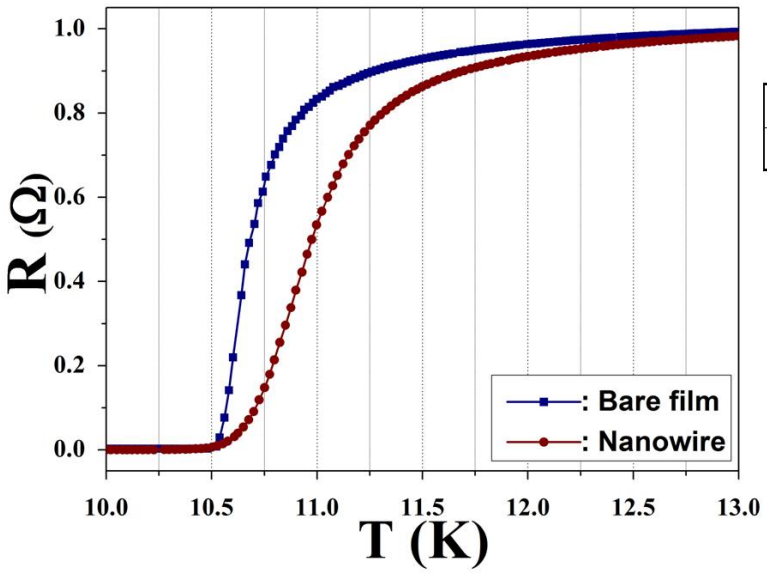

	Tc (K)	ΔTc (mK)
Bare film	10.89	650
Nanowire	11.21	880

Figure 5.5. Resistance as a function of temperature for a patterned meander (red circles) and for a bare film deposited in the same run as the film used for the processing (blue squares). The thickness of the NbN film was 7 nm. The film was deposited at I_c=250 mA, T_S=400°C, P_{tot}=2.5 mtorr, x_{N2}=33%, V_c=500 V (grooved target), V_S=0 V, d_{t-s}=85 mm.

6. Conclusions

As a first step towards the integration of SSPDs with advanced optical structures, a process was optimized for the deposition of high-quality few-nm thick NbN films on GaAs and AlAs/GaAs-based DBRs.

Because of the requirement of compatibility with GaAs, the substrate temperature used in this study is T_s=400°C in order to prevent As evaporation [8], so film deposition is realized in the so-called quenched growth (QG) regime: T_s/T_m=0.24.

As GaAs and DBRs are highly mismatched substrates, the deposition parameters were first optimized with respect to the superconducting properties of NbN films on MgO substrates, which allow the growth of high crystal quality NbN films at low temperature [3, 4]. This made easier to separate the influence of stoichiometry from that of microstructure. The optimized deposition parameters were then used to grow NbN films on GaAs and DBRs, under the reasonable assumption (which was later checked and confirmed) that changing the substrate would not produce a change in film stoichiometry, but only in its microstructure.

NbN films ranging from 150nm to 3nm in thickness were then deposited on epitaxial-quality single crystal MgO <100>, GaAs <100> undoped and DBRs structures. The deposition technique is

the current-controlled DC magnetron sputtering (planar, circular, balanced configuration) of Nb in an $Ar + N_2$ plasma.

The thinnest NbN films (th=3 nm) deposited on MgO exhibit T_C=8.6 K, ΔT_C=0.9 K and RRR=0.6, which are state of the art parameters, proof of the excellent quality of our low-temperature deposition process. The quality of films deposited on GaAs and on DBRs is lower than for NbN deposited on MgO, as for any thickness they systematically exhibit higher ΔT_C and lower T_C and RRR. However, 5.5 nm-thick NbN films on GaAs still exhibit T_C= 10.7 K, ΔT_C=1.1 K and RRR=0.7, which compares with 4.5 nm thick films on MgO, making them suitable for device fabrication. To our knowledge, the growth of such high quality thin NbN films on GaAs and DBRs, has never been reported in literature.

The degradation of the superconducting properties exhibited by NbN films on GaAs and DBRs was attributed to a highly defected microstructure, due both to a higher lattice misfit between NbN and GaAs and to a poorer quality of the substrate surface. Encouraging preliminary results show that the quality of these films can be improved both cleaning the GaAs/DBR substrate surface more effectively or adding an MgO buffer layer.

7. References

[1] V. Anant, A. J. Kerman, E. A. Dauler, J. K. W. Yang, K. M. Rosfjord, and K. K. Berggren, Opt. Express **16**, 10750 (2008).

[2] K. M. Rosfjord, J. K. W. Yang, E. A. Dauler, A. J. Kerman, V. Anant, B. M. Voronov, G. N. Gol'tsman, and K. K. Berggren, Opt. Express **14**, 527 (2006).

[3] S. Miki, Y. Uzawa, A. Kawakami, and Z. Wang, Electron. Comm. Japan II **85**, 77 (2002).

[4] Z. Wang, A. Kawakami, Y. Uzawa, and B. Komiyama, J. Appl. Phys. **79**, 7837 (1996).

[5] P. Yagoubov, G. Gol'tsman, B. Voronov, L. Seidman, V. Siomash, S. Cherednichenko, and E. M. Gershenzon, in *Proceedings of the 7th International Symposium On Space Terahertz Technology*, Boston, MA, 290 (1996).

[6] J. C. Villegier, N. Hadacek, S. Monso, B. Delnet, A. Roussy, P. Febvre, G. Lamura, and J. Y. Laval, IEEE Trans. Appl. Supercond. **11**, 68 (2001).

[7] R. E. d. Lamaestre, P. Odier, and J.-C. Villegier, Appl. Phys. Lett. **91**, 232501 (2007).

[8] K. Iizuka, K. Matsumaru, T. Suzuki, H. Hirose, K. Suzuki, and H. Okamoto, J. Cryst. Growth **150**, 13 (1995).

[9] V. G. Brauer, and R. Esselborn, Z. Anorg. Allg.Chem. **309**, 151 (1961).

[10] L. E. Toth, in Transition metal carbides and nitrides, New York: Academic Press, 1971, Chap. 7.

[11] V. G. Brauer, and H. Kirner, Z. Anorg. Allg.Chem. **328**, 34 (1964).

[12] Y. M. Shy, L. E. Toth, and R. Somasundaram, J. Appl. Phys. **44**, 5539 (1973).

[13] D. D. Bacon, A. T. English, S. Nakahara, F. G. Peters, H. Schreiber, W. R. Sinclair, and R. B. van Dover, J. Appl. Phys. **54**, 6509 (1983).

[14] L. Kang, P. H. Wu, J. R. Sh, W. X. Cai, S. Z. Yang, Z. M. Ji, and Z. Wang, Supercond. Sci. Technol. **16**, 1417 (2003).

[15] S. Kubo, M. Asahi, M. Hikita, and M. Igarashi, Appl. Phys. Lett. **44**, 258 (1984).

[16] R. Kampwirth, and K. Gray, IEEE Trans. Mag. **17**, 565 (1981).

[17] K. S. Keskar, T. Yamashita, and Y. Onodera, Jpn. J. Appl. Phys. **10**, 370 (1971).

[18] S. Thakoor, J. L. Lamb, A. P. Thakoor, and S. K. Khanna, J. Appl. Phys. **58**, 4643 (1985).

[19] J. C. Villegier, L. Vieux-Rochaz, M. Goniche, P. Renard, and M. Vabre, IEEE Trans. Mag. **21**, 498 (1985).

[20] K. L. Westra, M. J. Brett, and J. F. Vaneldik, J. Vac. Sci. Technol. A **8**, 1288 (1990).

[21] G. I. Oya, and Y. Onodera, J. Appl. Phys. **45**, 1389 (1974).

[22] A. Shoji, S. Kiryu, and S. Kohjiro, Appl. Phys. Lett. **60**, 1624 (1992).

[23] A. M. Kadin, in Introduction to superconducting circuits, Wiley, New York, 1999, Chap 2.

[24] N. Hadacek, M. Sanquer, and J. C. Villégier, Phys. Rev. B **69**, 024505 (2004).

[25] H. S. J. van der Zant, W. J. Elion, L. J. Geerligs, and J. E. Mooij, Phys. Rev. B **54**, 10081 (1996).

[26] A. Larkin, Ann. Phys. **8**, 785 (1999).

[27] R. Romestain, B. Delaet, P. Renaud-Goud, I. Wang, C. Jorel, J.-C. Villegier, and J.-P. Poizat, New J. Phys., 129 (2004).

[28] J. R. Gao, M. Hajenius, F. D. Tichelaar, T. M. Klapwijk, B. Voronov, E. Grishin, G. Gol'tsman, C. A. Zorman, and M. Mehregany, Appl. Phys. Lett. **91**, 062504 (2007).

[29] J. A. Thornton, Ann. Rev. Mater. Sci. **7**, 239 (1977).

[30] J. A. Thornton, J. Vac. Sci. Technol. **11**, 666 (1973).

[31] J. A. Thornton, J. Vac. Sci. Technol. A **4**, 3059 (1986).

[32] D. L. Smith, in Thin-Film Deposition: Principles and Practice, New York: McGraw-Hill, Inc., 1995, Chap. 5.
[33] K. H. Müller, J. Appl. Phys. **62**, 1796 (1987).
[34] M. Bhushan, J. Vac. Sci. Technol. A **5**, 2829 (1987).
[35] N. N. Iosad, B. D. Jackson, S. N. Polyakov, A. V. Varlashkin, P. N. Dmitriev, and T. M. Klapwijk, J. Vac. Sci. Technol. A **19**, 1840 (2001).
[36] D. L. Smith, in Thin-Film Deposition: Principles and Practice, New York: McGraw-Hill, Inc., 1995, Chap. 9.
[37] N. N. Iosad, V. V. Roddatis, S. N. Polyakov, A. V. Varlashkin, B. D. Jackson, P. N. Dmitriev, J. R. Gao, and T. M. Klapwijk, IEEE Trans. Appl. Supercond. **11**, 3832 (2001).
[38] B. Window, and G. L. Harding, J. Vac. Sci. Technol. A **8**, 1277 (1990).
[39] S. Maniv, and W. D. Westwood, J. Appl. Phys. **51**, 718 (1980).
[40] W. D. Westwood, J. Vac. Sci. Technol. **15**, 1 (1978).
[41] S. Dierks, *espimetals.com*. (1991).
[42] K. S. Keskar, T. Yamashita, Y. Onodera, Y. Goto, and T. Aso, J. Appl. Phys. **45**, 3102 (1974).
[43] N. N. Iosad, A. V. Mijiritskii, V. V. Roddatis, N. M. Van Der Pers, B. D. Jackson, J. R. Gao, S. N. Polyakov, P. N. Dmitriev, and T. M. Klapwijk, J. Appl. Phys. **88**, 5756 (2000).
[44] M. Gurvitch, J. Vac. Sci. Technol. A **2**, 1550 (1984).
[45] N. N. Iosad, T. M. Klapwijk, S. N. Polyakov, V. V. Roddatis, E. K. Kov'ev, and P. N. Dmitriev, IEEE Trans. Appl. Supercond. **9**, 1720 (1999).
[46] N. N. Iosad, N. M. Van der Pers, S. Grachev, M. Zuiddam, B. D. Jackson, P. N. Dmitriev, and T. M. Klapwijk, IEEE Trans. Appl. Supercond. **13**, 3301 (2003).
[47] H. C. Jones, Appl. Phys. Lett. **27**, 471 (1975).
[48] M. Benkahoul, E. Martinez, A. Karimi, R. Sanjinés, and F. Lévy, Surf. Coat. Technol. **180-181**, 178 (2004).
[49] M. Benkahoul, EPFL doctoral thesis n. 3325 (2005).
[50] A. Surrente, Projet de semestre d'hiver (2006).
[51] LASI, **www.lasihomesite.com**.

IV: SSPD characterization

1. Introduction

At the time this project started, high-sensitivity ultrafast SSPDs had been fabricated only on 3-4nm thick NbN films grown on sapphire at high substrates temperatures (typically 900°C) at the Moscow State Pedagogical University (MSPU, Moscow) [1] (at the time this report is written, only one other group, besides MSPU and our group, reported high performance SSPDs fabricated with a completely independent process [2]). This prevents the integration of SSPDs with advanced optical structures such as distributed Bragg reflectors (DBRs) and optical waveguides, typically realized on substrates not compatible with these high deposition temperatures. For instance, high reflectivity DBR realized on GaAs do not withstand such temperatures due to As evaporation [3] (see also chapter III). In order to fabricate new devices with improved performance, and to prove the challenging SSPD technology can be transferred to other substrates, we developed the whole fabrication process (i.e. the deposition of high-quality few-nm thick NbN films and the nano-patterning by electron beam lithography, see chapter III) for the integration of NbN SSPDs on MgO and GaAs and GaAs/AlAs-based DBR structures.

In this chapter we report the results of the characterization of these devices. The electrical characterization of SSPDs grown on MgO and GaAs is presented in section 2, where, by an extensive analysis of the I-V curves, we extract many important physical parameters of the film. Section 3 reports the optical characterization of high performance (η~20% at λ=1.3 μm, T=4.2 K) SSPDs on MgO. Finally, the results of the homogeneity characterization of our nanowires are discussed in section 4.

2. Elecrtical characterization

2.1.Self-heating effects in superconducting nanowires

The analysis of self heating effects in superconducting nanowires is detailed in [4] (Skocpol, Beasley, Tinkham (SBT) hotspot model). Here only the essential aspects of the model are reported, which are extensively used in the next sections.

Heat generated in a localized normal domain (hotspot) in a current-carrying superconducting nanowire is dissipated by thermal conduction either within the film, or to the environment, i.e. to the substrate and to the He bath, which are considered as reservoirs at a temperature T_S. The thermal conductivity (K) of the film can be estimated from the electrical resistivity using the Wiedemann-Franz law, and it is assumed to be the same in the superconducting and normal state (K_S=K_N=K). Assuming that the film can exchange heat only with the substrate, the heat-transfer coefficient per unit area of film (h) to the environment is of the order of 2 W/cm^{2}K for glass or sapphire, and it is not significantly modified immersing the nanowire in normal He. However, when the temperature of the hotspot exceeds that of the He bath by more than 1 K (which is the case of our devices, whose T_C is ~10K, see below), nucleation of bubbles occurs at the surface of the nanowire, which strongly increases h. Nevertheless, the heat-transfer coefficient is assumed as temperature-independent.

The balance between conduction within the film and to the environment is characterized by the thermal healing length:

$$L_{th} = \sqrt{Kt_h / h} \qquad (1)$$

where t_h is the thickness of the film. L_{th} is the characteristic length-scale of temperature spatial variations in the film.

The heat removed by these processes is generated by Joule effect in the hotspot. Solving the heat flow problem, it is possible to determine the temperature distribution associated with a normal domain of a given size and the current required to generate sufficient heat to sustain it. The voltage across the hotspot is determined by Ohm's law from its resistance and the current flowing through it. This approach leads to the parametric expression of the current-voltage (I-V) characteristic of a superconducting nanowire carrying a normal domain.

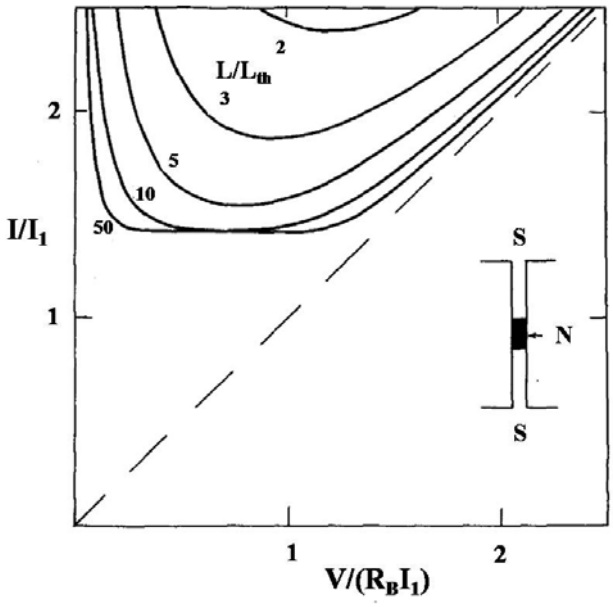

Figure 2.1. Theoretical I-V curves from the model described in [4] for different normalized lengths L/L_{th}. I_1 is defined in the test, R_B is the normal state resistance of the nanowire. The inset shows the geometry assumed. [4]

As shown in Figure 2.1, the shape of the I-V curve changes dramatically depending on the ratio of the nanowire length L to the thermal healing length L_{th}. For long nanowires ($L>>L_{th}$, which is the case of our devices), when the size of the hotspot is small compared to L, the I-V curve approaches a constant minimum current. This regime is referred to as the hotspot plateau, and it corresponds to the increase in size of the resistive domain as voltage increases. The constant current (hotspot plateau current I_{hs}) which generates enough heat to balance the dissipation processes described above and sustains a the growing hotspot can be written as [4]:

$$I_{hs} = \sqrt{2}\sqrt{\frac{hw^2 t_h (T_C - T_S)}{\rho}} = \sqrt{2} I_1 \qquad (2)$$

where I_1 is the current which generates enough heat to balance the heat flow towards the environment from a normal film at $T=T_C$.

2.2.Experimental results

i. Bias circuit

Before starting with the analysis of the SSPD I-V curves, some explanation of the bias circuit used for measurements is needed.

We consider a single nanowire. The "intrinsic" I-V curves of the nanowire (i.e. as predicted from the SBT hotspot model, see Figure 2.1) can be measured only if it is voltage-biased, i.e. it is connected in series to a voltage source V_B and an a resistance R_B. Considering this circuit (inset of Figure 2.2a), it is clear that each point on the measured I-V curve $I_B(V_{NW})$ is the solution of this system of equations:

$$\begin{cases} I_B = I_{NW}(V_{NW}) \\ I_B = (V_B - V_{NW})/R_B \end{cases} \qquad (3)$$

where $I_{NW}(V_{NW})$ is the intrinsic I-V curve and the second equation is the load-line of the circuit. Therefore, for each value of the bias voltage V_B, I_B can be found graphically on the plane V_{NW}-I_B by finding the intersection of the load-line with the intrinsic I-V curve $I_{NW}(V_{NW})$. The measured I-V curve $I_B(V_{NW})$ is the ensemble of the intersections of these two curves.

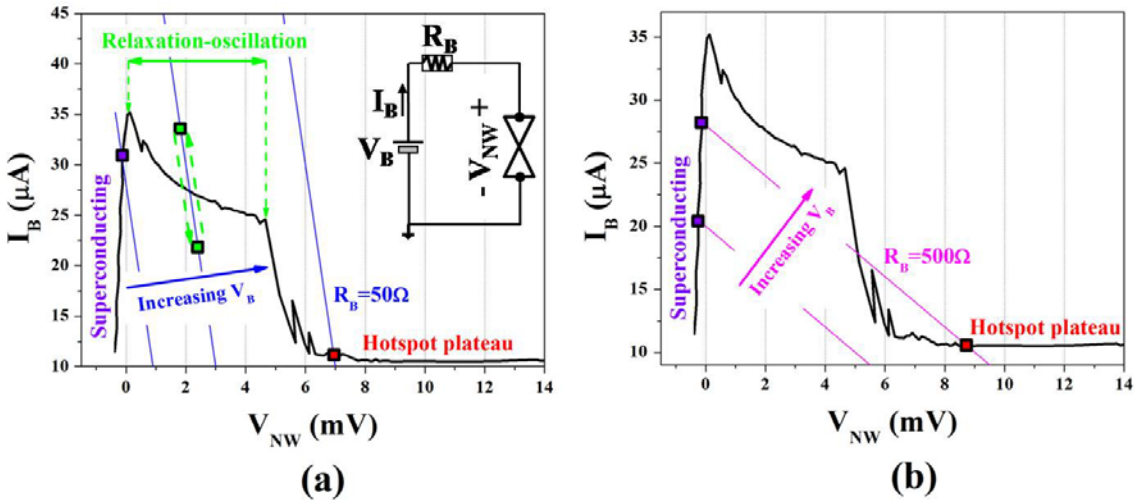

Figure 2.2. Initial part of the measured I-V curve at 4.2 K (black, solid line) of a 4 µm long, 200 nm wide and 10 nm thick nanowire. a. The superconducting, relaxation-oscillation and hotspot plateau regimes are highlighted. The load lines for R_B=50 Ω at different values of V_B are in blue. Inset: equivalent circuit of the setup for I-V measurements. b. The load lines for R_B=500 Ω at different values of V_B are in pink.

As long as the bias current (I_B) is lower than the superconducting critical current (I_C) of the nanowire, the device is superconducting and its current is limited by the external circuit. Thus the solution of the system (3) is $I_B=I_{NW}(0)=V_B/R_B$ (violet square in Figure 2.2a). When I_B exceeds I_C, the system (3) has no solution, i.e. the nanowire cannot switch along the load line to a stable resistive state. Therefore, the nanowire oscillates between the superconducting and the normal state at a frequency which depends on the inductance of the circuit. This is the relaxation-oscillation regime, represented by the green squares in Figure 2.2a (the oscillation represented is not in scale). The average of the oscillating voltage is measured by our DC instruments. With increasing voltage, the nanowire switches to the hotspot plateau regime. The solution of the system (3) is then $I_B=I_{hs}=(V_B-I_{hs}R_{hs})/R_B$, where R_{hs} is the resistance of the normal region of the nanowire (red square in Figure 2.2a). In this regime, an increase

of V_B results in an increase of R_{hs}, i.e. an enlargement of the normal domain. When the hotspot reaches the edges of the nanowire, which is then completely normal, an ohmic behavior is observed. The solution of the system (3) is then $I_B=V_{NW}/R_n=(V_B-V_{NW})/R_B$, where R_n is the resistance of the normal nanowire.
The behavior described above can be observed only if the value of the bias resistor R_B is "small" enough. Indeed, increasing R_B (Figure 2.2b), the load-line becomes less steep and consequently, for a given bias current $I_B^*<I_C$ (i.e. nanowire still superconducting), it may intersect the intrinsic I-V $I_{NW}(V_{NW})$ at two points, in the superconducting region and in the hotspot plateau (violet and red squares in Figure 2.2b). Thus the system (3) has two solutions: $I_B=I_{NW}(0)=V_B/R_B$ (superconducting state) and $I_B=I_{hs}=(V_B-I_{hs}R_{hs})/R_B$ (hotspot state). As the dissipative state is the stable one, the nanowire permanently switches from the superconducting to the hotspot regime even if its I_C was not exceeded.

ii. SSPDs on MgO

SSPD I-V curves

Our SSPD design is the series connection of N nanowires arranged in a meander pattern. The nanowires are 60 to 100 nm in width (w) and 1 to 10 μm in length (L), much longer than the NbN thermal healing length (of the order of L_{th}~70 nm, see below). Therefore, the I-V curves at T=4.2 K (i.e. far from NbN T_C) of each nanowire are expected to be well described by the SBT hotspot model (see above).
In the SSPD, the nanowires are connected one to the other through wider (w=0.5 to 1 μm) sections (see Figure 2.4 and chapter III) at the two ends. This broadenings are larger than the thermal healing length, so they thermally decouple the wires from each other, i.e. they prevent the normal domain in a wire to extend in any of the two neighboring ones. Because of this decoupling, the I-V curves of SSPDs (see Figure 2.3a, for N=6) deviate from the behavior expected from a single homogeneous nanowire (Figure 2.3b). The SSPD I-V curves can be interpreted as follows.
As long as the bias current (I_B) is lower than the superconducting critical current (I_C) of the most "constricted" wire of the N in series (i.e. the one whose critical current is the lowest), the device is superconducting and $I_B=V_B/R_B$. When I_B exceeds I_C, the circuit enters the relaxation oscillation regime (see Figure 2.2). With increasing voltage, the circuit switches to the hotspot plateau regime. The resistive domain in the most constricted nanowire grows in size until it reaches the broadenings at the edges of the nanowire, which is then completely normal. Now the normal region stops growing, and an ohmic branch is observed in the SSPD I-V. The constant resistance value corresponds to the resistance of a normal nanowire R_n (for the device of Figure 2.3, R_n~7 kΩ), thus, as V_B further increases, the bias current increases from the hotspot value as $V_B/(R_B+R_n)$. This is the same behavior showed by single homogeneous nanowires (Figure 2.3b).

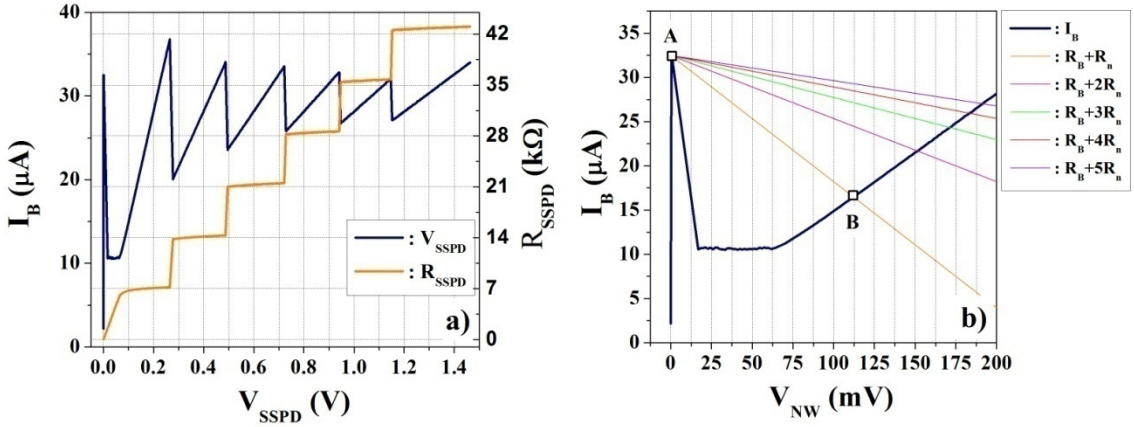

Figure 2.3. a. Complete I-V curve (in blue) at 4.2 K of a N=6 stripe meander (filling factor f=40%). The nanowires are 4 µm long, 200 nm wide and 10 nm thick. The orange plot is the resistance of the device (R_{SSPD}) as a function of voltage. b. Complete I-V curve (in blue) at 4.2 K of a 4 µm long, 200 nm wide and 10 nm thick nanowire. The straight lines are the load lines relative to the series resistances of R_B+iR_n (i=1,…5), which are the same as those experienced by the N-i (i=1,…,5) still superconducting nanowires when i nanowires are completely normal.

In an SSPD, after the complete transition of the most constricted nanowire, the other N-1 still superconducting sections experience a much higher series resistance than before. Therefore they are biased with a much less steep load-line, which is the same load line as the one experienced by a single nanowire connected in series with a resistance R_B+R_n (orange load-line of Figure 2.3b). It becomes then clear that, when I_B exceeds the critical current of the second section of the SSPD, the whole section switches directly from the superconducting to the normal state along the new load line (making a transition analogous to the switching from point A to B by the single nanowire of Figure 2.3b biased with the orange load line). As the SSPD resistance suddenly doubles, $R_{SSPD}=2R_n$, the bias current drops to $I_B=V_B/(R_B+2R_n)$.The N-2 still superconducting nanowires of the SSPD now are biased with the same load line as the one experienced by a single nanowire connected in series with a resistance R_B+2R_n (pink load-line of Figure 2.3b). As V_B increases, the same process described above occurs until the whole device is normal. The progressive decrease in the value of the critical currents of the nanowires sequentially switching to the normal state is not due to constrictions and can be explained as follows. The measured I_C of a nanowire may be lower than its real value, depending on the bias resistance used for the measurement (see previous section), thus the decrease in the critical currents observed in the SSPD I-V is due to the progressive increase of the series resistance experienced by the still superconducting sections. In addition, the temperature of the film increases as more and more nanowires switch to the normal state and dissipate.
As shown in the next section, from the I-V curves it is possible to deduce some important physical parameters of the nanowire.

Derivation of NbN physical parameters

From the SSPD I-V curve it is possible to deduce the resistivity of the nanowires (ρ), the penetration depth at T=0 K (λ(0)), the critical current density (J_C), the heat-transfer coefficient per unit area of film to the environment (h), the size of the initial normal domain (L_{hs}) and the thermal healing length (L_{th}). These parameters are important figures of merit to estimate the superconducting properties of the nanowires (ρ, λ(0), J_C), or they are useful for the design or the simulation of the devices (h, L_{hs}, L_{th}).

Test meander-structures with only six nanowires in series were fabricated (see chapter III) on a first generation 10 nm-thick NbN film grown on MgO. The film showed T_C=9 K, ΔT_C=700mK and no

degradation of the superconducting properties was observed after processing. The nanowires are 4 or 10 µm long and 100 or 200nm wide. The filling factor is f=40%. Nominally identical structures were fabricated varying the electron dose in the EBL step, so fluctuations in w and f are expected.

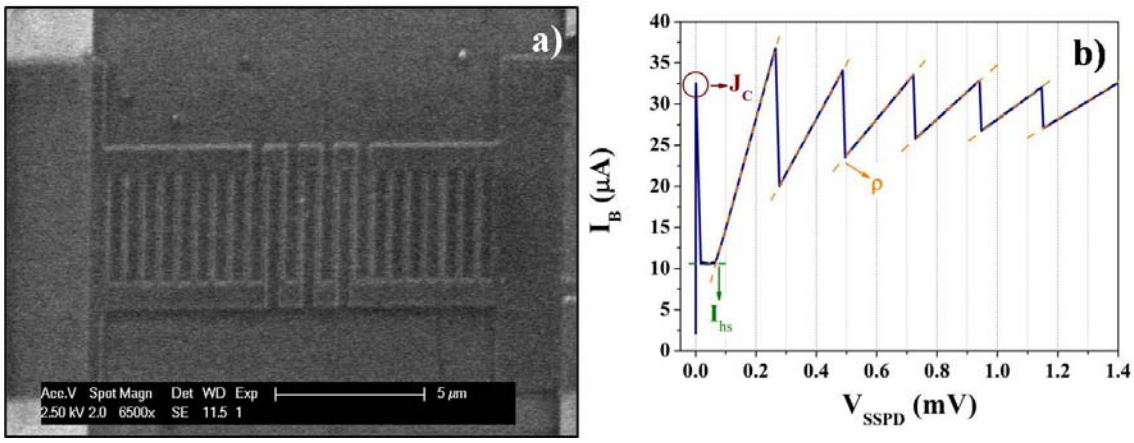

Figure 2.4. a. Scanning electron microscope (SEM) image of a test meander-structures with six nanowires in series. The nanowire is 200 nm wide, 4 µm long and the meander filling factor is f=40%. The nanowires are connected through w=1 µm sections. b. I-V curve at 4.2 K of the meander(in blue), from which the resisitivity (orange), the hotspot current (green) and the critical current density (red) can be derived.

The resistance of each nanowire of the meander was derived by linear regression from the measured I-V curves (orange lines in Figure 2.4), then an average was calculated on the resistance values for each meander. ρ was then calculated from the nominal width of the nanowires (w_n=100, 200 nm). Figure 2.5 shows the resistivity as a function of w_n for two different electronic doses used in the EBL patterning step.

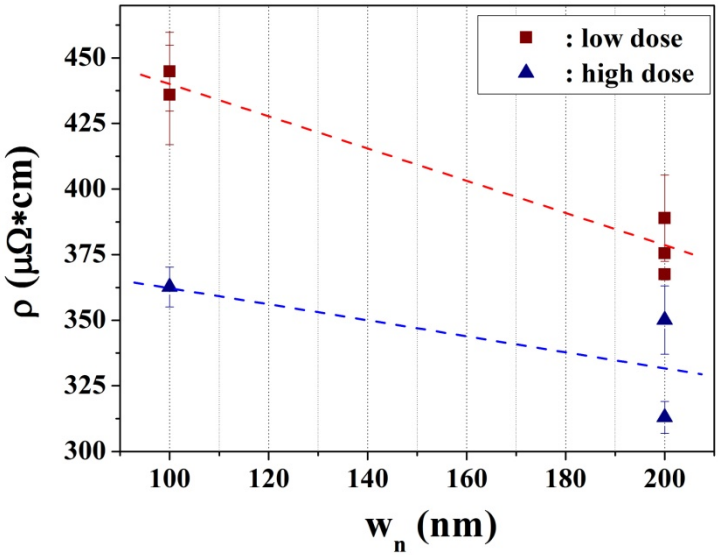

Figure 2.5. NbN resistivity (ρ) according to the nominal width of the nanowires (w_n) for two different electronic doses used in the EBL patterning step (high: triangles, low: squares).

For both electronic doses the resistivity of the meander with w_n=100 nm is higher than in the w_n=200 nm case. Moreover, meanders exposed with a higher electronic dose show a lower ρ.

These variations can be explained as follows. We suppose that the length of the meanders is a reliable data (being much higher than the EBL resolution) and that the thickness of the NbN layer is indeed 10 nm and it is homogeneous on all the substrate (as confirmed by AFM thickness measurements, see chapter II). On these assumptions, the different values of ρ for different w_n and for different doses is due to a deviation of the real width (w_r) of the nanowires from the nominal value.
As the value of ρ is necessary to calculate the other parameters of the film, we assumed $w_r=w_n$ for the 200 nm-wide nanowires and estimated the resistivity of NbN as the average on the resistivities calculated for these meanders. The value obtained is of ρ=365 μΩ·cm.
From this value we then estimate the real widths (w_r) of the nanowires, which we need to proceed with the analysis. The values obtained are w_r=90±10 nm for w_n=100 nm and w_r=200±20 nm for w_n=200 nm.

Following [5, 6], the NbN penetration depth at T=0 K (λ(0)) was calculated from its T_C and its 20 K resistivity ρ_{20K} using the two expressions given in [7]:

$$\lambda(0) = \sqrt{2} \cdot \lambda_{GL}^{BCS}(0) \sqrt{1.33} \cdot \eta_\lambda(0) \qquad (4)$$

$$\lambda_{GL}^{BCS}(0) = 6.42 \cdot 10^{-6} \left[\rho_{20K}(\mu\Omega cm) / T_C(K) \right]^{1/2} (cm) \qquad (5)$$

where $\lambda_{GL}^{BCS}(0)$ is the Ginsburg-Landau penetration depth at 0 K for a dirty superconductor in the BCS [8] weak coupling case. $\eta_\lambda(0)$ is the strong coupling correction for the penetration depth. Its value ($\eta_\lambda(0)$=0.91) was taken from [5], where it was deduced from measurements on films of approximately the same quality as the one reported here.
Using T_C=9 K, ρ_{20K}=365 μΩ·cm and $\eta_\lambda(0)$=0.91, the penetration depth for our nanowires was estimated as λ(0)~600 nm.

As thickness and width of the nanowires are well below λ(0), the supercurrent density is uniform across the cross section [9]: the critical current density J_C was then estimated from the measured value of I_C (red circle in Figure 2.4) and the geometrical cross-section of the meander.
The value for the bias resistor (R_B) was chosen to attain the highest ratio of the bias current I_B to I_C. Indeed, increasing R_B, the noise on I_B due to the voltage source is reduced, but the DC load line becomes less steep (see Figure 2.2b). As explained in section i, the load line may intersect the I-V in the superconducting region and in the hotspot plateau, so that the device permanently switches from the superconducting to the dissipative state for a given bias current < I_C.

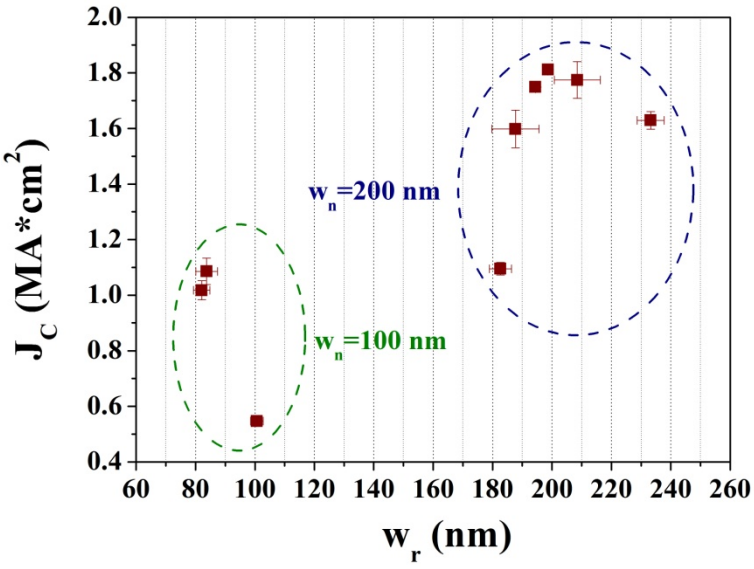

Figure 2.6. Critical current density (J_C) as a function of the real nanowire width (w_r).

J_C at 4.2K varied from 0.5 to 1.8 MA/cm^2 (Figure 2.6), which is below the state of the art value, due to the poor superconducting properties of the first-generation NbN film used to fabricate the devices, deposited with non-optimal growth parameters.
The hotspot current I_{hs} can be re-written from (2) as:

$$I_{hs} = \sqrt{2}\sqrt{\frac{hw^2 t_h \cdot (T_C - T_S)}{\rho}} = Mw \propto w$$

where T_C=9 K, T_S=4.2 K, ρ=365 μΩ·cm, t_h=10 nm.
Thus I_{hs} can be considered a linear function of the nanowire width (see Figure 2.7). Plotting I_{hs} as a function of w_r, the value of M can be estimated from a linear fit. From M we can then calculate the coefficient of heat transfer coefficient per unit area to the environment h=10.5±0.3 W/(cm^{2}K). This value is significantly higher than 2 W/(cm^{2}K) estimated in [4] for the heat transfer to the substrate (sapphire, see section 2.1) due to the nucleation of vapor bubbles at the surface of the device.

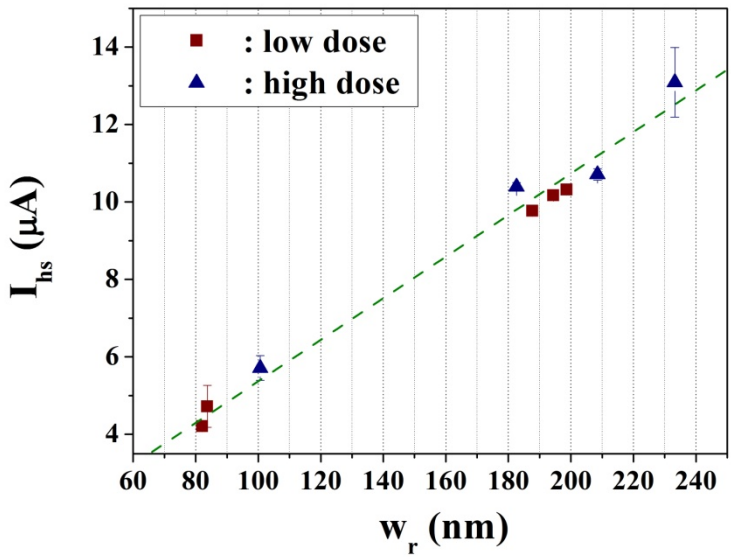

Figure 2.7. Hotspot current I_{hs} as a function of the real nanowire width (w_r) for two different electronic doses used in the EBL patterning step (high: triangles, low: squares). The green dashed line is the linear fit of the data.

The thermal healing length L_{th} can be then estimated from (1). The thermal conductivity K of the NbN film can be estimated with the Wiedemann-Franz law: $K=l\cdot T/\rho$, where $l=2.45\cdot10^{-8}$ $W\Omega/K^2$ is the Lorenz number for metals. Finally, we obtain:

$$L_{th} = \sqrt{\frac{lT_C t_h}{h\rho}} = 76 \pm 1 \text{ nm} .$$

The length of the initial normal domain (L_{hs}) is the lower bound for the size of a self-sustaining resistive region in the nanowire. L_{hs} is deduced from the resistance of the device at the beginning of the hotspot plateau regime. As shown from Figure 2.8, L_{hs} is roughly 2-3 squares.

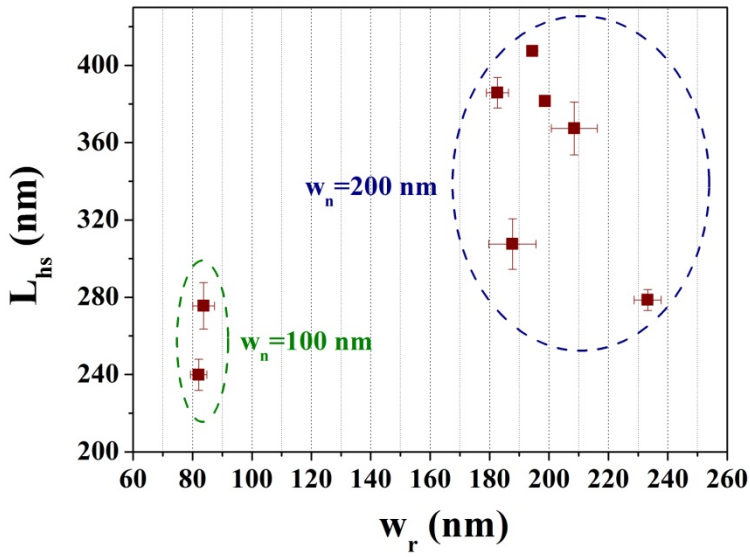

Figure 2.8. Minimum hotspot length L_{hs} as a function of the real nanowire width (wr).

The physical parameters estimated from the electrical characterization of our test structures are listed in Table 1.

Table 1

T_C	9 K
ΔT_C	700 mK
ρ_{20K}	365 μΩ·cm
$\lambda(0)$	600 nm
$J_C(4.2K)$	0.5-1.8 MA/cm2
h	10 W/(cm^{2}K)
L_{th}	76 nm
L_{hs}	~2-3□

We note that better material parameters were obtained in films grown subsequently, using optimized deposition conditions (see 3).

iii. SSPDs on GaAs

The same meander structures described in the previous section were fabricated on a 7 nm-thick NbN film grown on GaAs. The film showed T_C=11.6 K, ΔT_C=1250 mK, RRR=R(20K)/R(300K)=0.8. The parameters of the nanowires are L=5, 10 μm, w=100, 200 nm, f=40%.

Comparing the best I-V measured from these structures (Figure 2.9a, relative to a N=5 stripe meander with 5 μm-long and 200 nm-wide nanowires) with the results routinely obtained on MgO (see Figure 2.3) it is clear that meanders on GaAs are far more inhomogeneous. Devices fabricated on DBR are expected to show the same behavior.

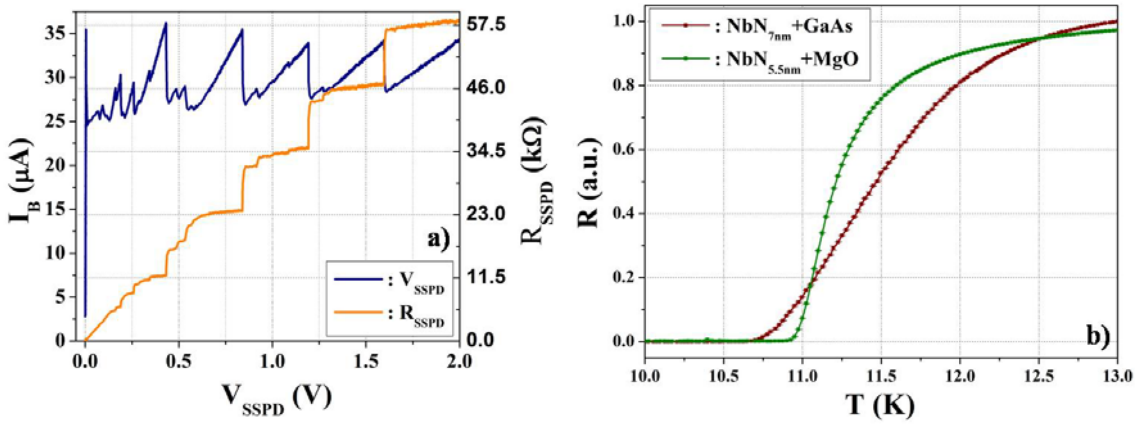

Figure 2.9. a. Complete I-V curve (in blue) at 4.2 K of a N=5 stripe meander (filling factor f=40%) on GaAs. The nanowires are 5 μm long, 200 nm wide and 7 nm thick. The orange plot is the resistance of the device (R_{SSPD}) as a function of voltage. b. Resistance vs temperature dependence of NbN films deposited on MgO (thickness 5.5 nm, in green) and on dusty GaAs (thickness 7 nm, in red). The films were deposited at I_c=250 mA, T_S=400°C, P_{tot}=2.5 mtorr, V_c~660 V (fresh target), V_S=0 V, d_{t-s}=85 mm.

One reason of the lower quality of devices on GaAs can of course be the poorer superconducting properties of NbN films deposited on GaAs (see chapter III). However this might not be the entire

picture. Indeed, the superconducting properties of the 7 nm-thick NbN film used here (T_C=11.6 K, ΔT_C=1250 mK, RRR=0.8, ρ=320 μΩ·cm, J_C=2.5 MA/cm^2) roughly compares with a 5.5 nm-thick film deposited on MgO (T_C=11.35 K, ΔT_C=625 mK, RRR=0.71, ρ=310 μΩ·cm, J_C=3.7 MA/cm^2), on which detecting devices could be fabricated (see section 3). Furthermore, it important to consider that these results are relative to first-generation devices, i.e. fabricated on dusty GaAs substrates (see chapter III). Better results are expected from devices fabricated on the improved NbN films grown on clean or MgO-buffered GaAs substrates.

A possible additional source of complications is the EBL nano-patterning step. Indeed, as the molecular weight of GaAs (Z_{GaAs}=64) is higher than MgO (Z_{MgO}=20), the backscattered electron coefficient (BSE) of GaAs is higher than MgO. From the montecarlo simulation (Casino [10]) of the interaction of our electron beam (100 keV energy, see chapter III) with the HSQ_{160nm} + NbN_{5nm} multilayer structure on the two substrates (MgO (Figure 2.10a,b) and GaAs (Figure 2.10c,d)) a BSE of 27% was estimated for GaAs and of 6% for MgO. The far higher BSE on GaAs causes strong proximity effects which may result in a poorer electron lithography.

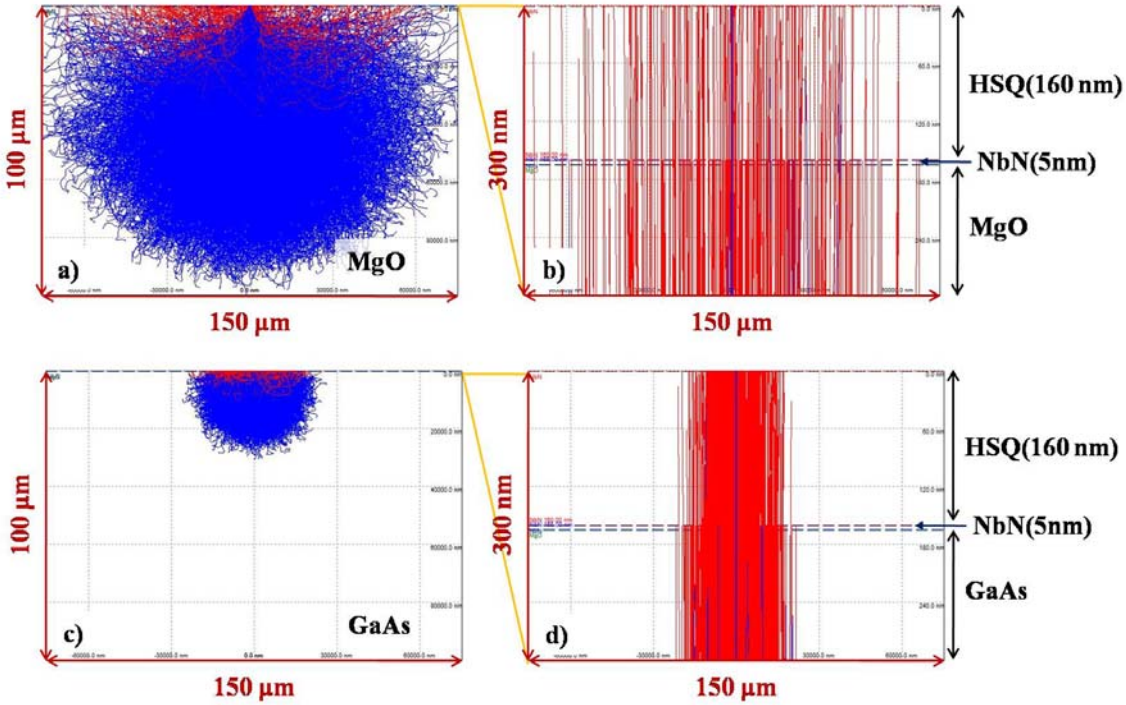

Figure 2.10. Trajectories of the incoming beam electrons (in blue) and of the backscattered electrons (in red) inside the cross sections the HSQ160nm+NbN5nm multilayer structure on MgO (a,b) and GaA (c,d), resulting from a random flight montecarlo simulation (Casino [10]). The energy of the electrons is 100 keV. The arrivals of 5000 electrons was simulated.

3. Optical characterization

In order to optimize the geometry of our meanders, we first identified the critical design parameters influencing the single-photon detection efficiency η of an SSPD.

In the simple SGK hotspot model (see chapter I and [11]), as a photon is absorbed in the superconducting nanowire biased close to its critical current, a normal spot is formed and it grows in size, forcing the supercurrent to flow through the still superconducting portion of the film. If the hotspot maximum diameter d_{HS}, the bias current and the nanowire width w are such that the critical current density is exceeded in the regions adjacent to the hotspot, they also switch to the normal state.

Thus the absorption of a photon causes the formation of a normal barrier across the whole cross section of the nanowire, so almost all the bias current is pushed to the external load (see chapter II for a description of the measurement setup), producing an output voltage pulse which can be measured.
η is the product of the intrinsic detection efficiency (η^I, the probability that the absorption of a photon results in the current-assisted formation of the resistive barrier) and of the absorbance (α, the ratio of the number of photons absorbed in the SSPD nanowire to the number of incident photons on the device active area A_d): $\eta=\alpha\cdot\eta^I$.
η^I depends on the relative values of d_{HS} and of the nanowire width (w). As the superconducting properties of the NbN film depend on its thickness t_h (see chapter III), d_{HS} at a given photon wavelength is in the end just a complicated function of t_h [12]. Therefore η^I can be thought as a function of w and t_h. As α increases with t_h and the filling factor (f) of the meander structure, η of an SSPD depends on w, f, and t_h only. Our aim was to maximize η in the part of this three-dimensional parameter space accessible with our technology, keeping the size and aspect ratio of our meanders fixed.

SSPDs were fabricated on few-nm thick NbN films deposited under optimal conditions on MgO by a two mask process using electron beam lithography and reactive ion etching (see chapter III for details). Detectors are 5x5 μm^2 in size, and composed of nanowires ranging from 60 to 100 nm in width, folded in a meander pattern with fill factors ranging from 40% to 60%.
The same structures were fabricated on films of 4 different thicknesses: 7, 5.5, 4 and 3 nm (Figure 3.1). The thickness of NbN films was measured by AFM (see chapter II). T_C varies from 13.7 K (ΔT_C=0.4 K) for t_h=7 nm to 8.6 K (ΔT_C =0.9 K) for t_h=3 nm. T_C and ΔT_C of the patterned SSPD were found to be the same as those of the original NbN films, which confirms that the fabrication process does not affect their superconducting properties.

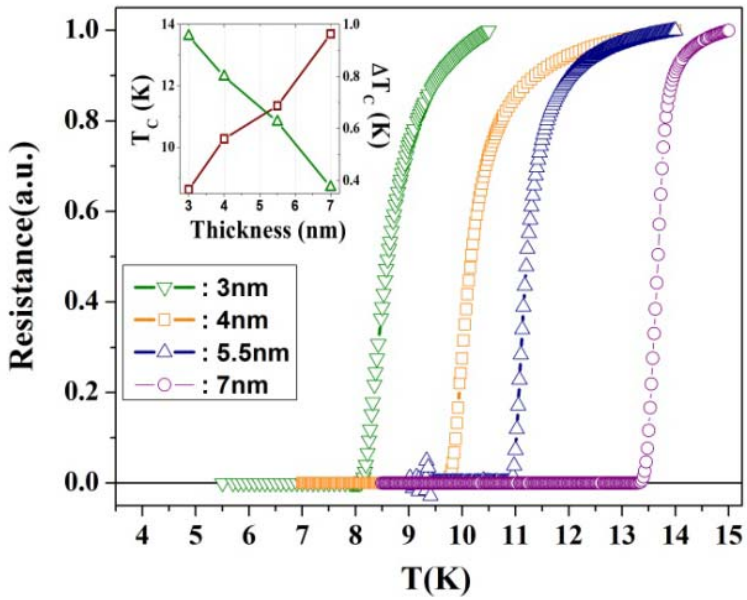

Figure 3.1. Resistance vs temperature dependence of NbN films for four thicknesses: 7nm (circles), 5.5nm (stars), 4nm (squares) and 3nm (triangles). The films were deposited at I_c=250 mA, T_S=400°C, P_{tot}=2.5 mtorr, x_{N2}=33%, V_c=620 to 660 V (fresh target), V_S=0 V, d_{t-s}=85 mm. Inset: T_C and ΔT_C vs. thickness(t_h).

Electrical and optical characterizations have been performed on the SSPDs. In total, 320 devices were tested, 80 for each of the four different film thicknesses of interest. For each chip, the best devices were first selected measuring their current-voltage (I-V) curves inside the cryogenic probe station (see chapter II for experimental details). The physical parameters estimated from the electrical

characterization of the detectors are listed in Table 2. Data relative to the 3 nm-thick film are not reported because they are too scattered, due to the low quality of the devices. In particular, the value of J_C at 4.2K varied in the 2-4 MA/cm^2 range, which is a state of the art value.

Table 2

t_h	7 nm	5.5 nm	4 nm	3 nm	
T_C	13.7	11.3	10.3	8.6	K
ΔT_C	440	620	800	950	mK
RRR	0.76	0.71	0.76	0.66	
ρ_{20K}	190	310	360	--	μΩ·cm
$\lambda(0)$	350	500	560	--	nm
$J_C(4.2K)$	4.2	3.7	2.2	--	MA/cm^2

The ten devices which showed the highest J_C in each chip were mounted on the cryogenic D-dipstick and optically tested at 4.2 K (see chapter II for experimental details). This selection criterion relies on the fact that the most constricted segment of a nanowire determines its I_C. Devices with a constriction (which show a low I_C) are biased well below J_C in most of the meander length, and thus they have a lower detection efficiency.

The dependence of the number of detector counts per second on the average number of photons per pulse was investigated. The device was biased at I_B/I_C=0.85 to keep it superconducting even when I_C was thermally suppressed for high light intensities. As expected [13], the dependence was linear for the photon fluxes used in η measurements (~0.5 photons per pulse, see chapter II), proof that true single photon detection was observed.

Dark count rate (DK) was determined as the number of counts registered in one second when SSPD optical input was blocked. The single photon detection efficiency at a certain bias current I_B was calculated as $\eta=(N_C - DK)/N_{ph}$, where N_C is the number of detection events registered by the counter in one second, N_{ph} is the number of photons incident on the device area in the same time and DK is the dark counts rate at I_B.

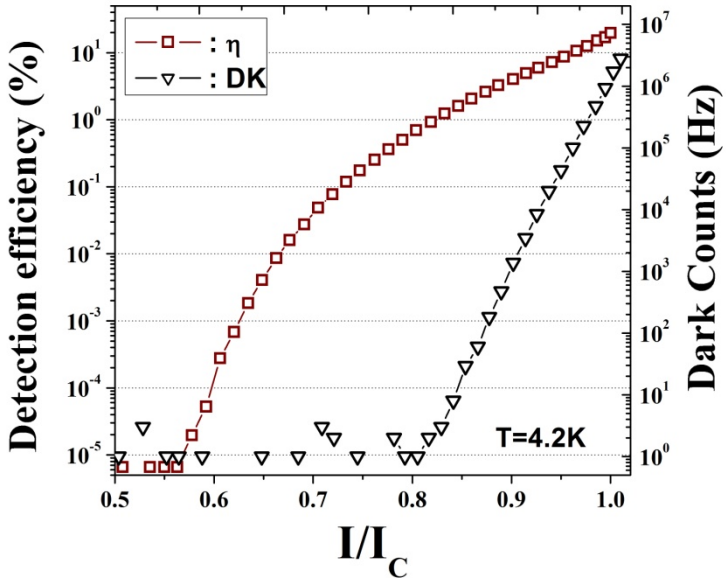

Figure 3.2. Single photon detection efficiency (open squares) and dark count rate (open triangles) as a function of the normalized bias current for the single photon detection regime of an optimum 5x5 μm^2 SSPD: w=100nm, f=40% and t_h=4 nm. The incident photon wavelength was 1.3 μm. Temperature was 4.2K.

Measurements of the η and DK dependence on the bias current were performed. The value for the bias resistor (R_B=10 Ω) was chosen to attain the highest ratio of the bias current I_B to I_C (see section 2.2.i and Figure 2.2). The photons are fed to the devices through a single-mode optical fiber fed to the D-dipstick head and coupled with a short focal length lens placed far from the plane of the chip in order to insure uniform illumination of the devices. By an extensive calibration of the intensity distribution on the sample plane it has been possible to estimate the number of incident photons per device area with an error of 5% (see chapter II for further details).

The best performance was exhibited by a w=100 nm, f=40%, t_h=4 nm meander, which reaches η=20% at 1.3 μm wavelength (Figure 3.2) before saturation.

As the largest detection efficiency values correspond to rather high dark count rates, the optical operation regime of the SSPD is a trade-off of maximum η and the highest acceptable DK. The relation between η and DK for a given photon energy can be quantitatively given in terms of the noise equivalent power (NEP), which can be defined for quantum detectors as [14]: $NEP = h\nu\sqrt{2DK}/\eta$. Using η and DK from Figure 3.2, the NEP at 1.3 μm was estimated to be of the order of 10^{-16} W/Hz$^{1/2}$, which is a state of the art value at the temperature of the experiment. We note that a higher η and a much lower DK may be obtained by cooling the device down to 2K [15].

In order to quantify the speed of the device, we take $f_0=(t_{reset})^{-1}$ as the maximum repetition frequency, where t_{reset} is the time that the current through the device needs to recover to 95% of its regime value after a detection event. The reset time can be estimated from the time constant (τ_{fall}) of the exponential decay of the photoresponse $t_{reset}\sim 3\tau_{fall}$. Fitting of the time resolved response pulse of our best SSPD (Figure 3.3) the fall time constant can be estimated as τ_{fall}=1.5 ns, which means f_0~200 MHz.

Moreover, τ_{fall} can be used to roughly estimate the kinetic inductance (L_{kin} [16]) of the meander as $\tau_{fall}=L_{kin}/R_{out}$, with R_{out} the external load resistance. As the RF part of the measurement circuit is matched (see chapter I and V for the SSPD equivalent circuit), we can put R_{out}=50Ω and estimate the kinetic inductance per square as $L_{kin}/\square\sim$70pH, which agrees in the order of magnitude with the value calculated using the magnetic penetration depth for the film [16] ($\lambda(4.2K)\sim\lambda(0)$=560 nm, see Table 2). $L_{kin}/\square=\mu_0\lambda(4.2K)^2/t_h\sim$100 pH.

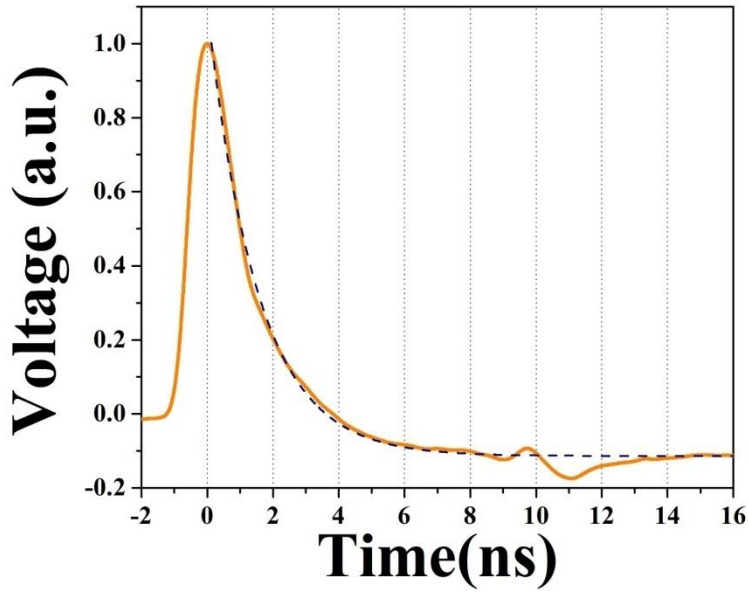

Figure 3.3. The orange continuous plot is the photoresponse of an optimum 5x5 μm^2 SSPD: w=100nm, f=40% and t_h=4 nm. The 100 ps-wide light pulses at 1.3 μm from a fiber-pigtailed, gain-switched laser diode had a repetition rate of 26 MHz. The device was tested under uniform illumination in the cryogenic D-dipstick dipped in a liquid He bath at 4.2 K. The blue, dashed plot is the fitting of the exponential decay.

4. Nanowire homogeneity characterization

Although some SSPDs have shown high detection efficiency, the fabrication of the meander geometry is challenging and the production yield of high performance detectors has to be improved. Variations of the critical current along a nanowire are responsible for the wide distribution in efficiency values of nominally identical SSPDs. Indeed, as a consequence of the photodetection mechanism (see chapter I for an introduction), the detection efficiency critically depends on the I_B/I_C ratio (Figure 3.2). If the critical current is not homogeneous along the nanowire, the low critical current sections (in the following referred as "constrictions") limit the maximum bias current the nanowire can sustain before switching from the superconducting state to the hotspot plateau. In such a condition, only the regions near the constrictions are correctly biased and they are really sensitive to the incoming radiation, while in the sections with high I_C the bias current is well below their critical current and they have low efficiencies. This was evidenced through inductance measurements [17] and by submicrometer photoresponse mapping [18].

Furthermore, it is believed [19] that the jitter of SSPDs is due to the delayed superconducting energy gap suppression mechanism (see [20] and chapter I) during the formation of the photo-induced normal barrier across the nanowire, and that it is currently limited by constrictions.

It is thus important to characterize the homogeneity of the nanowires.

The homogeneity issue was first addressed by fabricating meanders where each wire is separately contacted and by measuring the critical current distributions for the different wires (measurements performed by Dr. F. Mattioli and Dr. R. Leoni at the Photonics and Nanotechnology Institute (IFN), Rome, section 4.1). In order to understand the physical origin of these constrictions we the performed a spatially-resolved characterization of the η of a long straight nanowire (measurements performed by Dr. D. Bitauld) followed by a high resolution SEM scan on its whole length (section 4.2).

4.1.Contacted meander

A constriction in the nanowire can affect considerably its critical current, without changing too much its normal resistance and hence the total resistance of the meander. Therefore, for diagnostic purposes it is better to characterize the critical current than the resistances of the single parts of a meander.

Test meander structures, designed to allow the electrical access to each nanowire of the series (Figure 4.1), have been fabricated specifically to investigate the distribution of the critical current in the various stripes of the meander. The nanowires are 100 nm wide but the spacing is varied from 150 nm (Figure 4.1a, structure A) to 1.5 μm (Figure 4.1b, structure B).

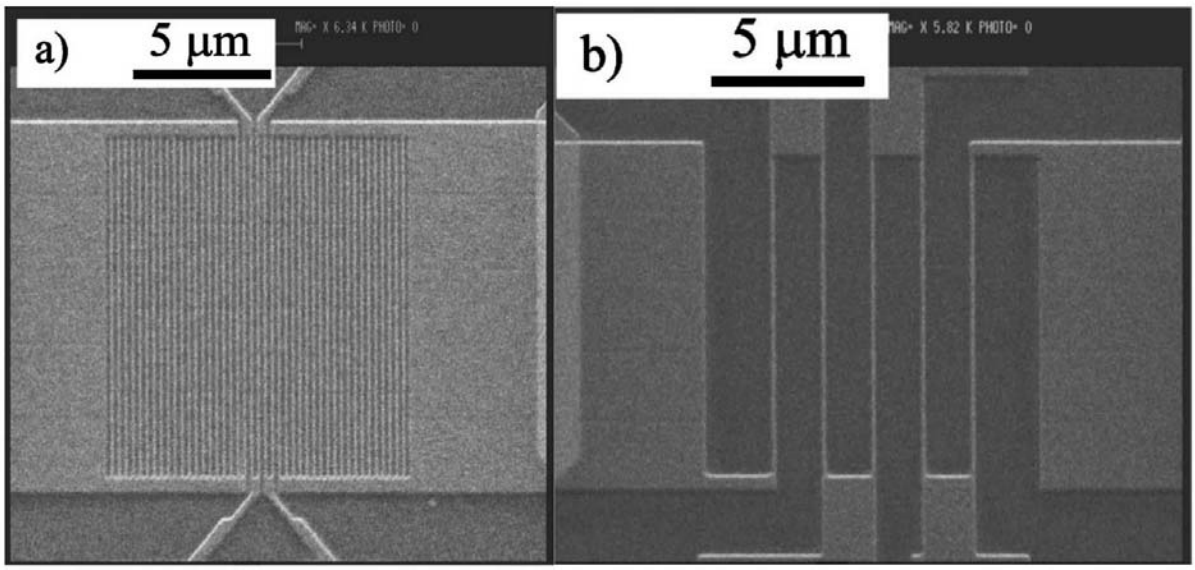

Figure 4.1. Scanning electron microscope (SEM) image of a type A (a) and type B (b) test meander-structures with five nanowires in series. The nanowire is 100 nm wide and 10 μm long. All five nanowires are electrically connected to external pads. The spacing between two adjacent nanowires is 150 nm (a) or 1.5 mm (b). The other "dummy" stripes visible in figure a have been added to improve the dose uniformity over the whole device area.

The two structures have been electrically characterized (at IFN, Rome) with a setup similar to the one described in chapter II. To study in detail the homogeneity of each nanowire of the meanders, their I-V curves were repeatedly measured using the dedicated contacts in order to build a statistical ensemble of their critical current values. As shown in Figure 4.2, histogram plots of the I_C values of each nanowire of the meanders could be built.

From this analysis we can compare the critical current uniformity of a type A structure in Figure 4.2a (filling factor 0.4) with that of a B structure in Figure 4.2b (filling factor 0.06). The results obtained show that the critical current uniformity is about the same, i.e. 6% and 8.5% for types A and B, respectively. These values indicate the good nanowire homogeneity even when the filling factor is increased by a factor of 10. As proximity effect becomes more and more important when spacing between stripes decreases, we would expect a poorer width control in the highly packed structure. The fact that the uniformity is instead quite similar in both structures is an encouraging result, probably due to the high-acceleration voltage (100 kV) of the electrons in our lithography system. Such a high energy electron beam allows to spread the backscattered electrons in a larger area, decreasing the amplitude of the local spurious effect due to electron overdosing (see Figure 2.10a, b).

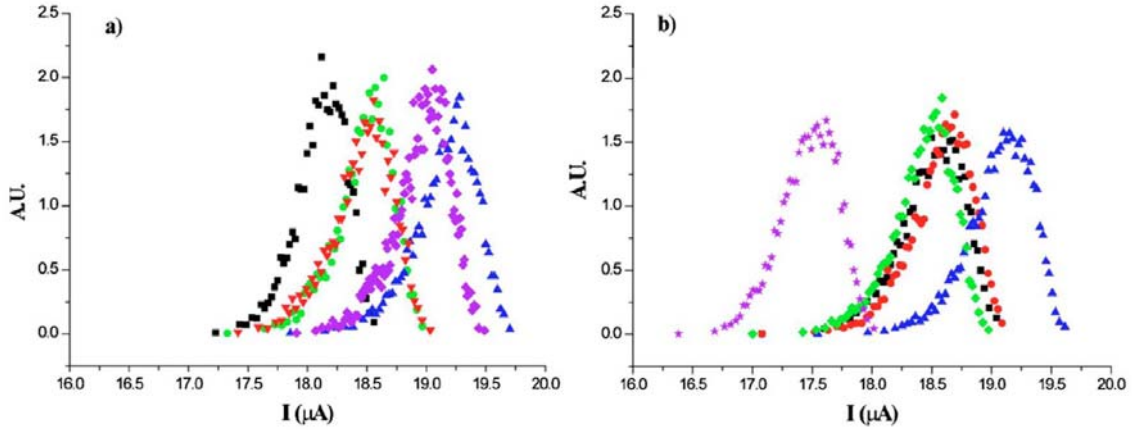

Figure 4.2. Distributions of the critical current at 4.2 K of the five nanowires of structure A (a) and B (b).

4.2.Spatially-resolved characterization

i. Mapping

As in the cryogenic probe-station the whole optics is mounted on an XYZ translation stage, it is possible to move the spot on the surface of the sample (see chapter II), which makes this setup suitable for the spatially resolved characterization of nanowires. However, the smallest spot at λ=1.3 μm that can be produced in the cryogenic probe-station is 2 μm FWHM, which is still comparable to the SSPD area, preventing to map the response along the wire length. Therefore, a straight 250 μm long nanowire (as long as two standard 5x5 μm^2) was fabricated in order to highlight the efficiency inhomogeneities along its length. Indeed, in this way it is possible to illuminate only a small part of the SSPD even with a micrometer-size beam.

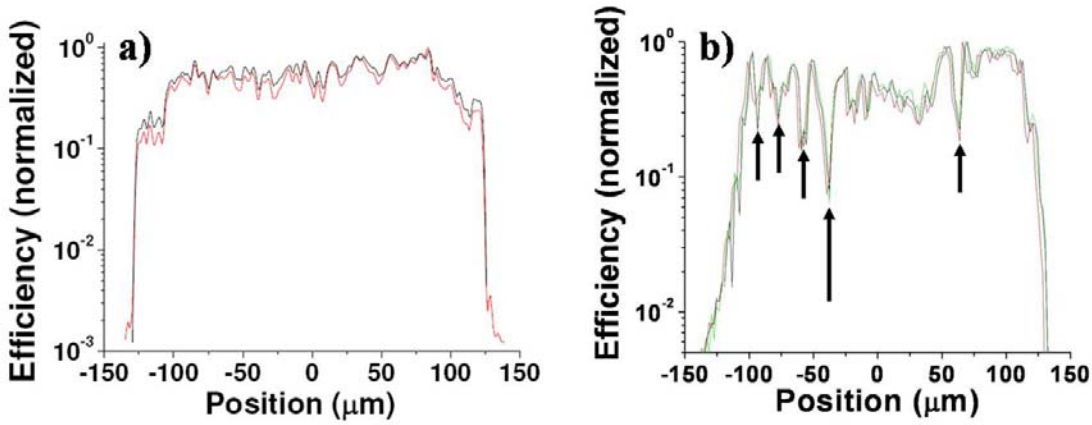

Figure 4.3. Efficiency profile for a 150 nm wide nanowire (a) and for a 100 nm wide nanowire showing efficiency dips (b). The experiment is repeated two or three times, yielding the three curves in each graph. The start point of each measurement not being exactly the same, the curves have been slightly shifted horizontally to obtain a good superposition. The characterization was performed with a spot size of 5 μm FWHM.

For the efficiency profile measurement, we move the spot along the nanowire at steps of 1-2 μm and measure the number of counts per second with constant beam intensity (Figure 4.3). The experiment has been carried out two or three times on each device to check the repeatability of the inhomogeneities. The shapes of the curves are exactly the same, proving that the measured profile is

due to a spatial variation of the efficiency and not to temporal variations for instance. Several devices were tested, with different wire widths (w=100, 150 nm).

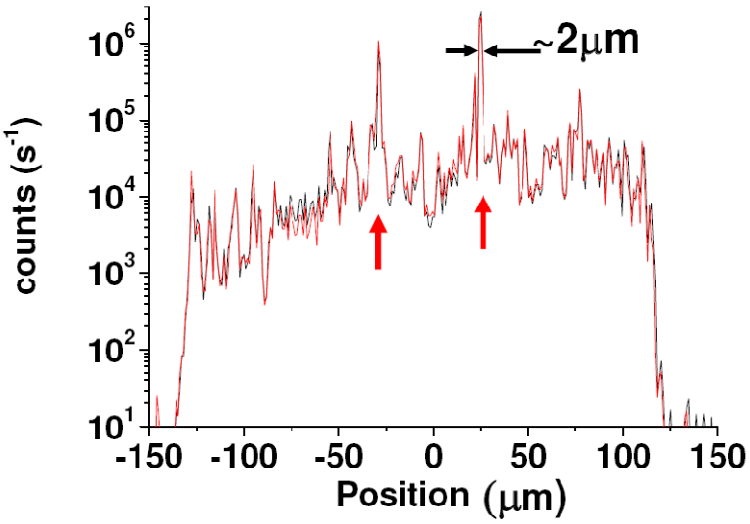

Figure 4.4. Efficiency profile for a 150 nm wide nanowire with two constrictions. The characterization was performed with a spot size of 2 μm FWHM.

On some meanders, the efficiency inhomogeneities were not very important (Figure 4.3a), apart from a slight efficiency decrease at both ends of the nanowire, which could be due to proximity effects related to the contact pads during the EBL step (see chapter III). On the other hand, some devices showed important efficiency variations as a function of position. Two types of inhomogeneities were observed: efficiency dips (Figure 4.3b) and peaks (Figure 4.4). The main dips, pointed by arrows on Figure 4.3b), have a spatial dimension of about 10 μm FWHM (not limited by the 5 μm spot size used for the characterization, see chapter II) and some of them have an amplitude of almost a decade. On the contrary, the efficiency peaks pointed by the two arrows on Figure 4.4 are approximately 2 μm (FWHM) in size, limited by the resolution of the objective (2 μm spot size). The difference between the efficiency when the beam is centered on the constriction and the efficiency in the rest of the device is about two orders of magnitude.

A study of the efficiency and of the dark count rate as a function of the bias current was performed on the constricted device (Figure 4.5). The number of photons per pulse incident on the intersection between the 2 μm circular spot and the 150 nm wide nanowire is estimated at 137 photons/pulse at a repetition rate of 26 MHz. The absolute number of counts for the three curves is shown on the left axis and the value of the efficiency for the illumination on and off the constriction is shown on the right axis. We can see that even for the constriction the efficiency is below 0.2%. This value has to be compared to the best detection efficiencies usually obtained in the cryogenic probe station (sample temperature of 5 *K*), which are in the range of 1%. The difference between the detection efficiency of a good meander SSPD and the constriction is probably due to the fact that the constriction is much smaller than the illuminated length of the nanowire (about 2 μm).

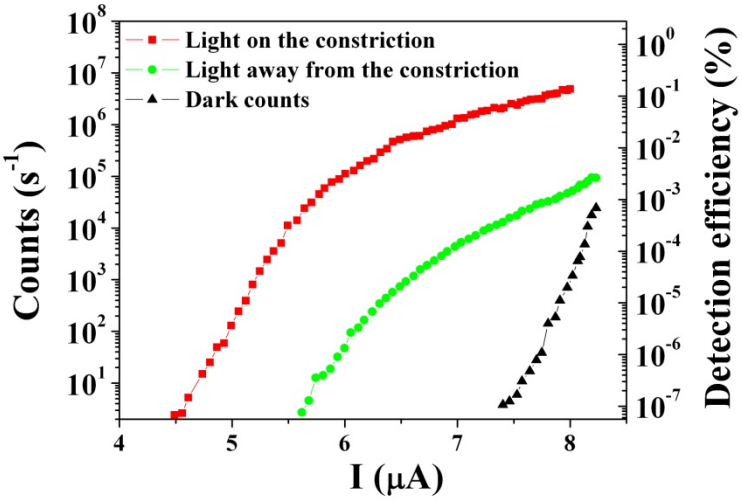

Figure 4.5. Dark counts and detection efficiency of a constricted device illuminated on the constriction and away from the constriction as a function of the bias current.

ii. Scanning Electron Microscopy (SEM)

High resolution SEM scans were performed on the whole 250 μm nanowire length (with 1 or 2 μm step-size see) both on the device with efficiency dips and on the constricted device in order to check the width uniformity along the nanowire and thus to determine whether inhomogeneities are due to lithographic defects. Indeed, a decrease of the efficiency by one order of magnitude (as on Figure 4.3b) would be caused by an increase of the local critical current of about 10% corresponding to an increase of about 10 nm in width. An increase of the efficiency by two orders of magnitude (as on Figure 4.4) would be caused by a decrease of the critical current of about 20% on a length comparable to the illumination spot, which corresponds to a 30 nm decrease in width in the present case. For a constriction smaller than the spot, we expect even more than 30 nm.

For the nanowire presented in Figure 4.3b, the top layer of HSQ used during the process has been removed after the optical characterization to image directly the NbN stripe. The HSQ was removed with a cotton swab soaked with triclorethylene. This technique was tested on another sample and has proven not to alter the critical current of the SSPD. At every location where we previously saw an efficiency drop (pointed by the arrows on Figure 4.3b), we found the type of lithography-induced defects shown on Figure 4.6, while the rest of the stripe was found to be perfectly uniform. These defects consist of regions where the HSQ resist was protruding outside the stripe (tentatively attributed to underdevelopment), and thus has masked the NbN etching. They were spread on lengths of a few hundreds of nanometers. Thus their presence alone cannot explain an efficiency drop in 10 μm-long section. Nevertheless, the correlation between their location and that of the efficiency dips is striking. The protrusions might then be the symptoms of another problem having an effect on a larger scale. Indeed, the underexposure could also be responsible for a slight increase in width on a longer range, 10 nm being approximately the limit of the microscope resolution.

For the nanowire presented in Figure 4.4, the top layer of HSQ was removed even before the optical characterization, thus ensuring that the sample used for optical characterization and SEM is exactly in the same condition. On this sample, we found no evidence of lithographic defects at the positions of efficiency peaks. In fact, the wire appeared uniform on its entire length.

In summary, this SEM investigation shows that the processing of the devices might be responsible for some problems affecting the efficiency, but there is no evidence that constrictions, which are the most critical problems for the efficiency, are due to processing defects. They might then

more probably be due to thickness or quality inhomogeneities of the film occurring during the film deposition or later in the process.

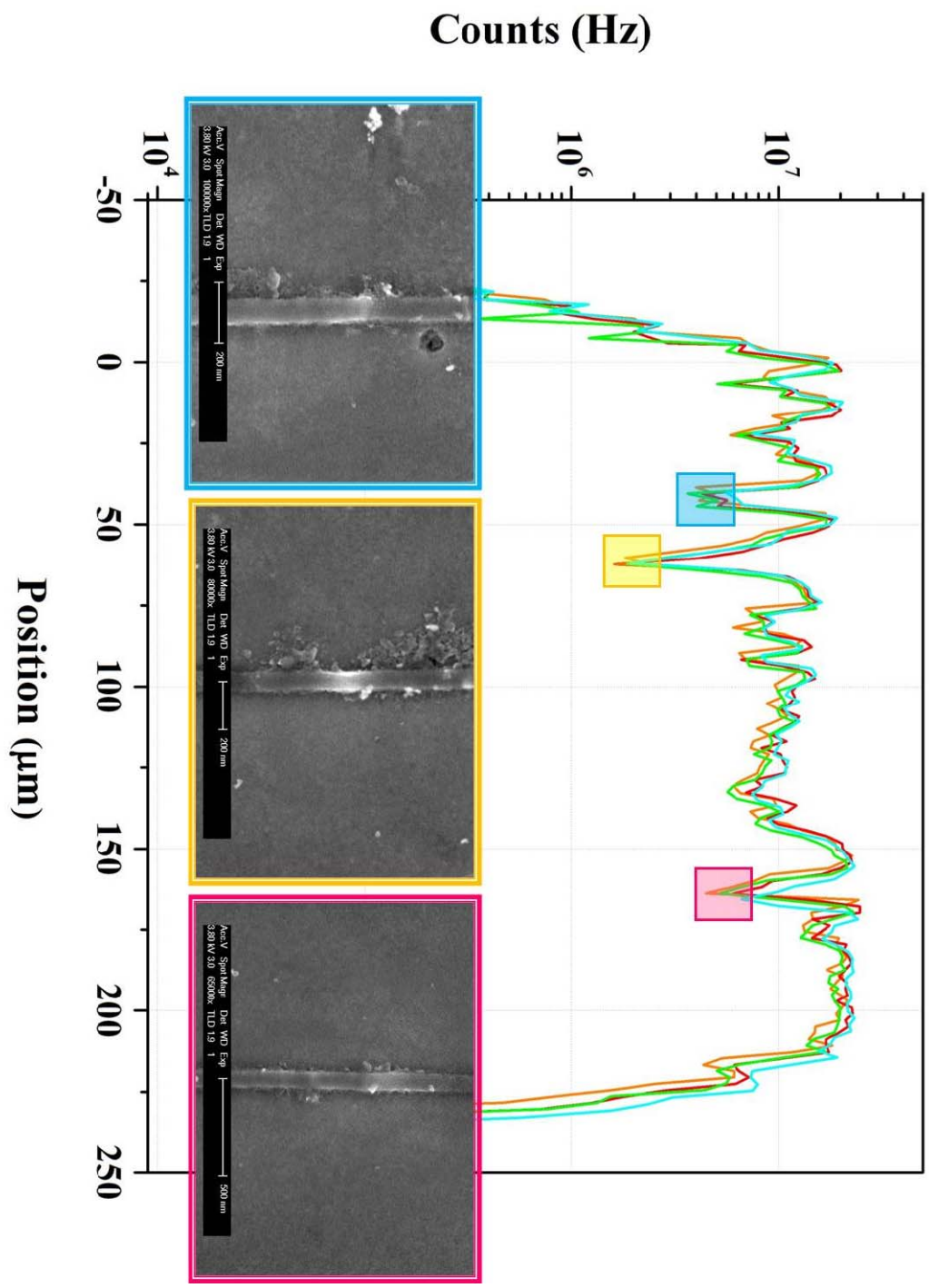

Figure 4.6. SEM images of the nanowire of Figure 4.3b relative to the sections presenting the three deepest efficiency dips.

5. Conclusions

This chapter reports the results of the electrical and optical characterization of SSPDs fabricated on high-quality few-nm thick NbN films on MgO, GaAs and AlAs/GaAs-based DBRs deposited at low substrate temperature (~400°C).

I-V curves of test structures were measured, from which it was possible to deduce important physical parameters used as figures of merit to estimate the superconducting properties of the nanowires (ρ, $\lambda(0)$, J_C), or for the design or the simulation of the devices (h, L_{hs}, L_{th}). The quality of the devices fabricated on GaAs is poorer than those on MgO, most likely due to the lower quality of NbN films deposited on GaAs and to issues related to the EBL nano-patterning step.

Measurements of detection efficiency (η) and of dark cont rate (DK) as a function of the bias current were performed on SSPDs fabricated on few-nm thick NbN films (t_h= 3 to 7nm) deposited under optimal conditions on MgO. Detectors are 5x5 μm^2 in size, and composed of nanowires ranging from 60 to 100 nm in width, folded in a meander pattern with fill factors ranging from 40% to 60%. The best performance was exhibited by a w=100 nm, f=40%, t_h=4 nm meander, showing η=20% and NEP=10^{-16} W/$Hz^{1/2}$ (at λ=1.3 μm and T=4.2 K), which are state of the art values. This result showed for the first time that high performance NbN SSPDs can be realized on a different substrate and from a deposition process at lower temperature than previously reported (more recently, similar results were reported also by [2]).

High detection efficiencies could not be measured with SSPDs fabricated on GaAs, but it should be noted that at present only first-generation devices (fabricated on dusty GaAs substrates) have been tested. Better results are expected from devices fabricated on the improved NbN films grown on clean or MgO-buffered GaAs substrates.

Although SSPDs on MgO have shown high detection efficiency, the fabrication of the meander geometry is challenging and the production yield of high performance detectors has to be improved.

The nanowire homogeneity issue was first addressed by fabricating meanders where each wire is separately contacted and by measuring the critical current distributions for the different wires. The results obtained show that the critical current uniformity is about 6% for closely packed meanders (f=40%), proof of the good nanowire homogeneity.

Finally, in order to understand the physical origin of the nanowire constrictions we performed a spatially-resolved characterization of the η of a long straight nanowire, followed by a high resolution SEM scan on its whole length. Two types of inhomogeneities have been evidenced, corresponding to localized efficiency dips and peaks. The peaks likely correspond to constrictions. SEM observations did not evidence any width narrowing at the position of the efficiency peaks, which suggests that constrictions might be due to thickness or quality inhomogeneities of the film occurring during the film deposition or later in the process. On the other hand, the efficiency dips have been correlated with lithography problems discovered on SEM images but those defects do not affect the global efficiency as much as constrictions.

6. References

[1] G. N. Gol'tsman, O. Okunev, G. Chulkova, A. Lipatov, A. Semenov, K. Smirnov, B. Voronov, A. Dzardanov, C. Williams, and R. Sobolewski, Appl. Phys. Lett. **79**, 705 (2001).

[2] S. Miki, M. Fujiwara, M. Sasaki, B. Baek, A. J. Miller, R. H. Hadfield, S. W. Nam, and Z. Wang, Appl. Phys. Lett. **92**, 061116 (2008).

[3] K. Iizuka, K. Matsumaru, T. Suzuki, H. Hirose, K. Suzuki, and H. Okamoto, J. Cryst. Growth **150**, 13 (1995).

[4] W. J. Skocpol, M. R. Beasley, and M. Tinkham, J. Appl. Phys. **45**, 4054 (1974).

[5] S. Kubo, M. Asahi, M. Hikita, and M. Igarashi, Appl. Phys. Lett. **44**, 258 (1984).

[6] Z. Wang, A. Kawakami, Y. Uzawa, and B. Komiyama, J. Appl. Phys. **79**, 7837 (1996).

[7] T. P. Orlando, E. J. McNiff, S. Foner, and M. R. Beasley, Phys. Rev. B **19**, 4545 (1979).

[8] M. Tinkham, in Introduction to Superconductivity, McGraw Hill Inc., New York, 1996, Chap. 3.

[9] M. Tinkham, in Introduction to Superconductivity, McGraw Hill Inc., New York, 1996, Chap. 2.

[10] Casino, www.gel.usherbrooke.ca/casino/index.html.

[11] A. D. Semenov, G. N. Gol'tsman, and A. A. Korneev, Physica C **351**, 349 (2001).

[12] A. Semenov, A. Engel, K. Il'in, G. Gol'tsman, M. Siegel, and H. W. Hübers, Eur. Phys. J. AP **21**, 171 (2003).

[13] A. Verevkin, J. Zhang, R. Sobolewski, A. Lipatov, O. Okunev, G. Chulkova, A. Korneev, K. Smimov, G. N. Gol'tsman, and A. Semenov, Appl. Phys. Lett. **80**, 4687 (2002).

[14] A. J. Miller, S. W. Nam, J. M. Martinis, and A. V. Sergienko, Appl. Phys. Lett. **83**, 791 (2003).

[15] G. Gol'tsman *et al.*, IEEE Trans. Appl. Supercond. **17**, 246 (2007).

[16] A. M. Kadin, in Introduction to superconducting circuits, Wiley, New York, 1999, Chap. 2.

[17] A. J. Kerman, E. A. Dauler, J. K. W. Yang, K. M. Rosfjord, V. Anant, K. K. Berggren, G. N. Gol'tsman, and B. M. Voronov, Appl. Phys. Lett. **90**, 101110 (2007).

[18] R. H. Hadfield, P. A. Dalgarno, J. A. O'Connor, E. Ramsay, R. J. Warburton, E. J. Gansen, B. Baek, M. J. Stevens, R. P. Mirin, and S. W. Nam, Appl. Phys. Lett. **91**, 241108 (2007).

[19] A. Pearlman *et al.*, IEEE Trans. Appl. Supercond. **15**, 579 (2005).

[20] J. Zhang, W. Słysz, A. Pearlman, A. Verevkin, R. Sobolewski, O. Okunev, G. Chulkova, and G. N. Gol'tsman, Phys. Rev. B **67**, 1325081 (2003).

V: The parallel nanowire detector (PND)

1. Introduction

As already pointed out in chapter I, among the approaches proposed so far to PNR detection, detectors based on charge-integration or field-effect transistors [1-3] are affected by long integration times, leading to bandwidths <1 MHz. Transition edge sensors (TES [4, 5]) show extremely high (95%) detection efficiencies but they operate at 100 mK and show long response times (several hundreds of nanoseconds in the best case [6]). Approaches based on photomultipliers (PMTs) [7] and avalanche diodes (APDs), such as the visible light photon counter (VLPC) [8, 9], 2D arrays of APDs [10, 11] and time-multiplexed detectors [12, 13] are not sensitive or are plagued by high dark count rate and long dead times in the telecommunication spectral windows. Arrays of SPDs additionally involve complex read-out schemes [11] or separate contacts, amplification and discrimination [14].

Our approach, the Parallel Nanowire Detector (PND), uses spatial multiplexing on a subwavelength scale to provide a single electrical output proportional to the photon number. The device presented significantly outperforms existing PNR detectors in terms of simplicity, sensitivity, speed, and multiplication noise (see Table 1). In this chapter we present the working principle of the device (section 2), the results of the optical characterization (section to 3), an extensive analysis of the device operation and corresponding design guidelines (section 4) and the first application of a PND to reconstruct an unknown incoming photon number statistics (section 5).

Table 1. Reported performance for detectors with PNR functionality. SPEED: Repetition frequency used in reported experiments (does not necessarily represent the maximum possible rate). DK: Dark counts. η: Detection efficiency. NEP: Noise equivalent power. λ: Optical excitation wavelength. M_{noise}: Device affected by multiplication noise. M_{max}: Maximum number of detected photons. T: Operating temperature. READ-OUT: Required read-out. n.r.: not reported.

	REP. RATE (Hz)	DK (Hz)	η (%)	NEP ($W/Hz^{1/2}$)	λ (nm)	M_{noise}	M_{max}	T (K)	READ-OUT
CIPD[1]	40	n.r.	80	n.r.	1550	YES	n.r.	4.2	Cryo JFET
QD-FET[2,3]	$2\cdot10^5$	0.4	1.3	$2\cdot10^{-17}$	684	YES	3	4.2	Cryo MESFET
TES[5]	$5\cdot10^4$	400	89	$4\cdot10^{-18}$	1550	YES	11	<0.1	SQUID array
PMT[7]	$6.7\cdot10^5$	400	7	10^{-16}	523	YES	9	room T	room T amp.
VLPC[8,9]	$1.5\cdot10^4$	$2\cdot10^4$	85	$9\cdot10^{-17}$	543	YES	10	6-7	Cryo preamp.
MPPC[10]	10^4	$1\text{-}4\cdot10^5$	25-65	$7\cdot10^{-16}$	400	YES	100-1600	room T	room T amp.
APD array[11]	$2\cdot10^4$	$1.6\cdot10^8$	33	10^{-14}	1064	NO	1024	246	Multi channel
Time mult.[12,13]	10^4	n.r.	66	n.r.	700-800	NO	8-16	room T	2-channels
PND	$8\cdot10^7$	0.15	2	$4\cdot10^{-18}$	1300	NO	6	2	room T amp.

2. Photon Number Resolution principle

The basic structure of the PND is the parallel connection of N superconducting nanowires (N-PND). The detecting element is a few nm-thick, ≈100 nm-wide NbN wire folded in a meander pattern (see chapter III for the structure of a PND). Each branch acts as an SSPD (see chapters I, IV). In SPPDs, if a superconducting nanowire is biased close to its critical current, the absorption of a photon causes the formation of a normal barrier across its cross section, so almost all the bias current is pushed to the external circuit (see chapter II). In PNDs, the currents from different sections can sum

up on the external load, producing an output voltage pulse proportional to the number of photons absorbed (see Figure 3.1).

Let I_B^i for i=1,..,N be the bias current flowing through each section when the N-PND is superconducting and in the steady state. Biasing the device with a voltage source V_B in series with a bias resistor R_B (see chapter II for the equivalent electrical circuit of the setup), the current $I=V_B/R_B$ will spread equally between the N branches, so $I_B^i=I/N$. If all the N nanowires are exactly the same, all with a critical current I_C, the superconducting to normal transition of the whole structure takes place when the bias current through the device exceeds $I_C^{tot}=N\cdot I_C$. As the nanowires are differently constricted (see chapter IV), the bias current can be increased only till each current flowing through one of the N nanowires exceeds the critical value for that particular nanowire I_C^i, so $I_C^{tot}=\sum_{i=1}^{N} I_C^i$. Let the k-th nanowire be the most constricted and its I_C^k be the lowest. While increasing I, as long as $I_B^k<I_C^k$, $I_B^i=I/N$ for all the branches, but when the current through the k-th nanowire approaches the critical value $I_B^k=I/N\sim I_C^k$, it is fixed to that value. Indeed, if I_B^k is further increased beyond I_C^k, the k-th nanowire switches to the dissipative hot spot state. A voltage drop then appears across it and all the other still superconducting branches, which drains enough current out of the k-th nanowire to drive it back to the superconducting state. The same argument also applies to the other nanowires, so in this parallel structure it is possible to bias each branch very close to its own value of I_C. Let $\eta_i=\eta\left(i_B^i\right)$ (with $i_B^i=I_B^i/I_C^i$) be the current-depending single-photon detection efficiency of a section of the device (defined with respect to the photon flux incident on the area covered by that section). When the device is biased very close to I_C^{tot}, each nanowire will then give its best performance because its η_i is maximum, as $i_B^i\sim 1$.

When a photon reaches the i-th section, biased at a current I_B^i, it will cause the creation of a normal barrier across the entire cross section of the nanowire with a probability η_i. Because of the sudden increase in the resistance of the firing nanowire, its current (I_f) is then redistributed between the other N-1 unfiring branches and the 50 Ω input resistance R_{out} of the high frequency amplifier. This argument yields that if n sections fire simultaneously (in a time interval much shorter than the current relaxation time), part of their currents sum up on the external load.

The device shows PNR capability if the height of the current pulse through R_{out} for n firing stripes $\bar{I}_{out}^{(n)}$ is n times higher than the pulse for one $\bar{I}_{out}^{(1)}$, i.e. if the leakage current drained by each of the unfiring nanowires $\delta I_{lk}=I_u-I_B$ is negligible with respect to I_B. The leakage current is also undesirable because it lowers the signal available for amplification and temporary increases the current flowing through the still superconducting (unfiring) sections, eventually driving them normal. Consequently, δI_{lk} limits the maximum bias current allowed for the stable operation of the device and then the detection efficiencies of the sections. The leakage current depends on the ratio between the impedance of a section Z_S and R_{out}. As Z_S is due just to the kinetic inductance of the superconducting nanowire L_{kin}, the trade-off between δI_{lk} and the speed of the device is very narrow. In order to relax the design constraints, a PND with integrated series resistors (R_0) in each section (PND-R) was developed (see chapter III for the structure of a PND-R). In a PND-R, $Z_S=j\omega L_{kin}+R_0$, so δI_{lk} can be minimized by engineering the dimensions of the nanowire (thus its kinetic inductance) and of the series resistor (see sec. 4).

3. Device optical characterization

In this section we present the results of the optical characterization of PNDs and PND-Rs, i.e. their speed performance (section 3.1), the proof of their PNR capability and their detection efficiency at λ=1.3 μm (3.2).
Most of the devices were designed by the author and fabricated at the Photonics and Nanotechnology Institute (IFN, Rome) by A. Gaggero, Dr. F. Mattioli and Dr. R. Leoni) on NbN films deposited on MgO (see chapter III for details).

3.1.Speed performance

Figure 3.1a shows a single-shot oscilloscope trace of the photoresponse of a 8.6x8 μm^2 5-PND under laser illumination (λ=700 nm, 80 MHz repetition rate). Pulses with five different amplitudes can be observed, corresponding to the transition of one to five sections. The measured 80 MHz counting rate represents an improvement of three orders of magnitude over most of the PNR detectors at telecom wavelength [1, 5, 11], with the only exception of the SSPD array [14].

We investigated the temporal response of a 10x10 μm^2 4-PND-R probed with light at 1.3 μm wavelength using a 40 GHz sampling oscilloscope (Figure 3.1b). All four possible amplitudes can be observed. The pulses show a full width at half maximum (FWHM) as low as 660ps. In a traditional 10x10 μm^2 SSPD, the pulse width would be of the order of 10 ns FWHM, so the recovery of the output current I_{out} through the amplifier input resistance is a factor ~4^2 faster (see section 4.3), which agrees with results reported by other groups [15, 16]. As shown in section 4.3, the very attractive N^2 scaling rule for the output pulse duration unfortunately does not apply to the device recovery time.

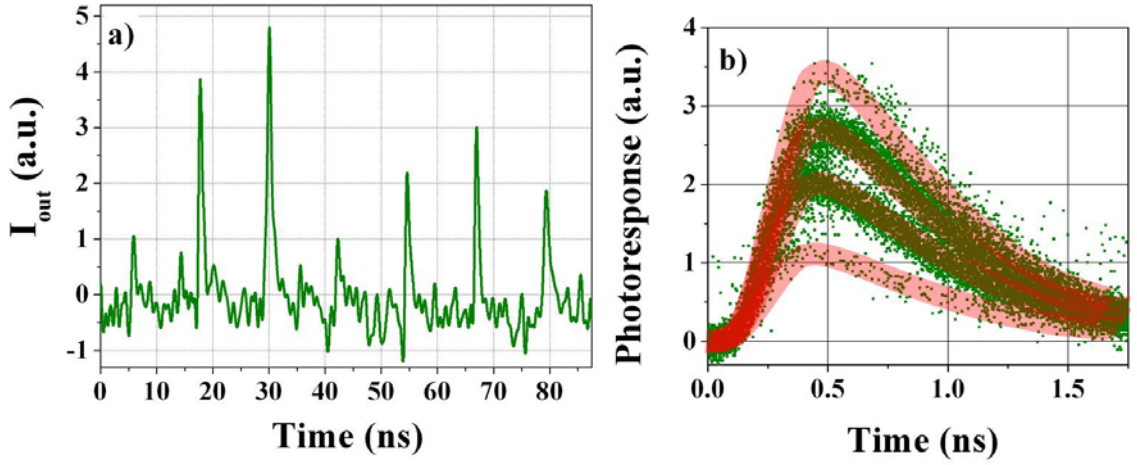

Figure 3.1. a. Single-shot oscilloscope trace during photodetection by a 8.6x8 μm^2 5-PND. The device was tested under uniform illumination in the cryogenic D-dipstick (see chapter II) dipped in a liquid He bath at 4.2 K. The light pulses at 700 nm form a mode-locked Ti:sapphire laser had a repetition rate of 80 MHz. b. Photoresponse transients taken with a 40 GHz sampling oscilloscope while probing a 10x10 μm^2 4-PND-R in the cryogenic probe station under illumination with 1.3 μm, 100ps-long pulses from a laser diode, at a repetition rate of 26MHz. The solid curves are guides to the eyes.

3.2.Proof of PNR capability

Let an N-PND be probed with a light whose photon number probability distribution is **S**=[S(m)]=[s_m]. The probability distribution of the number of measured photons **Q**=[Q(n)]=[q_n] is related to **S** by the relation:

$$Q(n) = \sum_m P^N(n|m) \cdot S(m) \qquad (1)$$

where $P^N(n|m)$ is the probability that n photons are detected when m are sent to the device.

In order to infer whether a PND is able to measure the number of incoming photons, it can be probed with a poissonian distribution $S(m)=\mu^m \cdot \exp(-\mu)/m!$ (μ: mean photon number). The limited efficiency $\eta<1$ of the detector is equivalent to an optical loss, and reduces the mean photon number to: $\mu^*=\eta\mu$. In the regime $\mu^*<<1$, $S(m) \sim (\mu^*)^m/m!$, and for μ* low enough (1) can be written as:

$$Q(n) \sim P(n|n) \cdot S(n) \propto (\mu^*)^n / n! \qquad for\ \mu^* << 1 \qquad (2)$$

Consequently, the probability Q(1) of detecting one photon is proportional to μ, Q(2) is proportional to μ^2, and so on.

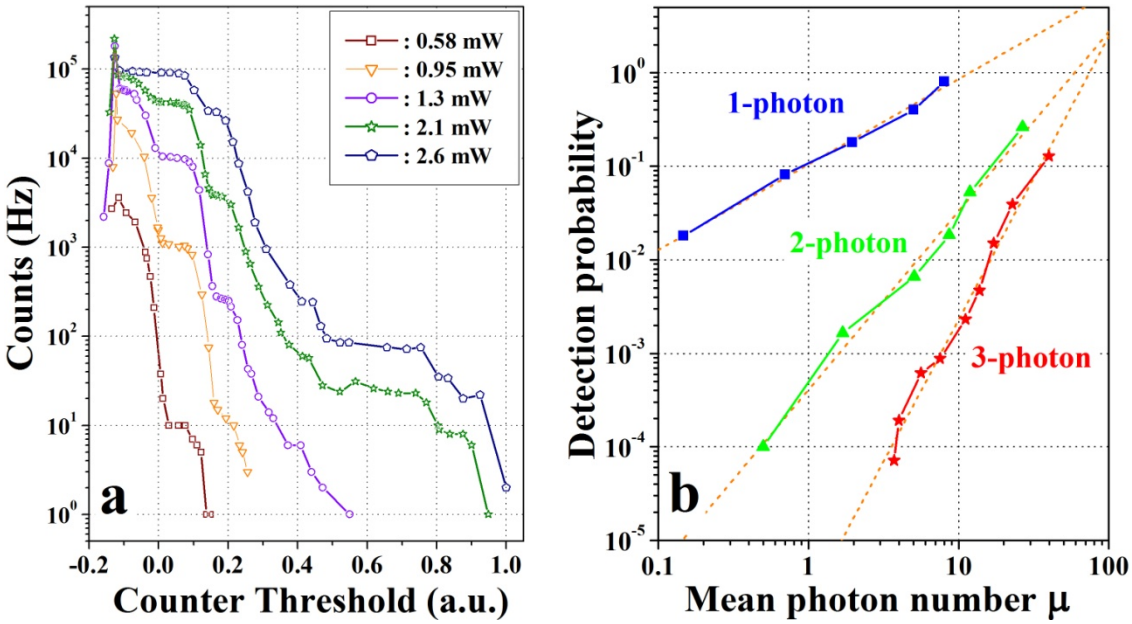

Figure 3.2. a. Photocounts vs threshold level at different light powers for a 10x10 μm² 5-PND-R. The device was mounted in cryogenic dipstick dipped in a liquid He bath at 2.2 K. A single-mode optical fiber was put in direct contact and aligned with the active area of the device. The light pulses at 0.85μm form the GaAs pulsed laser were 30 ps wide and the repetition rate was 100kHz. The power level was set with a variable fiber-based optical attenuator. The photoresponse from the device was sent to the 150 MHz counter. b Detection probabilities relative to the one (squares), two (triangles) and three-photon (stars) absorption events as a function of the mean photon number per pulse *μ*.

The following experimental results were obtained at Moscow state Pedagogical University (Moscow, Russia) by the group of Prof. G. Gol'tsman with devices fabricated on sapphire with a process similar to the one reported in chapter III (see [15] for details). The setup used for measurements is analogous to the one reported in chapter II.

A 10x10 μm² 5-PND-R was tested with the coherent light from a 850 nm GaAs pulsed laser, whose photon number distribution is close to a poissonian. The photoresponse from the device was sent to a 150 MHz counter. The photo-counts were measured as a function of the threshold level, for different light powers (Figure 3.2a). As expected, plateaus appear, corresponding to intervals of the output voltage between the well-defined n-photon levels (see Figure 3.1). In order to measure the

count rates for each level, the thresholds of the counter were chosen so that for any n and light intensity the counts corresponding to an n-photon absorption event were significantly higher than the counts corresponding to the absorption of more than n photons. In fig. 5b the corresponding detection probabilities relative to one-, two- and three-photon absorption events are plotted for μ varying from 0.15 to 40. As the mean single-photon detection efficiency $\tilde{\eta}$ of the device (defined with respect to the photon flux incident on the total active area covered by the device A_d) is a few percent (Figure 3.3) and μ is a few tens, the condition $\eta\mu=\mu^{*}<<1$ is verified and (2) is therefore valid. Indeed, the fittings clearly show that $Q(1) \propto \mu$, $Q(\mu,2) \propto \mu^2$ and $Q(\mu,3) \propto \mu^3$, which demonstrates the capability of the detector to resolve one, two and three photons simultaneously absorbed.

The device mean single-photon detection efficiency $\tilde{\eta}$ at λ=1.3 μm and the dark-counts rate DK were measured as a function of bias current at T= 2.2 K (Figure 3.3). The lowest DK value measured was 0.15 Hz for $\tilde{\eta}$=2% (yielding a noise equivalent power [17] NEP=$4.2\text{x}10^{-18}$ W/$\text{Hz}^{1/2}$), limited only by the room temperature background radiation coupling to the PND. This sensitivity outperforms most of the other approaches by one-two orders of magnitude (with the only exception of transition-edge sensors [5], which require a much lower operating temperature).

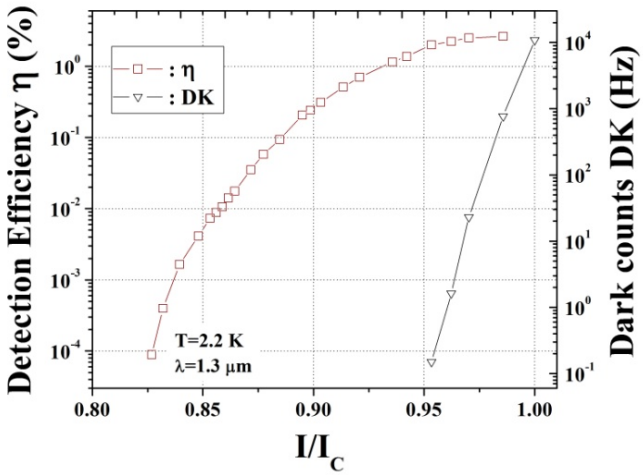

Figure 3.3. Mean detection efficiency at 1.3 μm and dark-counts rate vs bias current of a 10x10 μm^2 5-PND-R. The device was fiber-coupled and mounted a on cryogenic dipstick dipped in a liquid He bath at 2.2 K.

4. PND Design

We aim at providing a detailed understanding of the device operation and guidelines for the design of PNDs with optimized performance in terms of efficiency, speed and sensitivity.

The first step is to define the relevant parameter space. The width of the nanowire (w=100 nm) and the filling factor (f=50%) of the meander are fixed by technology, the thickness of the superconducting film (t=4nm) is the optimum value yielding the maximum device efficiency and the active area (A_d=10 x 10 μm^2) is fixed by the size of the core of single mode fibers to which the device must be coupled. We consider single-pass geometries (no optical cavity), but the same guidelines can be applied to cavity devices with optimized absorption [18]. The parameters of the PND-R that can be used as free design variables are: the number of sections in parallel N, the value of the series resistor R_0 and the value of the inductance of each section L_0. The number of sections in parallel N can be chosen within a discrete set of values (N=2, 3, 4, 6, 7, 10, 17), which satisfy the constraints of w, f, size of the pixel and that the number of stripes in each sections is to be odd (we consider the geometry shown in

chapter III). The value of L_0 is the sum of the kinetic inductance of each meander L_{kin} and of a series inductance which can be eventually added. L_{kin} is not a design parameter, as it is fixed by w, t, f, A_d and N. If no series inductors are added (bare devices, $L_0=L_{kin}$), the value of L_0 for each N is listed in Table 2.

Table 2. Inductance (L_0) and number of squares (SQ) of each section for all possible values of N. The width of the nanowires is w=100 nm, the thickness is t=4 nm. The kinetic inductance per square was estimated ($L_{kin}/\square$=90 pH) from the time constant of the exponential decay of the output current ($\tau_{out}=\tau_f=L_{kin}/R_{out}$, see sec. 4.3) for a standard 5x5μm^2 SSPD.

N	L_0	SQ
2	225 nH	2500
3	153 nH	1700
4	117 nH	1300
6	81 nH	900
7	63 nH	700
10	45 nH	500
17	27 nH	300

An additional free parameter, relative to the read-out, is the impedance seen by the device on the RF section of the circuit R_{out}, which is 50 Ω (of the matched transmission line) in the actual measurement setup (see chapter II), but which can be varied in principle from zero to infinite introducing a cold preamplifier stage.
The target performance specifications are the single-photon detection efficiency (η), the signal to noise ratio and the maximum repetition rate (speed), which must be optimized under the constraints that the operation of the device is stable and that it is possible to detect a certain maximum number of photons (n_{max}) dependent on the specific application.

This section is organized as follows. First we present the electrical equivalent model of the device developed in order to study its working principle and to define design guidelines (section 4.1). Then then figures of merit of the device performance in terms of efficiency (section 4.2), speed (section 4.3) and sensitivity (section 4.4) are defined and their dependency on the design parameters (L_0, R_0, R_{out}, N) is analyzed.

4.1.Electrical model

A comprehensive description of PND operation should combine thermal and electrical modeling of the nanowires [19]. In this work, a purely electrical model has been used to make a reliable guess on how the performance of the device varies when moving in the parameter space.
The time evolution of the device after the absorption of a photon was simulated using the equivalent circuit of
Figure **4.1**a ([20], see also chapter I). Each section is modeled as the series connection of a switch which opens on the hotspot resistance R_{HS} for a time t_{HS}, simulating the absorption of a photon, of an inductance L_{kin}, accounting for kinetic inductance [21] and of a resistor R_0. The device is connected through a bias T to the bias voltage source V_B and to the input resistance of the preamplifier R_{out}. The n firing sections, in pink, all carry the same current I_f and the N-n still superconducting sections (unfiring), in green, all carry the same current I_u. I_{out} is the current flowing through R_{out}.

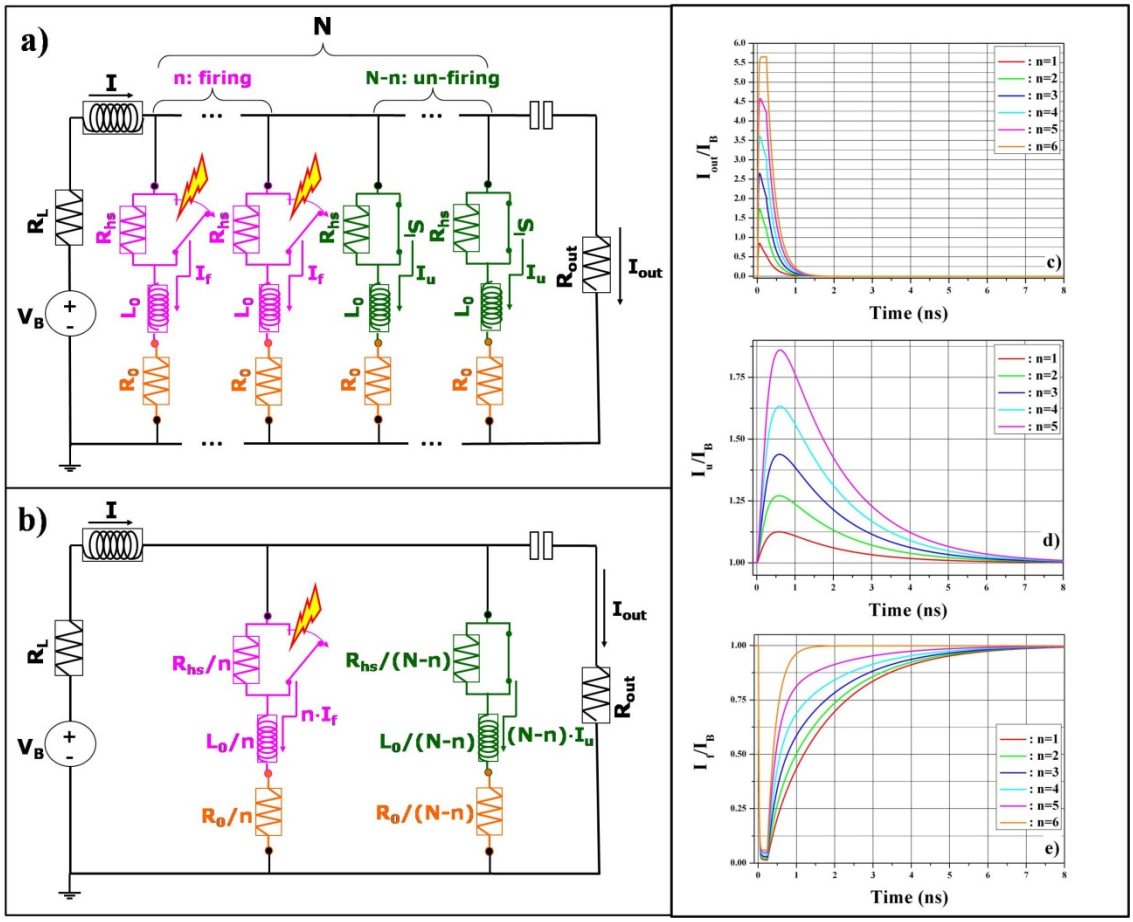

Figure 4.1. a. Circuit equivalent of a N-PND-R. The n firing sections, in pink, all carry the same current and the N-n still superconducting sections (unfiring), in green, all carry the same current I_u. I_{out} is the current flowing through the input resistance R_{out} of the preamplifier. b. Simplified circuit of a N-PND-R, where the two sets of n firing and the N-n unfiring sections have been substituted by their Thévenin-equivalents. (c-e) Simulated time evolution of I_u (c), I_{out} (d) and I_f (e) for a 6-PND-R as n increases from 1 to 6. The parameters of the circuit are: L_0=L_{kin}=81 nH, R_0=50 Ω, R_{out}=50 Ω, R_{HS}=5.5 kΩ, and t_{HS} =250ps.

In this model, the dependence of L_{kin} on the current flowing through the nanowire was disregarded, and it was assumed constant. Furthermore, it has been shown [19] that changing the values of the kinetic inductance of an SSPD or of a resistor connected in series to it results in a change of the hotspot resistance and of its lifetime, eventually causing the device to latch to the normal state. The simplified analysis presented here does not take into account these effects, and considers both R_{HS} and t_{HS} as constant (R_{HS}=5.5 kΩ, t_{HS} =250ps [19]), and that device cannot latch. However, the results of this approach can still quantitatively predict the behavior of the device in the limit where the fastest time constant of the circuit τ_f (see section 4.3) is much slower than the hotspot lifetime ($\tau_f >> t_{HS}$), and give a reasonable qualitative understanding of the main trends of variation of the performance of faster devices ($\tau_f \sim t_{HS}$).

In order to gain a better insight on the circuit dynamics (see sec. 4.3) and to reduce the calculation time, the N+1 mesh circuit of figure 4.1a can be simplified to the three mesh circuit of figure 4.1b applying the Thévenin theorem on the n firing sections and on the remaining N-n still superconducting (unfiring) sections, separately.

Figure 4.1c to e show the simulation results for the time evolution of the currents flowing through R_{out} and through the unfiring (I_u) and firing (I_f) sections of a PND with 6 sections and integrated resistors (6-PND-R), for the number of firing sections n ranging from 1 to 6. As n increases, the peak values of the output current (I_{out}, figure 4.1c) and of the current through the unfiring sections (I_u, figure 4.1d)

increase. The firing sections experience a large drop in their current (I_f, figure 4.1e), which is roughly independent on n. The observed temporal dynamics will be examined in the following sections.

4.2.Current redistribution and efficiency

Let $\overline{\delta I}_{lk}^{(n)}$ be the peak value of the leakage current drained by each of the still superconducting (unfiring) nanowires when n sections fire simultaneously. The stability requirement translates in the condition that for each unfiring section $I_B + \overline{\delta I}_{lk}^{(n_{max})} \leq I_C$ (as the leakage current increases with n, $\overline{\delta I}_{lk}^{(n_{max})}$ represents the worst case). This limits the bias current and therefore the single-photon detection efficiency (η), which, for a certain nanowire geometry (i.e. w, t fixed), is a monotonically increasing function of I_B/I_C (chapter I, [22]). For instance, in order to detect a single photon (at λ=1.3 μm, T=1.8K) in a section with an efficiency equal to 80% of the maximum value set by absorption (~32%, [15]), $\overline{\delta I}_{lk}^{(n_{max})}$ should be made ≤33% of I_B. Therefore the leakage current strongly affects the performance of the device and it is to be minimized, which makes it very important to understand its dependency from the design parameters: $\overline{\delta I}_{lk}^{(n)}\left(N, L_0, R_0, R_{out}\right)$.

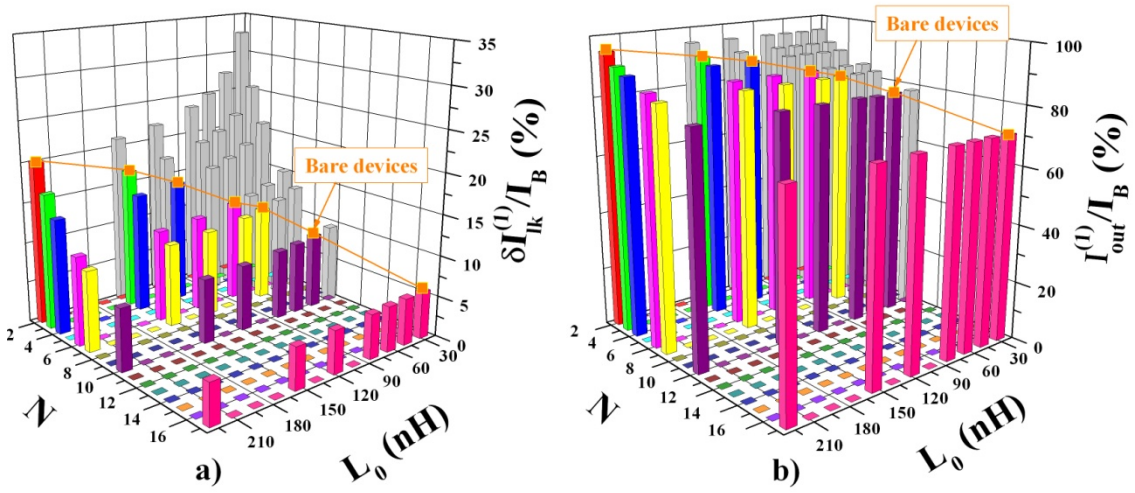

Figure 4.2. Peak value of the leakage current $\overline{\delta I}_{lk}^{(1)}$ drained by each of the still superconducting (unfiring) nanowires (a) and of the output current $\overline{I}_{out}^{(1)}$ (b) when only one section fires, plotted as a function of the number of sections in parallel N and of the value of the inductance of each section L_0. The value of the series resistor R_0 and of the output resistor R_{out} is 50 Ω. The orange line highlights bare devices, the colored bars correspond to devices which respect the constraints on the geometry of the structure while the grey bars refer to purely theoretical devices which just show the general trend. The leakage current and the output current are expressed in % of the bias current I_B because they are proportional to it.

The leakage current for n=1 is first investigated and its dependency on n is then presented for some particular combinations of design parameters. The dependency of $\overline{\delta I}_{lk}^{(1)}$ on N and L_0 at fixed R_0 and R_{out} (both equal to 50 Ω) is shown in figure 4.2a: an orange line highlights bare devices ($L_0=L_{kin}$, see Table 2) and the colored bars are relative to devices which respect the constraints on the geometry of the structure ($L_0>L_{kin}$), while the grey bars refer to purely theoretical devices which just show the general trend. For any N, the current redistribution increases as L_0 decreases, as the impedance of each

section decreases. Keeping L_0 constant, $\overline{\delta I}_{lk}^{(1)}$ decreases with increasing N, as the current to be redistributed is fixed and the number of channels draining current increases. For this reason, also the increase of redistribution with decreasing L_0 becomes weaker for high N.

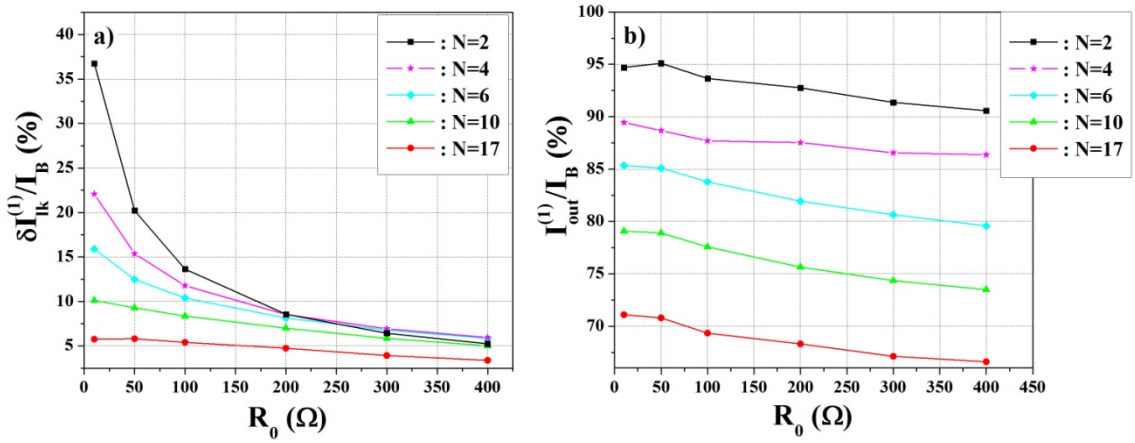

Figure 4.3. (a) Variation of the peak value of the leakage current per unfiring section of some bare devices for n=1 ($\overline{\delta I}_{lk}^{(1)}$) as the resistance of the series resistor R_0 varies from 10 Ω to 400 Ω. (b) Peak value of the output current for n=1 ($\bar{I}_{out}^{(1)}$) as a function of R_0 for some bare devices.

The dependency of $\overline{\delta I}_{lk}^{(1)}$ on R_0 is shown in figure 4.3a for some bare devices and R_{out}=50 Ω. As expected, the redistribution decreases as R_0 increases because the impedance of each section increases with respect to the output resistance. For the same reason, $\overline{\delta I}_{lk}^{(1)}$ is strongly reduced (to ~3% of I_B) when R_{out} is decreased of one order of magnitude from 50 to 5 Ω, keeping R_0 constant (figure 4.4a).

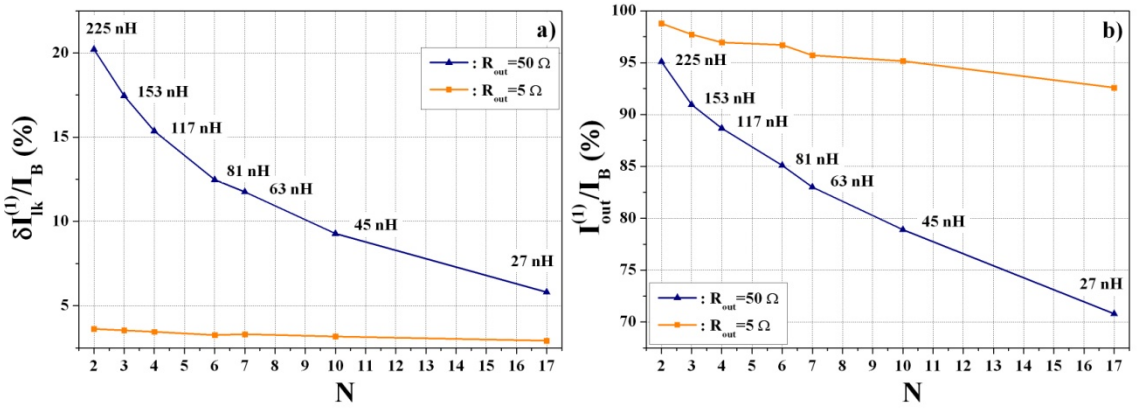

Figure 4.4. Variation of the peak value of the leakage current per unfiring section (a) and of the output current (b) of the set of bare devices for n=1 ($\overline{\delta I}_{lk}^{(1)}$ and $\bar{I}_{out}^{(1)}$, respectively) as the resistance of the output resistor R_{out} decreases of one order of magnitude from 50 to 5 Ω (in blue and orange, respectively), while R_0=50 Ω.

The variation of the leakage current with the number of firing stripes n ($\overline{\delta I}_{lk}^{(n)}$) for the set of bare devices is presented in figure 4.5a. The dependency is superlinear ($\overline{\delta I}_{lk}^{(n)} > n\overline{\delta I}_{lk}^{(1)}$), as the current to be redistributed per firing stripe is always the same (see sec. 4.4), but the number of channels draining

current decreases. Furthermore, as expected, the curves for different design parameter sets never cross, which means that all the design guidelines presented in Figure 4.3a, Figure 4.4a, Figure 4.5a for n=1 still apply for higher n.

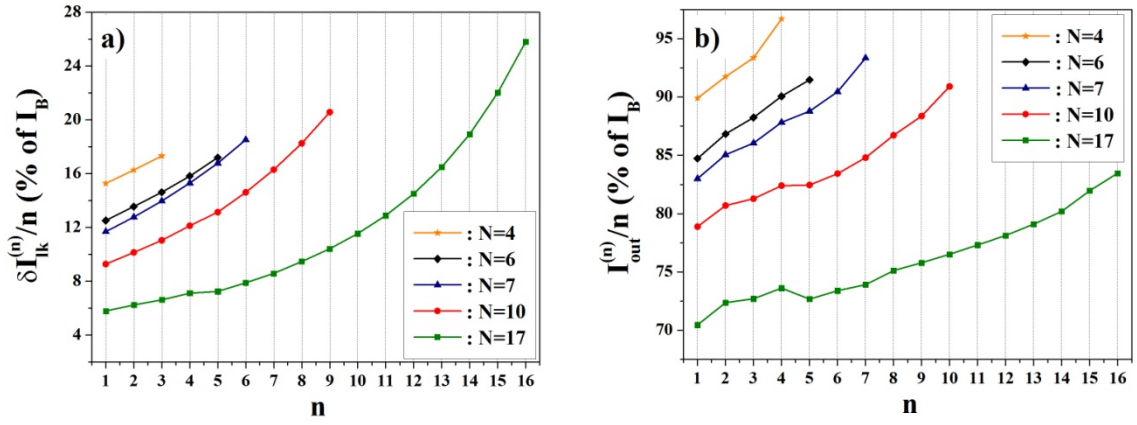

Figure 4.5. Variation of the leakage current $\overline{\delta I_{lk}}^{(n)}$ (a) and of the output current $\overline{I}_{out}^{(n)}$ (b) with the number n of firing stripes for the set of bare devices.

In conclusion, the result of this simplified analysis is that, in order to minimize the leakage current and thus maximize the efficiency, N, L_0 and R_0 must be made as high as possible and R_{out} as low as possible. We note however that R_0 cannot be increased indefinitely to avoid that the nanowire latches to the hotspot plateau before I_B reaches I_C (see chapter IV).

4.3.Transient response and speed

Before proceeding to the analysis of the SNR and speed performances of the device, it is necessary to discuss the characteristic recovery times of the currents in the circuit.

The transient response of the simplified equivalent electrical circuit of the N-PND (figure 4.1b) to an excitation produced in the firing branch can be easily found analytically. Therefore, the transient response of the current through the firing sections I_f, through the unfiring sections I_u and through the output I_{out} after the nanowires become superconducting again ($t \geq t_{HS}$) can be written as:

$$\begin{cases} I_f \propto \dfrac{N-n}{N}\exp\left(-t/\tau_s\right)+\dfrac{n}{N}\exp\left(-t/\tau_f\right) \\ I_u \propto \exp\left(-t/\tau_s\right)-\exp\left(-t/\tau_f\right) \\ I_{out} \propto \exp\left(-t/\tau_f\right) \end{cases} \qquad (3)$$

where $\tau_s=L_0/R_0$ and $\tau_f=L_0/(R_0+NR_{out})$ are the "slow" and the "fast" time constant of the circuit, respectively.

This set of equations describes quantitatively the time evolution of the currents after the healing of the hotspot in the case $\tau_f >> t_{HS}$, and it provides a qualitative understanding of the recovery dynamics of the circuit for shorter τ_f.

The recovery transients ($t \geq t_{HS}$) of I_{out}, δI_{lk} and I_f for a 4-PND-R simulated with the circuit of figure 4.1b are shown in figure 4.6a, b, c, respectively (in blue) for different number of firing sections (n=1

to 4). As n increases from 1 to 4, the recoveries of I_{out} and δI_{lk} change only by a scale factor. On the other hand, the transient of I_f depends on n and becomes faster increasing n, as qualitatively predicted by the first of equations (3). Indeed, I_f consists in the sum of a slow and a fast contribution, whose balance is controlled by the number of firing sections n. To prove the quantitative agreement with the analytical model in the limit $\tau_f >> t_{HS}$, the simulated transients of I_{out}, δI_{lk} and I_f have been fitted (figure 4.6a, b, c, respectively, in orange) using the set of equations (3) and four fitting parameters (τ_s, τ_f, a time offset t_0 and a scaling factor K). The values of τ_s and τ_f obtained from the three fittings (of I_{out}, of δI_{lk} and of the whole set of four I_f for n=1,…, 4) closely agree with the values calculated from the analytical expressions presented above and the parameters of the circuit (τ_s^*=2.30 ns ,τ_f^*=460 ps).

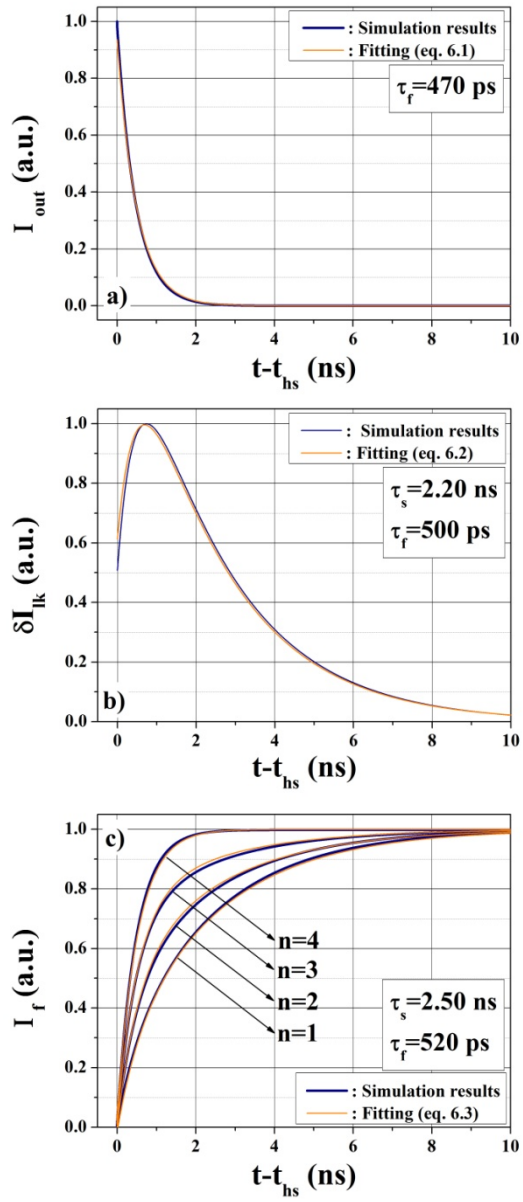

Figure 4.6. Recovery transients ($t \geq t_{HS}$) of I_{out} (a), δI_{lk} (b), and I_f (c) for a 4-PND-R as n increases from 1 to 4. The simulated transients are in blue, the fitted curves are in orange. The parameters of the circuit used for the simulations are: $L_0=L_{kin}$=117 nH, R_0=50 Ω, R_{out}=50 Ω, R_{HS}=5.5 kΩ, and t_{HS}=250ps. The three sets of curves are fitted by equations (3) (multiplied by K, and shifted by t_0), where the values of τ_s and τ_f are shown in the insets.

In order to quantify the speed of the device, we take $f_0=(t_{reset})^{-1}$ as the maximum repetition frequency, where t_{reset} is the time that I_f needs to recover to 95% of the bias current after a detection event.

According to the results presented above, which are in good agreement with experimental data (figure 3.1b), I_{out} decays exponentially with the same time constant for any n ($\tau_{out}=\tau_f$), which, for a bare N-PND, is N^2 times shorter than a normal SSPD of the same surface [15, 16]. This however does not relate with the speed of the device. Indeed, t_{reset} is the time that the current through the firing sections I_f needs to rise back to its steady-state value ($I_f \sim I_B$). In the best case of n=N, I_f rises with the fast time constant τ_f, but in all other cases the slow contribution becomes more important as n decreases (see figure 4.1e and figure 4.6c), until, for n=1, I_f is roughly $\propto \left[1-\exp\left(-t/\tau_s\right)\right]$. The speed performance of the device is then limited by the slow time constant ($t_{reset} \sim 3\cdot\tau_s$), which means that an N-PND is only N times faster than normal SSPD of the same surface, being as fast as a normal SSPD whose kinetic inductance is the same as one of the N section of the N-PND.

Figure 4.7 shows the dependence of f_0 on L_0 and R_0. For $\tau_s<t_{HS}$ (i.e. $f_0>4$ GHz in our model) the speed of the device may be limited by the hotspot temporal dynamics, and so no reliable predictions can be made using our simplified model.

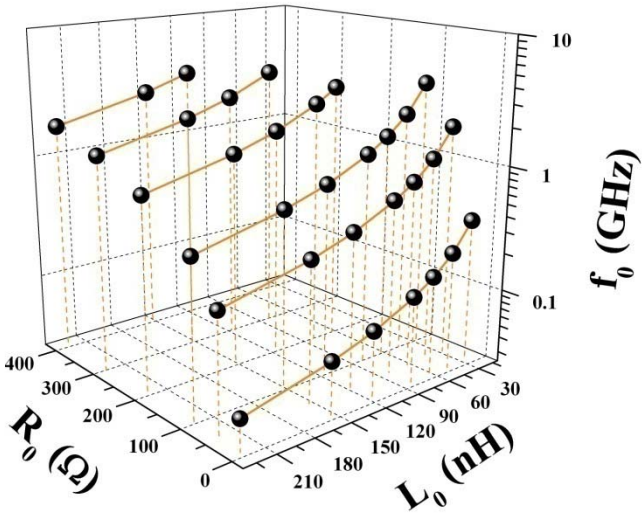

Figure 4.7. Dependence of f_0 on L_0 and R_0. No data are presented for $f_0>4$ GHz, where no reliable predictions can be made using this simplified model.

4.4.Signal to noise ratio

The peak value and the duration of the output current pulse are a function of the design parameters (see below and section 4.3, respectively). As the output pulse becomes faster, amplifiers with larger bandwidth are required and thus electrical noise become more important. In order to assess the possibility to discriminate the output pulse from the noise, we define the signal to noise ratio (SNR) as the ratio between the maximum of the output current $\bar{I}_{out}$ and the rms value of the noise-current at the preamplifier input I_n, $SNR=\bar{I}_{out}/I_n$.

The peak value of the output current when n sections fire simultaneously (see figure 4.1c, relative to a 6-PND-R) can be written as:

$$I_{out}^{(n)} = n\left(I_B - I_f^{(n)*}\right) - \left(N-n\right)\delta I_{lk}^{(n)*}$$

where the starred values refer to the time $t=t^*$ when the output current peaks.
As n=1 represents the worst case, in order to evaluate the performance of the device in terms of the SNR, the dependency of $\bar{I}_{out}^{(1)}$ from the design parameters is investigated: $\bar{I}_{out}^{(1)}\left(N, L_0, R_0, R_{out}\right)$. The dependency of $\bar{I}_{out}^{(1)}$ on N and L_0 at fixed R_0 and R_{out} (both equal to 50 Ω) is shown in figure 4.2b. Inspecting the values of $\bar{I}_{out}^{(1)}$ and of $\overline{\delta I}_{lk}^{(1)}$ for the same device in figure 4.2, it becomes clear that they add up to a value well above to I_B, which is due to the fact that the output current and of the leakage current peak at two different times t* and t_{lk}, respectively (figure 4.1). Furthermore, as $t_{lk}>t^*$, the output current is not significantly affected by redistribution, because I_{out} is maximum when δI_{lk} is still beginning to rise.
The expression for t_{lk} can be derived from (3): $t_{lk}=L_0/(N\cdot R_{out})\ln(1+N\cdot R_{out}/R_0)$, which means that increasing the device speed (decreasing L_0 or R_0, N or R_{out}) makes the redistribution faster and then $\bar{I}_{out}^{(1)}$ lower.

So, for any given N, $\bar{I}_{out}^{(1)}$ decreases (figure 4.2b) with decreasing L_0, both because $\overline{\delta I}_{lk}^{(1)}$ is higher and because t_{lk} is lower. Keeping L_0 constant, $\bar{I}_{out}^{(1)}$ decreases with increasing N because even though $\overline{\delta I}_{lk}^{(1)}$ decreases, the redistribution peaks earlier and the number of channels draining current increases.

The dependency of $\bar{I}_{out}^{(1)}$ on R_0 is shown in figure 4.3b for some bare devices and R_{out}=50 Ω. Even though $\overline{\delta I}_{lk}^{(1)}$ decreases as R_0 increases (figure 4.3a), the output current decreases due to the redistribution speed-up (decrease of t_{lk}): $\delta I_{lk}^{(1)*}$ increases despite of the decrease of the peak value of the leakage current. On the other hand, a decrease in R_{out} makes the redistribution much less effective, as t_{lk} decreases slower with decreasing R_{out} than with increasing R_0. Indeed, as shown in figure 4.4b for bare devices, $\bar{I}_{out}^{(1)}$ significantly increases when R_{out} is decreased by one order of magnitude from 50 to 5 Ω, keeping R_0 constant.
In conclusion, in order to maximize the output current, N, R_0 and R_{out} must be minimized, while L_0 must be made as high as possible.

The rms value of noise-current at the preamplifier input I_n can be written as $I_n=\sqrt{S_n\Delta f}$, where S_n is the noise spectral power density of the preamplifier and Δf is the bandwidth of the output current I_{out}, which is estimated as $\Delta f=1/\tau_{out}$, where $\tau_{out}=\tau_f=L_0/(R_0+NR_{out})$ is the time constant of the exponential decay of I_{out} (see sec. 4.3). I_n is then a function of the parameters of the device and of the read-out through S_n and τ_f, and like I_{out} it is minimized minimizing N, R_0 and R_{out} and maximizing L_0.
The same optimization criteria apply then naturally to the SNR. The dependence of the SNR from N and L_0 is shown in figure 4.8 for cryogenic (77 K working temperature, in blue) and room-temperature amplifiers (in yellow). Amplifiers with different -3 dB bandwidths have been considered, depending on the bandwidth of the output current pulse that they were supposed to amplify. Depending on the amplifier bandwidth, noise figures of F=0.44 to 1.8 dB (F=1.1 to 5 dB) have been considered in the calculation of Sn for the room-temperature (cryogenic) amplifier. The input resistance is Rout=50Ω.

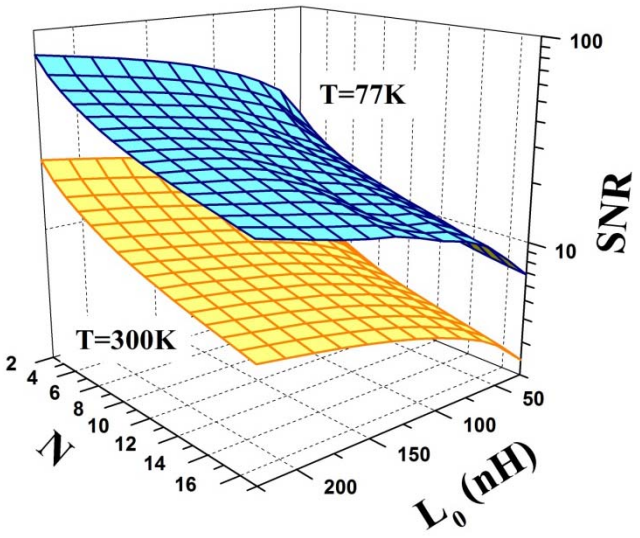

Figure 4.8. SNR as a function of N and L_0 relative to commercially available cryogenic (77 K working temperature, in blue) and room-temperature amplifiers (in yellow). For the cryogenic amplifiers the following noise figures were used, relative to different -3 dB bandwidths: F=0.44 dB (Δf=0.1-4 GHz), F=1.3 dB (Δf=0.5-20 GHz), F=1.8 dB (Δf=0.5-40 GHz). For the room-temperature amplifiers: F=1.1 dB (Δf=0.1-4 GHz), F=2.13 dB (Δf=0.1-20 GHz), F=5 dB (Δf=0.1-40 GHz).

The main design guidelines which can be deduced from the analysis of sections 4.2 to 4.4 are summarized in Table 3. The type of dependency of $\overline{\delta I_{lk}}$, f_0, $\bar{I}_{out}$ and I_n from the design parameters (L_0, R_0, R_{out}, N) is indicated.

Table 3. Dependency of the figures of merit from the design parameters: increasing with increasing the parameter (↗), decreasing with increasing the parameter (↘), independent (—).

	L_0	R_0	R_{out}	N
δI_{lk}	↘	↘	↗	↘
f_0	↘	↗	—	—
I_{out}	↗	↘	↘	↘
I_n	↘	↗	↗	↗

5. Application to the measurement of photon number statistics

We wish to determine whether the PND can be used to measure an unknown photon number probability distribution **S** (see section 3.2). Indeed, the light statistics measured with a PND differ from the original one due to non-idealities such as the limited number of sections and limited and non-uniform efficiencies (η_i) of the different sections.

In this section, we present the modeling tools (section 5.1) used to fully characterize the device (section 5.2) and to develop an algorithm to estimate the photon number statistics of an unknown light (section 5.3).

5.1.Modeling and simulation

i. Analytical model

Equation (1) may be rewritten in a matrix form as $\mathbf{Q}=\mathbf{P}^{\mathbf{N}}\cdot\mathbf{S}$, where $P^N=\left[P^N\left(n|m\right)\right]=\left[p^N_{nm}\right]$ is the matrix of the conditional probabilities of an N-PND. Assuming that the illumination of the device is uniform, the parallel connection of N nanowires can be considered equivalent to a balanced lossless N-port beam splitter, every channel terminating with a single photon detector (SPD) (Figure 5.1a). Each incoming photon is then equally likely to reach one of the N SPDs (with a probability 1/N). Each SPD can detect a photon with a probability η_i (i=1,..,N) different from all the others, and gives the same response for any number (n≥1) of photons detected (Figure 5.1b). The number of SPDs firing then gives the measured photon number. Following [13], two classes of terms in P^N can be calculated directly, the others being derived from these by a recursion relation. These terms are the probabilities $p^N_{m,m}$ that all the m≤N photons sent are detected and $p^N_{0,m}$ that no photons are detected when m are sent.

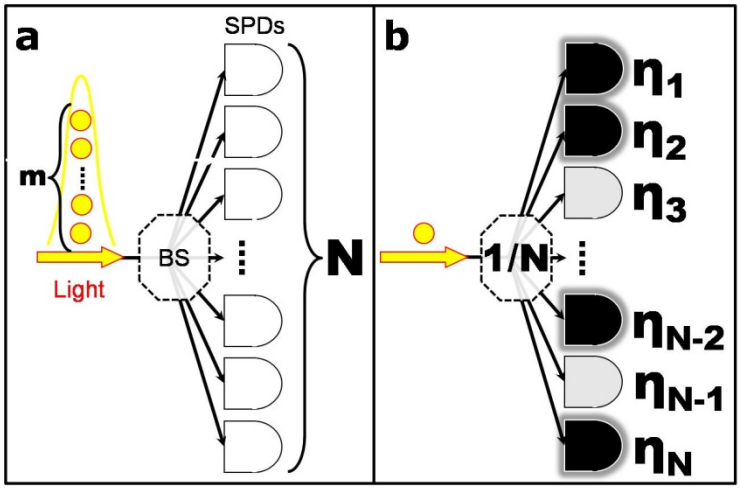

Figure 5.1. Optical equivalent of an N-PND. a. The parallel connection of N nanowires is equivalent to a balanced lossless N port beam splitter (BS), every channel terminating with a single photon detector (SPD). b. k^{th} possible configuration of n firing (in black) and N-n unfiring (in grey) sections. Each incoming photon is equally likely to reach one of the N SPDs (with a probability 1/N). Each SPD can detect a photon with a probability η_i (i=1,..,N) different from all the others, and it gives the same response for any number (n≥1) of photons detected.

In the case of zero detections, $p^N_{0,m}$ is given by:

$$p^N_{0,m}=\sum_{i_1=1,\ldots,i_m=1}^{N}\left[\frac{1-\eta_{i_1}}{N}\cdot\ldots\cdot\frac{1-\eta_{i_m}}{N}\right] \qquad (4)$$

which assumes that a photon incident in the i-th nanowire fails to be detected with an independent probability of $(1-\eta_i)$. The sum in (4) accounts for all the possible combinations when taking m elements in an ensemble of N with order and with repetition (permutations with repetitions). This because more than one photon can hit the same stripe (which gives the repetition), and the photons are considered distinguishable (which gives the order). The sum has then N^m terms. If all the stripes are the same ($\eta_i=\eta$), (4) reduces to (A1) in [13].

In the case that all the photons are detected, since m photons must reach m distinct nanowires:

$$p_{m,m}^{N} = \sum_{\substack{i_1=1,\ldots,i_m=1 \\ i_p \neq i_q \text{ for } p\neq q}}^{N} \left[\frac{\eta_{i_1}}{N} \cdot \ldots \cdot \frac{\eta_{i_m}}{N} \right] \quad \text{for } m \leq N \qquad (5)$$

The sum in (5) accounts for all the possible combinations when taking m elements in an ensemble of N with order and without repetition (permutations without repetitions). This because only one photon can hit the same stripe (which gives the non-repetition), and the photons are considered distinguishable (which gives the order). The sum has then N!/(N-m)! terms. If all the stripes are the same ($\eta_i=\eta$) (5) reduces to (A2) in [13].

The recursion relation for p_{nm}^{N} is:

$$\begin{aligned} p_{nm}^{N} = {} & p_{n,m-1}^{N} \left[\frac{n}{N} + \frac{n!}{N!} \cdot \sum_{\substack{i_1=1,\ldots,i_{N-n}=1 \\ i_p \neq i_q \text{ for } p\neq q}}^{N} \left(\frac{1-\eta_{i_1}}{N} + \ldots + \frac{1-\eta_{i_{N-n}}}{N} \right) \right] + \\ & + p_{n-1,m-1}^{N} \left[\frac{(n-1)!}{N!} \cdot \sum_{\substack{i_1=1,\ldots,i_{N-(n-1)}=1 \\ i_p \neq i_q \text{ for } p\neq q}}^{N} \left(\frac{1-\eta_{i_1}}{N} + \ldots + \frac{1-\eta_{i_{N-(n-1)}}}{N} \right) \right] \end{aligned} \qquad (6)$$

The first term on the right-hand side of (6) is the probability that n photons are detected when m-1 are sent, times the probability that the m^{th} photon reaches one of the n nanowires already occupied (first term in the square brackets) or that it fails to be detected reaching one of the N-n unoccupied nanowires (second term in the square brackets). To clarify how the latter probability is derived, it is sufficient to consider a particular configuration k (see Figure 5.1b) of n firing stripes (which have already detected a photon) and N-n unfiring stripes (still active). The probability that the incoming photon will not be detected when incident on any of the N-n unfiring stripes is then written as:

$$p_k = \frac{1-\eta_{i_1}}{N} + \ldots + \frac{1-\eta_{i_{N-n}}}{N} \qquad (7)$$

where $i_1 \ldots i_{N-n}$ are the N-n stripes active in the k^{th} configuration of (n)firing-(N-n)unfiring stripes considered. So a mean must be calculated on all the possible (n)firing-(N-n)unfiring configurations for the N stripes. Let C be the number of all these configurations. The mean is then calculated summing C terms of the type (7), and dividing by C: $1/C \cdot \sum_{k=1}^{C} p_k$. C is the number of permutations without repetitions of N-n elements in an ensemble of N, and it is given by the binomial coefficient: $C=N!/\left(N-\left(N-n\right)\right)!=N!/n!$.

The second term on the right-hand side of (6) is the probability that n-1 photons are detected when m-1 are sent times the probability that the m^{th} photon reaches one of the N-(n-1) unoccupied nanowires and it is detected. In the limit $\eta_i=\eta$, the recursion relation agrees with that given in [13].

ii. Monte Carlo simulation

In order to prove the consistency of the analytical model, the probability distribution of the number of measured photons **Q** calculated from P^N by (1) was cross-checked with the $\mathbf{Q_{MC}}$ resulting from a Monte Carlo simulation. The input parameters of the simulation are the incoming photon number probability distribution **S**, the number of parallel stripes N, and the vector of the single-photon detection efficiencies of the different sections of the device $\boldsymbol{\eta}=[\eta_i]$. The probability distribution of the number of measured photons was calculated using the following algorithm:

1. All the N sections of the N-PND are marked as unfiring. The number of photons incident on the detector n is determined measuring a random variable with probability distribution **S**.
2. Each photon hits the i^{th} section with uniform probability (1/N). If this section has not already detected a photon, it will be marked as firing with a probability η_i.
3. The number n of firing sections is kept as the result of this iteration for statistical analysis.
4. Repeat step 1. to 3. for 10^6 times.

5.2.Matrix of conditional probabilities

It has been shown [23, 24] that an unknown incoming photon number distribution **S** can be recovered if **Q** and $\mathbf{P^N}$ are known.

Let an N-PND be probed with a light whose photon number probability distribution is **S**, and its output be sampled H times. The result of the observation can be of N+1 different types (i.e. 0,..., N stripes firing), so an histogram of the H events can be constructed, which can be represented by a (N+1)-dimensional vector $\mathbf{r}=[r_i]$, where r_i is the number of runs in which the outcome was of the i^{th} type. The expectation value of the statistics obtained from the histogram is $E[\mathbf{Q_{ex}}=\mathbf{r}/H]=\mathbf{Q}$.

Considering equations (4) to (6), it is clear that the matrix of the conditional probabilities of a N-PND depends only on the vector of the N single-photon detection efficiencies of the different sections of the device $\boldsymbol{\eta}=[\eta_i]$. The vector $\boldsymbol{\eta}$ can be determined from the statistics $\mathbf{Q_{ex}}$ measured when probing the device with a light of known statistics **S** as described in the following.

A 5-PND was tested with the coherent emission from a mode-locked Ti:sapphire laser under uniform illumination (in the cryogenic D-dipstick, see chapter II for details of the setup), whose photon number probability distribution is close to a poissonian and could be fully characterized by the mean photon number μ with a power measurement. To determine $\mathbf{Q_{ex}}$, histograms of the photoresponse voltage peak V_{pk} were built for values of μ ranging from ~1 to ~100. The signal from the device was sent to the 1 GHz oscilloscope, which was triggered by the synchronization generated by the laser unit. The photoresponse was sampled for a gate time of 5ps, making the effect of dark counts negligible. The discrete probability distribution $\mathbf{Q_{ex}}$ was reconstructed from the continuous probability density $q(V_{pk})$ fitting the histograms to the sum of 6 gaussian distributions (corresponding to the five possible pulse levels plus the zero level) and calculating their area (Figure 5.2).

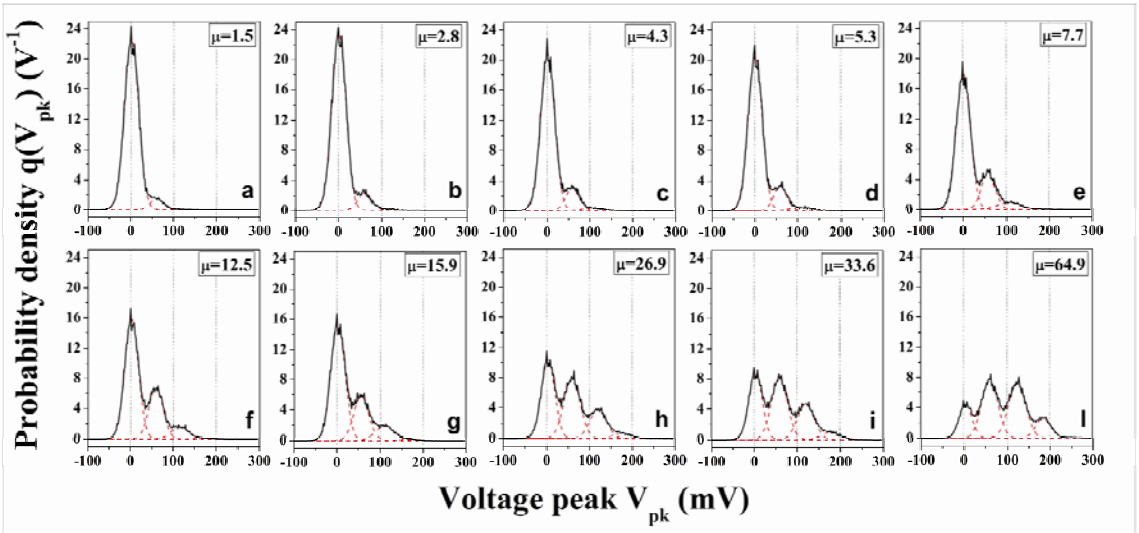

Figure 5.2. Histograms of the photoresponse voltage peak. Histograms were built by sampling the photoresponse of an 8.6x8 μm^2 5-PND. The device was tested under uniform illumination in the D-dipstick (see chepter II) dipped in a liquid He bath at 4.2 K. The light pulses at 700nm form the mode-lock Ti:sapphire laser were 40ps wide (after the propagation in the optical fiber) and the repetition rate was 80MHz. The average input photon number per pulse μ was set with a free space variable optical attenuator. Increasing μ, form 1.5 (a) to 64.9 (l), the shape of the histograms changes as the probability to observe higher response amplitudes increases. The solid lines are the experimental histograms. The dashed lines represent the fitted gaussian distribution of each possible pulse level.

The probability distribution of the number of measured photons **Q** (expressed by (1)) was then fitted to the experimentally measured distribution $\mathbf{Q_{ex}}$ using **η** as a free parameter (Figure 5.3). The resulting **η** and matrix of the conditional probabilities are shown in figure 5.4. The fitted efficiencies are rather uniform (2.9±0.5%), indicating a high-quality fabrication process.

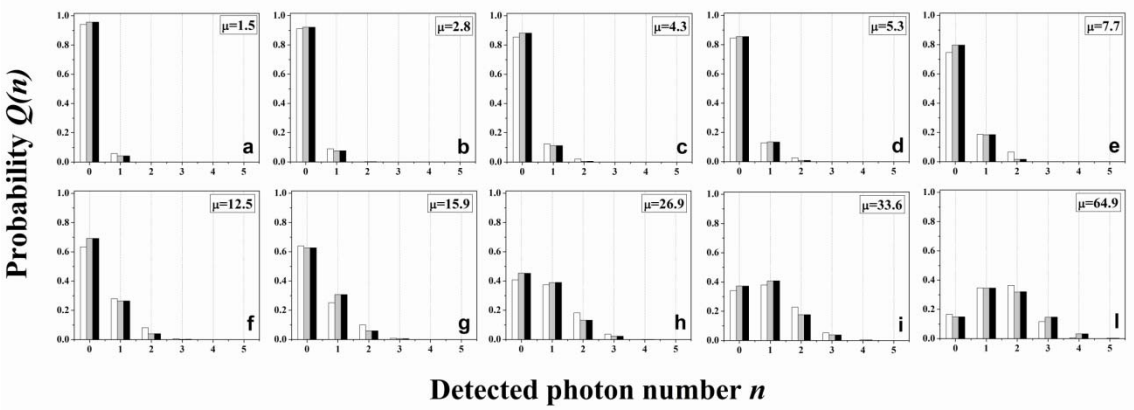

Figure 5.3. Experimental (Q_{ex}), fitted (Q) and simulated (Q_{MC}) probability distributions of the number of measured photons. The experimental probability distribution Q_{ex} (white bins) was estimated from the continuous probability density $q(V_{pk})$ of Figure 5.2. The 5-PND was probed with several incident mean photon numbers μ: 1.5, 2.8, 4.3, 5.3, 7.7, 12.5, 15.9, 26.9, 33.6, 64.9. The experimental values for Q_{ex} were then fitted (gray bins) using a genetic algorithm to recover the vector of detection efficiencies η. The value of η obtained was used to calculate Q_{MC} for each value of μ by Monte Carlo simulations (black bins).

The value of **η** obtained from the fitting was then used as an input parameter of Monte Carlo simulations (see above) used to calculate $\mathbf{Q_{MC}}$ for each value of μ. The three sets of values for the photocount statistics of six levels are in good agreement over almost two orders of magnitude of μ, confirming the validity of the analytical model.

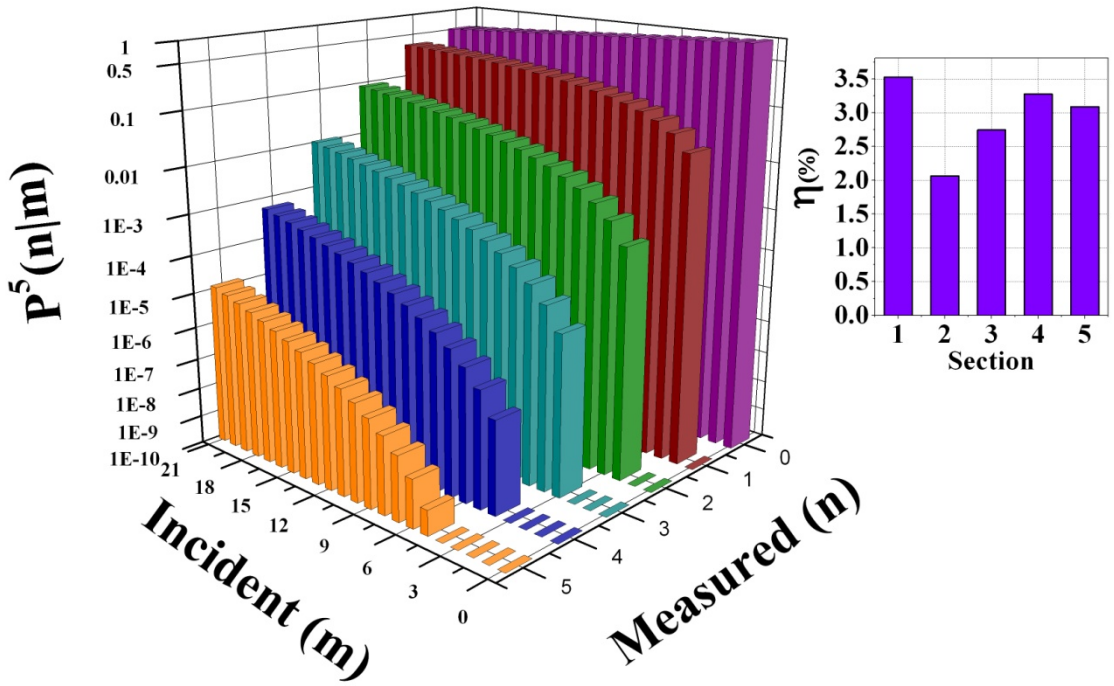

Figure 5.4. Conditional probability matrix for a 8.6x8 μm^2 5-PND (with no integrated series resistors), calculated from the vector η of the 5 single-photon detection efficiencies (relative to T=4.2 K, λ=700nm) of the different sections of the device (inset).

5.3.Maximum-Likelihood (ML) estimation

i. ML method

The $\mathbf{P^N}$ matrix provides a full description of the detector. Once $\mathbf{P^N}$ is known, several approaches can be used to reconstruct **S** from the histogram **r**. In the case no assumptions on the form of **S** are made, the maximum likelihood (ML) method is the most suitable, as it is the most efficient in solving this class of problems [25].

Let $\mathbf{R}=R_0,\ldots, R_N$ be the random vector of the populations of the (N+1) different bins of the histogram after H observations. The joint probability density function $L(\mathbf{r}|\mathbf{Q})$ for the occurrence of the particular configuration $\mathbf{r}=r_0,\ldots, r_N$ of **R** is called the likelihood function of **r** and it is given by [25]:

$$L(\mathbf{r}|\mathbf{Q}) = H!\prod_{i=0}^{N}\frac{q_i^{r_i}}{r_i!} \qquad (8)$$

where $\mathbf{Q}=[q_i]$ is the probability distribution of the number of measured photons, i.e. the vector of the probabilities to have an outcome in the bin i (i=0,…, N) in a single trial.

Considering **Q** as a function of **S** through (1), we can rewrite the likelihood function of the vector **r**, depending on the parameter **S**:

$$L(\mathbf{r}|\mathbf{S}) = H!\prod_{i=0}^{N}\frac{\left(\sum_m p_{i,m}^N s_m\right)^{r_i}}{r_i!} \qquad (9)$$

which is then the probability of the occurrence of the particular histogram **r** when the incoming light has a certain statistics **S**.
As **r** is measured and then it is known, L(**r**|**S**) can be regarded as a function of **S** only, i.e. L(**r**|**S**) is the probability that a certain vector **S** is the incoming probability distribution when the histogram **r** is measured. The best estimate of the incoming statistics which produced the histogram **r** according to the ML method is the vector $\mathbf{S_e}$ which maximizes L(**r**|**S**), where **r** is treated as fixed. So, the estimation problem can in the end be reduced to a maximization problem.

ii. Description of the algorithm

For numerical calculations, it is necessary to limit the maximum number of incoming photons to m_{max} (in the following calculations, m_{max}=21). As **S** is a vector of probabilities, the maximization must be carried out under the constraints that the s_n are positive and that they add up to one. The positivity constraint can be satisfied changing variables: $s_n=\sigma_n^2$. Instead of L, we maximize the logarithm of L:

$$l(\mathbf{\Sigma}) = \ln\left(L(\Sigma)\right) = \ln(C) + \sum_{i=0}^{N} r_i \ln\left(\sum_{m=0}^{m_{max}} p_{i,m}^N \sigma_m^2\right) \qquad (10)$$

where $\mathbf{\Sigma}=[\sigma_n]$ and C is a constant.
The condition that the s_n add up to one can be taken into account using the Lagrange multipliers method: $F(\Sigma,\alpha)=l(\Sigma)-\alpha\left(\sum_{m=0}^{m_{max}}\sigma_m^2-1\right)$.

After developing [26] the set of m_{max}+2 gradient equations $\nabla F(\Sigma,\alpha)=0$, we obtain that α=H and that the set of m_{max}+1 nonlinear equations to be solved respect to Σ is:

$$\sigma_l\left[\sum_{i=0}^{N}\frac{r_i p_{i,l}^N}{\sum_{m=0}^{m_{max}} p_{i,m}^N\sigma_m^2} - H\right] = 0 \qquad (11)$$

for l=0,…, m_{max}. The set of equations (11) can be solved by standard numerical methods.

iii. ML reconstruction

To test the effectiveness of the reconstruction algorithm, a 8.6x8 μm^2 5-PND was tested with the coherent emission from a mode-locked Ti:sapphire laser. $\mathbf{Q_{ex}}$ was determined as described in section 5.2.

The device was already characterized in terms of its conditional probability matrix $\mathbf{P^5}$ (figure 5.4), so it was possible to carry out the ML estimation of the different incoming distributions with which the device was probed. Because of the bound on the number of incoming photons which is possible to represent in our algorithm (m_{max}=21) and as, for a coherent state, losses simply reduce the mean of the distribution, the ML estimation was performed considering $\mu^*=\mu/10$ and $\boldsymbol{\eta}^*=10\boldsymbol{\eta}$ (the efficiency of each section being lower than 10%)**.**

Figure 5.5 shows the experimental probability distribution of the number of measured photons $\mathbf{Q_{ex}}$ obtained from the histograms measured when the incoming mean photon number is μ=1.5, 2.8, 4.3 photons/pulse (figure 5.5 a, b, c respectively, in orange), from which the incoming photon number distribution is reconstructed. The ML estimate of the incoming probability distribution $\mathbf{S_e}$ is plotted in figure 5.5 d, e, f, (light blue), where it is compared to the real incoming probability distribution **S** (green). The estimation is successful only for low photon fluxes (μ=1.5, 2.8 figure 5.5 d, e) and it fails already for μ=4.3 (figure 5.5 f). In figure 5.5 a, b, c, $\mathbf{Q_{ex}}$ (orange) is compared to the ones obtained from **S** and $\mathbf{S_e}$ through relation (1) (**Q**, $\mathbf{Q_e}$ in green and light blue, respectively).

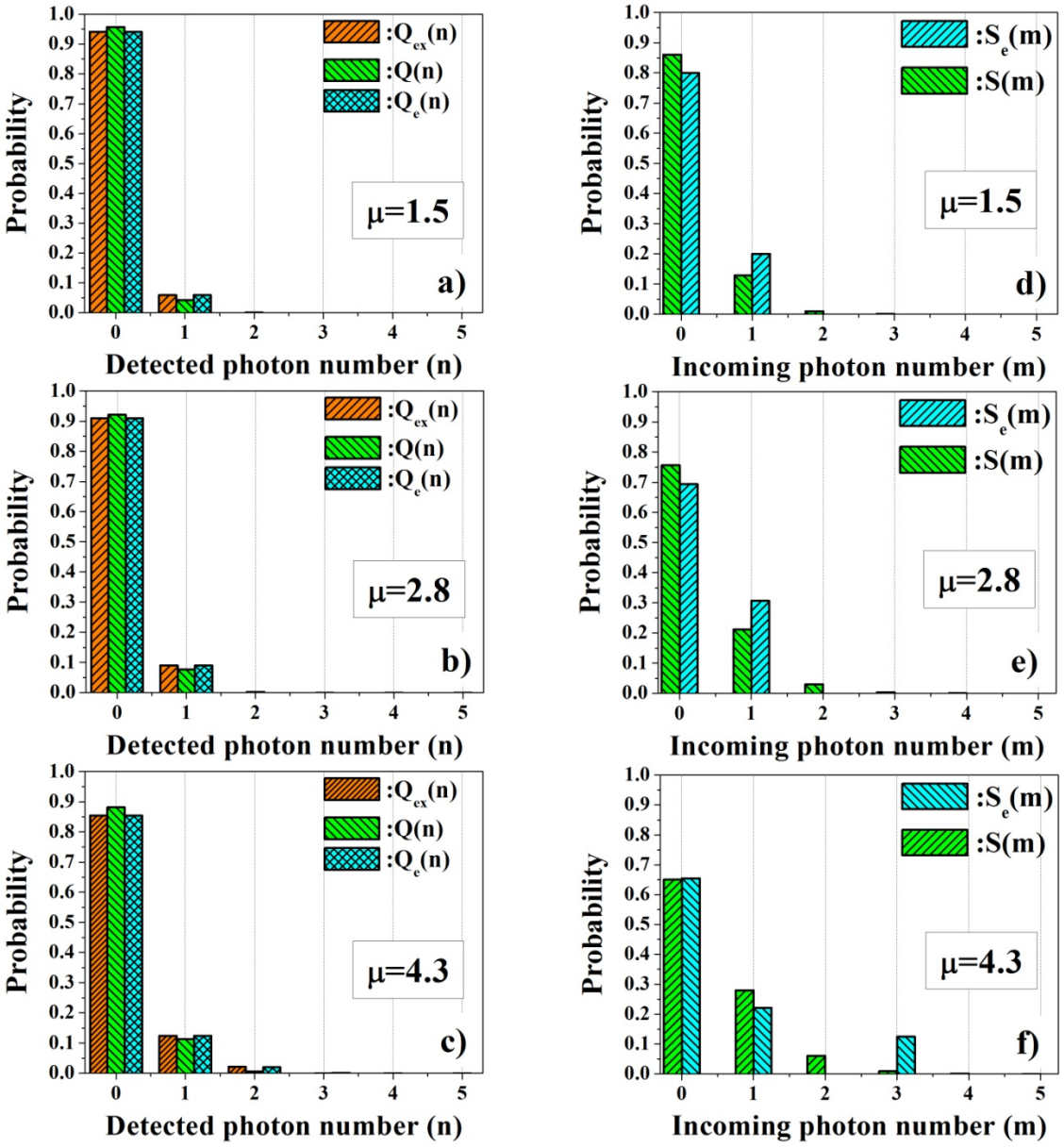

Figure 5.5. a, b, c. Probability distribution of the number of measured photons obtained from experimental data Q_{ex} (orange) from S (Q, in green) and S_e (Q_e, in light blue) through relation (1), for μ=1.5, 2.8, 4.3 photons/pulse, respectively. d, e, f. Real incoming probability distribution S (green) and its ML estimate S_e (light blue) for μ=1.5, 2.8, 4.3 photons/pulse, respectively. The 8.6x8 μm2 5-PND was tested under uniform illumination in the D-dipstick (see chater II) dipped in a liquid He bath at 4.2 K. The light pulses at 700nm form a mode-locked Ti:sapphire laser were 40ps wide (after the propagation in the optical fiber) and the repetition rate was 80MHz. The average input photon number per pulse μ was set with a free space variable optical attenuator.

The main reasons why the reconstruction fails are not the low efficiencies of the sections of the PND or the or the spread in their values, but rather the limited counting capability (N=5) and a poor calibration of the detector, i.e. an imperfect knowledge of its real matrix of conditional probabilities. This assessment is supported by the following argument. If we generate $\mathbf{Q_{ex}}$ with a montecarlo simulation (see section 5.1.ii) using the same $\boldsymbol{\eta}$ vector of Figure 5.4 and a poissonian incoming photon number distributions and then we run the ML reconstruction algorithm (using the same $\mathbf{P^5}$, which this time describes perfectly the detector), **S** can be estimated up to much higher mean photon numbers (μ≥16, see Figure 5.6). Additional simulations will be needed to evaluate the performance of PNDs for

the measurement of other, nonclassical photon number distributions. However, to alleviate this problem, a self-referencing measurement technique might be used [27].

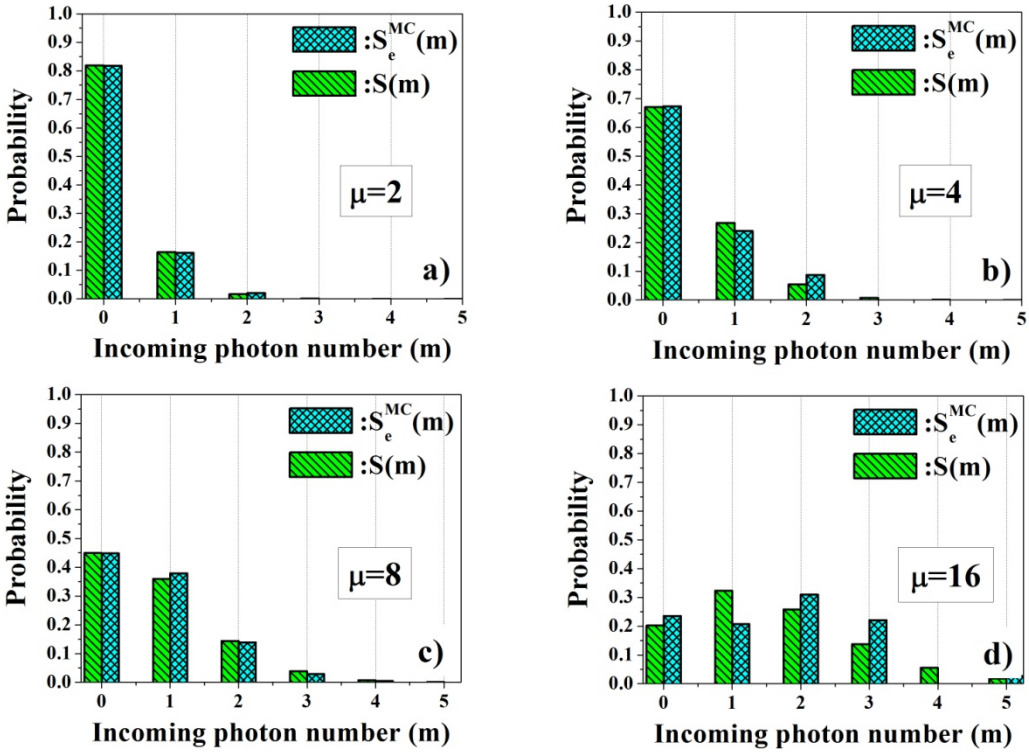

Figure 5.6. Real incoming probability distribution S (green) and its ML estimate S_e^{MC} (light blue), reconstructed from a Q_{ex} generated with a montecarlo simulation (see section 5.1.ii) using the same η vector of Figure 5.4 for μ=2 (a), 4 (b), 8 (c), 16 (d) photons/pulse.

6. Discussion on the counting capability

Several effects may limit the counting capability M_{max} of a PNR detector.

One is the detection efficiency. From (5), assuming the detector saturation is negligible (n<<N) and that all the branches are equal ($\eta_i=\eta$), the probability Q(n) of detecting n photons is proportional to η^n. In the PND tested $\tilde{\eta}$~2% at 1.3 μm (section 3.2), which we attribute to unoptimised film thickness and device design. This obviously prevents the application of the present device to n-photon states measurement for n>>1. Nevertheless, the η of SSPDs, which are based on the same detection mechanism, can be increased up to ~60% [18], and could potentially exceed 90% using optimized optical cavities. We also stress that uniform illumination of the wires is needed to achieve the optimum performance.

The second limitation is the intrinsic noise of the detector. As the currents from the sections of the PND are summed up to build the output, pulse height discrimination is used to achieve photon number resolution. This makes the noise performance of the device critical for its counting capability, as independent noisy signals are summed. Indeed, photon-number discrimination can be performed as long as the noise on the signal amplitude remains lower than the height of the one-photon pulse.

The noise properties of any avalanche-based photon counting device are limited by its inner multiplication noise. In other avalanche PNR detectors [1-3, 7-10] the amplitude of the output signal is

directly proportional to the number of carriers generated by single photon absorption events through a multiplication process which is intrinsically noisy. The noise on the multiplication gain is then completely transferred to the signal, which is then affected by a fluctuation of the same order. In contrast, with PNDs, the noisy avalanche carrier-multiplication process ([28] and chapter I) causes a fluctuation only in the resistance R_{HS} of the branch driven normal after the absorption of a photon and not in the output current. Indeed, the amplitude of the photocurrent peak is determined by the partition between the fluctuating resistance R_{HS} of few kΩ and a resistance R_{out} almost 2 orders of magnitude lower, which is of fixed value. Comparing the broadening of the histogram peaks relative to different numbers of detected photons n (Figure 5.2), no multiplication noise buildup is observable, as the variance of the peak does not increase with n. The broadening of the peaks is then exclusively due to electrical noise originating from amplifiers and is not a fundamental property of the detector. To a good approximation the excess noise factor F [29] of the PND is then close to unity and is not limiting M_{max}, which is not the case for most of the other approaches to PNR detection [1-3, 5, 7-10].
In PNDs, a third limitation to M_{max} arises from the leakage current δI_{lk}, which limits the bias current and therefore η. However, as discussed in section 4.2, this issue can be overcome with a careful design of the device.

7. Conclusions

A new PNR detector, the Parallel Nanowire Detector, has been demonstrated, which significantly outperforms existing approaches in terms of sensitivity, speed and multiplication noise in the telecommunication wavelength range. In particular (see Table 1), it provides a repetition rate (80 MHz) three orders of magnitude larger than any existing detector at telecom wavelength [1, 5, 11], and a sensitivity (NEP=$4.2\text{x}10^{-18}$ W/$\text{Hz}^{1/2}$) one-two orders of magnitude better, with the exception of transition-edge sensors [5] (which require a much lower operating temperature).
An electrical equivalent model of the device was developed in order to study its operation. The modeling predicts a physical limit to the reset time of the PND, which is lower than initially estimated. Furthermore, the figures of merit of the device performance in terms of efficiency, speed and sensitivity ($\overline{\delta I_{lk}}$, f_0, SNR) are defined and their dependency on the design parameters (L_0, R_0, R_{out}, N) is analyzed.
Additionally, we developed modeling tools to fully characterize the device and an algorithm to estimate the photon number statistics of an unknown light using the PND. The reconstruction proved to be successful only for low photon fluxes, most likely due to the limited counting capability and the poor calibration of the detector.
In conclusion, the PND, with its high repetition rate and high sensitivity, is suitable for measuring an unknown photon number probability distribution assuming accurate calibration and sufficient counting capability. Furthermore, by increasing the efficiency, the performance needed for the single-shot measurement of photon number can be reached. Finally, increasing the maximum photon number to 20-30 photons, the PND could be used as an “analog” detector with single-photon sensitivity, bridging the gap between conventional and single-photon detectors.

8. References

[1] M. Fujiwara, and M. Sasaki, Appl. Opt. **46**, 3069 (2007).
[2] E. J. Gansen, M. A. Rowe, M. B. Greene, D. Rosenberg, T. E. Harvey, M. Y. Su, R. H. Hadfield, S. W. Nam, and R. P. Mirin, Nature Photon. **1**, 585 (2007).
[3] B. E. Kardynal, S. S. Hees, A. J. Shields, C. Nicoll, I. Farrer, and D. A. Ritchie, Appl. Phys. Lett. **90**, 181114 (2007).
[4] A. E. Lita, A. J. Miller, and S. W. Nam, Opt. Express **16**, 3032 (2008).
[5] D. Rosenberg, A. E. Lita, A. J. Miller, and S. W. Nam, Phys. Rev. A **71**, 1 (2005).
[6] D. Fukuda, G. Fujii, A. Yoshizawa, H. Tsuchida, R. M. T. Damayanthi, H. Takahashi, S. Inoue, and M. Ohkubo, J. Low Temp. Phys. **151**, 100 (2008).
[7] G. Zambra, M. Bondani, A. S. Spinelli, F. Paleari, and A. Andreoni, Rev. Sci. Instr. **75**, 2762 (2004).
[8] E. Waks, E. Diamanti, B. C. Sanders, S. D. Bartlett, and Y. Yamamoto, Phys. Rev. Lett. **92**, 113602 (2004).
[9] E. Waks, K. Inoue, W. D. Oliver, E. Diamanti, and Y. Yamamoto, IEEE J. Sel. Top. Quant. **9**, 1502 (2003).
[10] K. Yamamoto, K. Yamamura, K. Sato, T. Ota, H. Suzuki, and S. Ohsuka, IEEE Nuclear Science Symposium Conference Record, 2006 **2**, 1094 (2006).
[11] L. A. Jiang, E. A. Dauler, and J. T. Chang, Phys. Rev. A **75**, 62325 (2007).
[12] D. Achilles, C. Silberhorn, C. S?liwa, K. Banaszek, and I. A. Walmsley, Opt. Lett. **28**, 2387 (2003).
[13] M. J. Fitch, B. C. Jacobs, T. B. Pittman, and J. D. Franson, Phys. Rev. A **68**, 043814 (2003).
[14] E. A. Dauler, B. S. Robinson, A. J. Kerman, J. K. W. Yang, K. M. Rosfjord, V. Anant, B. Voronov, G. Gol'tsman, and K. K. Berggren, IEEE Trans. Appl. Supercond. **17**, 279 (2007).
[15] G. Gol'tsman *et al.*, IEEE Trans. Appl. Supercond. **17**, 246 (2007).
[16] M. Tarkhov *et al.*, Appl. Phys. Lett. **92**, 241112 (2008).
[17] A. J. Miller, S. W. Nam, J. M. Martinis, and A. V. Sergienko, Appl. Phys. Lett. **83**, 791 (2003).
[18] K. M. Rosfjord, J. K. W. Yang, E. A. Dauler, A. J. Kerman, V. Anant, B. M. Voronov, G. N. Gol'tsman, and K. K. Berggren, Opt. Express **14**, 527 (2006).
[19] J. K. W. Yang, A. J. Kerman, E. A. Dauler, V. Anant, K. M. Rosfjord, and K. K. Berggren, IEEE Trans. Appl. Supercond. **17**, 581 (2007).
[20] A. J. Kerman, E. A. Dauler, W. E. Keicher, J. K. W. Yang, K. K. Berggren, G. Gol'tsman, and B. Voronov, Appl. Phys. Lett. **88**, 111116 (2006).
[21] A. M. Kadin, in Introduction to superconducting circuits, Wiley, New York, 1999, Chap 2.
[22] A. Verevkin, J. Zhang, R. Sobolewski, A. Lipatov, O. Okunev, G. Chulkova, A. Korneev, K. Smimov, G. N. Gol'tsman, and A. Semenov, Appl. Phys. Lett. **80**, 4687 (2002).
[23] H. Lee, U. Yurtsever, P. Kok, G. M. Hockney, C. Adami, S. L. Braunstein, and J. P. Dowling, J. Mod. Opt. **51**, 1517 (2004).
[24] D. Achilles, C. Silberhorn, C. Siliwa, K. Banaszek, I. A. Walmsley, M. J. Fitch, B. C. Jacobs, T. B. Pittman, and J. D. Franson, J. Mod. Opt. **51**, 1499 (2004).
[25] W. T. Eadie, D. Drijard, F. E. James, M. Roos, and B. Sadoulet, in Statistical Methods in Experimental Physics, North-Holland, Amsterdam, 1971, Chap 8, and references therein.
[26] K. Banaszek, Phys. Rev. A **57**, 5013 (1998).
[27] D. Achilles, C. Silberhorn, and I. A. Walmsley, Phys. Rev. Lett. **97**, 043602 (2006).
[28] A. D. Semenov, G. N. Gol'tsman, and A. A. Korneev, Physica C **351**, 349 (2001).
[29] R. J. McIntyre, IEEE Trans. Electron Devices **13**, 164 (1966).

VI: Conclusions

1. Summary

As a first step towards the integration of nanowire superconducting single photon detectors (SSPDs) with advanced optical structures, a process was optimized for the deposition of high-quality few-nm thick NbN films on GaAs and AlAs/GaAs-based DBRs (see chapter III).
Because of the requirement of compatibility with GaAs, the substrate temperature used for the depositions is T_s=400°C, in order to prevent As evaporation [1].
As GaAs and DBRs are highly mismatched substrates, the deposition parameters were first optimized with respect to the superconducting properties of NbN films on MgO substrates, which allow the growth of high crystal quality NbN films at low temperature [2, 3]. This made easier to separate the influence of stoichiometry from that of microstructure. The optimized deposition parameters were then used to grow NbN films on GaAs and DBRs, under the reasonable assumption (which was later checked and confirmed) that changing the substrate would not produce a change in film stoichiometry, but only in its microstructure.

NbN films ranging from 150nm to 3nm in thickness (th) were then deposited on epitaxial-quality single crystal MgO <100>, GaAs <100> and DBRs structures. The deposition technique is the current controlled DC magnetron sputtering (planar, circular balanced configuration) of Nb in an Ar + N_2 plasma.
NbN films deposited on MgO exhibit T_C=10 K, ΔT_C=0.8 K and RRR=R(20K)/R(300K)=0.8 for thicknesses of 4 nm, which are state of the art values, proof of the excellent quality of our low-temperature deposition process. The quality of films deposited on GaAs and on DBRs is lower than for NbN deposited on MgO, as for any thickness they systematically exhibit higher ΔT_C and lower T_C and RRR. However, 5.5 nm-thick NbN films on GaAs still exhibit T_C= 10.7 K, ΔT_C=1.1 K and RRR=0.7, which compares with 4.5 nm thick films on MgO, making them suitable for device fabrication. To our knowledge, the growth of such high quality NbN thin films on GaAs and DBRs, has never been reported in literature.
The degradation of the superconducting properties exhibited by NbN films on GaAs and DBRs was attributed to a highly defected microstructure, due both to a higher lattice misfit between NbN and GaAs and to a poorer quality of the substrate surface. Encouraging preliminary results show that the quality of these films can be improved both cleaning the GaAs/DBR substrate surface more effectively or adding an MgO buffer layer.

SSPDs were fabricated on few-nm thick NbN films (thickness 3 to 10nm) deposited under optimal conditions on MgO and GaAs by electron beam lithography (EBL) and reactive ion etching (RIE) at the Photonics and Nanotechnology Institute (IFN, Rome by A. Gaggero, Dr. F. Mattioli and Dr. R. Leoni). For standard detectors the active area is A_d=5x5 μm^2. The nanowires are 60 to 200 nm wide (w) and folded in a meander pattern with fill factors (f) ranging from 40% to 60% (see chapter III).

The devices were then characterized both electrically and optically (chapter IV). I-V curves of test structures were measured, from which it was possible to deduce important physical parameters used as figures of merit to estimate the superconducting properties of the nanowires (ρ, $\lambda(0)$, J_C), or for the design or the simulation of the devices (h, L_{hs}, L_{th}). The quality of the devices fabricated on GaAs is poorer than those on MgO, most likely due to the lower quality of NbN films deposited on GaAs and to issues related to the EBL nano-patterning step.
Measurements of detection efficiency (η) and of dark cont rate (DK) as a function of the bias current were performed on SSPDs fabricated on MgO. The best performance was exhibited by a w=100 nm,

f=40%, th=4 nm meander, showing η=20% and noise equivalent power NEP=10^{-16} W/Hz$^{1/2}$ (at λ=1.3 μm and T=4.2 K), which are state of the art values. This result showed for the first time that high performance NbN SSPDs can be realized on a different substrate and from a deposition process at lower temperature than previously reported (more recently, similar results were reported also by [4]).
High detection efficiencies could not be measured with SSPDs fabricated on GaAs, but it should be noted that at present only first-generation devices (fabricated on dusty GaAs substrates) have been tested. Better results are expected from devices fabricated on the improved NbN films grown on clean or MgO-buffered GaAs substrates.

Although SSPDs on MgO have shown high detection efficiency, the fabrication of the meander geometry is challenging and the production yield of high performance detectors has to be improved. Variations of the critical current along a nanowire are responsible for the wide distribution in efficiency values of nominally identical SSPDs.
The nanowire homogeneity issue was first addressed by fabricating meanders where each wire is separately contacted and by measuring the critical current distributions for the different wires. The results obtained show that the critical current uniformity is about 6% for closely packed meanders (f=40%), proof of the good nanowire homogeneity.
Furthermore, in order to understand the physical origin of the nanowire constrictions (i.e. regions of suppressed superconductivity) we performed a spatially-resolved characterization of the η of a long straight nanowire, followed by a high resolution SEM scan on its whole length. Two types of inhomogeneities were evidenced, corresponding to localized efficiency dips and peaks. The peaks likely correspond to constrictions. SEM observations did not evidence any width narrowing at the position of the efficiency peaks, which suggests that constrictions might be due to thickness or quality inhomogeneities of the film occurring during the film deposition or later in the process. On the other hand, the efficiency dips have been correlated with lithography problems discovered on SEM images but those defects do not affect the global efficiency as much as constrictions.

Finally, a new photon number resolving detector, the Parallel Nanowire Detector (PND), has been demonstrated (chapter V), which significantly outperforms existing approaches in terms of sensitivity, speed and multiplication noise in the telecommunication wavelength range. In particular, it provides a repetition rate (80 MHz) three orders of magnitude larger than any existing detector at telecom wavelength [5-7], and a sensitivity (NEP=4.2x10^{-18} W/Hz$^{1/2}$) one-two orders of magnitude better, with the exception of transition-edge sensors [7] (which require a much lower operating temperature).
An electrical equivalent model of the device was developed in order to study its operation. The modeling predicts a physical limit to the reset time of the PND, which is lower than initially estimated. Furthermore, the figures of merit of the device performance in terms of efficiency, speed and sensitivity ($\overline{\delta I}_{lk}$, f_0, SNR) are defined and their dependency on the design parameters (L_0, R_0, R_{out}, N) is analyzed.
Additionally, we developed modeling tools to fully characterize the device and an algorithm to estimate the photon number statistics of an unknown light using the PND. The reconstruction proved to be successful only for low photon fluxes, most likely due to the limited counting capability and the poor calibration of the detector.
The PND, with its high repetition rate and high sensitivity, is then suitable for measuring an unknown photon number probability distribution assuming accurate calibration and sufficient counting capability. Furthermore, by increasing the efficiency, the performance needed for the single-shot measurement of photon number can be reached. Finally, increasing the counting capability to 20-30 photons, the PND could be used as an “analog” detector with single-photon sensitivity, bridging the gap between conventional and single-photon detectors.

2. Future prospects

Some interesting issues could not be addressed during the four years of experimental activity whose results are presented in this report. The research lines that, according to the author, would be worth to follow in the future are presented in the following.

2.1. Fabrication

i. Thin film technology

As presented in chapter III, the superconducting properties of NbN thin films (th=90 to 120 nm) deposited on MgO and GaAs were optimized studying the effects of the variation of the nitrogen concentration (x_{N2}) and of the total pressure (P_{tot}) of the sputtering gas mixture on the critical temperature T_C, on the superconducting transition width ΔT_C and on the critical current density J_C. This optimizations were performed using a grooved target and it is known that target erosion affects the stoichiometry of reactively sputtered films [8]. However, 100 nm-thick NbN films deposited using fresh targets at the optimum x_{N2} (found using grooved targets) show T_C of ~16 K (close to the bulk value), which suggest that no significant improvement could be obtained further optimizing x_{N2}. Few-nm thick films (th<10 nm) are still far from this limit (T_C=8 to 13 K). It would be then interesting to investigate the dependency of the superconducting properties of few-nm thick NbN films on x_{N2} when performing the depositions with a fresh target, in order to check if the optimum x_{N2} is the same as that previously found, and eventually obtain an improvement of T_C.

In literature it is often reported a chemical wet etch of the substrates before deposition in order to remove native oxides or layers mechanically damaged during the polishing process (see e.g. [9] and [10], respectively). Thus , tests could be run to check if an enhancement in the quality of the films is achieved depositing NbN on chemically etched MgO and GaAs substrates.

The thickness of few-nm thick NbN films deposited on GaAs and DBRs could not be directly measured, as the NbN etch used in the AFM method (see chapter III) is selective for MgO but not for GaAs. Indeed, the thickness of was estimated measuring the thickness of the NbN film deposited on an MgO substrate in the same deposition run. Although thicker NbN films (whose thickness could thus be measured by the profilometer method) deposited on MgO and GaAs in the same deposition run always have the same thickness, the situation might be different for few-nm thick films. Indeed, in this latter case the deposition rate depends strongly on the sticking coefficient between NbN and the substrate. Therefore, the estimate of the thickness of few-nm thick films on GaAs and DBRs given by the measured thickness of films on MgO might not be accurate after all. An etch process for NbN selective for GaAs should then be developed.

The results obtained with NbN films deposited on GaAs substrates with an MgO buffer layer are very encouraging. It would be then important to continue with this approach. A few possible improvements are proposed in the following.

MgO buffer layer depositions have been performed up to now on a different sputtering system than that used for NbN deposition. This means that the vacuum must be broken and the samples transferred. MgO is very sensitive to moisture, so exposing few nm thick MgO films at the atmosphere could affect their quality. A process to deposit MgO buffer layers and NbN films in the same chamber and in the same vacuum cycle should be then developed.

Furthermore, up to now the thickness of MgO films has been measured only by a profilometer, which means that films thinner than ~20 nm could not be characterized accurately. A process to etch MgO on

GaAs selectively should then be developed, so the thickness of few-nm thick films could be measured with the AFM method described in chapter II.

Finally, it should be noted that all the optimizations which directly affect film crystal structure (and then indirectly its superconducting properties) have been performed without the feedback of structural analysis, but just characterizing the superconducting properties of the films. Therefore, changes in film structure could be only inferred from the changes in its superconducting properties. As our target was not the complete characterization of NbN films, but just the optimization of their superconducting properties, this approach could provide the necessary level of detail. This is true for a simple system, such as film+substrate. Dealing with more complex, multilayer structures (which is the case of MgO-buffered GaAs substrates already introduced), a more detailed analysis of film structure in terms of crystal phase, lattice parameter and microstructure might be a very useful guide for the optimization process.

ii. Device fabrication and design

At present, the fabrication of high efficiency SSPDs has still a very low yield. Although improving the yield remains a major target, it is a hard technological challenge as it implies further optimization of the thin film deposition process and of the EBL steps. A much easier way to obtain more high performance devices per fabrication run would be to integrate more devices on the 10x10 mm^2 sample. This can be achieved changing the actual design of the device pads (see chapter III). Indeed, instead of integrating twenty (4x5) 4-devices clusters electrically isolated from each other, we could let all the devices share the same ground. This would increase the number of devices per cm^2 of a factor 5.

The current design of the circular PND (see chapter III), conceived for the efficient coupling with the core of a telecom-wavelength optical fiber, has the drawback that the circular pixel is divided into N sections longitudinally. As the light beam coupled to it has a gaussian profile, the incident photons more likely reach the sections close to the centre of the pixel than those at the edges. Therefore, the chances are higher that, in a light pulse, more photons after the first hit the same (central) section and remain undetected. The circular PND could then be improved designing a structure with radial symmetry.

Moreover, as discussed in chapter V, the kinetic inductance of each section (L_0) of the PND influences its performance in terms of efficiency, speed and sensitivity. However, in the present design, L_0 is equal to the kinetic inductance of the detecting nanowire (bare device case, $L_0=L_{kin}$), so it is not a design parameter, because it is fixed by the nanowire width, by the meander filling factor, by the device active area and by the number of sections in parallel. A process could be then developed to integrate an inductor in series with the detecting nanowire of each section of the PND. For instance, this inductor can be simply an NbN nanowire wider than the detecting one, which thus remains superconducting during the device operation so that its contribution to the inductance L_0 is mostly kinetic.

2.2. Measurements and modeling

At present, the kinetic inductance of our devices (L_{kin}) has never been estimated directly, i.e. by measuring the phase of the reflection coefficient $S_{11}=(j2\pi fL_{kin}-50\Omega)/(j2\pi fL_{kin}-50\Omega)$ as a function of the input signal frequency (f). Knowing the value of the kinetic inductance per square of our films would very useful for the design. Moreover, as reported in [4, 11], measuring L_{kin} as a function of the bias current gives an important information about the degree of constriction of a device.

The model used in this work to simulate the PND operation and estimate its performance (see chapter V) is purely electrical, and it neglects the influence of the circuit in which the device is embedded on the hotspot resistance and on its lifetime, which has been proven to be significant [12]. A comprehensive model of the nanowire, which describes its thermal and electrical behavior, should then be developed in order to extend the simulation presented in chapter V to zones of the design parameter space where the present simplified model fails, but which are very interesting to investigate, such as the case of high number of sections in parallel with low L_{kin}, i.e. high counting capability and high speeds.

3. References

[1] K. Iizuka, K. Matsumaru, T. Suzuki, H. Hirose, K. Suzuki, and H. Okamoto, J. Cryst. Growth **150**, 13 (1995).
[2] S. Miki, Y. Uzawa, A. Kawakami, and Z. Wang, Electron. Comm. Japan II **85**, 77 (2002).
[3] Z. Wang, A. Kawakami, Y. Uzawa, and B. Komiyama, J. Appl. Phys. **79**, 7837 (1996).
[4] S. Miki, M. Fujiwara, M. Sasaki, B. Baek, A. J. Miller, R. H. Hadfield, S. W. Nam, and Z. Wang, Appl. Phys. Lett. **92**, 061116 (2008).
[5] M. Fujiwara, and M. Sasaki, Appl. Opt. **46**, 3069 (2007).
[6] L. A. Jiang, E. A. Dauler, and J. T. Chang, Phys. Rev. A **75**, 62325 (2007).
[7] D. Rosenberg, A. E. Lita, A. J. Miller, and S. W. Nam, Phys. Rev. A **71**, 1 (2005).
[8] N. N. Iosad, T. M. Klapwijk, S. N. Polyakov, V. V. Roddatis, E. K. Kov'ev, and P. N. Dmitriev, IEEE Trans. Appl. Supercond. **9**, 1720 (1999).
[9] J. R. Gao, M. Hajenius, F. D. Tichelaar, T. M. Klapwijk, B. Voronov, E. Grishin, G. Gol'tsman, C. A. Zorman, and M. Mehregany, Appl. Phys. Lett. **91**, 062504 (2007).
[10] A. Shoji, IEEE Trans. Mag. **27**, 3184 (1991).
[11] A. J. Kerman, E. A. Dauler, W. E. Keicher, J. K. W. Yang, K. K. Berggren, G. Gol'tsman, and B. Voronov, Appl. Phys. Lett. **88**, 111116 (2006).
[12] J. K. W. Yang, A. J. Kerman, E. A. Dauler, V. Anant, K. M. Rosfjord, and K. K. Berggren, IEEE Trans. Appl. Supercond. **17**, 581 (2007).

Appendix: Table of abbreviations

i. Deposition parameters

$\mathbf{f_{Ar}}$	argon flux
$\mathbf{f_{N2}}$	nitrogen flux
$\mathbf{I_c}$	cathode current
$\mathbf{P_{Ar}}$	partial pressure of argon in the chamber (before the plasma is turned on)
$\mathbf{P_{N2}}$	partial pressure of nitrogen in the chamber (before the plasma is turned on)
$\mathbf{P_{RF}}$	RF power (for MgO deposition)
$\mathbf{P_{tot}}$	total pressure in the chamber (before the plasma is turned on)
$\mathbf{r_d}$	deposition rate
$\mathbf{r_d^{(n)}}$	nomnal deposition rate
$\mathbf{r_n}$	target nitridization rate
$\mathbf{r_{s,NbN}}$	NbN sputtering rate
$\mathbf{T_d}$	deposition time
th, $\mathbf{t_h}$	film thickness
$\mathbf{th_n}$	nominal film thickness
$\mathbf{T_S}$	substrate temperature
$\mathbf{V_c}$	cathode voltage
$\mathbf{x_{N2}}$	nitrogen concentration: P_{N2}/Ptot

ii. SSPD geometrical parameters

$\mathbf{A_d}$	SSPD active area
f	meander filling factor
L	length of the nanowire
N	number of nanowires in series/parallel
w	width of the nanowire
th	thickness of the NbN film
$\mathbf{th_{MgO}}$	thickness of the MgO buffer layer

iii. SSPD physical parameters

$\mathbf{\Delta T_C}$	superconducting to normal transition width
$\mathbf{I_{hs}}$	hotspot current
$\mathbf{J_C}$	superconducting critical current density
$\mathbf{\lambda(0)}$	magnetic penetration depth at 0 K
$\mathbf{L_{hs}}$	minimum hotspot length
$\mathbf{L_{kin}}$	nanowire kinetic inductance
$\mathbf{L_{th}}$	NbN thermal healing length
$\mathbf{T_C}$	superconducting critical temperature
RRR	residual resistivity ratio
$\mathbf{R_{SSPD}}$	SSPD resistance

iv. Device optical parameters

α	absorbance
DK	dark count rate
η	SSPD single-photon quantm efficiency: $\alpha \cdot \eta^{I}$
η^{I}	nanowire intrinsic single-photon quantum efficiency
NEP	noise equivalent power
R	reflectivity
SDE	SSPD system detection efficiency: $\chi \cdot \eta$
χ	coupling efficiency

Acknowledgements

First of all, I would like to thank my thesis advisor, Prof Andrea Fiore. From the very first day his dedication to research has been an inspiring model for me. With his huge scientific knowledge and his physical intuitions he has been a constant source of ideas in the last four years. The hours we have spent on scientific discussions are countless. I also thank him for always believing in me and giving me so much freedom (and responsibility) in conducting my research, which made me grow as a scientist. He really taught me a lot.

I would like to thank Dr Roberto Leoni, Dr Francesco Mattioli and Alessandro Gaggero (Institute of Photonics and Nanotechnology (IFN), Rome) for their extraordinary work in optimizing the nanofabrication process of the devices, and for the continuous stimulating scientific discussions.

I would like to thank my colleague and friend Dr David Bitauld for his valuable collaboration to the characterization of the devices, which contributed significantly to most of the results presented in this report.

I would like to thank Prof Francis Lévy**,** Henri Jotterand and Dr Moushab Benkahoul (Laboratory of Thin Film Physics (LPCM), EPFL) for their collaboration to the thin film deposition process.

I would like to thank Prof Gregory Gol'tsman, Dr Alexander Korneev and Olga Minaeva (Moscow State Pedagogical University (MSPU), Moscow) for their collaboration in the characterization of the PNDs, for the fruitful exchange of scientific ideas and for their kind hospitality when I visited their labs.

I would like to thank my colleagues Dr Carl Zinoni and Dr Blandine Alloing, and Dr Benjamin Dwir (Laboratory of Physics of Nanostructures (LPN), EPFL) for the valuable scientific and technical advice they gave me in the first period of my PhD research.

I would like to thank Nicolas Leiser, Yoan and Damien Trolliet, and Roger Rochat for their technical support.

I would like to thank the students I had under my supervision for their master thesis and/or semester project: Pierre-Yves Vannay, Stephanie Hold and Alessandro Surrente. They did an outstanding work (which has partly been integrated in this report), showing uncommon dedication and competence.

I would like to thank Aline Gruaz, Oana Chiper, Margriet van Doorne and in particular Pierrette Paulou for their invaluable assistance in all the administrative matters.

I would also like to thank the president of the jury Prof Olivier Martin and the reviewers Prof Benoit Deveaud-Pledran, Prof Gregory Gol'tsman and Dr Jean-Philippe Poizat for evaluating my work and for the interesting discussion at the defense.

Finally, a special thanks to the group members who contributed in making the working environment very pleasant: Laurent Balet, Dr Nicolar Chauvin, Dr Philip Ridha, Saeedeh Jahanmiri Nejad, Matthias Skacel, Dr Pablo Moreno, Dr Lianhe Li, Dr Marco Rossetti, Dr Alexander Marcus and Dr Christelle Monat.

Francesco Marsili

Hertogstraat 27C
5611 PA Eindhoven (NL)
Mobile: +41786490609 (CH)
+31648630372 (NL)
Email: francesco.marsili@epfl.ch

Single
27 years old
Italian

EDUCATION

02.2005 – Present: Doctoral school in Photonics, the Swiss Federal Institute of Technology of Lausanne (EPFL), Switzerland. Working toward the degree (expected in 02.2009).

09.2004 – Present: Bachelor degree in Physics (Chemistry and technology of materials), University of Pisa, Italy. Working toward the degree (expected in 01.2009).

09.2002 – 07.2004: Master degree in Electronic Engineering (Micro-Electro-Mechanical Systems, MEMS), University of Pisa, Italy.
Degree grade: 110/110 cum laude.
Master diploma work: "*Realization of a low junction capacitance single electron transistor*".

09.1999 - 07.2002: Bachelor degree in Electronic Engineering, University of Pisa, Italy.
Degree grade: 110/110 cum laude.
Bachelor diploma work: "*Theoretical study of Coulomb Blockade effects in metallic nanostructures at low temperature*".

09.1994 – 07.1999: High school degree, Liceo Scientifico Statale G. Marconi, Piombino (LI), Italy. Degree grade: 100/100.

EXPERIENCE

09.2007 – Present: Visiting PhD student in the Photonics and Semiconductor Nanophysics Group of Prof. A. Fiore, Eindhoven University of Technology (TU/e), the Netherlands.

02.2005 – 09.2007: PhD candidate and assistant in the Quantum Devices Group of Prof. A. Fiore, EPFL.

09.2003 – 07.2004: Master diploma Candidate in the Information Engineering Institute, University of Pisa, under the supervision of Prof. A. Nannini.

PUBLICATIONS

1. D. Bitauld, F. Marsili, et al., "*NbN nanowire superconducting single photon detectors fabricated on MgO substrates*" J. Mod. Opt., *to be published* (2008).
2. F. Marsili, D. Bitauld, et al., "*Superconducting parallel nanowire detector with photon number resolving functionality*" J. Mod. Opt., *to be published* (2008).
3. A. Divochiy, F. Marsili, et al., "*Superconducting nanowire photon-number-resolving detector at telecommunication wavelengths*" Nature Photon. **2**, 302 - 306 (2008).
4. F. Marsili, D. Bitauld, et al., "*High efficiency NbN nanowire superconducting single photon detectors fabricated on MgO substrates from a low temperature process*" Opt. Express **16** (5), 3191-3196 (2008).
5. R. Leoni, A. Gaggero, et al., "*Characterization of Superconducting Single Photon Detectors Fabricated on MgO Substrates*" J. Low Temp. Phys. **151**, 580-584 (2008).
6. A. Korneev, Y. Vachtomin, et al., "*Single-photon detection system for quantum optics applications*" IEEE J. Sel. Topics Quant. Electron. **13** (4), 944-950 (2007).
7. F. Mattioli, R. Leoni, A. Gaggero et al., "*Electrical characterization of superconducting single-photon detectors*" J. Appl. Phys. **101** (5) (2007).
8. C. Zinoni, B. Alloing, et al., "*Single-photon experiments at telecommunication wavelengths using nanowire superconducting detectors*" Appl. Phys. Lett. **91** (3) (2007).

MAJOR CONFERENCE CONTRIBUTIONS

17-22.08.2008: 2008 Applied Superconductivity Conference (ASC 2008), Chicago, Illinois, USA (contributed oral).
25-28.09.2007: Single Photon Workshop 2007, Torino, Italy (contributed oral).
17-22.06.2007: The European Conference on Lasers and Electro-Optics (CLEO®/Europe 2007), Munich, Germany (contributed oral).

TEACHING

Winter semester 2006: Teaching assistant: "Metrology**"** course (Prof. R. Shaller and G.Germaud).
Supervisor of the semester work by student Alessandro Surrente.
Supervisor of the master diploma work by student Stephanie Hold.
Summer semester 2006: Teaching assistant: "Analysis IV" course (Dr. M. Cibils).
Supervisor of the semester work by student Pierre-Yves Vannay.
Supervisor of the semester-work by student Stephanie Hold.
Winter semester 2005: Teaching assistant: "Linear Algebra" course (Dr. A. Prodon).

SUMMER SCHOOLS

13-18.08.2006: "*Summer School of Advances in Photonics*", University of California, Berkeley (U.S.).
6-9.09.2005: "*The Photon: Generation, Detection and Application*", Bad Honnef (Germany).
18-30.07.2005: "*6th SCENET School on Superconducting Materials and Applications*", Turku (Finland).

LANGUAGES

Italian: mother-tongue.
English: fluent.
French: fluent.

COMPUTER LITERACY

Origin, LabVIEW, Matlab, SPICE, LASI, C++, Pascal, SQL, Microsoft Office.

PRIZES/OTHER ACCOMPLISHMENTS

05.2005: Medal of Excellence of the University of Pisa (Italy) for the Master degree in Electronic Engineering.
05.2003: Medal of Excellence of the University of Pisa (Italy) for the Bachelor degree in Electronic Engineering.
04.2002: Scholarship as a Socrates exchange student at Swansea University (Wales): declined.
1-10.09.1999: Scholarship offered by Soroptimist International at Luigi Bocconi Commercial University of Milan (Italy) for the seminar: "*Towards year 2000 challenges and answers for new generations*".